Landscape evolution at a young rifted margin: the Loreto region of Baja California Sur, Mexico.

Chris Mark

Submitted in total fulfilment of the requirements for the award of the degree of Doctor of Philosophy

Imperial College London

Department of Earth Science and Engineering

May 2013

Declaration

I declare that this thesis is solely the result of my own work during the course of my PhD studies, except for those parts indicated in the text for which appropriate and full references have been provided.

Chris Mark

May 2013

Abstract

Continental rifts are commonly flanked by zones of high elevation. Proposed uplift mechanisms include active and induced asthenospheric upwelling, and isostatically driven lithospheric flexure. Although these hypotheses make testable and distinct predictions of the relative timing of crustal extension and rift flank uplift, the difficulty of closely constraining these processes in modern or ancient rift zones means that the issue remains controversial. This study focuses on the Loreto rift segment of the Baja California peninsula, which forms the western margin of the Late Neogene Gulf of California rift. The Loreto region is characterised by a prominent east-facing rift escarpment which separates a low-elevation coastal plain, which hosts rift-bounding faults, from a west-tilted, topographically asymmetric rift flank, incised by west-draining canyons. On the coastal plain, slip on the rift-bounding Loreto fault has driven westward retreat of the escarpment. Footwall exhumation due to escarpment retreat is reconstructed using the apatite fission track and apatite (U-Th)/He low-temperature thermochronometers to constrain the minimum age of escarpment retreat and thus also Loreto fault slip. On the rift flank west of the escarpment, canyon incision depths are obtained by analysis of digital elevation models and used as a proxy for minimum uplift magnitude. The timing and rate of rift flank canyon incision, a proxy for the timing and magnitude of rift flank surface uplift, is constrained using $^{40}Ar/^{39}Ar$ dating of lavas which display cut and fill relations with the rift flank canyons. These lavas also provide a resistant cap atop canyon interfluve mesas, and the extent of this resistant cap likely controls the extent of rift flank catchment denudation in response to uplift. The principal finding of this thesis is that rift flank surface uplift was coeval with crustal extension at Loreto, consistent with predictions made by models of rift flank uplift driven by the flexurally-distributed isostatic response to the lithospheric unloading associated with crustal extension.

Contents

List of figures and tables

Acknowledgements

I have been told that this is the hardest part of a thesis to write. Personally, though, I can't help feeling that the two hundred or so pages that follow were actually rather more tricky. However, I certainly have a long list of people and organisations to thank. Firstly, I would like to thank my supervisor, Sanjeev Gupta. Not only is he an inspirational teacher, but his wonderfully eclectic approach to science and firm conviction that geology is a discipline best discussed in the pub have helped make the past four years hugely enjoyable. His off-road driving skills and relaxed attitude to military checkpoints also came in very handy in the field. Also in the field, massive thanks to Moira Cruickshanks and Tristan Horner for all your help, and managing to remain calm in the face of such terrors as Mexican HGV drivers, armed ranchers, scorpions (under every rock!), and my cooking. It wouldn't have been the same without you both! In the lab, huge thanks are owed to Andy Carter at UCL, who displayed endless patience while explaining the finer points of low-temperature thermochronology to me. On my trips north of the border to SUERC, I was made to feel really welcome by Darren Mark, Ross Dymock, and Jim Imlach, who also managed to teach me a few things about argon isotopes at the same time – thanks guys! For getting us permission to work in Mexico, and many useful insights into Gulf geology, warm thanks to Arturo Martín at CICESE; likewise, sincere thanks to Cécile Gautheron at UMR-IDES for stepping in at short notice to permit the apatite helium analysis. Thanks also to Tobias Schwennicke at UABC, Paul Umhoefer at NAU, Becky Dorsey at UO, and Estelle Mortimer at UL for insightful discussions on the geology of Loreto, and to Alex Densmore at DU for providing the swath profiler MATLAB tool. Grateful thanks to the Mexican authorities for permitting us to carry out fieldwork and collect samples. Conducting fieldwork in Mexico whilst based in London is expensive, so thanks to NERC and Santander UK for providing funding (NERC via doctoral training grant NE/G523547/1 and argon isotope facility grant IP-1153-

1109, and Santander via an International Mobility Award). Thanks also to the many ranchers in Mexico who were both kind and helpful to the strange foreigners who wanted to walk all over their land just to look at the rocks, particularly Señor Cunningham who remembered his Scottish great-grandfather; Thomas Baumgarten and his wife Rosa; and Ian and Sam (and their barbeque). Thanks to Mum, Dad, and Jen; all your love and support have made this possible; I blame all the hikes I was taken on as a kid for sparking my interest in geology! Thanks to Arlette and Sarah, who each in your own way gave me the confidence to start and finish this project; to the usual suspects at Glenroy and Wakeman who kept me supplied with laughter and cups of tea; and to all my friends at Imperial, particularly the Fellwanderers Club. Finally, thanks to the armed squad of Mexican marines who raided our camp one evening in Baja for being surprisingly polite once they realised we weren't *narcos*, just foolish *gringos*.

"Trying to remember the Gulf is like trying to recreate a dream. And since we have returned, there is always in the back of our minds the positive drive to go back again. If it were lush and rich, one could understand the pull, but it is fierce and hostile and sullen. The stone mountains pile up to the sky, and there is little fresh water. But we know we must go back if we live, and we don't know why."

John Steinbeck, *The Log from the Sea of Cortez.*

1. Introduction

"I have observed that before beginning to write their histories, the most famous chroniclers compose a prologue in exalted language, in order to give lustre and repute to their narrative, and to whet the curious reader's appetite."

Bernal Diaz, *The Conquest of New Spain*.

1.1 Study motivation

Continental rifts and passive margins are often flanked by regions of high topography. The existence of elevated topography atop thinned crust is counterintuitive, given that mountain building is more usually associated with crustal thickening (Airy, 1855). A number of mechanisms have been proposed to explain rift flank uplift, principally topographic doming as a result of pre-rift active asthenospheric upwelling; upwelling induced by the formation of convectional instabilities during lithospheric thinning; and isostatic flexure in response to lithospheric unloading during rifting (Sengor and Burke, 1978; Buck, 1986; Braun and Beaumont, 1989; Weissel and Karner, 1989; Ziegler, 1992; Huismans et al., 2001; Allen and Allen, 2005; Kusznir and Karner, 2007). Crucially, these hypotheses make testable predictions of the relative timing of rift flank uplift and crustal extension. Asthenospheric upwelling prior to rifting generates surface doming, the wavelength and amplitude of which are dependent on the magnitude of the upwelling. If the resulting tensional stresses imposed on the lithosphere by the uplift are sufficient to trigger extension, then the elevated topography of the surface dome may be inherited by the non-extended flanks of the developing rift (Cox 1989; Ebinger et al, 1989; Underhill and Partington, 1993; Moucha and Forte, 2011). In this instance, therefore, surface uplift predates crustal extension. Other hypotheses predict synchroneity of surface uplift and extension. The mechanical and erosional thinning of the crust which occurs during extension and lithospheric rupture will produce an isostatic response. This will result in regional uplift or subsidence, as dictated by the vertical distribution ('necking depth') of crustal thinning and the consequent replacement of crustal material by denser mantle from beneath and less dense air, water, and sediment from above (Braun and Beaumont, 1989). The vertical motions which are the outcome of the competition between these processes will be distributed flexurally, with a wavelength and amplitude largely dependent on the strength of the lithosphere and the

magnitude of the resultant vertical motion. As a result, any uplift occurring as a result of the isostatic response to crustal thinning may be transmitted beyond the rift zone to the non-extended flanks, and would occur synchronously with rifting (Braun and Beaumont, 1989; Weissel and Karner, 1989; Kusznir and Karner, 2007). Crustal thinning during rifting will also result in the compression of isotherms within the rift zone, as the hotter lower lithosphere and asthenosphere are advected towards the surface. This process generates the elevated surface heat flows relative to neighbouring non-extended terranes which are characteristic of rift zones (Ziegler, 1992). The consequent juxtaposition of hot rift zone and cool non-extended rift flanks can induce localised small-scale convection of the upper asthenosphere and lower lithosphere, which in turn can drive rift flank uplift through a combination of upward flow beneath the flank margin and increased upper lithospheric buoyancy driven by thermal expansion. Surface uplift driven by induced small-scale convection is expected to operate synchronously with, or shortly lagging, crustal extension (Steckler, 1985; Buck, 1986; Huismans et al, 2001). This is also the case for models of rift flank uplift driven by depth-dependent stretching, which posit greater extension of the lower lithosphere relative to the upper lithosphere. Such a distribution of stretching would emplace hotter, more buoyant extended lower lithosphere beneath non-extended, colder upper lithosphere, generating a buoyant isostatic response beneath the rift flanks (Royden and Keen, 1980; Rowley and Sahagian, 1986). Post-rift, the lateral juxtaposition of thinned or ruptured lithosphere, and the associated high surface heat flow, with non-extended, cooler rift flanks, can generate rift flank uplift by thermal conduction and the associated increase in buoyancy. However, numerical modelling indicates that even prolonged post-rift conductive heating fails to generate surface uplift of more than ~250 m (Leroy et al, 2008).

In principle, therefore, the mechanism of rift flank uplift can be identified by closely constraining the timing of surface uplift and crustal extension. However, in practice the ages of these processes have proved difficult to constrain at the ancient rifts which are commonly studied. This study therefore

examines the development of topography at a young rifted margin where key rift-related structures have been little affected by post-rift processes of erosion and burial: the Gulf of California.

1.2 The Gulf of California and the Loreto rift segment

The Late Neogene Gulf of California is a highly oblique transtensional rift, which developed to accommodate divergent Pacific/North American plate motion subsequent to foundering of the oceanic Farallon plate, although the details of the tectonic sequence which led to strain localisation in the Gulf and lithospheric rupture are disputed (Karig and Jensky, 1972; Stock and Hodges, 1989; Fletcher et al., 2007; Umhoefer, 2011). Prior to rifting, the margin of North America experienced repeated episodes of widespread volcanism from at least the Oligocene onwards, driven by long-lived subduction of the Farallon plate throughout much of the Cenozoic (Ferrari et al, 2002). Divergent plate motion is currently accommodated by a system of en-echelon spreading centres and transform faults which runs the length of the Gulf (Moore and Buffington, 1968). The Baja California peninsula, which forms the western margin of the rift, has undergone near-complete transfer from North America to the Pacific plate (Dixon et al., 2000), and is characterised by a prominent east-facing rift escarpment which runs the length of the peninsula, dividing a west-tilted uplifted rift flank to the west from a low-elevation coastal plain to the east which hosts rift-bounding faults and rare syn-rift basins. The youth of the rift means that the rift-related structures and landscape are well-preserved; this combines with the excellent rock exposure arising from the arid environment to render the Gulf an ideal natural laboratory in which to study the landscape response to rifting.

This study focuses primarily on the Loreto rift segment. Here, the escarpment has retreated westward from the rift-bounding east-dipping Loreto fault, exposing a basement piedmont in the fault footwall. The hangingwall of the Loreto fault hosts a well-studied syn-rift basin, largely filled with coarse clastic deposits (McLean, 1988; Umhoefer et al., 1994; Dorsey and Umhoefer, 2000; Mortimer et al, 2005). West of the escarpment crest, the west-tilted rift flank has been incised by a network of west-draining canyons, which attain depths of ~400-600 m at the escarpment crest,

where many have been beheaded. These canyons exhibit cut and fill relationships to lava flows which have been erupted across the rift flank near-continuously since the foundering of the Farallon plate (Sawlan and Smith, 1984; Bellon et al., 2006). However, despite considerable previous work on the stratigraphy and structure of the Loreto segment coastal plain and rift flank, the timing of the onset of crustal extension remains poorly constrained. The mechanism of rift flank uplift remains unknown, although asthenospheric upwelling hypothesised to have occurred through a proposed slab window which opened beneath the peninsula during the final subduction of the Farallon plate may have been responsible (Ferrari et al., 2002; Fletcher et al., 2007; Castillo, 2008). Alternately, the elevated topography may possibly have been inherited from older subduction-generated landforms, or rift flank uplift may have been driven by one of the syn-rift processes outlined in the previous section. The key to determining the mechanism of rift flank uplift will be the timing of surface uplift and crustal extension, and the attraction of the Loreto area is that the exceptional preservation of the rift landscape makes this possible. On the rift flank, the intersection of the west-draining canyons with the dateable marker units of the lavas allows the timing of incision to be determined, which can be used as proxy for surface uplift (e.g. Schildgen et al, 2007). On the eastern coastal plain, escarpment retreat and piedmont exhumation, driven by slip on the Loreto fault, have exposed plutonic basement which is a suitable target for low-temperature thermochronologic techniques. These permit the timing of exhumation, a proxy for the timing of fault initiation and crustal extension, to be determined. Together, these comprise the two key unknowns which this study targets, together with the development of the rift flank landscape in response to uplift.

1.3 Aims

The project aims to:

· Constrain the timing of crustal extension at the Loreto fault.

· Constrain the timing of rift flank uplift at the Loreto rift segment.

· Determine the mechanism of rift flank uplift at the Loreto segment.

· Describe the response of the rift flank catchments to transient uplift.

· Determine the factors controlling the extent of the rift flank catchment response to uplift.

1.4 Thesis structure

In **Chapter 2**, the exploitation of the basement piedmont west of the rift-bounding Loreto fault to constrain the timing of escarpment retreat is described. The apatite fission track (AFT) and apatite (U-Th)/He (AHe) low-temperature thermochronometers, which are sensitive to the thermal changes associated with exhumation of shallow crustal levels, are used to constrain the timing of piedmont denudation and escarpment retreat. As escarpment retreat and piedmont denudation are driven by slip on the Loreto fault, the timing of piedmont denudation provides a proxy for the age of the Loreto fault and thus for the onset of crustal extension at Loreto. In **Chapter 3**, the timing and mechanism of rift flank uplift at the Loreto segment is investigated. LANDSAT imagery, digital elevation models, and field observations are used to demonstrate that the pre-uplift landscape is preserved atop the interfluve mesas which separate the west-draining rift flank canyons. The depths of canyon incision below this landscape provide incision magnitudes. The $^{40}Ar/^{39}Ar$ method is used to date lava flows which form part of this landscape and which have been incised by the rift flank canyons; these lavas must pre-date the canyon networks and therefore provide a maximum age of incision. Lavas which have flowed into the canyons during and after incision are also dated using the $^{40}Ar/^{39}Ar$ method, and provide a minimum age for canyon incision. Climate change is discussed and dismissed as a cause of canyon incision, and incision is inferred to have been driven by rift flank uplift. The timing of canyon incision therefore provides a proxy for the timing of rift flank uplift. Synchronous rift flank uplift and crustal extension at the Loreto rift segment indicate that rift flank uplift was driven by the flexurally-distributed isostatic adjustment to lithospheric rupture during rifting. Simple two-dimensional modelling indicates that isostatic flexure can explain the magnitude of observed rift flank uplift, and that there is no need to invoke asthenospheric upwelling through an

inferred slab window beneath the Baja California peninsula, as hypothesised by Fletcher et al. (2007). **Chapter 4** considers the spatial variation of the response of the west-draining rift flank catchments to uplift. LANDSAT imagery and digital elevation models are used to map the extent and composition of the relict landscape on the rift flank west of the Loreto rift segment and neighbouring Timbabichi segment. Higher proportions of resistant lava are associated with greater interfluve mesa preservation, indicating that the response of catchments dominated by fluvial processes to transient uplift may be strongly influenced by lithology. **Chapter 5** provides a brief summary of the previous chapters, and outlines proposed future work around the Gulf of California.

1.5 References

Airy, G.B., 1855, On the computation of the effect of the attraction of mountain-masses, as disturbing the apparent astronomical latitude of stations of geodetic surveys: Philosophical Transactions of the Royal Society, v. 145, p. 101–104.

Allen, P.A., and Allen, J.R., 2005, Basin Analysis: Blackwell Publishing, Malden, USA.

Bellon, H., Aguillón-Robles, A., Calmus, T., Maury, R.C., Bourgois, J., and Cotten, J., 2006, La Purísima volcanic field, Baja California Sur (Mexico): Miocene to Quaternary volcanism related to subduction and opening of an asthenospheric window: Journal of Volcanology and Geothermal Research, v. 152, no. 3-4, p. 253–272.

Braun, J., and Beaumont, C., 1989, A physical explanation of the relation between flank uplifts and the breakup unconformity at rifted continental margins: Geology, v. 17, no. 8, p. 760-764.

Buck, W.R., 1986, Small-scale convection induced by passive rifting: the cause for uplift of rift shoulders: Earth and Planetary Science Letters, v. 77, p. 362–372.

Castillo, P.R., 2008, Origin of the adakite-high-Nb basalt association and its implications for postsubduction magmatism in Baja California, Mexico: Geological Society of America Bulletin, v. 120, no. 3-4, p. 451–462.

Cox, K., 1989, The role of mantle plumes in the development of continental drainage patterns: Nature, v. 342, no. 21, p. 873–877.

Dixon, T., Farina, F., DeMets, C., and Suarez-Vidal, F., 2000, New kinematic models for Pacific-North America motion from 3 Ma to present, II: Evidence for a “Baja California shear zone:” Geophysical Research Letters, v. 27, no. 23, p. 3961–3964.

Dorsey, R.J., and Umhoefer, P.J., 2000, Tectonic and eustatic controls on sequence stratigraphy of the Pliocene Loreto basin, Baja California Sur, Mexico: GSA Bulletin, v. 112, no. 2, p. 177–199.

Ebinger, C.J., Bechtel, T.D., Forsyth, D.W., and Bowin, C.O., 1989, Effective elastic plate thickness beneath the East african and Afar Plateax and dynamic compensation of the uplifts: Journal of Geophysical Research, v. 94, no. B3, p. 2883–2901.

Ferrari, L., Lopez-Martinez, M., and Rosas-Elguera, J., 2002, Ignimbrite flare-up and deformation in the southern Sierra Madre Occidental, western Mexico: Implications for the late subduction history of the Farallon plate: Tectonics, v. 21, no. 4, DOI: 10.1029/2001TC001302.

Fletcher, J.M., Grove, M., Kimbrough, D., Lovera, O., and Gehrels, G.E., 2007, Ridge-trench interactions and the Neogene tectonic evolution of the Magdalena shelf and southern Gulf of California: Insights from detrital zircon U-Pb ages from the Magdalena fan and adjacent areas: GSA Bulletin, v. 119, no. 11-12, p. 1313–1336.

Huismans, R., Podladchikov, Y.Y., and Cloetingh, S., 2001, Transition from passive to active rifting: relative importance of asthenospheric doming and passive extension of the lithosphere: Journal of Geophysical Research, v. 106, no. B6, p. 11,271–11,291.

Karig, D.E., and Jensky, W., 1972, The proto-Gulf of California: Earth and Planetary Science Letters, v. 17, p. 169–174.

Kusznir, N.J., and Karner, G.D., 2007, Continental lithospheric thinning and breakup in response to upwelling divergent mantle flow: application to the Woodlark, Newfoundland and Iberia margins: Special Publications of the Geological Society of London, v. 282, p. 389–419.

Leroy, M., Gueydan, F., and Dauteuil, O., 2008, Uplift and strength evolution of passive margins inferred from 2-D conductive modelling: Geophysical Journal International, v. 172, no. 1, p. 464–476.

McLean, H., 1988, Reconnaissance geologic map of the Loreto and part of the San Javier quadrangles, Baja California Sur, Mexico: Map MF1799, USGS.

Moore, D.G., and Buffington, E.C., 1968, Transform Faulting and Growth of the Gulf of California Since the Late Pliocene: Science, v. 161, p. 1238–1241.

Mortimer, E., Gupta, S., and Cowie, P., 2005, Clinoform nucleation and growth in coarse-grained deltas, Loreto basin, Baja California Sur, Mexico: a response to episodic accelerations in fault displacement: Basin Research, v. 17, p. 337-359.

Moucha, R., and Forte, A.M., 2011, Changes in African topography driven by mantle convection: Nature Geoscience, v. 4, no. 8, p. 707–712.

Rowley, D.B., and Sahagian, D., 1986, Depth-dependent stretching: A different approach: Geology, v. 14, p. 32–35.

Royden, L., and Keen, C.E., 1980, Rifting processes and thermal evolution of the continental margin of eastern Canada determined from subsidence curves: Earth and Planetary Science Letters, v. 51, p. 343–361.

Sawlan, M.G., and Smith, J.G., 1984, Petrological characteristics, age, and tectonic setting of Neogene volcanic rocks in northern Baja California Sur, Mexico, *in* Frizzel, V.A. ed., Geology of the Baja California Peninsula, Pacific Section, Society of Economic Paleontologists and Mineralogists, p. 237–251.

Schildgen, T.F., Hodges, K. V, Whipple, K.X., Reiners, P.W., and Pringle, M.S., 2007, Uplift of the western margin of the Andean plateau revealed from canyon incision history, southern Peru: Geology, v. 35, no. 6, p. 523–526.

Sengor, A.M.C., and Burke, K., 1978, Relative timing of rifting and volcanism on Earth and its tectonic implications: Geophysical Research Letters, v. 5, no. 6, p. 419–421.

Steckler, M.S., 1985, Uplift and extension at the Gulf of Suez: indications of induced mantle convection: Nature, v. 317, no. 12, p. 135–139.

Stock, J.M., and Hodges, K.V., 1989, Pre-Pliocene extension around the Gulf of California and the transfer of Baja California to the Pacific plate: Tectonics, v. 8, p. 99–115.

Umhoefer, P.J., 2011, Why did the Southern Gulf of California rupture so rapidly?—Oblique divergence across hot, weak lithosphere along a tectonically active margin: GSA Today, v. 21, no. 11, p. 4–10.

Umhoefer, P.J., Mayer, L., and Dorsey, R.J., 1994, Tectonics of the Pliocene Loreto basin, Baja California Sur, Mexico, and evolution of the Gulf of California: Geology, v. 22, p. 649–652.

Underhill, J.R., and Partington, M.A., 1993, Jurassic thermal doming and deflation in the North Sea: implications of the sequence stratigraphic evidence, *in* Parker, J.R. ed., Petroleum Geology of Northwest Europe: Proceedings of the 4th Conference, The Geological Society, London, p. 337–345.

Weissel, J.K., and Karner, G.D., 1989, Flexural uplift of rift flanks due to mechanical unloading of the lithosphere during extension: Journal of Geophysical Research, v. 94, no. B10, p. 13919–13950.

Ziegler, P.A., 1992, Plate tectonics, plate moving mechanisms and rifting: Tectonophysics, v. 215, no. 1-2, p. 9–34.

2. Low-temperature thermochronology of the Loreto rift segment

"How many years can a mountain exist, before it is washed to the sea?"

Bob Dylan, *The Times They Are A-Changing*.

2.1 Introduction

2.1.1 Study aim

The Gulf of California is a youthful, highly oblique rift which initiated during the Late Miocene in response to a major plate boundary reorganisation, resulting in the transfer of the Baja California Peninsula from North America to the Pacific plate. Subsequent to foundering of the oceanic Farallon plate beneath North America between ~15-12 Ma, Pacific/North America relative motion was accommodated by extension of North America inboard of the former subduction zone, eventually leading to lithospheric rupture and the onset of oceanic spreading at ~6-3 Ma (Lonsdale, 1991; Lizarralde et al., 2007). This process provides a modern-day analogue for the terrane translation and accretion events often inferred from ancient active margins, which are thought to be an important process of continent growth (Umhoefer and Dorsey, 1997; Umhoefer, 2011). However, the early spatial distribution and timing of extension in the Gulf of California remain poorly understood. In particular, the question of whether early deformation prior to the onset of extension around the Gulf was accommodated east of the Gulf, on pre-existing faults of the southern Basin and Range province, remains unanswered. Seiler et al. (2011) reported that the onset of extension along the western margin of the rift in the northern Gulf occurred at ~9-7 Ma, post-dating the destruction of the Farallon plate by at least ~5-3 Ma, and hypothesised that extension was accommodated east of the Gulf region during this time. It is unclear whether this delayed onset of faulting along the western rift-bounding faults is symptomatic of the whole western Gulf margin, as the ages of extensional structures in the southern Gulf are poorly known. The aim of this study is therefore to determine the timing of extension along a major rift segment of the western rift margin in the southern Gulf, to better constrain the distribution and timing of deformation during rift development. This study focusses on the Loreto rift segment, situated on the western margin of the

southern Gulf (Figure 2.1). The Loreto segment is characterised by an array of rift-bounding east-dipping normal faults and monoclines hosted in a narrow coastal plain which lies east of the Main Gulf Escarpment (MGE), a prominent east-facing rift escarpment which runs the length of the Baja California Peninsula. Despite being structurally and stratigraphically well understood (McLean, 1988; Zanchi, 1994; Umhoefer et al., 1994; Umhoefer and Stone, 1996; Dorsey and Umhoefer, 2000; Dorsey et al., 2001; Umhoefer et al., 2002; Willsey et al., 2002; Mortimer et al., 2005; Mortimer and Carrapa, 2007), a detailed chronology of rift development at the Loreto segment prior to the mid-Pliocene is lacking. To remedy this, this study exploits the presence of an eroded basement piedmont on the footwall of the Loreto fault east of the MGE. The apatite fission track (AFT) and apatite (U-Th)/He (AHe) thermochronometers, commonly used to detect episodes of exhumation affecting shallow crustal levels, are used to obtain the timing of escarpment retreat and the resulting piedmont exhumation. As this progressive unroofing of the piedmont is driven by slip on the Loreto fault, it provides a proxy for the age of extension at Loreto.

2.1.2 Geological and tectonic setting of southern Baja California

Observations of seafloor magnetic anomalies offshore western North America (Figure 2.1) indicate that the Farallon plate, subducting beneath North America since at least the Late Cretaceous (Liu et al., 2008), fragmented as the Pacific-Farallon spreading ridge approached the North America trench (Lonsdale, 1991; Michaud et al., 2006; McCrory et al., 2009). The Farallon plate segment adjacent to northern Baja California between the Arguello and Soledad fracture zones, including the associated ridge, was wholly subducted at ~16-14 Ma (Lonsdale, 1991; Wilson et al, 2005), while the Guadalupe and Soledad microplates to the south ceased spreading and subducting at ~14.7-13.7 Ma (Lonsdale, 1991), or possibly as late as ~12.5 Ma (Wilson et al, 2005), and were captured by the Pacific plate. South of the Guadalupe microplate, the Magdalena microplate developed in a more complex manner: the ridge fragmented as it approached the trench, and between ~15-14 Ma these

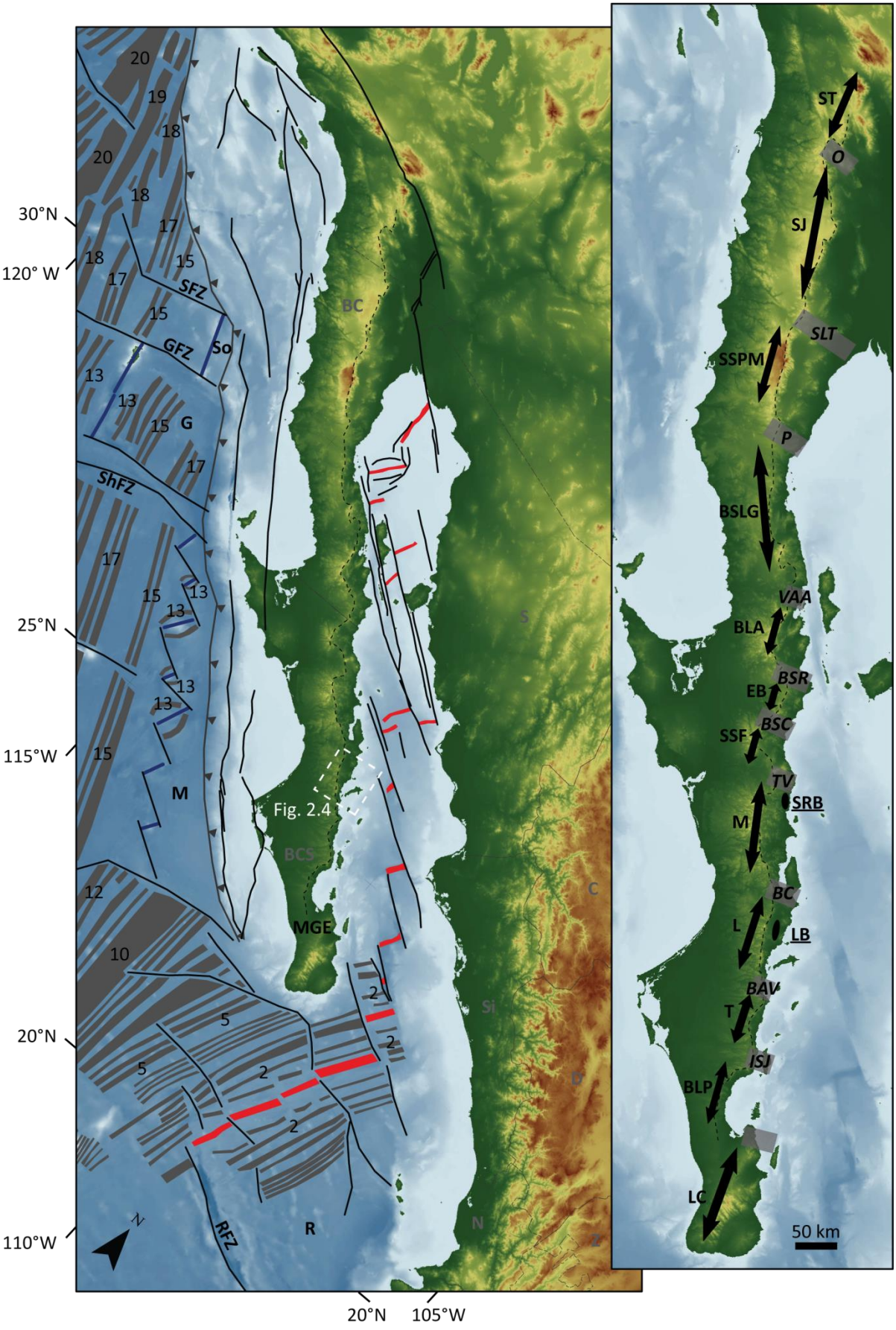
30°N
120° W
25°N
115°W
20°N
110°W
20°N
105°W
SFZ
GFZ
So
ShFZ
G
M
MGE
RFZ
R
BC
BCS
S
C
Si
D
N
Z
Fig. 2.4
ST
O
SJ
SLT
SSPM
P
BSLG
VAA
BLA
BSR
EB
BSC
SSF
TV
SRB
M
BC
L
LB
BAV
T
ISJ
BLP
LC
50 km

Figure 2.1 (Previous page): Overview of the Gulf of California. *Main figure shows topography and bathymetry from Global Multi-Resolution Topography (GMRT) synthesis (Ryan et al., 2009); seafloor magnetic anomaly locations with ages in Ma (Lonsdale, 1991; Tian et al., 2011); Farallon-derived microplates; extinct Pacific/Farallon spreading ridges (blue); active spreading ridges (red); major transform and fracture zones (black lines); location of the Main Gulf Escarpment (MGE) crest (black dashed line); and Mexican state boundaries (grey dashed lines). Fracture zones: SFZ – Soledad fracture zone; GFZ – Guadalupe fracture zone; ShFZ – Shirley fracture zone; RFZ – Rivera fracture zone. Microplates: So – Soledad microplate; G – Guadalupe microplate; M – Magdalena microplate; R – Rivera microplate. States: BC – Baja California; BCS – Baja California Sur; S – Sonora; Si – Sinaloa; C – Chihuahua; D – Durango; N – Nayarit. Inset shows rift segments, accommodation zones, and selected onshore rift basins. Rift segments: ST – Salton trough; SJ – Sierra Juarez; SSPM – Sierra San Pedro Martír; BSLG – Bahía San Luis Gonzaga; BLA – Bahía de Los Angeles; EB – El Barril; SSF – Sierra San Francisco; M – Mulegé; L – Loreto; T – Timbabichi; BLP – Bahía de La Paz; LC – Los Cabos. Accommodation zones (italicised): O – Ocotillo; SLT – Sierra Las Tinajas; P – Puertecitos; VAA – Valle Agua Amarga; BSR – Bahía San Rafael; BSC – Bahía San Carlos; TV – Tres Virgenes; BC – Bahía Concepción; BAV – Bahía Agua Verde; ISJ – Isla San Jose (Axen, 1995). Basins: LB – Loreto basin; SRB – Santa Rosalía basin.*

fragments rotated 45-60° clockwise, likely in response to a loss of slab pull following slab detachment (Lonsdale, 1991; Tian et al., 2011). Spreading probably ceased at ~12.5-11.5 Ma (Lonsdale, 1991; Tian et al, 2011), although it may have continued at a greatly reduced rate until as late as ~8-7 Ma (Michaud et al, 2006). Subduction also ceased during this time, likely shortly after ridge rotation.

Following foundering of the Farallon slab and the cessation of spreading, divergent Pacific-North America motion was accommodated by deformation of North America. This was accomplished by a major plate boundary reorganisation during which the Gulf of California developed as the new

Pacific/North America plate boundary, resulting in near-complete transfer of Baja California to the Pacific plate (Dixon et al., 2000). Rifting of the Gulf of California was thus driven by divergent plate motion, although why the plate boundary jumped westward into North America is unclear (Umhoefer, 2011). A prominent role has been proposed for active asthenospheric upwelling through a slab window opened beneath the Gulf region by the combination of ridge subduction in the north and slab tear-off following ridge-trench collision in the south, which may have thermally weakened the overlying lithosphere (Ferrari et al., 2002; Fletcher et al., 2007; Castillo, 2008). Alternately, the location of the volcanic arc generated by prolonged Farallon subduction may have provided the weak zone which focussed extension in the Gulf region (Umhoefer, 2011).

Early models envisaged rifting as a two-stage process, with transtensional plate motion initially kinematically partitioned into two zones either side of the Baja California microplate (Figure 2.2). Between ~12.5-11.5 Ma and ~6 Ma, a series of shear zones west of Baja California accommodated dextral strike-slip motion, while orthogonal NE-directed extension occurred in the Gulf region, forming a 'proto-gulf'. Subsequent to ~6 Ma, motion on the offshore shear zone decreased as Baja California was increasingly transferred to the Pacific plate and the Gulf became a region of integrated transtension, culminating in the current arrangement of en-echelon oceanic spreading centres linked by an array of shear zones (Stock and Hodges, 1989; Lonsdale, 1991; Oskin et al., 2001). However, subsequent studies have challenged this two-stage 'proto-gulf' model; both Michaud et al. (2006) and Fletcher et al. (2007) argued that the offshore shear zone has accommodated transtensional strain since ~12.5 Ma, while Seiler et al. (2010) showed that transtensional deformation in the northern Gulf likely began at ~9-8 Ma. These authors proposed an alternative model of integrated transtensional deformation across the Gulf region and offshore shear zone subsequent to the cessation of Pacific-Farallon spreading at ~12.5-11.5 Ma. Recent seismic surveys indicate that this led to lithospheric rupture and the onset of oceanic spreading in the southern and central Gulf between ~6-3 Ma (Lizarralde et al., 2007). A summary of this controversy is given by Fletcher et al. (2007).

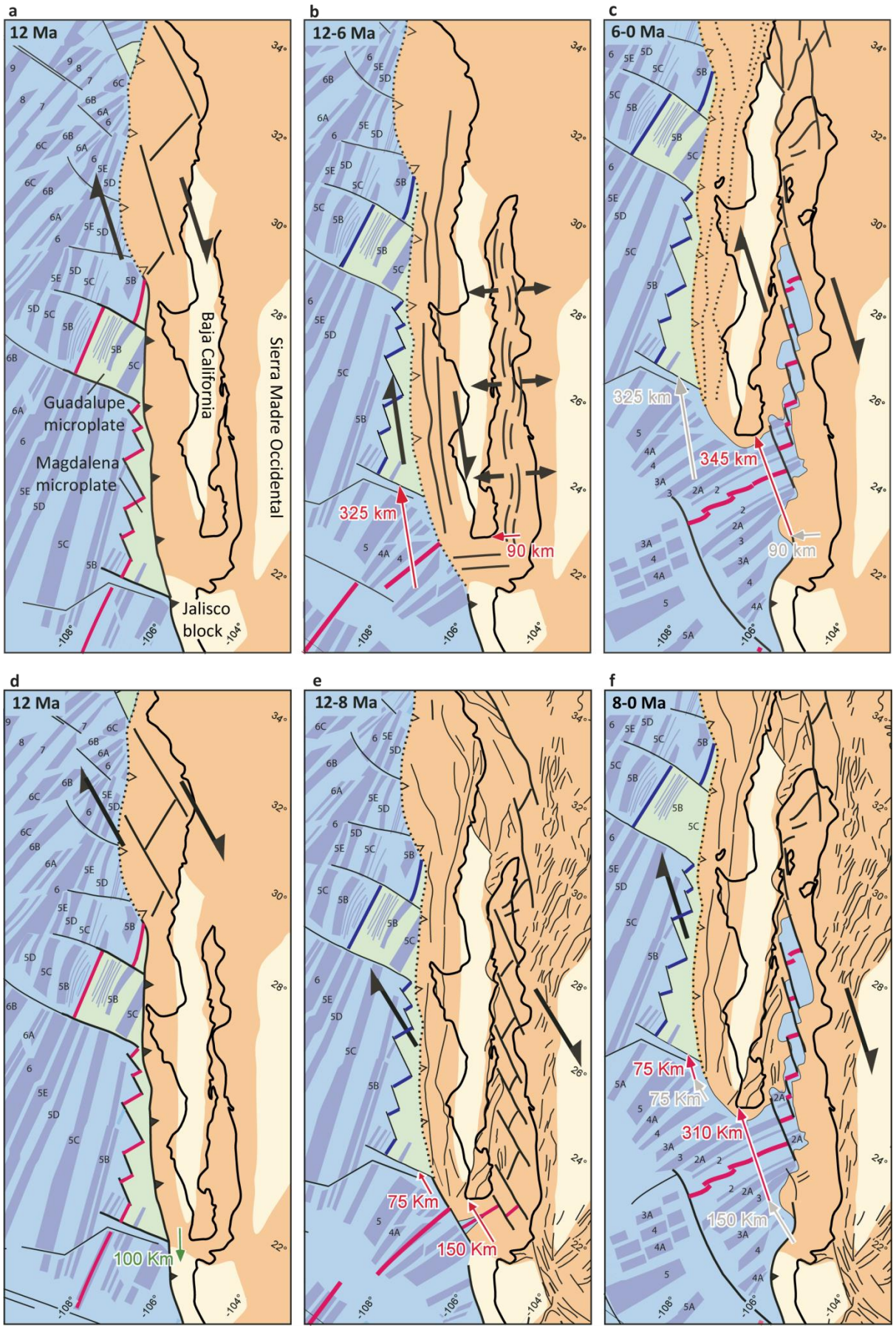
a
12 Ma
Guadalupe microplate
Magdalena microplate
Baja California
Sierra Madre Occidental
Jalisco block
b
12-6 Ma
325 km
90 km
c
6-0 Ma
325 km
345 km
90 km
d
12 Ma
100 Km
e
12-8 Ma
75 Km
150 Km
f
8-0 Ma
75 Km
75 Km
310 Km
150 Km

Figure 2.2 (Previous page): Alternate models for development of the Gulf of California. *Modified from Fletcher et al. (2007). Undeformed continental blocks are white; deformed continental blocks are beige; oceanic crust is pale blue with labelled magnetic anomalies in grey; named oceanic microplates are pale green; faults are black; active spreading ridges are red, abandoned ridges are blue. Deformation is shown relative to 'mainland' Mexico, which is fixed.* ***a-c:*** *Traditional two-stage rifting model of Stock and Hodges (1989).* ***a:*** *Between ~14-12 Ma, following Pacific/Farallon ridge subduction north of ~28° N, Pacific/North America relative motion is initially accommodated by a combination of transtensional deformation in the continental borderland, and continued spreading on the surviving Guadalupe and Magdalena ridges to the south. The Magdalena microplate detaches during this time from the larger fragment of the Farallon plate to the south.* ***b****: Spreading at the Guadalupe and Magdalena ridges ceases, probably at ~12-11 Ma, and both microplates accrete to the continental borderland. Pacific/North America relative motion is partitioned between strike-slip motion west of Baja California, and inboard orthogonal extension which forms a proto-gulf. Red arrows indicate magnitude of deformation.* ***c:*** *From ~6 Ma, Pacific/North America motion is accommodated wholly by transtensional deformation within the gulf, east of Baja California; this coincides with the onset of lithospheric rupture and seafloor spreading at ~6-3 Ma.* ***d-e:*** *Integrated single-stage transtensional model of Fletcher et al. (2007).* ***d:*** *As for* ***a****, but Baja California restores ~100 km further SE, relative to 'mainland' Mexico.* ***e-f:*** *Cessation of spreading at the Guadalupe and Magdalena ridges is followed by a single phase of transtensional deformation both west and east of Baja California; Pacific/North America relative motion rotates slightly clockwise at ~8 Ma.*

Both models require the onset of extension in the Gulf following the progressive north-south cessation of spreading and subduction between ~16-14 Ma and ~12.5-11.5 Ma. However, the onset of extension and development of the eastern margin of Baja California appear to consistently lag the cessation of spreading (Figure 2.1). In the extreme north of the Gulf, at the Sierra Juarez and west of the Salton Trough, the onset of significant extension is reported between ~12-10 Ma (Lee et al., 1996; Axen et al., 2000; Shirvell et al., 2009), and ~8 Ma (Dorsey et al., 2007; Dorsey et al., 2011), ~4-

8 Ma after the cessation of spreading at ~14-16 Ma. Immediately to the south, in the Sierra San Felipe and Puertecitos areas, the onset of significant extension is documented at ~9-8 Ma and ~6 Ma, respectively (Lewis and Stock, 1998; Oskin et al., 2001; Seiler et al., 2011), ~5-8 Ma after the cessation of spreading at ~14 Ma. Seiler et al. (2011) proposed that between the cessation of spreading and the onset of extension around the modern northern Gulf in the late Miocene, extension was accommodated on structures east of the Gulf region in Sonora associated with extension of the southern Basin and Range province, which extends across much of northern and central Mexico, as shown in Figure 2.3 (Henry and Aranda-Gomez, 2000). Extension across Sonora has been documented between ~27-10 Ma (Gans, 1997; McDowell et al., 1997; Wong and Gans, 2008), and further south in Sinaloa, Durango, Nayarit and Jalisco between ~23-10 Ma (Henry and Aranda-Gomez, 2000; Ferrari et al., 2002); extension ages generally young westward (Figure 2.3). Assigning a boundary between areas of southern Basin and Range extension and Gulf-related extension (the 'Gulf Extensional Province') has proved difficult, possibly because deformation migrated continuously over time and no discrete boundary can in fact be drawn, as discussed by Henry and Aranda-Gomez (2000) and Calmus et al. (2011).

Whether the lag in extension onset observed in the northern Gulf also occurred in the southern Gulf is unclear, as the timing of extension here is poorly constrained. The oldest units in the Santa Rosalía basin were deposited at ~7 Ma (Holt et al., 2000; Conly et al., 2005), indicating the onset of extension prior to this time, and the onset of significant extension at the southern tip of Baja California is documented at ~10 Ma (Fletcher et al., 2000). On Isla del Carmen and Isla San Jose, the onset of deposition in minor syn-rift basins is inferred to have occurred at ~6-4.5 Ma and ~8-4 Ma, respectively, based on extrapolated mean sedimentation rates (Dorsey et al., 2001; Umhoefer et al., 2007). On the eastern margin of the Gulf, extension has been documented from ~11 Ma in central Sinaloa (Henry and Aranda-Gomez, 2000); and between ~15-10 Ma in Nayarit (Ferrari et al., 2002). These data are generally consistent with the delayed extension hypothesis of Seiler et al. (2011), but across southern Baja California constraints on extension timing are sparse. This hinders

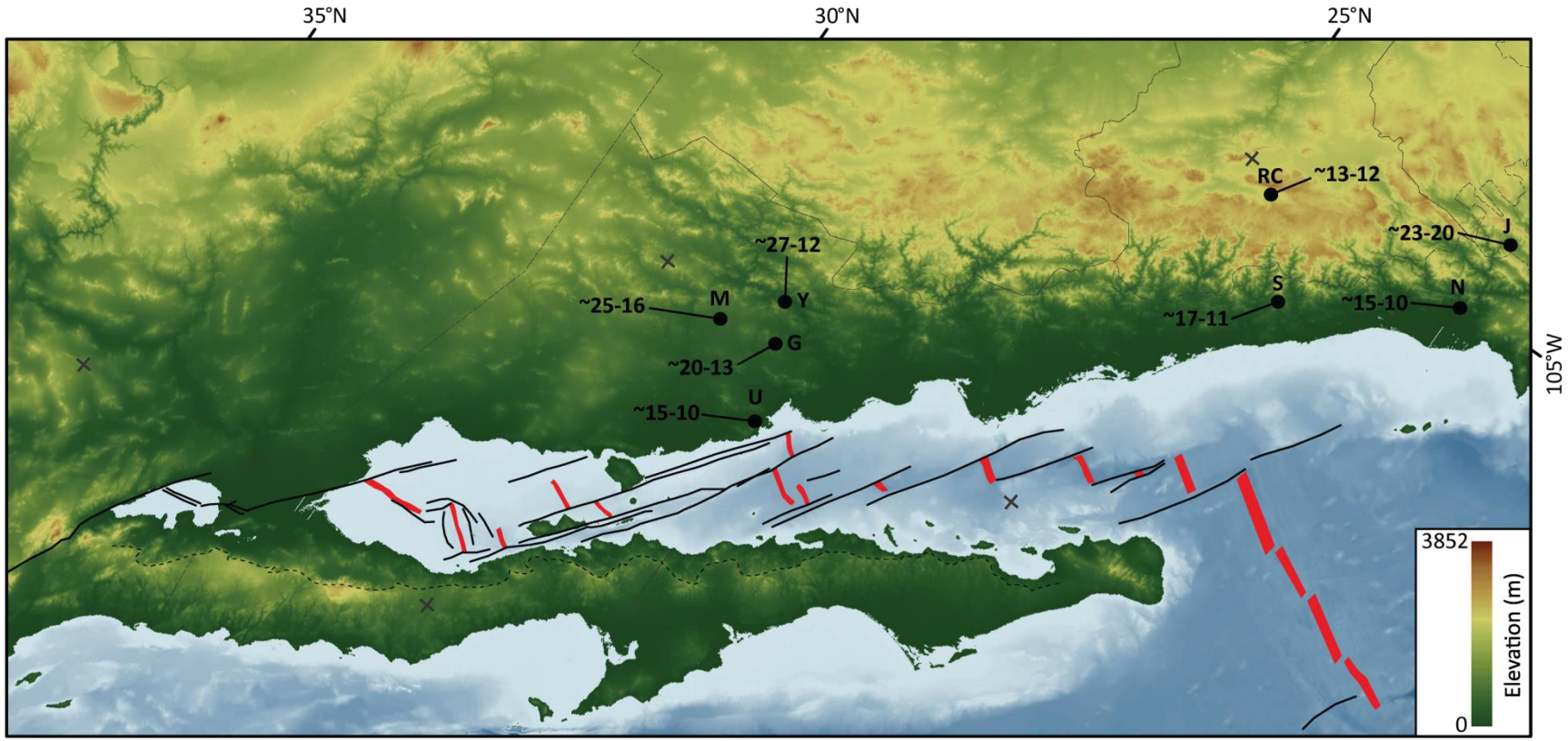

Figure 2.3: Ages of extensional structures east of the Gulf of California. *Modern en-echelon spreading centres and transform faults in the gulf are red and black, respectively; dashed black line marks MGE crest; dashed grey lines mark state boundaries. Ages in Ma. M – Sierra Mazatan core complex (Wong and Gans, 2008); Y – Rio Yaqui graben (McDowell et al., 1997); G – Suaqui Grande graben; U – Sierra Santa Ursula faults (Gans, 1997); RC – Rio Chico graben; S – southern Sinaloa faults (Henry and Aranda-Gomez, 2000); J – Jalisco grabens; N – Nayarit grabens (Ferrari et al., 2002).*

understanding of the distribution of extension during the early stages of rifting.

2.2 Geology and structure of the Loreto rift segment

In common with many rifts, the western margin of the Gulf of California is bounded by a series of rift segments, each comprising one or more major faults sharing similar orientations, and separated by complex accommodation or transfer zones. In the north of the Gulf, from the Salton Trough as far south as the Sierra San Pedro Martír, these segments have been confidently identified (Axen, 1995), but segmentation of the central and southern margin is less well understood (Figure 2.1). Along the length of the Baja California Peninsula, the faults which define these segments are hosted either offshore or in a narrow low-elevation coastal plain east of the Main Gulf Escarpment, an east-facing rift escarpment ~0.5-2 km in height which separates the west-sloping, unextended western peninsula from the extended coastal plain and offshore Gulf. This study focusses on the ~85 km long Loreto rift segment, one of the best-studied in the southern Gulf (Figure 2.4). The Loreto segment comprises four principal rift-bounding structures, all of which are east-dipping and strike ~NNW-SSE. From south to north, these are the Escondido fault, the Nopolo monocline and fault, the eponymous Loreto fault, and the northern monocline (Umhoefer et al., 2002). The ~14 km long Escondido fault is located at the base of the escarpment, ~2-3 km east of the escarpment crest, and has accommodated dip-slip motion with no lateral component; the age of the fault is unknown, although it post-dates the youngest pre-rift units of the Comondú Group, which are ~11-12 Ma in age (Umhoefer et al., 2001; Bellon et al., 2006). The proximity of the fault to the escarpment and the presence of well-defined triangular facets on the interfluves of footwall streams crossing the fault suggest that it is younger than the Nopolo and Loreto faults. The amount of slip the fault has accommodated is also unclear, although the topographic offset across the fault suggests throw of at least ~1000 m. The ~15 km long Nopolo fault is situated ~10 km north of the Escondido fault, and comprises a partially breached east-dipping monocline with a minimum of ~300-400 m of structural

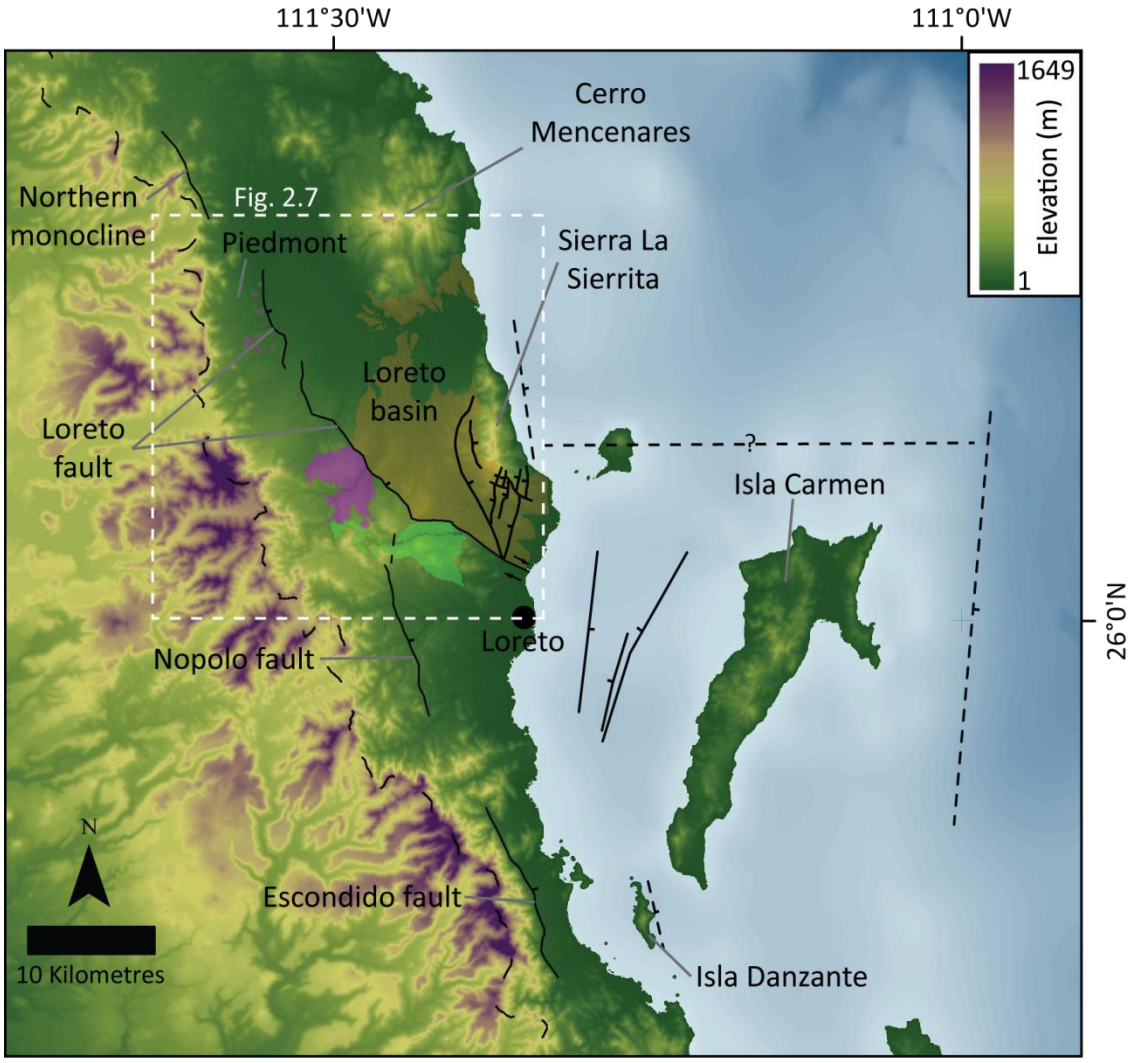

Figure 2.4: Overview of the Loreto rift segment. *Topography obtained from the Advanced Spaceborne Thermal Emission and Reflection Radiometer (ASTER) dataset, horizontal resolution ~28 m. Extent of Pliocene Loreto basin sediments (brown), and basement granodiorite (purple) and metavolcaniclastic units (green) taken from McLean (1988) and Dorsey and Umhoefer (2000). Location and vergence of rift-bounding structures of the Loreto segment, and inferred offshore structures, taken from Umhoefer et al. (1994); Umhoefer and Stone (1996); Nava-Sanchez et al. (2001); and Umhoefer et al. (2002).*

relief, thought to have developed above the upward-propagating normal Nopolo fault (Willsey et al., 2002). As the topographic offset across the fault is ~800-900 m, total structural relief accommodated by the monocline was likely considerably higher. Where the monocline is breached by the fault,

stratigraphic offsets across the fault itself are typically only a few tens of metres (Willsey et al., 2002). The fault lies ~5-8 km east of the escarpment crest, and the interfluves of the east-draining footwall streams are degraded, lacking the facets of their Escondido counterparts. The ~35 km long dextral-normal Loreto fault lies ~4-6 km north of the Nopolo fault, and has two main parts. The northern, larger, part strikes NNW-SSE, and lies ~5-9 km east of the escarpment crest; the smaller southern part strikes abruptly NW-SE, and cuts the modern coastline just north of the town of Loreto. West of the fault, the escarpment rises abruptly from the coastal plain; the interfluves of the east-draining streams crossing the fault have been almost entirely removed, leaving a low-elevation, low-relief piedmont ~3-5 km wide between the fault and the escarpment (Dorsey and Umhoefer, 2000; Umhoefer et al., 2002). This piedmont exposes basement granodiorite and metavolcaniclastic units, overlain by a few metres of coarse alluvium, and is incised by numerous east-draining arroyos incised up to ~10 m beneath the piedmont surface. The hangingwall of the Loreto fault hosts the only significant syn-rift sediments of the Loreto segment, in the Pliocene Loreto basin. North of the Loreto fault, the final component of the Loreto segment is an east-dipping monocline situated at the base of the escarpment, which strikes NNW for ~9-10 km (Umhoefer et al., 2002).

The rift-bounding faults of the Loreto segment are thought to be linked to further extensional and transtensional faults offshore. Strain appears to be transferred from the southern Loreto fault to the east-dipping fault inferred east of the Sierra La Sierrita via a complex accommodation zone which cuts the Pliocene units of the southern Loreto basin (Umhoefer and Stone, 1996; Dorsey and Umhoefer, 2000; Umhoefer et al., 2002). The Loreto fault is likely also linked to the border faults of an offshore graben between Isla del Carmen and the town of Loreto, which facilitated the inferred clockwise rotation of Isla del Carmen, and possibly also to an inferred east-dipping extensional fault east of Isla Danzante (Nava-Sanchez et al., 2001; Umhoefer et al., 2002). Strain is thought to be transferred from this fault and the Escondido fault to the east-dipping offshore faults of the Timbabichi rift segment to the south via the poorly known Bahía Agua Verde accommodation zone (Axen, 1995; Umhoefer et al., 2002; Drake, 2005; Piñero-Lajas, 2008). To the north of the Loreto

segment, the manner in which strain is transferred to the neighbouring Mulegé rift segment via the inferred Bahía Concepción accommodation zone is unknown; faulting is absent from the coastal plain between Bahía Concepción and the northern monocline of the Loreto segment, and the extent and vergence of the Mulegé rift segment are unclear (Axen, 1995; Dorsey and Umhoefer, 2000; Umhoefer et al., 2002).

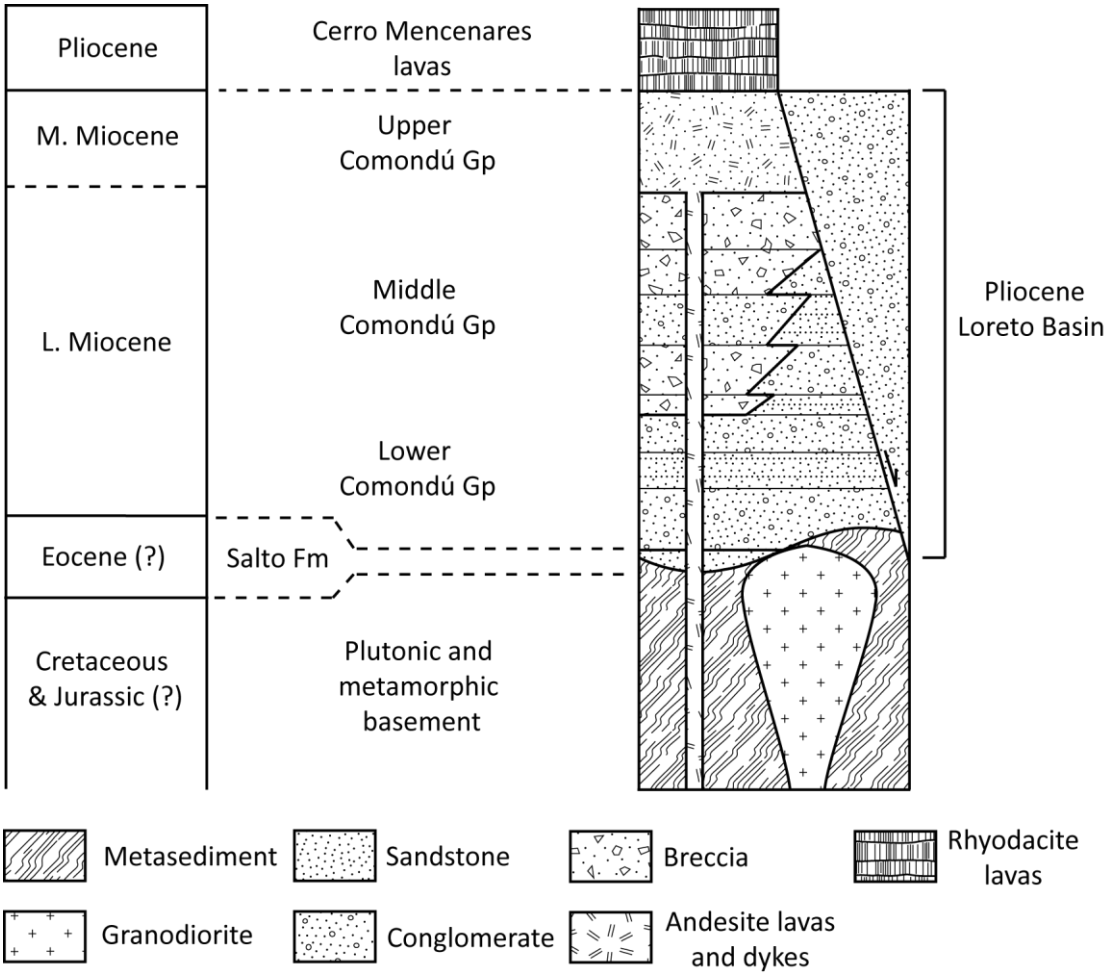

Figure 2.5: Schematic stratigraphic column for the Loreto coastal plain. *Based on previous work by McLean (1988), Dorsey and Umhoefer (2000), and Umhoefer et al. (2001).*

The rift-bounding structures of the Loreto segment are hosted in the pre-rift units common to much of the southern Baja California Peninsula (Figure 2.5). These comprise a basement of Jurassic (?) metavolcaniclastic units intruded by Late Cretaceous granodiorite; in the Loreto area, these are only exposed in the piedmont west of the Loreto fault. These are discontinuously overlain by rare, thin

aeolian(?) sandstones, possibly of Eocene age (McLean, 1988), which in turn are overlain by the dominant unit of the southern Baja California Peninsula; the volcaniclastic Comondú Group. On the coastal plain, the Comondú Group has a composite thickness of ~1.5-2 km, comprising a lower clastic unit ~200-300 m thick largely deposited between ~23-19 Ma, although deposition onset was possibly as early as ~25-30 Ma; a middle unit consisting of ~750 m of andesite breccia and subordinate lavas, deposited between ~19-15 Ma; and a ~600 m thick upper unit of andesite lava flows erupted between ~15-12 Ma. The lower and middle unit comprise much of the rift flank west of the rift-bounding faults and escarpment, and thin westwards; the upper unit is restricted to the coastal plain (Umhoefer et al., 2001). The three constituent units of the Comondú Group have been interpreted as the distal, proximal, and core facies, respectively, of a calc-alkaline volcanic arc generated by subduction of the Farallon plate beneath North America, and the vertical succession indicates that the arc must have shifted westwards during the Miocene (Hausback, 1984; Umhoefer et al., 2001). Restriction of the upper units to the coastal plain, coupled with radially distributed andesitic feeder dykes west of Loreto which are interpreted as the location of a volcanic edifice (Zanchi, 1994), suggest that the arc was located as far west as the modern coastal plain during the Middle Miocene.

The principal syn-rift units at the Loreto segment are those of the Loreto basin. These have an inferred thickness of ~1.5-1.8 km in the deepest part of the basin immediately east of the Loreto fault, although only a composite thickness of ~1.3 km of basin fill is exposed (Dorsey and Umhoefer, 2000). The base of the syn-rift basin fill is not exposed. The basin fill comprises near-fault and basal clastic conglomerate, interpreted as the deposits of subaerial debris flows and braided streams on alluvial fans. Higher and more distal units are marine, comprising stacked coarse-grained shoal water and Gilbert deltas and associated distal mudstones, separated by shell beds recording abrupt increases in water depth; these are thought to record episodic subsidence on the Loreto fault (Dorsey and Umhoefer, 2000; Mortimer et al., 2005). These deltaic units form the bulk of the exposed basin fill; their deposition is bracketed between ~2.6-2 Ma by four tuffs (Umhoefer, Dorsey, et al., 1994; Mortimer, 2004). These were likely erupted from the Cerro Mencenares calc-alkaline

volcanic complex which developed in the northern Loreto basin during the Pliocene (Bigioggero et al., 1995).Uppermost basin units comprise relatively minor evaporites, and bioclastic and coralgal limestones, and appear to record a significant reduction in subsidence after ~2 Ma. The onset of basin filling is inferred to be between ~5-3.6 Ma, based on estimates of sedimentation rates (Dorsey and Umhoefer, 2000).

Therefore, although the structure and stratigraphy of the Loreto segment are relatively well known, the chronology of rifting remains unclear. The principal age constraints are the youngest lavas of the Comondú group, erupted at ~12 Ma, and the oldest tuff of the Loreto basin, erupted at ~2.6 Ma. The timing of the onset of faulting, and development and westward retreat of the escarpment remain controversial; Dorsey and Umhoefer (2000) and (Umhoefer et al., 2002) propose the onset of faulting at ~5-6 Ma and development of the basement piedmont subsequent to ~2 Ma; Mortimer and Carrapa (2007) proposed piedmont development could have been as late as the Quaternary. The results of this study allow this uncertainty to be resolved.

2.3 Analytical methods

2.3.1 The zircon U-Pb technique

To further constrain the thermal histories obtained from time-temperature (*t*-*T*) modelling of the thermochronometer results, this study also includes U-Pb dating of the basement granodiorite to establish the age of pluton emplacement. The U-Pb geochronological technique utilises the ^{238}U-^{206}Pb and ^{235}U-^{207}Pb radioisotope systems. The host mineral, in this case zircon, is abundant in continental rocks and is highly resistant to both chemical and mechanical weathering. During crystallisation, zircon readily incorporates U into its crystal lattice at typical abundances of 10-1000 ppm, but excludes Pb, removing the need to detect and correct for nonradiogenic Pb during U-Pb analysis. For each isotope system, the elapsed time *t* since host mineral closure is calculated using the equation (Parrish and Noble, 2003):

$$t = \left(\frac{1}{\lambda}\right) ln\left(1 + \frac{D}{P}\right) \qquad \text{(Equation 2.1)}$$

where λ is the isotope system decay constant, and *D/P* the daughter-parent atomic ratio. The ratio *D/P* for any value of *t* can be calculated from:

$$\frac{D}{P} = e\lambda^{T} - 1 \qquad \text{(Equation 2.2)}$$

As the closure temperature for both the ^{238}U-^{206}Pb and ^{235}U-^{207}Pb systems in zircon is >900 °C, U-Pb ages are generally considered to represent crystallisation ages (Cherniak and Watson, 2000).

In this study, U-Pb analysis was conducted using a laser ablation system linked to an inductively coupled plasma mass spectrometer (LA-ICP-MS); instrument drift and ablation fractionation bias were corrected by repeated reference to an external zircon standard of known age (see Appendix 1 for further details of analytical methods).

This study follows the standard convention of presenting the results of U-Pb analyses using a concordia diagram, which plots evolution of the ^{206}Pb/^{238}U and ^{207}Pb/^{235}U ratios over time. The resultant concordia curve thus defines all points where both isotope systems, if undisturbed, yield identical ages. Host mineral grains which have functioned as closed systems since formation will plot on this curve; those which have behaved as open systems will plot discordantly, typically an indication of Pb loss or gain. Concordia and U-Pb ages were calculated using the Isoplot plug-in for Microsoft Excel developed by Ludwig (2008).

2.3.2 The AFT technique

The apatite fission track (AFT) technique utilises the decay of ^{238}U to ^{206}Pb within the host mineral, apatite (calcium phosphate). Preferential incorporation of these elements within apatite grains during crystallisation, coupled with a resistance to mechanical weathering and a common occurrence in continental rocks, render apatite a particularly suitable target mineral for fission track dating. Decay of ^{238}U typically occurs by emission of a series of α-particles, which then form He by the process of electron capture, coupled with β- emission. However, ^{238}U can also decay by spontaneous fission, at the rate of one fission event for every ~2x10^{6} α-events. Although other

naturally occurring isotopes – notably ^{235}U and ^{232}Th – also occasionally undergo spontaneous fission, in practice the fission half-lives of these isotopes are so long that the number of fission events produced is negligible, even on geological timescales (Gallagher et al., 1998; Tagami and O'Sullivan, 2005).

The effect of spontaneous fission is to produce two charged, atomically heavy particles which recoil from each other, disrupting the crystal lattice of the mineral host as they do so. The elongate disruption which results is termed a fission track, and has a characteristic length of ~16-17 μm in apatite. The precise mechanism by which lattice disruption occurs is unclear, but is thought to be the result of electron stripping by the charged fission daughter products from the lattice surrounding their recoil path; the ionised lattice atoms then repel each other, creating a cylindrical damage zone around the recoil path. As the characteristic width of the damage track created by fission in apatite is only ~6-10 nm, apatite grains must be chemically etched to widen the tracks and render them visible at magnifications achievable by optical microscopy. A variety of etching protocols exist and there is as yet no standardised procedure, although the most common utilises 5M HNO_3 as the etchant (Donelick et al., 2005; Tagami and O'Sullivan, 2005).

Fission track abundance depends on the number of fission track events that have occurred within a host mineral, which in turn is dependent on U content. Therefore, fission track abundance can be used like any other radioisotope daughter product to calculate the elapsed time *t* since system closure. However, the closure dynamics of the parent isotope and daughter product of the apatite fission track system differ; apatite crystals are closed systems with respect to ^{238}U at temperatures < ~500 °C, but fission tracks are only preserved at temperatures < ~120 °C on geological timescales of $>10^6$ a. Whereas fission track abundance can be obtained by manual counting of tracks visible on a polished and etched crystal surface under an optical microscope, ^{238}U (parent) abundance cannot be directly detected without destroying the sample. To remedy this, the external detector method is used, which exploits the fixed natural ratio of ^{238}U to ^{235}U. The external detector is a sheet of U-free

mica, which is placed over the polished surface of the resin-mounted sample grains. Both sample and detector undergo neutron bombardment, which induces fission of U^{235}. Fission of Th isotopes in the sample, which would produce excess induced tracks in the detector, is avoided by the use of a thermalised neutron flux. The abundance of induced tracks in the detector can then be utilised to obtain the elapsed time *t* since host mineral closure with respect to fission track stability by comparing the induced track density to that of standard U-doped dosimeter glass which is irradiated with the sample.

For non-detrital samples, spontaneous and induced fission track abundances are typically measured for 20-30 grains and external detectors for each sample. These sample populations are sufficient to capture the natural variation in ratios described by Poissonian statistics, which are used to determine whether the distribution of sample ages can be attributed solely to the variation of measured spontaneous and induced track densities. Track counts are commonly combined to obtain a pooled age, t_p, which effectively treats all measured grains as a single grain surface. The pooled age is obtained from:

$$t_p = \frac{1}{\lambda_d} ln\left(1 + \lambda_d \zeta g \rho_d \frac{\sum N_s}{\sum N_i}\right) \qquad \text{(Equation 2.3)}$$

where λ_d is the total ^{238}U decay constant; ζ is a calibration factor to adjust for observer variation; g is a geometry factor for spontaneous fission track registration; ρ_d is induced fission track density in a neutron dosimeter corresponding to sample position during irradiation; ΣN_s is the total number of spontaneous fission tracks; and ΣN_i is the total number of induced fission tracks (Hurford and Green, 1982). However, use of pooled fission track ages is only acceptable if the grains within the sample have a common age. This can be assessed using the standard χ^2 test for over-dispersion; because fission tracks are the outcomes of random spontaneous fission events which occur at a known average rate over time, measured fission track single grain ages should display a Poissonian distribution around a 'true' age if all grains within the sample have a common age. In such a case, the variation leading to dispersion should be wholly the result of quantifiable experimental

uncertainties. Failure for the population of spontaneous and induced track densities recorded from each grain to pass the χ^2 test – by convention, at the 5% level – indicates that grain ages exhibit extra-Poissonian dispersion (Galbraith, 1981). This indicates either that the sample population contains multiple age components or that U distribution within grains is inhomogeneous, which impacts track density measurements. A variety of experimental problems can also contribute to over-dispersion, such as incomplete track etching, inaccurate track counting, or poor contact between the grain surface and the external detector during irradiation (Tagami and O'Sullivan, 2005). In such cases, the central age, t_c, of Galbraith and Laslett (1993) is preferred; this is essentially a weighted mean of the log normal distribution of single grain ages, weighted for the precision of track counts from each grain, providing a geometric mean age. The central age is calculated iteratively from:

$$t_c = \frac{1}{\lambda_\alpha} log\left(1 + \frac{1}{2}\lambda_\alpha \zeta \rho_d \frac{\eta}{1-\eta}\right) \qquad \text{(Equation 2.4)}$$

where η is the weighted average of single-grain variance and $\eta/(1-\eta)$ is the equivalent of N_s/N_i in Equation 2.3. The relative standard error is obtained from:

$$se(t_c) = {}^{t_c}\sqrt{\frac{1}{\eta^2(1-\eta)^2 \sum_{j=1}^{n} w_j} + \frac{1}{N_d} + \left(\frac{se(\zeta)}{\zeta}\right)^2} \qquad \text{(Equation 2.5)}$$

where w_j is the weighting of each single grain variance. Conveniently, in cases where sample populations pass the χ^2 test, the central age and pooled age will be identical, and hence the central age is routinely the reported age.

In order to interpret a fission track age, an understanding of fission track stability is required. The damage caused to the crystal lattice by fission track formation is reversible; as soon as a fission track is generated it will begin a process of self-repair, whereby atoms displaced by track formation

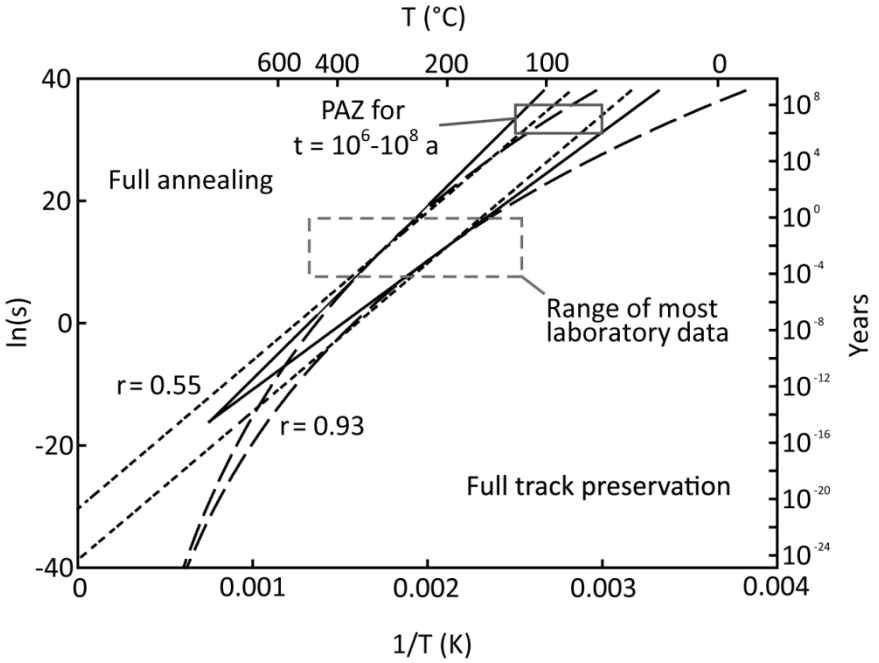

Figure 2.6: Pseudo-Arrhenius plot showing stability of fission tracks in apatite. *Modified from Ketcham (2005). Contours illustrate reduction in mean track length (projected to c-axis) relative to initial length (r) of 0.55, at which tracks segment and are no longer measurable, and 0.93, inferred to occur at near-surface temperatures at timescales of 10^6-10^8 a. Three different extrapolation models from laboratory data are shown: fanning linear (solid line) model of Green et al. (1985); parallel linear (dotted line) model of Laslett et al. (1987); and fanning curvilinear (dashed line) model of Ketcham et al. (1999). Temperature range of ~120-50 °C normally used to delineate effective partial annealing zone on geological timescales of 10^6-10^8 a shown by grey box.*

migrate towards their original sites in the crystal lattice. This process is termed annealing, and leads to progressive fission track shortening. The annealing process is dependent on both temperature and time; annealing behaviour at timescales of geological interest has been extrapolated from experimentally derived annealing data using inverse temperature versus log-time (pseudo-Arrhenius) plots, as shown in Figure 2.6 (Laslett et al., 1987; Ketcham et al., 1999). Annealing occurs initially by progressive track shortening, until the ratio of track length to original length (l/l_0) decreases to <~0.55-0.60, after which track widths decrease and track fragmentation occurs (Ketcham et al., 1999). As the lengths of fragmented tracks cannot realistically be measured, the

onset of track fragmentation effectively represents attainment of the annealed state. As shown in Figure 2.6, for geological timescales of $>10^6$-10^8 a, effective complete fission track annealing occurs at temperatures of >~120 °C. At temperatures <~50 °C, rates of annealing become extremely slow, and effective complete annealing does not occur on geological timescales (Laslett et al., 1987; Ketcham et al., 1999; Ketcham, 2005). The intermediate temperature range ~120-50 °C is referred to as the apatite partial annealing zone (PAZ). This dependency of fission track length on the *t*-*T* conditions the track has experienced gives rise to track length variation. For example, a sample which cools rapidly through the PAZ will exhibit only a narrow range of track lengths, and the fission track age – which is governed by the number of tracks intersecting the polished grain surface, and is thus dependent on track length – will closely reflect the time of cooling. In contrast, slow cooling will produce greater track length variation, and the fission track age will be intermediate between the times of PAZ entry and exit. Track lengths are therefore routinely measured during fission track analysis, in addition to track abundance. A complex protocol exists to determine which tracks are suitable for length measurement; this is discussed in Donelick et al. (2005). Typically, a population of ~100 track lengths will be measured. Measured tracks must be confined within the apatite grain, and accessed by the etchant during etching via a track or crystal defect intersecting both the polished grain surface and the confined track in order to accurately determine track length.

In addition to the strong temperature dependence of annealing rates, chemical and structural controls also exist. The chemical control is thought to arise from the common anionic substitutions of F and Cl for PO_4 in apatite; Cl-rich apatites are more resistant to annealing (O'Sullivan and Parrish, 1995; Barbarand, 2003). Fortunately, bulk grain chemical composition (the kinetic parameter) also affects grain susceptibility to etching, and can be corrected for by reference to the diameter of etched tracks which are orthogonal to the observed grain surface. This is the widely used D_{par} method of Donelick (1993). The structural control arises from anisotropy in annealing rates within the apatite crystal, such that tracks orientated parallel to the crystallographic *c*-axis anneal more

slowly than tracks which are oblique to this axis; however, this effect is thought to be significant only for samples which have experienced prolonged residence in the PAZ (Ketcham, 2003).

2.3.3 The AHe technique

The apatite (U-Th)/He (AHe) technique utilises the ^{238}U-^{206}Pb, ^{235}U-^{207}Pb, and ^{232}Th-^{208}Pb isotope systems. Complete decay of the parent radioisotopes generates 8, 7, and 6 α-particles, respectively; these decay chains are the principle α-emitters in most host minerals, together with a generally negligible addition from decay of ^{147}Sm. Following emission, α-particles capture electrons to form atoms of ^{4}He. As He is both highly volatile and present only in low abundances in the atmosphere, host mineral He content is virtually all radiogenic, although excess He can be present as a result of mineral or fluid inclusions. Complications arising from excess He can typically be avoided by visual screening of grains to exclude those which exhibit inclusions (Farley and Stockli, 2002).

Within the apatite crystal lattice, He atoms are considerably more mobile than their U or Th parents. As a result, the closure temperature for He is significantly lower, at ~70-80 °C. As the diffusion domain is the entire grain, as opposed to the few tens of nanometres around fission tracks in the AFT system, closure temperature varies slightly with grain size. At temperatures > ~70 °C, He diffuses rapidly from the apatite grain; at temperatures < ~40 °C, He diffusion rates approach zero on geological timescales. At temperatures intermediate between ~40-70 °C, only a fraction of the He produced is retained within the grain; this temperature interval is the partial retention zone (PRZ), analogous to the PAZ in the AFT system (Farley, 2000). Measurement of ^{238}U, ^{235}U, ^{232}Th, and ^{4}He abundances therefore permit the elapsed time *t* since grain closure with respect to ^{4}He to be calculated. He abundance is typically determined by step heating of the grain using a laser coupled to a quadrupole mass spectrometer; grains are then dissolved and U and Th abundances obtained using an ICP-MS. A disadvantage of the AHe technique is therefore that it requires destruction of the sample grains.

Traditionally, an iterative solution is applied to the AHe age equation, but a simpler direct solution which calculates the AHe age to within ~0.1% of the iterative method is also available (Meesters and Dunai, 2005):

$$t = \frac{1}{\lambda_{wm}} ln\left(\frac{\lambda_{wm}}{P}[He] + 1\right) \quad \text{(Equation 2.6)}$$

where λ_{wm} is the weighted mean decay rate for all three parent isotopes; P is the total production rate of He from all parents; and [*He*] is measured He abundance. However, He abundance must be corrected for the effect of the low mass of α-particles, which results in non-trivial stopping distances following ejection from the parent nuclide. In the apatite crystal lattice, mean stopping distances are ~19-22 μm, depending on the parent nuclide and the exact chemical and structural composition of the local lattice; such distances are significant given typical grain sizes of ~10^2 μm. As a result, a fraction of α-particles are ejected directly from the grain. Given knowledge of grain size, geometry, and relative parent nuclide abundance, this effect can be corrected for (the F_T correction of Farley et al., 1996), although this assumes homogenous parent nuclide distribution throughout the grain. As this assumption is often false, nonhomogenous parent nuclide distribution can affect AHe ages, although the effect can be reduced by visual screening of grains to exclude those with mineral inclusions; U- and Th-rich zircon is a particularly common inclusion in apatite. Likewise, analysis of fragmented grains should also be avoided, as these have geometries which are difficult to correct for (Farley and Stockli, 2002).

Unlike the AFT system, with its measurable track length variation, partial loss of the daughter product cannot be measured in the AHe system. As a result, an AHe age is an integrated age which reflects the entire thermal history of the grain subsequent to cooling below ~70 °C, and a wide variety of thermal histories can produce a given AHe age. Because the AHe system is highly sensitive to small changes in temperature within the PRZ, AHe ages obtained from grains which have resided for ~10^1-10^2 Ma in the PRZ can be highly variable. Application of constraints from geological

relationships or other thermochronometers is typically required to constrain plausible thermal histories (Farley and Stockli, 2002).

2.4 Sample locations

Samples for thermochronologic analysis were collected from the basement piedmont west of the Loreto fault along two transects ~12 km apart, orthogonal to the escarpment. Each followed an arroyo incised ~5-10 m into the basement; the Arroyo Perini in the case of the northern transect (AP sample prefix), and the Arroyo San Antonio in the case of the southern transect (SA sample prefix). Sampling locations were situated at ~1 km intervals, between ~100-200 m asl; samples were deliberately collected from the lowest basement exposures to maximise exhumation depths. Care was taken to avoid sampling basement affected by heating associated with the feeder dikes of the Upper Comondú, which were present in the area of the southern transect; sample locations were sited at least ~50 m from visible dikes. A single sample was also collected for $^{40}Ar/^{39}Ar$ analysis from Cerro Papini, an isolated degrading volcanic cone which overlies breccia of the Comondú Group at ~220 m asl on the western edge of the piedmont close to the escarpment.

2.5 Results

Southern transect mean AHe ages range from 4.8 ± 0.6 to 5.1 ± 0.3 Ma; northern ages are slightly older, at 6.5 ± 0.4 to 7.6 ± 0.6 Ma (see Figure 2.7 and Table 2.1). Southern and northern AFT ages are 17.0 ± 1.8 to 25.1 ± 2.6 Ma, and 79.3 ± 2.5 to 84.0 ± 3.0 Ma, respectively. Fission track lengths were measured for northern transect samples AP1 and AP2; mean track lengths were 13.74 ± 0.11 and 13.79 ± 0.11 µm, with standard deviations of 1.14 and 1.16 µm, respectively (see Figure 2.8, and Table 2.2). Track lengths for southern transect samples were unobtainable. Zircon U-Pb ages obtained from one sample from each transect yield ages of 91.0 ± 0.5 and 100.3 ± 0.8 Ma, respectively. The Cerro Papini lava sample yielded a $^{40}Ar/^{39}Ar$ age of 5.655 ± 0.152 Ma (See Figure

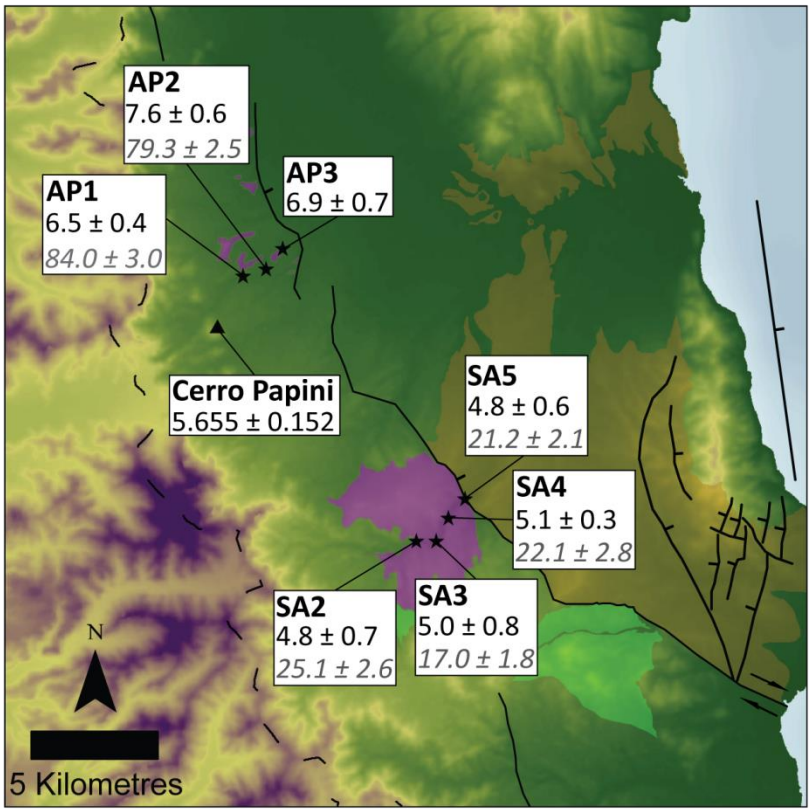

Figure 2.7: Piedmont sample locations and ages. *Black stars indicate basement sample locations; ages are in Ma; apatite (U-Th)/He (AHe) ages given in regular script, apatite fission track (AFT) ages are italicised. Black triangle indicates location of Cerro Papini lava, with* $^{40}Ar/^{39}Ar$ *age. Geological and structural symbols are as detailed in Figure 2.3.*

2.3). All data are reported at the 1σ confidence level; see Appendices A1 and A2 for details of sample preparation, analytical methods, and data tables.

U-Pb ages are likely emplacement ages given the high closure temperatures of the U-Pb system in zircon, and are consistent with Cretaceous ages reported for component plutons of the Peninsular Ranges Batholith in northern Baja California (Schmidt et al., 2009). Near overlap with the AFT ages of the northern transect indicates rapid cooling from temperatures >900 °C at ~91-100 Ma ago, to shallow crustal temperatures <120-90 °C by ~79-84 Ma ago. This is consistent with the observed long

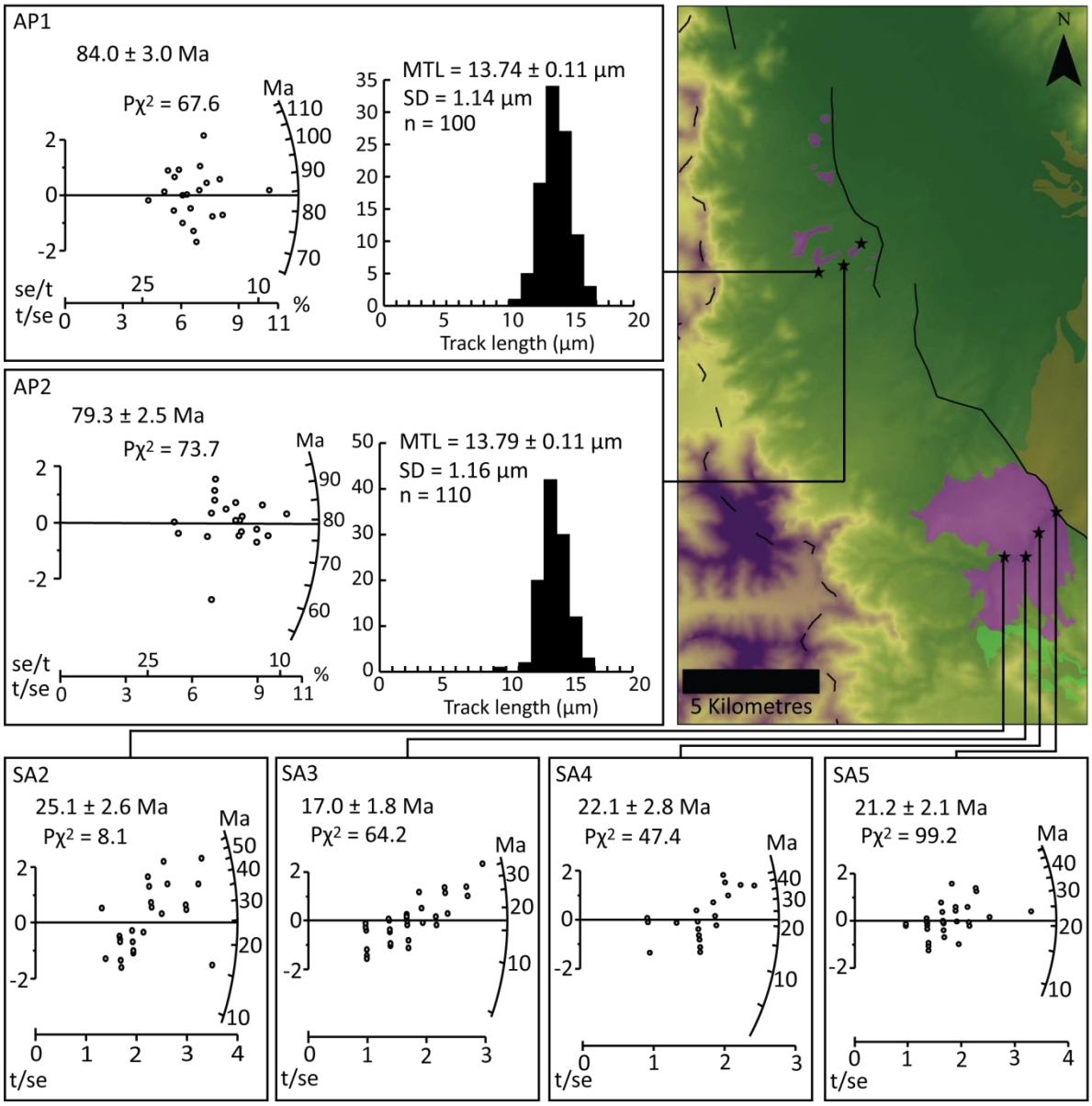

Figure 2.8: Details of piedmont AFT samples. *Histograms show track length distributions and mean track length (MTL) values; radial plots show variation (y-axis, ± 2σ), precision (x-axis, reciprocal of standard error) and value (z-axis, Ma) of grain age estimates for each sample (Galbraith, 1988). Note that precision increases away from the origin. $P\chi^2$ is probability of obtaining χ^2 value for v degrees of freedom, where v = no. crystals – 1. Geological and structural symbols as detailed in Figure 2.3.*

Sample	Latitude	Longitude	Elevation (m asl)	Packet	No. of xtals	Mass (μg)	U (ppm)	Th (ppm)	He (ncc/mg)	F_T	F_T corrected age (Ma)	Mean packet age ±1σ (Ma)
AP1	26.18853	-111.56005	140	1	4	3.9	91.5	110.5	58.9	0.63	6.6	6.5 ± 0.4
				2	4	7.7	46.4	55.9	30.4	0.70	6.0	
				3	4	5.1	68.3	77.2	48.5	0.67	6.9	
AP2	26.19102	-111.55077	120	1	3	6.1	105.6	103.6	92.3	0.71	8.3	7.6 ± 0.6
				2	3	4.2	121.7	118.4	84.8	0.67	7.0	
				3	3	3.7	92.2	99.6	68.2	0.66	7.3	
AP3	26.19844	-111.54419	120	1	4	4.6	25.5	39.9	22.2	0.69	7.6	6.9 ± 0.7
				2	3	4.6	48.1	92.6	59.7	0.70	10.0*	
				3	2	3.8	11.5	23.7	10.2	0.71	6.9	
				4	2	7.5	21.5	31.2	17.0	0.80	6.1	
SA2	26.09375	-111.49075	200	1	3	3.8	27.9	39.0	16.4	0.66	5.5	4.8 ± 0.7
				2	3	4.3	29.7	35.8	13.0	0.66	4.1	
				3	2	3.2	18.0	38.5	9.5	0.68	4.2	
				4	2	5.0	27.9	33.9	17.0	0.73	5.3	
SA3	26.09373	-111.48278	170	1	3	2.4	34.1	48.4	12.7	0.61	3.8	5.0 ± 0.8
				2	3	3.4	17.0	23.2	9.3	0.68	5.0	
				3	3	7. 2	16.4	24.5	10.5	0.71	5.5	
				4	3	4.2	21.3	34.0	12.9	0.66	5.5	
SA4	26.10193	-111.47810	160	1	4	4.9	18.0	31.3	11.0	0.68	5.3	5.1 ± 0.3
				2	2	6.5	12.4	24.6	8.0	0.75	4.9	
				3	4	1.9	57.5	109.1	57.3	0.54	10.6*	
SA5	26.10891	-111.47151	160	1	3	7.1	13.5	18.9	6.7	0.74	4.2	4.8 ± 0.6
				2	2	10.8	16.9	26.2	11.8	0.77	5.5	
				3	3	8.3	15.8	23.8	9.5	0.79	4.6	

Table 2.1: *Apatite (U-Th)/He data for samples from both Arroyo Perini (AP- sample series, northern transect) and Arroyo San Antonio (SA- sample series, southern transect). F_T is the α-particle fraction which is not ejected from the grain (Ketcham et al., 2011). Mean packet age errors are 1σ. The two packet ages marked * are considered anomalous outliers and excluded from analysis. Sample locations are given using the WGS84 coordinate system.*

Sample	No. of grains	Dosimeter		Spontaneous		Induced		$P\chi^2$	RE%	Central age (Ma ±1σ)	Mean track length (μm)	±1σ	No. of tracks	D_{par} (μm)
		ρd	Nd	ρs	Ns	ρi	Ni							
SA2	25	1.422	5911	0.135	148	1.427	1449	8.1	25.8	25.1±2.6	-	-	-	-
SA3	30	1.422	5911	0.129	105	1.859	1486	64.2	10.5	17.0±1.8	-	-	-	-
SA4	20	1.422	5911	0.066	69	0.685	752	47.4	8.8	22.1±2.8	-	-	-	-
SA5	30	1.422	5911	0.073	108	0.790	1223	99.2	0.0	21.2±2.1	-	-	-	-
AP1	20	1.422	5911	1.663	1250	4.729	3554	67.6	0.3	84.0±3.0	13.74±0.11	1.14	100	2.51
AP2	20	1.422	5911	2.283	1656	6.838	4991	73.7	0.1	79.2±2.5	13.80±0.11	1.16	110	2.97

Table 2.2: *Apatite fission track data for samples from Arroyo San Antonio (southern transect) and Arroyo Perini (northern transect). Note that sample AP3 was not analysed. Track length data for Arroyo San Antonio samples (SA- sample series, southern transect) could not be obtained. Track densities are (x10^6 tr cm^{-2}) based on number of tracks counted (Nd, Ns, Ni); analyses were by external detector method using 0.5 for the 4π/2π geometry correction factor; ages calculated using dosimeter glass CN-5, (apatite) ζ_{CN5} = 339±5, calibrated by multiple analyses of IUGS apatite and zircon age standards (Hurford, 1990); $P\chi^2$ is probability for obtaining χ^2 value for v degrees of freedom, where v = no. crystals – 1; central age is a modal age, weighted for different precisions of individual crystals (Galbraith and Laslett, 1993). Sample locations and elevations are given in Table 2.1.*

mean track lengths, which require rapid monotonic cooling through the apatite partial annealing zone. The AFT ages of the southern transect samples, however, are early Miocene; this disparity suggests a more complex post-emplacement cooling history. As the two sample transects are only ~12 km apart, it seems implausible that post emplacement cooling to shallow crustal temperatures was complete by the late Cretaceous at the northern transect, but lasted a further ~50-60 Ma at the southern transect. The younger southern transect AFT ages are therefore likely a product of reheating. Heating associated with reburial is an unlikely mechanism; southern transect samples are situated only ~175-400 m below the base of the Comondú Group (Figure 2.9). The exact age of onset of Comondú deposition is unclear, but depositional thickness prior to ~20 Ma was only ~150 m (Umhoefer et al., 2001). The southern transect samples were therefore resident within a few hundred metres of the surface in the early Miocene. The granodiorite basement hosts disseminated malachite and epidote in the area of the southern transect, suggesting localised hydrothermal processes are a possible cause of the early Miocene reheating; such alteration was not observed around the northern transect.

The AHe ages for both transects post-date the end of Comondú Group deposition at ~12-11 Ma (Umhoefer et al., 2001; Bellon et al., 2006), consistent with resetting caused by reburial beneath Comondú units, followed by erosional cooling driven by the onset of slip on the Loreto fault and exhumation of the escarpment and basement piedmont. Piedmont development in the late Miocene is also consistent with the age of the Cerro Papini lava. Generation of this late Miocene cooling episode by a regional unroofing event is inconsistent with negligible erosion of interfluves on the Loreto segment rift flank west of the escarpment crest, as recorded by the preservation of post-subduction lavas ranging in age from ~14.6-5.6 Ma (see Chapter 3). The disparity between northern and southern transect AHe ages could reflect a diachronous onset of late Miocene exhumation, but this seems unlikely given the short length scale involved (~12 km). Alternatively, the AHe age difference may be a reflection of the early Miocene heating event which affected the southern

transect, as recorded by the AFT ages. Partial retention of He accumulated during prolonged residence of northern transect samples at temperatures <90 °C following rapid post-emplacement cooling, as required by late Cretaceous AFT ages, would generate older AHe ages, whereas early Miocene heating of the southern transect samples to >120 °C, as required by the AFT ages, would completely reset the AHe ages of these samples.

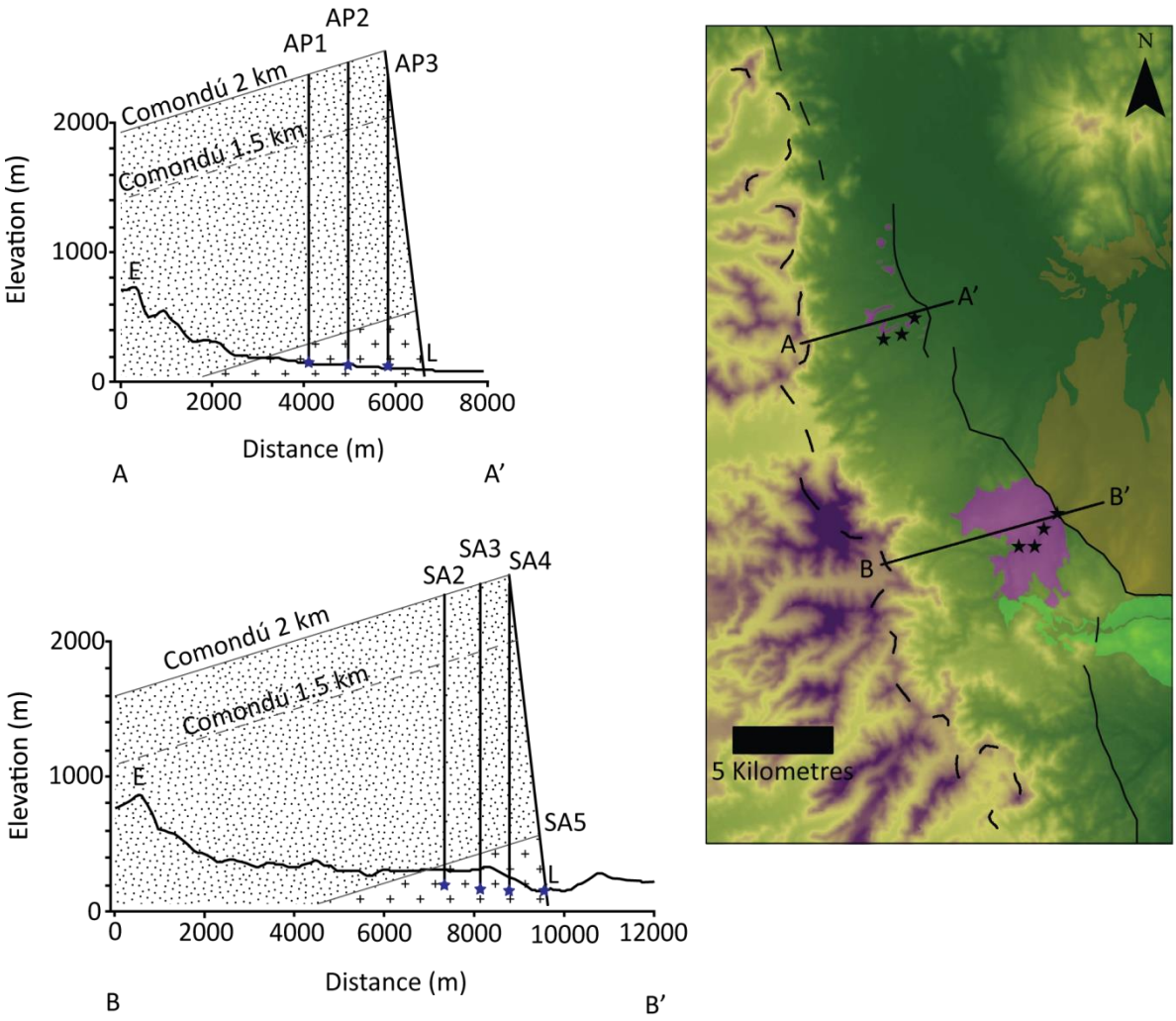

Figure 2.9: Inferred exhumation depths of piedmont basement samples. *E – location of escarpment crest. Burial depths for Comondú thicknesses of 1.5 and 2 km shown. Vertical exaggeration is 2:1; Loreto fault dip of 70° and Comondú dip of ~5° assumed, after Umhoefer et al. (2002). Geological and structural symbols as detailed in Figure 2.4.*

2.6 Time-temperature modelling

To reconcile the discrepancies between northern and southern transect AFT and AHe ages, inverse thermal history modelling utilising the HeFTy program was carried out, using standard annealing and He diffusion kinetics for apatite (Ketcham et al., 1999; Farley, 2000; Ketcham, 2005). The use of a model incorporating the effects of radiation damage on He diffusion (e.g., Flowers et al., 2009; Gautheron et al., 2009) was rejected, due to the young sample ages. For each sample, HeFTy generates random time-temperature (*t*-*T*) paths; those which acceptably reproduce AFT and AHe ages, and fission track length distributions, using Kuiper's statistic – a variant of the Kolmogorov-Smirnov test – to evaluate goodness of fit, are used to constrain plausible thermal histories (Ketcham, 2005). Initial fission track lengths for model runs are calculated using the kinetic parameter D_{par}, where available, using the method of Carlson et al. (1999); this was only possible for samples AP1 and AP2. For all other samples, the convention of constant initial track lengths of 16.3 μm was followed. The ratio of spontaneous to induced track length in the standard (Durango apatite), also used to calculate initial spontaneous track length, was set to 0.893. All AFT samples pass the χ^2 test, and are therefore modelled as single populations (see Figure 2.8).

2.6.1 Modelling approach

HeFTy permits a variety of conditions to be imposed on inverse models. These allow known or suspected geological events to be incorporated into the model, and take two forms: the properties governing the cooling and heating behaviour – either episodic or gradual – of segments comprising each *t*-*T* path, permitting paths to be more or less complex, and the presence or absence of defined areas of *t*-*T* space through which paths must pass (constraints). The selection of path properties and the degree to which constraints should be applied is discussed in Ketcham (2005). In this study, because the samples are suspected to have experienced complex thermal histories – post-emplacement cooling, reburial beneath the Comondú Group, possible hydrothermal effects, and

mechanical and erosional cooling – *t-T* paths were permitted to vary episodically; in addition, no maximum cooling rate was imposed. External constraints were applied as follows:

1. A mean surface temperature of 20 °C is assumed, consistent with previous thermochronologic studies of Baja California during the Cenozoic (Fletcher et al., 2000; Seiler et al., 2011);
2. Samples resided at temperatures >120 °C prior to 90 Ma ago, as indicated by U-Pb ages and northern transect AFT ages;
3. Samples resided at temperatures between 120-20 °C between 90-25 Ma, as indicated by AFT ages and the age of basal Comondú units;
4. Northern transect samples resided at temperatures of 30-20 °C between 25-20 Ma ago, as indicated by the age of basal Comondú units, and sample proximity to the basement/Comondú boundary; this constraint is discarded in models of southern transect samples, although they too were within a few hundred metres of the surface at this time;
5. Northern transect samples resided at temperatures between 90-20 °C between 20-5.6 Ma, as indicated by AHe ages, the absence of fission track annealing, and the presence of the ~5.6 Ma Cerro Papini lava overlaying the piedmont; this constraint is increased to 140 °C for southern transect samples.
6. Samples resided between 30-20 °C between 5.7 Ma and the present day, as indicated by the ~5.7 Ma Cerro Papini lava overlaying the piedmont.

2.6.2 Modelling results

Model results are shown in Figure 2.10. Pre-Miocene thermal histories are poorly constrained for all samples except AP1 and AP2. For these samples, plausible *t-T* paths exhibit rapid cooling to <80 °C by ~80 Ma ago, followed by residence at <60 °C until ~25-20 Ma. For all other samples, thermal histories prior to the Miocene are unconstrained, although given the identical structural setting and close spatial proximity, it seems reasonable to infer similar rapid post-emplacement cooling. All

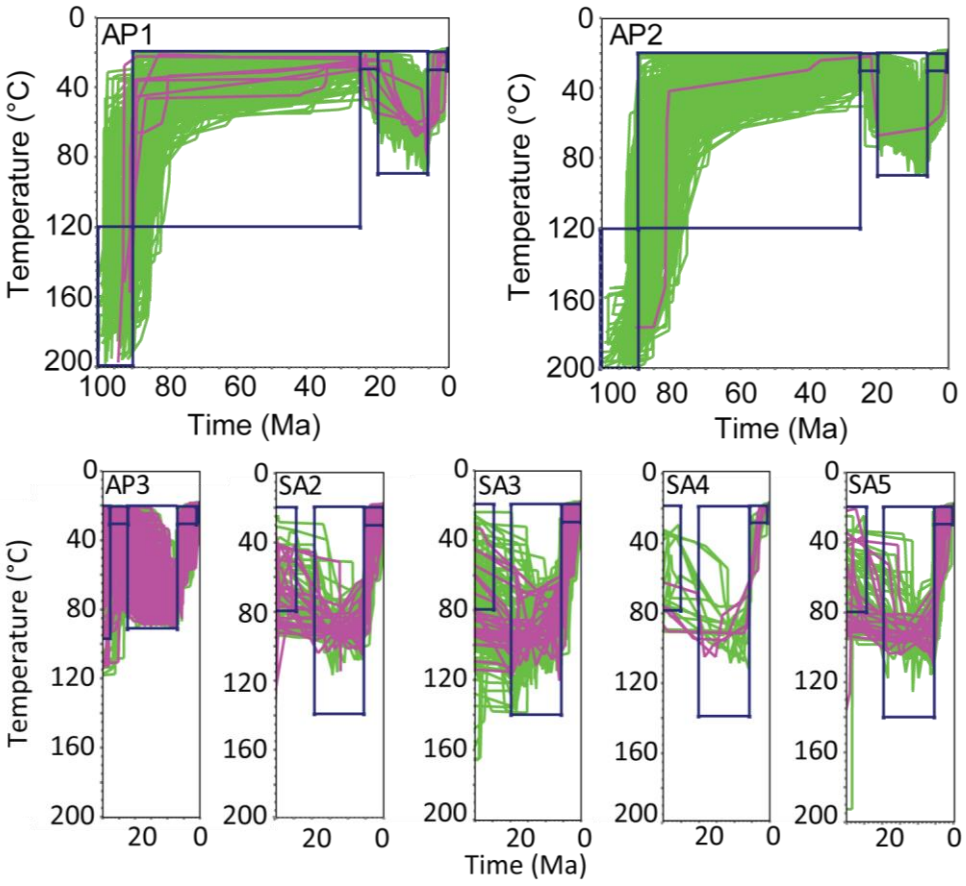

Figure 2.10: t-T paths for piedmont basement samples obtained from inverse modelling. *Path colours indicate good (purple) and acceptable (green) fits, based on comparison to measured AFT and AHe ages, and fission track lengths (Ketcham, 2005). Time axes for sample AP3 and SA-series samples are truncated because t-T histories for these samples are unconstrained prior to the early Miocene. Blue boxes indicate imposed t-T constraints.*

northern transect samples then exhibit a reheating event initiating at ~25-20 Ma and culminating in peak temperatures of ~60-80 °C, followed by rapid cooling to surface or near-surface temperatures starting between ~8-3 Ma. Rapid cooling to near-surface temperatures at ~8-3 Ma is also reproducible in the southern transect samples, which experienced temperatures of ~80-100 °C during the Miocene. All samples therefore indicate a requirement for rapid cooling to near-surface temperatures starting from ~8-3 Ma; the slight disparity between southern and northern transect

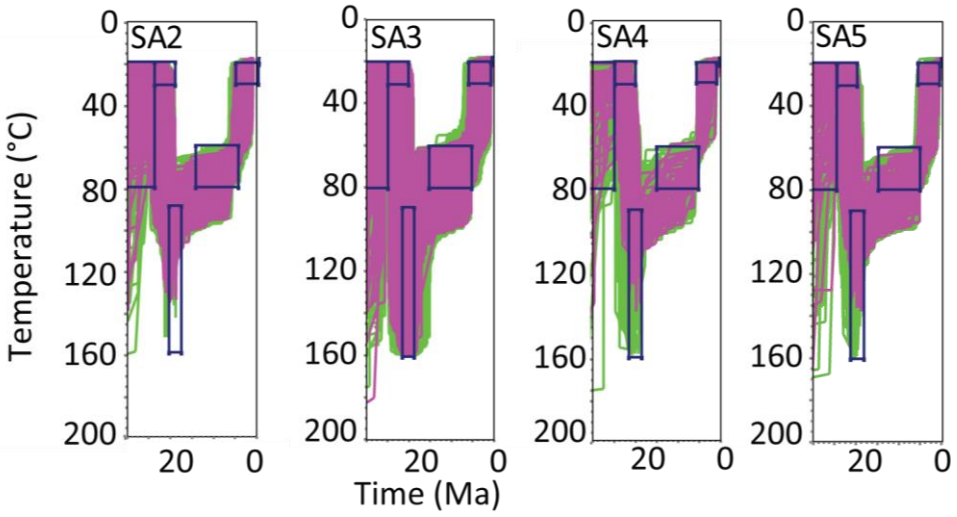

Figure 2.11: t-T paths for piedmont southern transect samples, incorporating an early Miocene heating event. *Path colours indicate good (purple) and acceptable (green) fits, based on comparison to measured AFT and AHe ages, and fission track lengths (Ketcham, 2005). Blue boxes indicate imposed constraints.*

AHe ages is likely the result of the long residence of the northern transect samples in the AHe partial and full retention zones, coupled with cooler Miocene peak temperatures. This combination has permitted retention of He over a longer period, resulting in the slightly older AHe ages of the northern transect.

The presence of the ~5.7 Ma lava overlaying the piedmont further constrains the onset of cooling driven by piedmont denudation to between ~8-6 Ma. However, although these model results reconcile all AHe ages with thermal histories incorporating a cooling event initiating between ~8-6 Ma, the source of the disparity between the AFT ages of the two transects remains unclear. To explore the plausibility of the southern transect AFT ages originating from a common heating event of greater intensity than that experienced by the northern transect samples, interactive forward modelling designed to replicate AFT and AHe ages was carried out to establish common *t-T* constraints for such an event. These constraints are shown in Figure 2.11, which indicates that, following cooling to near-surface temperatures at ~25-20 Ma, a reheating event attaining peak

temperatures of 120-160 °C at ~22-18 Ma can explain observed AFT and AHe ages, while still requiring rapid cooling to surface or near-surface temperatures from ~8-6 Ma. Prior to ~25 Ma, a wide variety of thermal histories are possible. This model outcome is non-unique – as are all inverse thermal history models to some degree – but is consistent with the requirements for samples to be at or near the surface at the onset of significant Comondú deposition at ~25-20 Ma and to return to the surface at ~5.7 Ma, the age of the Cerro Papini lava overlaying the piedmont. The model also has the virtue of reproducing all southern transect AFT ages from a common thermal event at ~22-18 Ma.

2.7 Implications of the Loreto rift segment thermal history

2.7.1 Late Miocene extension onset at Loreto

The rapid cooling from ~60-80 °C to surface temperatures observed in all sample *t-T* histories from between ~8-6 Ma is here interpreted as the result of footwall exhumation and piedmont development driven by slip on the Loreto fault. The thickness of the Comondú Group reported by Umhoefer et al. (2001) suggests piedmont exhumation depths of up to ~1.5-2 km (Figure 2.9), consistent with escarpment elevations of up to ~1.6 km west of the piedmont. Assuming a mean surface temperature of 20 °C, these values equate to a late Miocene geothermal gradient of ~40-20 °C km^{-1}; the lower end of this range is consistent with estimates from the Sierra San Felipe (Seiler et al., 2011) and the Los Cabos block (Fletcher et al., 2000), and the overall range is consistent with estimates of geothermal gradients affected by rifting, which promotes increased heat flow (Chapman, 1986). Generation of the modelled cooling by exhumation of the piedmont is therefore plausible, and slip on the Loreto fault must have initiated between ~8-6 Ma ago to permit the onset of detectable exhumational cooling at this time. The combination of rapid cooling from ~8-3 Ma and presence of the ~5.7 Ma Cerro Papini lava overlaying the piedmont indicates that the piedmont likely developed rapidly; the piedmont had evidently been exhumed to its modern depth prior to ~5.7 Ma, at least around Cerro Papini, and at least ~5 km of a total ~6 km of escarpment retreat

from the fault had occurred, if the 300 m contour is taken as the base of the escarpment. Initiation of fault slip and piedmont exhumation from between ~8-6 Ma implies vertical incision rates of ~0.7-6.7 mm a^{-1}, assuming overburden of ~1.5-2 km thickness was removed. Onset of Loreto fault slip after ~8 Ma and exhumation of much of the piedmont by ~5.7 Ma is slightly earlier than proposed by Dorsey and Umhoefer (2000) and Umhoefer et al. (2002), who inferred the onset of Loreto fault slip between ~6-3.5 Ma ago and piedmont formation after ~2 Ma, and is significantly older than the Late Pliocene-Quaternary piedmont exhumation proposed by Mortimer and Carrapa (2007).

The onset of faulting between ~8-6 Ma and development of the piedmont – at least around Cerro Papini – by ~5.7 Ma also predates at least ~1150 m out of ~1300 m of exposed Loreto basin fill, which was deposited after the oldest readily dateable marker in the basin: a tuff yielding an age of ~2.6 Ma (Umhoefer et al., 1994; Dorsey and Umhoefer, 2000). Based on the cross-sections of Dorsey and Umhoefer (2000), the volume of accommodation space in the Loreto basin available to material deposited prior to ~2.6 Ma is approximately ~99 km^3 (including part of the area subsequently buried beneath the mid-Pliocene Cerro Mencenares volcanic centre). This is less than the ~197-250 km^3 of material which would be produced by denudation of the piedmont to depths of 1.5-2 km, not allowing for the likely volumetric expansion of the material during erosion (Figure 2.12). Therefore, much of the sediment produced by exhumation of the piedmont may have been transported eastward into the Gulf. This has clearly been the case for the Escondido and Nopolo faults, which lack significant onshore hangingwall sediments. Alternatively, the thickness of the basin fill deposited prior to eruption of the ~2.6 Ma tuff may be greater than the ~150 m inferred by Dorsey and Umhoefer (2000), as the base is unexposed; the Loreto basin may be deeper than previously supposed.

More broadly, the onset of faulting and escarpment development at Loreto between ~8-6 Ma post-

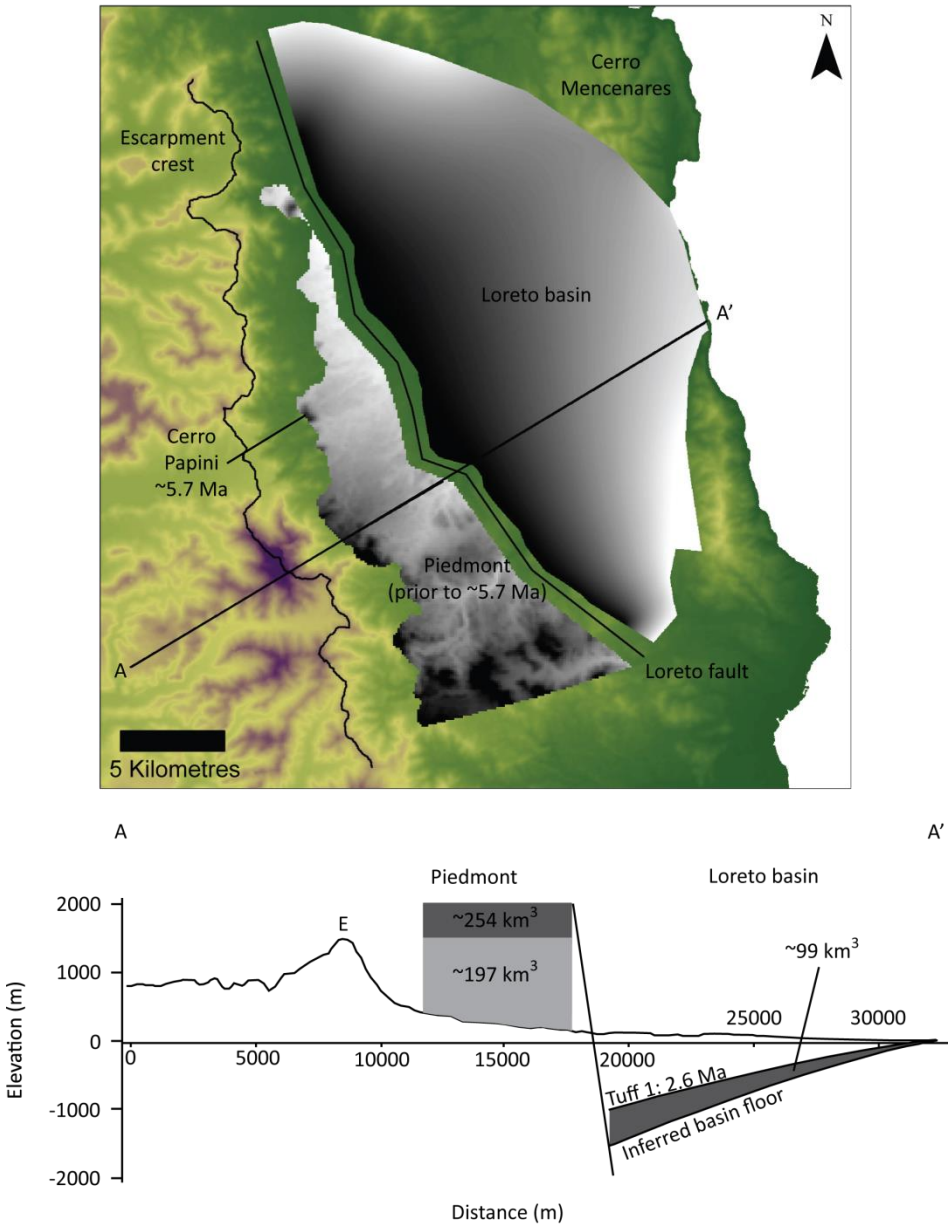

Figure 2.12: Estimates of piedmont denudation prior to ~5.7 Ma and Loreto basin accommodation space prior to ~2.6 Ma. *The majority of piedmont denudation occurred prior to ~5.7 Ma, but much of the Loreto basin fill is thought to have been deposited after ~2.6 Ma. Accommodation space estimate is after Dorsey and Umhoefer (2000), including part of the Loreto basin subsequently buried beneath the Cerro Mencenares volcanic edifice (Bigioggero et al., 1995). Volume of eroded piedmont assumes Comondú thickness of 2 km; area of piedmont which had formed by ~5.7 Ma was estimated by shifting modern MGE crest eastward to location of ~5.7 Ma Cerro Papini. E – modern location of escarpment crest.*

dates the cessation of Pacific-Magdalena spreading by ~6.5-3.5 Ma. As the shear zone west of Baja California has undergone only minor extension since this time (Fletcher et al., 2007), early extension must have been accommodated east of Loreto. There are two possible scenarios. The first is that initial extension along the western margin of the incipient Gulf may have been accommodated on an east-dipping fault inferred east of Isla del Carmen; this is thought to be linked to the Timbabichi and Espiritu Santo/Partida faults to the south, as shown in Figure 2.13 (Dorsey et al., 2001; Umhoefer et al., 2002; Drake, 2005). Extension on the Isla del Carmen – Timbabichi – Espiritu Santo/Partida system from ~12-10 Ma would make it coeval with the San Jose del Cabo fault at the southern tip of the Baja California Peninsula, as determined from AFT analysis of basement units exposed in the footwall (Fletcher et al., 2000). However, the age of initiation of the Isla del Carmen – Timbabichi – Espiritu Santo/Partida system appears to be younger; extension along the eastern side of the Isla San Jose accommodation zone, which links the Timbabichi and Espiritu Santo-Partida faults, and along the eastern side of Isla del Carmen itself, is inferred to have initiated at ~8-4 Ma and ~6-4.5 Ma, respectively (Dorsey et al., 2001; Umhoefer et al., 2007). The oldest of these ages permit these fault systems to have initiated slightly before, or synchronously with, the Loreto fault; the youngest suggest they slightly post-date the onset of faulting at Loreto. These ages are obtained by estimates of sedimentation rates prior to deposition of basin units datable by palaeontological or geochronological analysis; the example of the Loreto basin indicates that ages inferred by this method are not necessarily reliable. However, the onset of extension at ~8-6 Ma would be consistent not only with the age of slip onset on Loreto fault reported here, but also with the ~7 Ma age reported for the Santa Rosalía basin to the north, obtained from palaeomagnetic analysis of tuffaceous basal units (Holt et al., 2000), and more generally with the ~9-7 Ma onset of extension along the western margin of the Gulf proposed by Seiler et al. (2011).

If the proposed ages of the Isla del Carmen – Timbabichi – Espiritu Santo/Partida system are correct, then the second possibility is that extension prior to at least ~8-6 Ma was accommodated east of the modern Gulf. Henry and Aranda-Gomez (2000) reported that SW-directed extension was underway

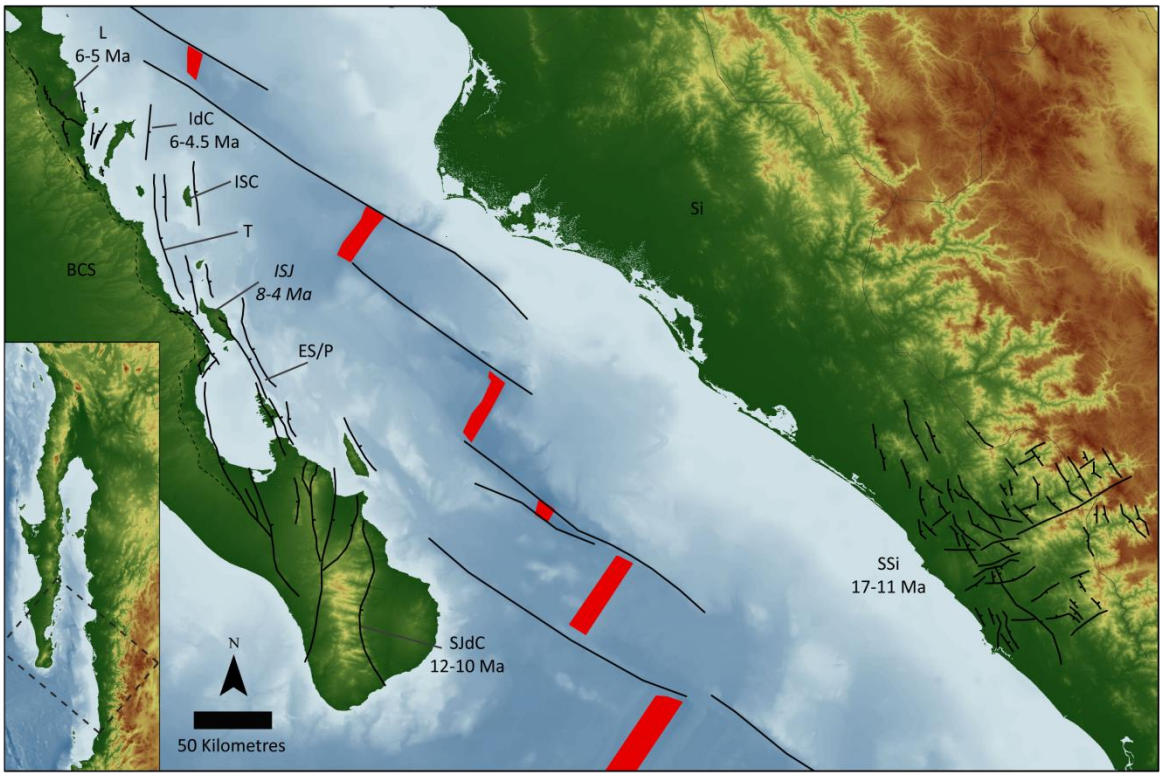

Figure 2.13: Structural overview of the southern Gulf of California. *Showing known and inferred faults (black lines, tick on downthrown side), state boundaries (grey lines), and gulf spreading centres (red) with associated transform faults (black lines). Faults: L – Loreto fault; IdC – Isla del Carmen fault; ISC – Isla Santa Catalina fault; T – Timbabichi fault; ES/P – Espiritu Santu/Partida faults; SJdC – San Jose del Cabo fault; SSi – southern Sinaloa faults. ISJ – Isla San Jose accommodation zone (italicised). States: BCS – Baja California Sur; SI – Sinaloa. Fault ages: Loreto – this study; Isla del Carmen – Dorsey et al. (2001); Isla San Jose – Umhoefer et al. (2007); and southern Sinaloa – (Henry and Aranda-Gomez, 2000). Fault locations also from Fletcher and Munguia (2000); Nava-Sanchez et al. (2001); Drake (2005); and Busch et al. (2011).*

by ~11 Ma in central Sinaloa; they further proposed that, between the cessation of spreading and the onset of significant opening of the Gulf, extension could have been accommodated by reactivation of pre-existing faults of the extensive southern Basin and Range province, which developed in the late Oligocene and early Miocene across central and northern Mexico east of the Gulf region. Accommodation of extension in central Sinaloa prior to the onset of faulting at Loreto is

consistent with the reconstruction of the pre-rift Gulf region by Fletcher et al. (2007), who place these areas together prior to rifting, although the alternative reconstruction of Oskin and Stock (2003) places Loreto opposite northern Sinaloa. The ages of extensional structures present in northern Sinaloa and southernmost Sonora are unclear. However, accommodation of extension across the large area of the southern Basin and Range province prior to localisation in the Gulf area prior to the Late Miocene is consistent with the appearance of widespread marine sediments around the Gulf at ~6 Ma (Oskin and Stock, 2003a), although marine microfossils possibly as old as ~15-12 Ma have been reported from sediment cores obtained from the deep basins of the northern Gulf (Helenes et al., 2009).

Clearly, further work is required to firmly establish the timing of the onset of extension around the southern Gulf, but the ~8-6 Ma age reported here for the onset of faulting at Loreto is consistent with other ages reported from southern Baja California, with the exception of the ~12-10 Ma age reported for the San Jose del Cabo fault (Fletcher et al., 2000). The results of this study are consistent with the hypothesis that Pacific/North America relative motion was initially accommodated east of the modern Gulf area (Seiler et al., 2011), possibly on pre-existing structures of the southern Basin and Range province (Henry and Aranda-Gomez, 2000).

2.7.2 An Early Miocene hydrothermal event at Loreto?

The ~22-18 Ma heating event inferred to have affected the samples of the Loreto piedmont southern transect overlaps with emplacement and eruption ages of ~23-19 Ma reported for silicic plutons and ignimbrites in Nayarit and southern Sinaloa (Ferrari et al., 2002; Duque et al., 2012). The presence of a granodiorite pluton exposed on Isla Santa Catalina which yields an emplacement age of ~22 Ma suggests this pluton emplacement event may have extended across the southern Gulf (Duque et al., 2012). There may also be a link between this episode of pluton emplacement and the spatially and temporally overlapping Comondú Group, largely deposited between ~23-12 Ma, although the silicic plutons cannot be the sole melt source of the generally andesitic Comondú lavas

and tuffs. Both the development of Comondú volcanism and the pluton emplacement episode are possible candidates for the source of the ~22-18 Ma heating event inferred for the southern transect samples. However, neither can be directly responsible. Firstly, the absence of this event from the thermal histories of the northern transect samples, and also from the Los Cabos block to the south (Fletcher et al., 2000), requires that the heating experienced by the southern transect samples was localised, rather than a regional event. Secondly, the results of this study have shown that the granodiorite basement which forms the Loreto piedmont is of Mid-Cretaceous age, and is therefore unrelated to the early Miocene emplacement event. Thirdly, heat conduction from shallow magma emplacements, such as dykes and sills, and surface lavas into the surrounding or underlying country rock is generally inefficient, and insufficient to reset AFT ages, unless samples are collected close to the intrusion (Ehlers, 2005). In the case of the Comondú dykes and sills in the southern transect area, which are typically ~1-2 m in thickness, this implies sample collection within a few tens of metres. Care was taken to avoid this during sampling.

A possible explanation is indicated by the presence of disseminated malachite and epidote observed during sample collection in the area of the Arroyo San Antonio, which suggests hydrothermal processes may have been responsible. A hydrothermal system would provide a mechanism to transport heat from a distal source, such as the Isla Santa Catalina pluton, to the southern piedmont, and would also be consistent with the requirement for the southern transect samples to be within a few hundred metres of the surface by ~25-20 Ma, the timing of the onset of significant Comondú deposition. Hydrothermal reheating has also been invoked to explain localised reheating of near-surface rocks from the Sierra las Animas in central Baja California, albeit at the younger age of ~8 Ma (Seiler, 2009). However, it remains unclear how heat transfer between the southern transect area and the nearest known early Miocene silicic pluton on Isla Santa Catalina was facilitated, and why hydrothermal activity did not also affect the area of the northern transect.

2.7.3 Implications of rapid Late-Cretaceous cooling to near-surface temperatures at Loreto

The results of this study indicate that, following emplacement in the Mid-Cretaceous, the granodiorite basement of the Loreto area had cooled to <80 °C by ~80 Ma, as recorded by samples AP1 and AP2. The ~100-90 Ma emplacement ages obtained for samples AP2 and SA5 suggest that the granodiorite exposed at Loreto is likely part of the Peninsular Ranges Batholith (PRB); constituent plutons of this batholith yielding similar emplacement ages are widely exposed throughout northern Baja California, spatially coincident with a prominent magnetic anomaly which runs the length of the Baja peninsula, suggesting the PRB also underlays the Cenozoic sediments of southern Baja California (Langenheim and Jachens, 2003). The rapid Late Cretaceous cooling observed at Loreto appears to be characteristic of much of the PRB, although cooling ages are complicated by extensional dissection of the easternmost PRB during late Miocene development of the Gulf of California. Samples obtained from PRB exposed west of the Salton trough yield biotite K-Ar ages of ~100-75 Ma (Grove et al., 2003), similar to biotite K-Ar and $^{40}Ar/^{39}Ar$ ages of ~92-74 Ma obtained from PRB exposures in the Sierra Juarez (Axen et al., 2000 and references therein), and also biotite K-Ar and $^{40}Ar/^{39}Ar$ ages of ~101-81 Ma and AFT ages of ~76-70 Ma, both from the Sierra San Pedro Martír (Schmidt et al., 2009 and references therein). The closure temperature of the biotite K-Ar and $^{40}Ar/^{39}Ar$ thermochronometers is ~350-400 °C (Reiners et al., 2005), and consistently overlapping emplacement and biotite K-Ar and $^{40}Ar/^{39}Ar$ ages indicate rapid post-emplacement cooling, as do the Late Cretaceous AFT ages reported here and by Schmidt et al. (2009), although Eocene AFT ages from parts of the PRB east of the Sierra San Pedro Martír suggest cooling may have been delayed in these areas (Seiler et al., 2011). This rapid Late Cretaceous cooling is thought to reflect significant erosional exhumation triggered by pluton emplacement during the Mid-Cretaceous; variations in the magnitude of cooling which had occurred by ~75 Ma presumably reflect spatially variable exhumation depths (Kimbrough et al., 2001; Grove et al., 2003; Schmidt et al., 2009), although refrigeration due to the inferred onset of flat-slab subduction after ~78 Ma may also have contributed (Grove et al., 2003). The consistency of the thermal histories presented in this

study of the granodiorite basement exposed at Loreto with those reported for much of the PRB in northern Baja California suggest that the Loreto granodiorite is a component of the PRB, consistent with the previously proposed southward continuation of the PRB beneath southern Baja California (Langenheim and Jachens, 2003).

2.8 Conclusions

The thermal history of the Loreto segment has been constrained using apatite fission track (AFT) and apatite (U-Th)/He (AHe) thermochronologic analysis, in conjunction with zircon U-Pb geochronology, and is summarised in Figure 2.14. These data indicate that exhumation of the footwall piedmont of the Loreto fault occurred rapidly at ~8-6 Ma, indicating the onset of faulting occurred shortly prior to

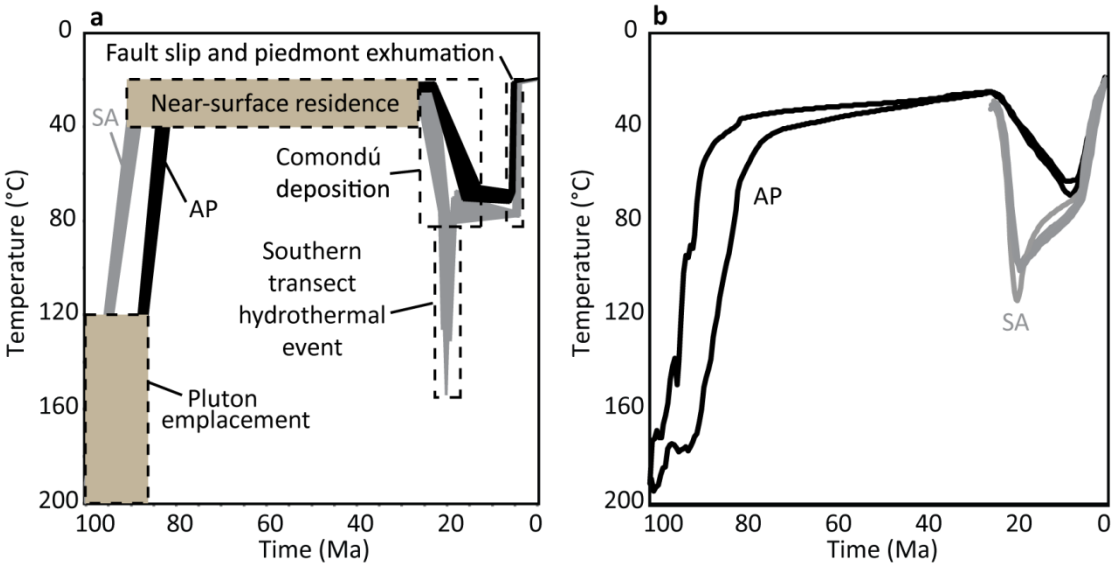

Figure 2.14: Summary cartoons for northern (NT) and southern (ST) transect samples. a*: Summary of acceptable northern (AP) and southern (SA) transect piedmont basement sample thermal histories derived from forward modelling. Thermal histories are poorly constrained prior to ~85 Ma, when zircon U-Pb ages suggest pluton emplacement occurred, and also between ~80 and ~25 Ma, when samples resided at < ~40 °C (likely within ~2 km of the surface).* ***b****: Weighted mean paths of acceptable thermal histories derived from inverse modelling. Thermal histories of southern transect samples are unconstrained prior to ~25 Ma but were likely similar to those of the northern transect.*

this time. The onset of significant extension at Loreto thus post-dates the cessation of Pacific/ Farallon spreading offshore at ~12.5-11.5 Ma by ~6.5-3.5 Ma, consistent with the delay in the onset of extension reported by Seiler et al. (2011) from northern Baja California. A delay in the onset of significant extension after foundering of the Farallon plate may be characteristic of the eastern margin of Baja California, and would support the proposal that early Pacific/North America relative motion was accommodated by distributed deformation of North America across the pre-existing southern Basin and Range structures east of the modern Gulf (Henry and Aranda-Gomez, 2000). However, further work is needed to constrain the age of extensional faults submerged in the Gulf east of Loreto, which may have developed prior to the onset of faulting at Loreto. In addition, the mid-Cretaceous emplacement ages reported by this study support the proposed southern extension of the Peninsula Ranges Batholith inferred to underlie southern Baja California (Langenheim and Jachens, 2003), while Late Cretaceous AFT ages indicate the rapid exhumational cooling reported for much of the batholith shortly following emplacement also affected the Loreto area; the episode of rapid uplift, plateau formation and subsequent denudation reported from northern Baja California by Schmidt et al. (2009) may have been more extensive than previously thought.

2.9 References

Axen, G., 1995, Extensional segmentation of the Main Gulf Escarpment, Mexico and United States: Geology, v. 23, no. 6, p. 515–518.

Axen, J., Grove, M., Stockli, D.F., Lovera, O.M., Rothstein, D.A., Fletcher, J.M., Farley, K.A., and Abbott, P.L., 2000, Thermal evolution of the Monte Blanco dome: Low-angle normal faulting during Gulf of California rifting and late Eocene denudation of the eastern Peninsular Ranges: Tectonics, v. 19, no. 2, p. 197–212.

Barbarand, J., 2003, Compositional and structural control of fission-track annealing in apatite: Chemical Geology, v. 198, no. 1-2, p. 107–137.

Bellon, H., Aguillón-Robles, A., Calmus, T., Maury, R.C., Bourgois, J., and Cotten, J., 2006, La Purísima volcanic field, Baja California Sur (Mexico): Miocene to Quaternary volcanism related to subduction and opening of an asthenospheric window: Journal of Volcanology and Geothermal Research, v. 152, no. 3-4, p. 253–272.

Bigioggero, B., Chiesa, S., Zanchi, A., Montrasio, A., and Vezzoli, L., 1995, The Cerro Mencenares volcanic centre, Baja California Sur: source and tectonic control on postsubduction magmatism within the Gulf Rift: GSA Bulletin, v. 107, p. 1108–1122.

Busch, M.M., Arrowsmith, J.R., Umhoefer, P.J., Coyan, J. A., Maloney, S.J., and Gutierrez, G.M., 2011, Geometry and evolution of rift-margin, normal-fault-bounded basins from gravity and geology, La Paz-Los Cabos region, Baja California Sur, Mexico: Lithosphere, v. 3, no. 2, p. 110–127.

Calmus, T., Pallares, C., Maury, R.C., Aguillón-Robles, A., Bellon, H., Benoit, M., and Michaud, F., 2011, Volcanic Markers of the Post-Subduction Evolution of Baja California and Sonora, Mexico: Slab Tearing Versus Lithospheric Rupture of the Gulf of California: Pure and Applied Geophysics, v. 168, no. 8-9, p. 1303–1330.

Carlson, W.D., Donelick, R.A., and Ketcham, R.A., 1999, Variability of apatite fission-track annealing kinetics: I. Experimental results: American Mineralogist, v. 84, no. 9, p. 1213–1223.

Castillo, P.R., 2008, Origin of the adakite-high-Nb basalt association and its implications for postsubduction magmatism in Baja California, Mexico: Geological Society of America Bulletin, v. 120, no. 3-4, p. 451–462.

Chapman, D.S., 1986, Thermal gradients in the continental crust: Geological Society, London, Special Publications, v. 24, no. 1, p. 63–70.

Cherniak, D.J., and Watson, E.B., 2000, Pb diffusion in zircon: Chemical Geology, v. 172, p. 5–24.

Conly, A.G., Brenan, J.M., Bellon, H., and Scott, S.D., 2005, Arc to rift transitional volcanism in the Santa Rosalia Region, Baja California Sur, Mexico: Journal of Volcanology and Geothermal Research, v. 142, p. 303 – 341.

Dixon, T., Farina, F., DeMets, C., and Suarez-Vidal, F., 2000, New kinematic models for Pacific-North America motion from 3 Ma to present, II: Evidence for a “Baja California shear zone:” Geophysical Research Letters, v. 27, no. 23, p. 3961–3964.

Donelick, R.A., 1993, Method of fission track analysis utilizing bulk chemical etching of apatite, US patent no. 5267274, 35pp.

Donelick, R.A., O'Sullivan, P.B., and Ketcham, R.A., 2005, Apatite fission-track analysis, *in* Reiners, P.W. and Ehlers, T.A. eds., Low-temperature thermochronology: techniques, interpretations, and applications, Mineralogical Society of America, p. 49–94.

Dorsey, R.J., Fluette, A., Mcdougall, K., Housen, B.A., Janecke, S.U., Axen, J., Shirvell, C.R., and Sciences, G., 2007, Chronology of Miocene – Pliocene deposits at Split Mountain Gorge , Southern California: A record of regional tectonics and Colorado River evolution: Geology, v. 35, p. 1–5.

Dorsey, R.J., Housen, B. A., Janecke, S.U., Fanning, C.M., and Spears, A. L.F., 2011, Stratigraphic record of basin development within the San Andreas fault system: Late Cenozoic Fish Creek-Vallecito basin, southern California: Geological Society of America Bulletin, v. 123, no. 5-6, p. 771–793.

Dorsey, R.J., and Umhoefer, P.J., 2000, Tectonic and eustatic controls on sequence stratigraphy of the Pliocene Loreto basin, Baja California Sur, Mexico: Geological Society of America Bulletin, v. 112, no. 2, p. 177–199.

Dorsey, R.J., Umhoefer, P.J., Ingle, J.C., and Mayer, L., 2001, Late Miocene to Pliocene stratigraphic evolution of northeast Carmen Island, Gulf of California: implications for oblique-rifting tectonics: Sedimentary Geology, v. 144, p. 97–123.

Drake, W.R., 2005, Structural analysis, stratigraphy, and geochronology of the San Jose island accommodation zone, Baja California Sur, Mexico: MSc Thesis, Northern Arizona University, US.

Duque, J., Ferrari, L., Orozco-Esquivel, T., Lopez-Martinez, M., and Lonsdale, P., 2012, Rapid exhumation of early to middle Miocene intrusive rocks in the southern Gulf of California: The early stages of continental breakup: Geological Society of America Abstracts with Programs, v. 44.

Ehlers, T.A., 2005, Crustal Thermal Processes and the Interpretation of Thermochronometer Data, *in* Reiners, P.W. and Ehlers, T.A. eds., Reviews in mineralogy and geochemistry 58: Low-temperature thermochronology: Techniques, interpretations, and applications, Mineralogical Society of America, p. 315–350.

Farley, K.A., 2000, Helium diffusion from apatite: general behavior as illustrated by Durango fluorapatite: Journal of Geological Research, v. 105, no. B2, p. 2903–2914.

Farley, K.A., and Stockli, D.F., 2002, (U-Th)/He Dating of Phosphates: Apatite, Monazite, and Xenotime, *in* Kohn, M.L., Rakovan, J., and Hughes, J.M. eds., Reviews in Mineralogy and Geochemistry, p. 559–577.

Farley, K.A., Wolf, R.A., and Silver, L.T., 1996, The effects of long alpha-stopping distances on (U-Th)/He ages: Geochimica et Cosmochimica Acta, v. 60, no. 21, p. 4223–4229.

Ferrari, L., Lopez-Martinez, M., and Rosas-Elguera, J., 2002, Ignimbrite flare-up and deformation in the southern Sierra Madre Occidental, western Mexico: Implications for the late subduction history of the Farallon plate: Tectonics, v. 21, no. 4, DOI: 10.1029/2001TC001302.

Fletcher, J.M., Grove, M., Kimbrough, D., Lovera, O., and Gehrels, G.E., 2007, Ridge-trench interactions and the Neogene tectonic evolution of the Magdalena shelf and southern Gulf of California: Insights from detrital zircon U-Pb ages from the Magdalena fan and adjacent areas: GSA Bulletin, v. 119, no. 11-12, p. 1313–1336.

Fletcher, J.M., Kohn, B.P., Foster, D.A., and Gleadow, A.J.W., 2000, Heterogeneous Neogene cooling and exhumation of the Los Cabos block, southern Baja California: Evidence from fission-track thermochronology: Geology, v. 28, no. 2, p. 107–110.

Fletcher, J.M., and Munguia, L., 2000, Active continental rifting in southern Baja California, Mexico: implications for plate motion partitioning and the transition to seafloor spreading in the Gulf of California: Tectonics, v. 19, no. 6, p. 1107–1123.

Flowers, R.M., Ketcham, R. A., Shuster, D.L., and Farley, K. A., 2009, Apatite (U–Th)/He thermochronometry using a radiation damage accumulation and annealing model: Geochimica et Cosmochimica Acta, v. 73, no. 8, p. 2347–2365.

Galbraith, R.F., 1988, Graphical display of estimates having differing standard errors: Technometrics, v. 30, no. 3, p. 271–281.

Galbraith, R.F., 1981, On statistical models for fission track counts: Journal of the International Association for Mathematical Geology, v. 13, no. 6, p. 471–478.

Galbraith, R.F., and Laslett, G.M., 1993, Statistical models for mixed fission track ages: Nuclear Tracks and Radiation Measurements, v. 21, no. 4, p. 459–470.

Gallagher, K., Brown, R.W., and Johnson, C., 1998, Fission track analysis and its applications to geological problems: Annual Review of Earth and Planetary Sciences, v. 26, p. 519–572.

Gans, P.B., 1997, Large-magnitude Oligo-Miocene extension in southern Sonora: Implications for the tectonic evolution of northwest Mexico: Tectonics, v. 16, no. 3, p. 388–408.

Gautheron, C., Tassan-Got, L., Barbarand, J., and Pagel, M., 2009, Effect of alpha-damage annealing on apatite (U–Th)/He thermochronology: Chemical Geology, v. 266, no. 3-4, p. 157–170.

Green, P.F., Duddy, I.R., Gleadow, A.J.W., Tingate, P.R., and Laslett, G.M., 1985, Fission-track annealing in apatite: track length measurements and the form of the Arrhenius plot: Nuclear Tracks and Radiation Measurements, v. 10, p. 323–328.

Grove, M., Lovera, O., and Harrison, M., 2003, Late Cretaceous cooling of the east-central Peninsular Ranges batholith (33° N): Relationship to La Posta pluton emplacement, Laramide shallow subduction, and forearc sedimentation: Geological Society of America Special Papers, v. 374, p. 355–379.

Hausback, B., 1984, Cenozoic volcanic and tectonic evolution of Baja California Sur, Mexico, *in* Frizzell, V. ed., Geology of the Baja California Peninsula, Pacific Section SEPM, p. 219–236.

Helenes, J., Carreño, A.L., and Carrillo, R.M., 2009, Marine Micropaleontology Middle to late Miocene chronostratigraphy and development of the northern Gulf of California: Marine Micropaleontology, v. 72, no. 1-2, p. 10–25.

Henry, C.D., and Aranda-Gomez, J.J., 2000, Plate interactions control middle – late Miocene, proto-Gulf and Basin and Range extension in the southern Basin and Range: Tectonophysics, v. 318, p. 1–26.

Holt, J.W., Holt, E.W., and Stock, J.M., 2000, An age constraint on Gulf of California rifting from the Santa Rosalia basin, Baja California Sur, Mexico: GSA Bulletin, v. 112, no. 4, p. 540–549.

Hurford, A., 1990, Standardization of fission track dating calibration: Recommendation by the Fission Track Working Group of the I.U.G.S. Subcommission on Geochronology: Chemical Geology: Isotope Geoscience section, v. 80, no. 2, p. 171–178.

Hurford, A.J., and Green, P.F., 1982, A users' guide to fission track dating calibration: Earth and Planetary Science Letters, v. 59, p. 343–354.

Ketcham, R.A., 2005, Forward and Inverse Modeling of Low-Temperature Thermochronometry Data, *in* Reiners, P.W. and Ehlers, T.A. eds., Low-temperature thermochronology: techniques, interpretations, and applications, Mineralogical Society of America, p. 275–314.

Ketcham, R.A., 2003, Observations on the relationship between crystallographic orientation and biasing in apatite fission-track measurements: American Mineralogist, v. 88, p. 817–829.

Ketcham, R.A., Donelick, R.A., and Carlson, W.D., 1999, Variability of apatite fission-track annealing kinetics III: Extrapolation to geological time scales: American Mineralogist, v. 84, p. 1235–1255.

Ketcham, R.A., Gautheron, C., and Tassan-Got, L., 2011, Accounting for long alpha-particle stopping distances in (U–Th–Sm)/He geochronology: Refinement of the baseline case: Geochimica et Cosmochimica Acta, v. 75, no. 24, p. 7779–7791.

Kimbrough, D.L., Smith, D.P., Mahoney, J.B., Moore, T.E., Grove, M., Gastil, R.G., Ortega-Rivera, A., and Fanning, C.M., 2001, Forearc-basin sedimentary response to rapid Late Cretaceous batholith emplacement in the Peninsular Ranges of southern and Baja California: Geology, v. 29, no. 6, p. 491–494.

Langenheim, V.E., and Jachens, R., 2003, Crustal structure of the Peninsular Ranges batholith from magnetic data: Implications for Gulf of California rifting: Geophysical Research Letters, v. 30, no. 11, DOI: 10.1029/2003GL017159.

Laslett, G.M., Green, P.F., Duddy, I.R., and Gleadow, A.J.W., 1987, Thermal annealing of fission tracks in apatite 2. A quantitative analysis: Chemical Geology: Isotope Geoscience section, v. 65, p. 1–13.

Lee, J., Miller, M.M., Crippen, R., Hacker, B., and Vazquez, J.L., 1996, Middle Miocene extension in the Gulf extensional province, Baja California: evidence from the southern Sierra Juarez: GSA Bulletin, v. 108, no. 5, p. 505–525.

Lewis, C.J., and Stock, J.M., 1998, Late Miocene to Recent transtensional tectonics in the Sierra San Fermin , northeastern Baja California , Mexico: Journal of Structural Geology, v. 20, no. 8, p. 1043–1063.

Liu, L., Spasojevic, S., and Gurnis, M., 2008, Reconstructing Farallon plate subduction beneath North America back to the Late Cretaceous: Science, v. 322, p. 934–938.

Lizarralde, D., Axen, G.J., Brown, H.E., Fletcher, J.M., González-Fernández, A., Harding, A.J., Holbrook, W.S., Kent, G.M., Paramo, P., Sutherland, F., and Umhoefer, P.J., 2007, Variation in styles of rifting in the Gulf of California: Nature, v. 448, p. 466–469.

Lonsdale, P.F., 1991, Structural patterns of the Pacific floor offshore of Peninsular California, *in* Dauphin, J.P. and Simoneit, R.T. eds., The Gulf and Peninsular Province of the Californias, AAPG Memoir 47, p. 87–125.

Ludwig, K.R., 2008, Isoplot 3.6: A geochronological toolkit for Microsoft Excel: Berkeley Geochronological Centre Special Publication No.4.

McCrory, P., Wilson, D., and Stanley, R., 2009, Continuing evolution of the Pacific–Juan de Fuca–North America slab window system—A trench–ridge–transform example from the Pacific Rim: Tectonophysics, v. 464, no. 1-4, p. 30–42.

McDowell, F.W., Roldán-Quintana, J., and Amaya-Martínez, R., 1997, Interrelationship of sedimentary and volcanic deposits associated with Tertiary extension in Sonora, Mexico: Geological Society Of America Bulletin, v. 109, p. 1349–1360.

McLean, H., 1988, Reconnaissance geologic map of the Loreto and part of the San Javier quadrangles, Baja California Sur, Mexico: Map MF1799, USGS.

Meesters, A.G.C.A., and Dunai, T.J., 2005, A noniterative solution of the (U-Th)/He age equation: Geochemistry Geophysics Geosystems, v. 6, no. 4, p. 4–6.

Michaud, F., Royer, J.Y., Bourgois, J., Dyment, J., Calmus, T., Bandy, W., Sosson, M., Mortera-Gutierrez, C., Sichler, B., Rebolledo-Viera, M., and Pontoise, B., 2006, Oceanic-ridge subduction vs slab break off: Plate tectonic evolution along the Baja California Sur continental margin since 15 Ma: Geology, v. 34, no. 1, p. 13–16.

Mortimer, E., 2004, Tectonic controls on the growth of coarse-grained delta clinoforms in the Pliocene Loreto basin, Baja California Sur, Mexico: PhD thesis, University of Edinburgh.

Mortimer, E., and Carrapa, B., 2007, Footwall drainage evolution and scarp retreat in response to increasing fault displacement: Loreto fault, Baja California Sur, Mexico: Geology, v. 35, no. 7, p. 651-654.

Mortimer, E., Gupta, S., and Cowie, P., 2005, Clinoform nucleation and growth in coarse-grained deltas, Loreto basin, Baja California Sur, Mexico: a response to episodic accelerations in fault displacement: Basin Research, v. 17, p. 337–359.

Nava-Sanchez, E.H., Gorsline, D.S., and Molina-Cruz, A., 2001, The Baja California Peninsula borderland: structural and sedimentological characteristics: Sedimentary Geology, v. 144, p. 63–82.

Oskin, M., and Stock, J., 2003a, Marine incursion synchronous with plate-boundary localization in the Gulf of California: Geology, v. 31, p. 23–26.

Oskin, M., and Stock, J., 2003b, Pacific–North America plate motion and opening of the Upper Delfín basin, northern Gulf of California, Mexico: Geological Society of America Bulletin, v. 115, no. 10, p. 1173-1190.

Oskin, M., Stock, J., and Martín-Barajas, A., 2001, Rapid localization of Pacific–North America plate motion in the Gulf of California: Geology, v. 29, no. 5, p. 459-462.

O'Sullivan, P.B., and Parrish, R.R., 1995, The importance of apatite composition and single-grain ages when interpreting fission track data from plutonic rocks: a case study from the Coast Ranges, British Columbia: Earth and Planetary Science Letters, v. 132, p. 213–224.

Parrish, R.R., and Noble, S.R., 2003, Zircon U-Th-Pb Geochronology by Isotope Dilution — Thermal Ionization Mass Spectrometry (ID-TIMS), *in* Hanchar, J.M. and Hoskin, P.W.O. eds., Zircon, Mineralogical Society of America Reviews, p. 183–213.

Piñero-Lajas, D., 2008, Seismic reflection and 40Ar/39Ar dating of the continental basement in the western margin of the Farallon Basin (southern Gulf of California, Mexico): MSc thesis, CICESE, Ensenada, Mexico.

Reiners, P.W., Ehlers, T.A., and Zeitler, P.K., 2005, Past, present, and future of thermochronology, *in* Reiners, P.W. and Ehlers, T.A. eds., Reviews in mineralogy and geochemistry 58: Low-temperature thermochronology: Techniques, interpretations, and applications, Mineralogical Society of America, p. 1–18.

Ryan, W.B.F., Carbotte, S.M., Coplan, J.O., O'Hara, S., Melkonian, A., Arko, R., Weissel, R.A., Ferrini, V., Goodwillie, A., Nitsche, F., Bonczkowski, J., and Zemsky, R., 2009, Global Multi-Resolution Topography synthesis: Geochemistry Geophysics Geosystems, v. 10, no. 3, DOI: 10.1029/2008GC002332.

Schmidt, K.L., Paterson, S.R., Blythe, A.E., and Kopf, C., 2009, Mountain building across a lithospheric boundary during arc construction: The Cretaceous Peninsular Ranges batholith in the Sierra San Pedro Martir of Baja California, Mexico: Tectonophysics, v. 477, no. 3-4, p. 292–310.

Seiler, C., 2009, Structural and thermal evolution of the Gulf Extensional Province in Baja California, Mexico: Implications for Neogene rifting and opening of the Gulf of California: PhD thesis, University of Melbourne, Australia.

Seiler, C., Fletcher, J.M., Kohn, B.P., and Gleadow, A.J.W., 2011, Low-temperature thermochronology of northern Baja California, Mexico: Decoupled slip-exhumation gradients and delayed onset of oblique rifting across the Gulf of California: Tectonics, v. 30, DOI: 10.1029/2009TC002649.

Seiler, C., Fletcher, J.M., Quigley, M.C., Gleadow, A.J.W., and Kohn, B.P., 2010, Neogene structural evolution of the Sierra San Felipe, Baja California: Evidence for proto-gulf transtension in the Gulf Extensional Province?: Tectonophysics, v. 488, no. 1-4, p. 87–109.

Shirvell, C.R., Stockli, D.F., Axen, G.J., and Grove, M., 2009, Miocene-Pliocene exhumation along the west Salton detachment fault, southern California, from (U-Th)/ He thermochronometry of apatite and zircon: Tectonics, v. 28, DOI: 10.1029/2007TC002172.

Stock, J.M., and Hodges, K.V., 1989, Pre-Pliocene extension around the Gulf of California and the transfer of Baja California to the Pacific Plate: Tectonics, v. 8, no. 1, p. 99–115.

Tagami, T., and O'Sullivan, P.B., 2005, Fundamentals of Fission-Track Thermochronology, *in* Reiners, P.W. and Ehlers, T.A. eds., Low-temperature thermochronology: techniques, interpretations, and applications, Mineralogical Society of America, p. 19–47.

Tian, L., Castillo, P.R., Lonsdale, P.F., Hahm, D., and Hilton, D.R., 2011, Petrology and Sr-Nd-Pb-He isotope geochemistry of postspreading lavas on fossil spreading axes off Baja California Sur, Mexico: Geochemistry Geophysics Geosystems, v. 12, no. 2, DOI: 10.1029/2010GC003319.

Umhoefer, P.J., 2011, Why did the Southern Gulf of California rupture so rapidly?—Oblique divergence across hot, weak lithosphere along a tectonically active margin: GSA Today, v. 21, no. 11, p. 4–10.

Umhoefer, P.J., and Dorsey, R.J., 1997, Translation of terranes: Lessons from central Baja California, Mexico: Geology, v. 25, no. 11, p. 1007–1010.

Umhoefer, P.J., Dorsey, R.J., and Renne, P., 1994, Tectonics of the Pliocene Loreto basin, Baja California Sur, Mexico, and Evolution of the Gulf of California: Geology, v. 22, p. 649–652.

Umhoefer, P.J., Dorsey, R.J., Willsey, S., Mayer, L., and Renne, P., 2001, Stratigraphy and geochronology of the Comondú Group near Loreto, Baja California Sur, Mexico: Sedimentary Geology, v. 144, p. 125–147.

Umhoefer, P.J., Mayer, L., and Dorsey, R.J., 2002, Evolution of the margin of the Gulf of California near Loreto, Baja California Peninsula, Mexico: Geological Society of America Bulletin, v. 114, no. 7, p. 849–868.

Umhoefer, P.J., Schwennicke, T., Del Margo, M.T., Ruiz-Geraldo, G., Ingle, J.C., and McIntosh, W., 2007, Transtensional fault-termination basins: an important basin type illustrated by the Pliocene San Jose Island basin and related basins in the southern Gulf of California, Mexico: Basin Research, v. 19, p. 297–322.

Umhoefer, P.J., and Stone, K.A., 1996, Description and kinematics of the SE Loreto basin fault array, Baja California Sur, Mexico: a positive field test of oblique-rift models: Journal of Structural Geology, v. 18, no. 5, p. 595–614.

Willsey, S.P., Umhoefer, P.J., and Hilley, G.E., 2002, Early evolution of an extensional monocline by a propagating normal fault: 3-D analysis from combined field study and numerical modeling: Journal of Structural Geology, v. 24, p. 651–669.

Wong, M.S., and Gans, P.B., 2008, Geologic, structural, and thermochronologic constraints on the tectonic evolution of the Sierra Mazatan core complex, Sonora, Mexico: New insights into metamorphic core complex formation: Tectonics, v. 27, DOI: 10.1029/2007TC002173.

Zanchi, A., 1994, The opening of the Gulf of California near Loreto, Baja California, Mexico: from basin and range extension to transtensional tectonics: Journal of Structural Geology, v. 16, no. 12, p. 1619–1639.

3. Development of the Loreto segment rift flank

"Will it give rise to flexure and low bending?"

William Shakespeare, *Henry V, IV.1*

3.1 Introduction

3.1.1 Rift flank uplift mechanisms

It has long been recognised that many continental rifts are flanked by zones of high topography, typically attaining elevations of 1-2 km asl. These uplifts control regional drainage, sediment routing, and deposition, which are thought to exert a strong feedback on rift development through thermal blanketing of thinned crust and incipient spreading centres (Lizarralde et al., 2007; Bialas and Buck, 2009). Such sediment insulation facilitates greater melt extraction, which in turn generates more extensive igneous crust following lithospheric rupture. Elevated rift flanks are also associated with regional perturbation of atmospheric circulation and climate (e.g., Sepulchre et al., 2006; Spiegel et al., 2007), which influence patterns and rates of erosion.

A considerable volume of research on rift flank uplifts exists, and there is growing theoretical consensus that the knowledge of the causal mechanism of a given rift flank uplift provides important insights into the driving forces of the associated rift. Early, binary models (e.g., Sengor and Burke, 1978) of plume-driven ("active") rifting versus rifting driven by far-field extensional tectonic stresses ("passive") have given way to more complex models, in which active and passive rifts are considered end members in a range of possible rifting modes which combine both active and passive characteristics (Ziegler, 1992; Ruppel, 1995; Huismans et al., 2001; Ziegler and Cloetingh, 2004).

Broadly, the active rifting model (Figure 3.1) envisages the impingement of actively upwelling asthenosphere on the base of continental lithosphere. The upwelling imposes a buoyant (upward-directed) load on the lithosphere, warping the lithosphere-asthenosphere boundary upwards. The resulting lithospheric tensional stresses drive rifting, possibly aided by divergent basal shear stresses imposed on the lower lithosphere by asthenospheric return flow. Although active rifting is often

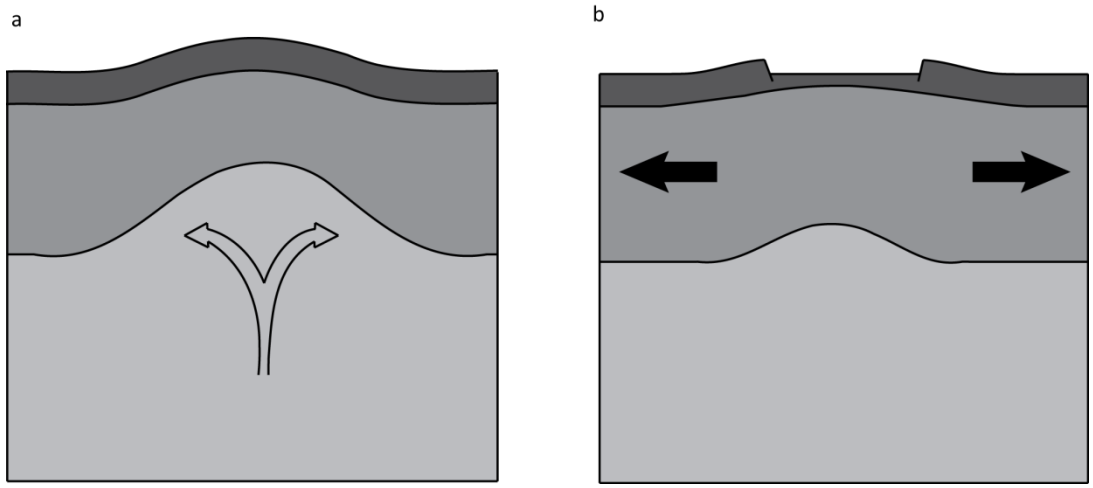

Figure 3.1: End-member models of continental rifting. a: *Active asthenospheric upwelling drives pre-rift topographic doming, generating tensional stresses in the overlying lithosphere which lead to extensional faulting.* ***b:*** *Passive rifting, driven by far-field tensional stresses. Topographic doming is synchronous with or subsequent to extension. Note that many rifts are thought to be hybrids, with lithospheric thinning driving localised convectional asthenospheric upwelling which further promotes rifting (Sengor and Burke, 1978; Huismans et al., 2001; Ziegler and Cloetingh, 2004).*

considered to presuppose plume-like upwelling from a source deep within the mantle, this need not be the case; asthenospheric upwelling may be relatively local and shallow, particularly if associated with the subduction and post-subduction dynamics of oceanic slabs (e.g., Groome and Thorkelson, 2009; Guillaume et al., 2009; Miller and Agostinetti, 2011). The passive model (Figure 3.1) requires the imposition of far-field tensional stresses on the continental lithosphere, typically due to tectonic plate motions, which drive rifting; the resulting lithospheric thinning then accommodates passive upwelling of the underlying asthenosphere. Mixed mode models infer an initial phase of passive rifting which destabilises the lower lithosphere and induces some combination of convective asthenospheric upwelling and partial melting, which weakens the overlying lithosphere and promotes further rifting (Huismans et al., 2001; Kusznir and Karner, 2007; Nielsen and Thybo, 2009).

Crucially, although all these models can explain elevated rift flanks, they make differing predictions about the timing of surface uplift during rift development. Active rifting would trigger surface

doming prior to rifting, on a scale dependent on the diameter of the upwelling asthenosphere; this elevated topography is then inherited by the developing rift flanks (Cox, 1989; Ebinger et al., 1989; Underhill and Partington, 1993; Moucha and Forte, 2011). Surface uplift during passive rifting should be synchronous with extension, in the form of a buoyant isostatic response to tectonic unloading of the lithosphere, as crustal material is replaced with lower-density air, water, and sediment. Provided lithospheric strength during rifting is finite, this isostatic response will be flexurally distributed, uplifting the rift flanks as well as the basin (Braun and Beaumont, 1989; Weissel and Karner, 1989; Kooi et al., 1992). Models of induced asthenospheric upwelling and small-scale convection also envisage rift flank surface uplift occurring synchronously with rifting, but there is some evidence that uplift by this mechanism occurs on the order of ~10-60 Ma following the onset of lithospheric thinning (Steckler, 1985; Buck, 1986; Ziegler, 1992; Huismans et al., 2001); in contrast, significant flexural isostatic uplift is expected to occur within <1 Ma of lithospheric density perturbations (Watts, 2001).

However, closely constraining rift flank uplift timing has commonly proven problematic. This is especially the case for ancient or long-lived rifts, which have often undergone significant post-rift modification by erosional, burial, or tectonic processes (Morgan, 1983; Bohannon et al., 1989; House et al., 2003; Allen and Allen, 2005; Sepulchre et al., 2006; Spiegel et al., 2007; van Wijk et al., 2008; Pik et al., 2008; Japsen et al., 2009; Ferraccioli et al., 2011).

3.1.2 Study Area

This study examines the development of the Loreto rift segment of the Baja California Peninsula, which forms the western margin of the Gulf of California rift (Figure 3.2). The Gulf of California is a youthful, highly oblique transtensional rift; crustal extension is thought to have begun in the Mid to Late Miocene (~15-9 Ma) and rapidly progressed to lithospheric rupture and the onset of seafloor

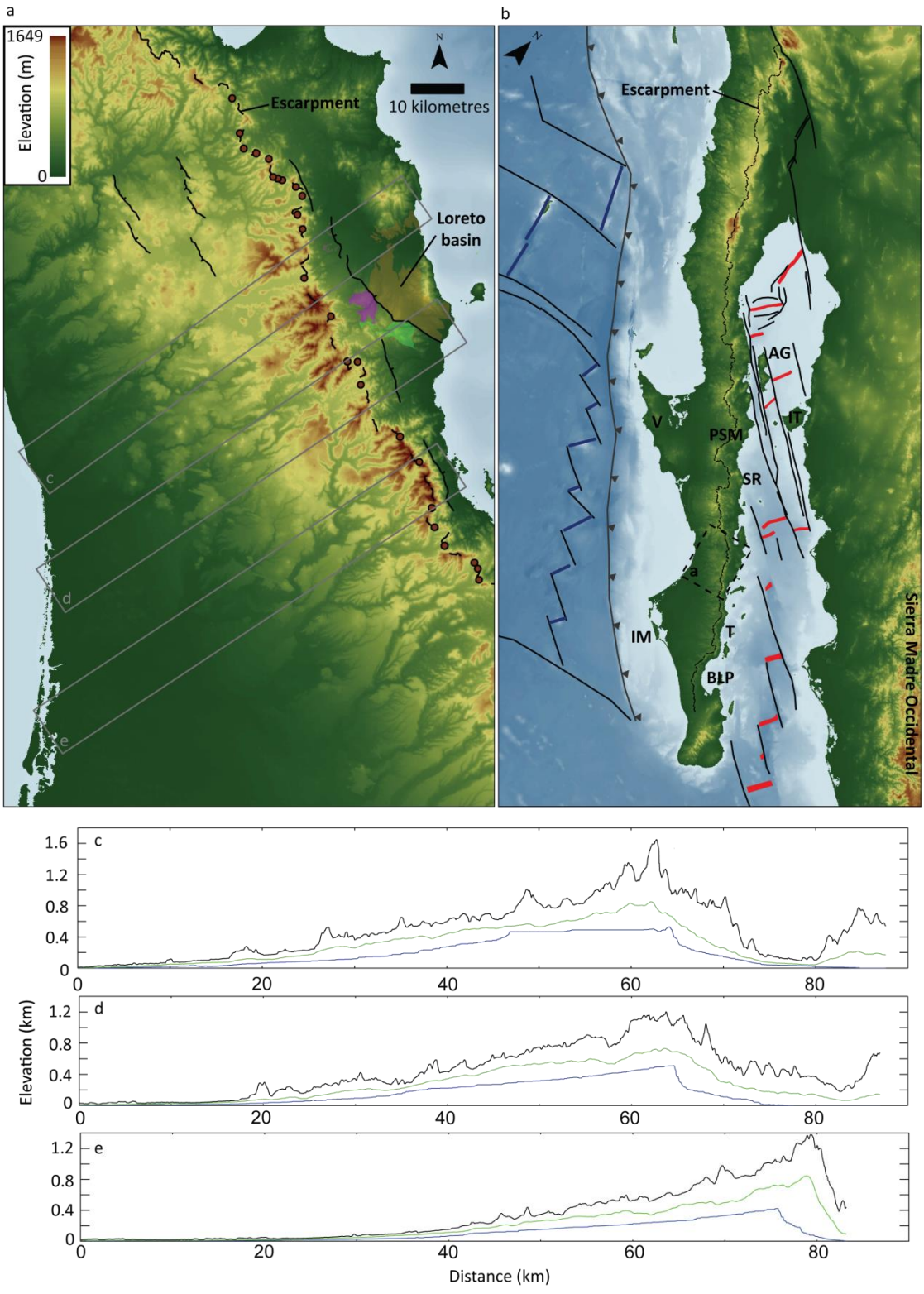

spreading at ~6-3 Ma (Lee et al., 1996; Oskin et al., 2001; Lizarralde et al., 2007; Umhoefer, 2011; Seiler et al., 2011). Rifting initiated in response to a major plate boundary reorganisation following foundering of the oceanic Farallon plate beneath North America and the need to accommodate

Figure 3.2 (Previous page): Overview of the Gulf of California and study area. a: *Topography of the study area from Advanced Spaceborne Thermal Emission and Reflection Radiometer (ASTER) digital elevation model (DEM). Extent of exposed Loreto basin sediments shown in brown; extent of basement granodiorite and metavolcaniclastic exposures shown in purple and green, respectively; faults shown as solid black lines (tick indicates downthrown side); escarpment crest delineated by dashed black line; beheaded canyon locations indicated by red dots. Grey boxes indicate locations of swath profiles* ***c****-****e****.* ***b:*** *Topography and bathymetry of the Gulf of California, from ASTER and Global Multi-Resolution Topography (GMRT) data, respectively (Ryan et al., 2009). Major structures indicated by solid black lines; inactive and active spreading centres indicated by blue and red lines, respectively; escarpment crest marked by dashed black line; abandoned Farallon trench marked by toothed grey line. AG – Isla Angel de la Guarda; IT – Isla Tiburon; PSM – Punta San Miguel; SR – Santa Rosalia; T – Timbabichi; IM – Isla Magdalena; BLP – Bahia de la Paz.* ***c-e:*** *10 km swath profiles illustrating asymmetric rift flank topography. Maximum, mean, and minimum elevations shown in black, green, and blue, respectively.*

divergent Pacific – North America motion (Atwater, 1970; Stock and Hodges, 1989; Oskin et al., 2001). However, as shown in Figure 3.3, a rift-initiating role has also been proposed for active asthenospheric upwelling. Upwelling is thought to have occurred through a window which opened in the subducted Farallon slab as it tore away from the abandoned spreading centres stalled at the trench (Ferrari et al., 2002; Fletcher et al., 2007; Castillo, 2008). Upwelling triggered by the opening of a slab window would be expected to result in regional pre-rift topographic doming and surface uplift. Both numerical and analogue modelling, and geomorphic analyses of other regions of inferred slab detachment, indicate that asthenospheric flow through a slab window and the associated topographic response should occur within ~2 Ma of detachment (see Table 4.1). In the absence of such upwelling, flank uplift should occur synchronously with rifting. Crucially, the youthfulness and rapid development of the Gulf of California means that post-rift geological processes have had little

opportunity to modify the rift topography through processes of erosion or burial, making the Gulf a particularly suitable target for investigation.

Study	Window depth	Response time	Study type
van de Zedde and Wortel, 2001	~50 km ~60 km ~150 km	<1 Ma <1 Ma >30 Ma	Numerical modelling
Rogers et al., 2002*	~50 km	<6 Ma (uplift coeval with breakoff)	P-wave tomography and geomorphological analysis
Miller and Agostinetti, 2011	~70 km	<10 Ma (poorly constrained)	S-wave seismic receiver function analysis
Guillaume et al., 2010	130 - 330 km	~2 Ma	Analogue modelling
Guillaume et al., 2009*	?	<1 Ma	Geomorphological analysis
Duretz et al., 2011*	~100 km ~200 km ~300 km	<0.7 Ma <1.1 Ma <1.5 Ma	Numerical modelling
Duretz et al., 2012	35 – 200 km	<2 Ma	Numerical modelling
Burkett and Billen, 2009	59 – 221 km	<1 Ma	Numerical modelling
Gerya et al., 2004*	108 – 408 km	~1.7 Ma	Numerical modelling
Chatelain et al., 1992*	~85 km	<1 Ma	Geomorphic analysis

Table 3.1: *Response times for asthenospheric flow following slab detachment; studies marked * include estimates of topographic response times.*

In common with many rift flank landscapes, the topography of the Baja California Peninsula is highly asymmetric. An unextended west-sloping rift flank, which attains elevations of 1-2 km asl, is separated from a narrow, low-elevation eastern coastal plain by a prominent east-facing rift escarpment; the crest of the escarpment forms the regional drainage divide. The rift flank is incised by a network of west-draining canyons; these are typically up to ~400-600 m deep, and are commonly beheaded at the escarpment crest. West of the escarpment, a low-elevation coastal plain hosts the rift-bounding faults of the Gulf of California's western margin. At the Loreto segment, the plain broadens to include a well-exposed syn-rift sedimentary basin, hosted in the hangingwall of the Loreto fault. Significantly, the fault is not situated at the base of the escarpment, but is separated

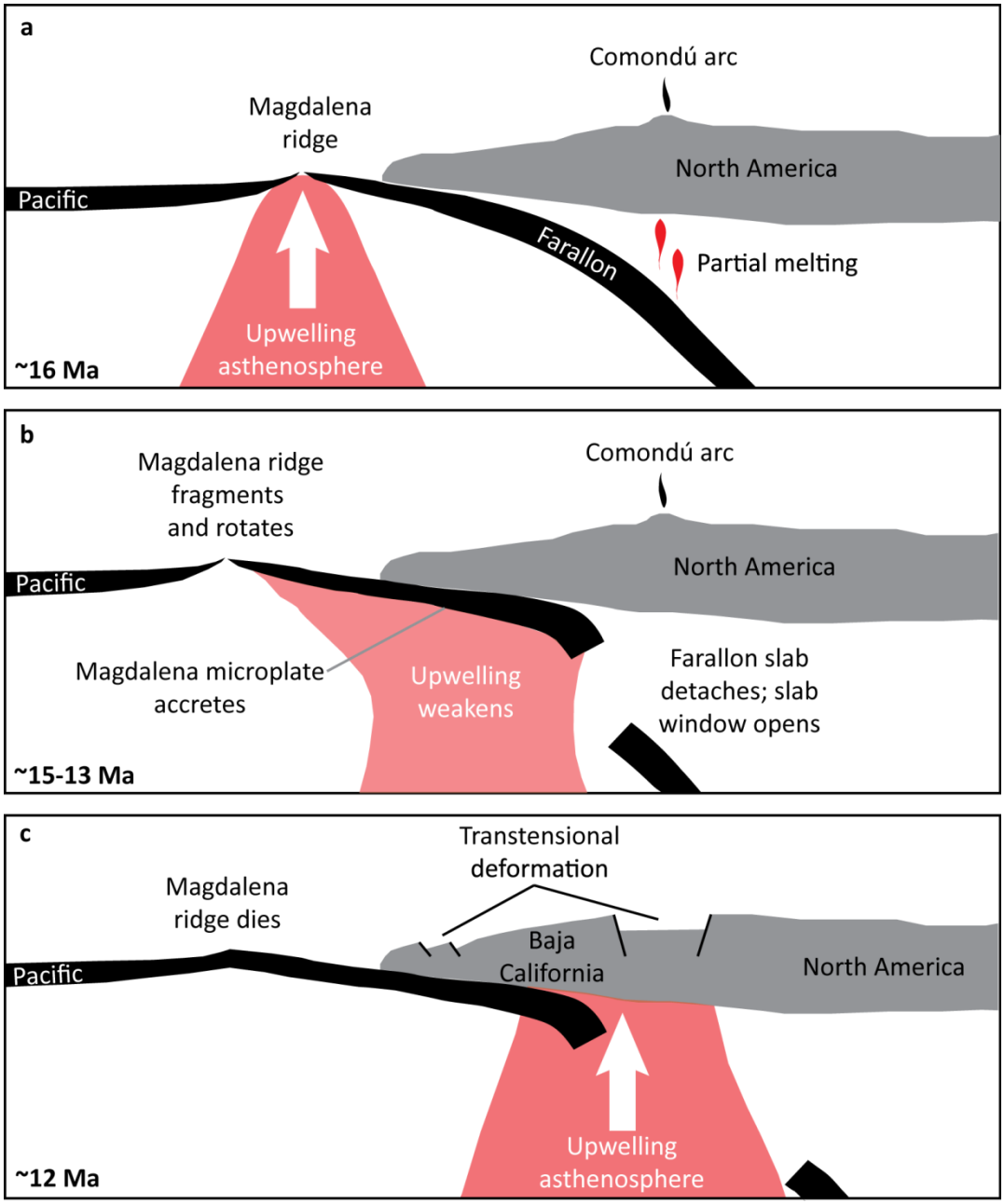

from it by a low-elevation, low-relief eroded piedmont which exposes the regional granodiorite basement (Umhoefer et al., 1994; Dorsey and Umhoefer, 2000; Umhoefer et al., 2002).

The combination of the basement piedmont and the beheaded rift flank canyons permits the tectonic and topographic evolution of the Loreto segment to be deduced. Canyon incision was likely driven by surface uplift associated with formation of the elevated rift flank, while beheading of the canyons at the escarpment crest suggests the existence of a palaeodivide east of the modern escarpment. Two hypotheses of canyon formation can be outlined. In the first, canyon incision was

Figure 3.3 (Previous page): Cartoon showing proposed role of asthenospheric upwelling in driving Gulf of California rifting. *Modified from Fletcher et al. (2007).* ***a:*** *Magdalena ridge converges on North America until ~16 Ma as a component of the Pacific-Farallon ridge; subduction of the Farallon plate generates Comondú arc volcanism in what will become the Gulf region.* ***b:*** *As the buoyant ridge approaches North America, slab detachment occurs; the Magdalena ridge fragments and rotates between ~15-13 Ma in response to the loss of slab pull, and gradually accretes to North America as spreading slows. The asthenospheric root of the ridge becomes dislocated from the dying ridge, and is overridden by North America.* ***c:*** *Spreading ceases at the Magdalena ridge, probably at ~12.5-11.5 Ma. Transtensional deformation of North America commences on both sides of Baja California to accommodate divergent Pacific/North America motion. Asthenospheric upwelling through the developing slab window weakens the lithosphere east of Baja California and preferentially focuses deformation inboard, around the gulf region. Proposed alignment of the dislocated Magdalena ridge root and the slab window may have further promoted asthenospheric upwelling.*

driven by regional pre-rift surface doming prior to rifting, with a drainage divide east of the rift-bounding faults and the modern escarpment; the pre-rift dome was subsequently tectonically dissected by rift-related faulting. In the second, incision occurred synchronously with rifting, with a drainage divide at the crest of a developing escarpment located at the rift bounding fault. Knowledge of the relative timing of escarpment formation and canyon incision permits distinction between these two scenarios. Here, the timing of canyon incision is constrained by $^{40}Ar/^{39}Ar$ geochronology of lavas displaying cross-cutting or infilling relationships with the rift flank canyons. The canyons are shown to be incised into a pre-uplift, low-relief palaeosurface which can be used as a reference for estimates of depths and rates of incision. In Chapter 2, the timing of exhumation of the escarpment piedmont as a proxy for the timing of crustal extension was investigated utilising apatite (U-Th)/He and apatite fission track thermochronology; in this chapter, the relevance of the timing of extension to the timing of rift flank surface uplift is discussed.

3.2 Background

3.2.1 Geology of the rift flank

The geology of southern Baja California is considered here in some detail for the topographic information which can be deduced from facies types and distributions. In particular, given the long history of subduction west of Baja California and the focus of this study on topographic development, it is necessary to consider whether the area has experienced prior episodes of tectonic uplift; complex tectonic histories are not uncommon at active margins (e.g. Thouret et al., 2007; Schildgen et al., 2009; Schildgen et al., 2012).

The overall stratigraphy of southern Baja California is summarised in Figure (3.4). Although much of southern Baja California is covered by Cenozoic sediment, most of the region is thought to be underlain by tonalite-granodiorite plutons similar to those exposed in the north of the Baja Peninsula which comprise the late Cretaceous Peninsula Ranges batholith (Hausback, 1984; McLean et al., 1987). Plutons of this batholith were intruded into Jurassic and early Cretaceous arc rocks and ophiolite, which are preserved as metamorphic roof pendants (Gastil et al., 1975). Basement exposures east of the escarpment support this model, as does a significant linear magnetic anomaly, which tracks the Peninsular Ranges batholith in the north of the peninsula, and continues as far south as Bahía de la Paz (Langenheim and Jachens, 2003). Basement exposures are unknown west of the escarpment crest on the rift flank, with the exception of a late Jurassic – early Cretaceous ophiolite complex with associated blueschist and amphibolite metamorphic units, exposed off the Pacific coast on Isla Magdalena and Isla Santa Margarita (Bonini and Baldwin, 1998).

The oldest sedimentary units exposed on the rift flank comprise marine sandstones, shales, and rare diatomites (Hausback, 1984; McLean et al., 1987). Although early micropalaeontological analysis suggested these were deposited in upper to mid bathyal depths, recent work suggests more likely depositional depths of <150 m (Carreno et al., 2000; Schweitzer et al., 2007) in the Early to Mid

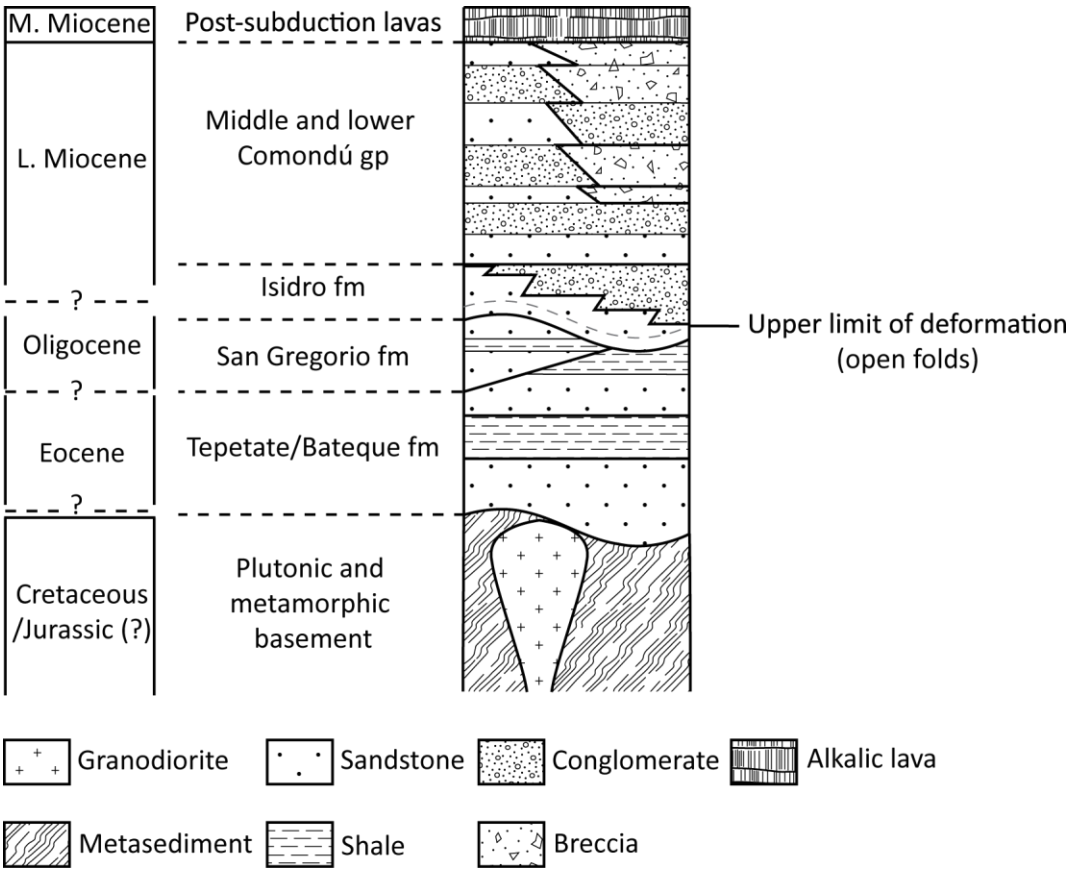

Figure 3.4: Schematic stratigraphic column for the Loreto segment rift flank. *Based on previous work by Hausback (1984); Sawlan and Smith (1984); McLean et al. (1987); Umhoefer et al. (2001).*

Eocene. Petrology of the clastic units suggests derivation from a granitic source terrane (Hausback, 1984). These units are sparsely exposed west of Bahía de La Paz and north of the La Purísima canyon; their stratigraphic affinity is a source of some controversy, with some authors assigning them solely to the Tepetate Formation (Heim, 1922; Hausback, 1984), while others propose two isochronous but spatially distinct formations, the Tepetate and the Bateque (McLean et al., 1987). Although the base of these units is unexposed, they have a thickness of at least ~500 – 800 m. The units also exhibit open folds, with fold axes trending NW.

The San Gregorio Formation (Beal, 1948) unconformably overlies the Tepetate/Bateque Formations, and comprises marine shales and sandstones, sometimes phosphatic, and rhyolite tuffs. These units are exposed west of La Purísima and Bahía de La Paz, and also on the coastal plain east of the

escarpment at Bahía de La Paz and Timbabichi. Applegate (1986) proposed that the units west of Bahía de La Paz be termed the El Cien formation. Micropalaeontologic analysis indicates the western units were deposited at depths of ~150 – 500 m, while the eastern units exhibit shallow marine, near-shore facies and fossils (Hausback, 1984; McLean et al., 1987; Grimm and Foellmi, 1994). The formation attains thicknesses of ~70 – 130 m, and tuffaceous units have yielded late Oligocene K-Ar ages of 27.2 ± 0.6 to 23.4 ± 0.3 Ma (Hausback, 1984). The eastern units of the San Gregorio are undeformed and flat-lying, but the western units exhibit syn-sedimentary slumping and deformation, as well as north-trending open folds (Hausback, 1984; McLean et al., 1987).

The San Gregorio Formation is unconformably overlain by the Isidro Formation; at some localities, the San Gregorio is absent, and the Isidro Formation directly overlies the Tepetate/Bateque Formation, indicating a period of post-Oligocene erosion prior to deposition of the Isidro Formation. The Isidro Formation comprises up to 80 m of shallow marine sandstones, shell hash, conglomerate, and tuffs, interpreted as lagoonal deposits and exposed east of the escarpment crest at Bahía de La Paz and Timbabichi, and west of the escarpment at La Purísima (Hausback, 1984). Mollusc assemblages suggest an early Miocene age (McLean et al., 1987). The Isidro Formation also contains debris reworked from the Tepetate/Bateque and San Gregorio Formations, suggesting small-scale uplift and erosion during the early Miocene. This is consistent with the observation that basal Isidro units in the west of the peninsular exhibit small-scale open folds with NW trending axes, while overlying units are flat-bedded (McLean et al., 1987). Isidro units exposed east of the escarpment are undeformed, and some record subaerial conditions.

Collectively, these units record persistent shallow marine conditions (typically <150 m depth) west of the escarpment from mid-Eocene to early Miocene time, marked by repeated hiatuses in deposition and minor erosion. This was followed by a minor deformation episode of unknown cause which was likely of early Miocene age and which produced gentle N to NW trending open folds. East of the escarpment, sedimentary rocks older than the Oligocene are absent; Oligocene and early Miocene

units record shallow marine to subaerial conditions. Crucially, the preservation of numerous thin sedimentary units ranging in age from the Mid-Eocene to the Early Miocene strongly suggests that the study area has not experienced significant uplift and denudation during this time; the persistence of shallow marine conditions also suggests remarkably little change in elevation occurred during this time.

The key stratigraphic events which affected the study area leading up to and during rifting can now be considered. These comprise a major depositional episode, associated with the westward migration of subduction-related volcanism into southern Baja California and recorded by the units of the volcaniclastic Comondú Group, and a subsequent period of anomalous volcanism. In the Early Miocene, following the prolonged post-Eocene tectonic and depositional quiescence, deposition of the Comondú Group commenced. The Comondú Group is the dominant sedimentary unit of Baja California Sur, extending ~600 km north from Bahía de La Paz to approximately Punta San Miguel, with related units extending discontinuously northward through northern Baja California; related units are also exposed in Isla Angel de La Guarda and Isla Tiburon, and in coastal Sonora (Dorsey and Burns, 1994; Umhoefer et al., 2001). Near the escarpment, the Comondú Group has a composite thickness of ~1.5 – 2 km and overlies the Isidro formation; further west, it thins to ~100 m or less and interfingers with the upper units of the Isidro formation. The Comondú consists of three units: the lower, comprising ~200-300 m of fluvial sandstones, conglomerates, tuffs, and rare lava flows, mostly deposited between ~23-19 Ma, although deposition onset may have been as early as ~25-30 Ma; the middle, comprising ~750 m of andesite breccia and minor andesite lavas, deposited between ~19-15 Ma; and an upper unit comprising ~600 m of andesite lava flows erupted between ~15-12 Ma, which is restricted to the coastal plain east of the escarpment (Hausback, 1984; McLean et al., 1987; McLean, 1988; Umhoefer et al., 2001). With the exception of minor shallow marine components near Timbabichi (Schwennicke and Plata-Hernandez, 2003), the Comondú was deposited under subaerial conditions. The three constituent units – lower, middle, and upper – have been interpreted as the distal, proximal, and core units, respectively, of the volcanic arc generated

by subduction of the Farallon plate beneath North America (Hausback, 1984; Umhoefer et al., 2001). The vertical succession therefore indicates that arc volcanism migrated westward two to three times during the Early to Middle Miocene, consistent with Late Oligocene extinction of arc-related voluminous rhyolite ignimbrite volcanism in the Sierra Madre Occidental volcanic province of central Mexico (Ferrari et al., 1999; Umhoefer et al., 2001). It should be noted that the oldest reported Comondú units overlap temporally with both the San Gregorio and Isidro Formations; these may be the distal equivalents of the Comondú (Umhoefer et al., 2001), but as the San Gregorio and lower units of the Isidro are deformed, while overlying Comondú units are not, it seems more likely that the San Gregorio at least is older, which would imply that the K-Ar ages reported by Hausback (1984) are too young.

West of the escarpment crest, the Tepetate/Bateque and Isidro Formations, and the Comondú Group, are discontinuously overlain by mafic lavas and scoria cones, typically attaining thicknesses of a few tens of metres to a maximum of ~100 m (McLean et al., 1987; Bellon et al., 2006). These lavas were erupted along the Baja peninsula between ~25-30 °N from ~15 Ma to the late Quaternary, and many exhibit unusual compositions, being enriched in strontium (>1000 ppm) and magnesium relative to equivalent calc-alkaline series lavas; these characteristics are thought to reflect melt formation through partial dehydration melting of mantle wedge peridotite previously metasomatised by interaction with adakitic magma formed by partial slab melting (Pallares et al., 2007). The high heat flux and presence of slab melt required by this petrogenetic model is consistent with the proposed slab window beneath Baja California and also with the presence of small volumes of adakite lava at Isla Santa Margarita, the Vizcaino peninsula, and the Santa Rosalia basin (Pallares et al., 2007; Calmus et al., 2011). However, alternative interpretations propose either that melting of the metasomatised mantle wedge was enabled by the influx of hot Pacific asthenosphere, overridden by westward migration of North America (Castillo, 2008); or that chemically diverse pockets of metasomatised mantle were melted by the thermal re-equilibration of the stalled Farallon slab following the cessation of subduction (Negrete-Aranda and Cañón-Tapia, 2008). The

first of these alternative models is also consistent with the opening of a slab window beneath the Baja Peninsula following subduction; the second is not. Reflecting this unusual geochemistry, these lavas have been variously termed alkali basalts (Sawlan and Smith, 1984); bajaites (Rogers et al., 1985); and magnesian basalts, basaltic andesites, and magnesian andesites (Bellon et al., 2006; Calmus et al., 2011). Also reported from the rift flank is a major tholeiitic basalt flow, north of La Purísima, and rare lavas with compositions transitional between calc-alkaline and alkali basalt or magnesian andesite (Sawlan and Smith, 1984; Bellon et al., 2006). These classifications are based on geochemical analysis of whole-rock compositions; in the field these lavas, although highly distinct from those of the Comondú Group, are visually indistinguishable from each other, and for simplicity they are referred to as post-subduction lavas, here and throughout.

3.2.2 Stream incision as a recorder of uplift

This study exploits incision of the rift flank canyons to constrain the magnitude, timing, and rate of rift flank uplift. Fluvial incision is directly dependent on the ability of a stream to perform work by the conversion of potential energy to kinetic energy through altitude loss, which can be expressed as

$$\Omega = \frac{\Delta PE}{\Delta t\, \Delta x} \qquad \text{(Equation 3.1)}$$

where stream power Ω is the rate of change of potential energy (PE) over a unit length. As

$$\Delta PE = mg\Delta h \qquad \text{(Equation 3.2)}$$

where m is mass; g is gravitational acceleration, and h is height, and

$$\frac{m}{\Delta t} = \rho_w Q \qquad \text{(Equation 3.3)}$$

where ρ_w is water density and Q is discharge, Eqn. 4.1 can be written

$$\Omega = kQS \qquad \text{(Equation 3.4)}$$

where S is slope, and k is a constant incorporating $\rho_w g$ (Burbank and Anderson, 2012). Stream power therefore depends directly on discharge and slope, which on geological timescales are controlled by climate and tectonic activity, respectively. Tectonic uplift of any part of a stream relative to the base level it drains to will therefore act to promote the potential for incision, as will any increase in precipitation. However, promotion of incision by climate change can be excluded because analysis of types and stable isotope compositions of palaeosols in the Fish Creek – Vallecito basin of the northern Gulf of California indicates increasing aridity in the region during the Pliocene (Peryam et al., 2011). Likewise, a palynologic record obtained from a marine sediment core offshore southern California also shows increasing aridity during the late Miocene and Pliocene (Ballog and Malloy, 1981). These results are in accordance with a global shift to a cooler, more arid regime during this time (Raymo et al., 2011). As enhanced aridity should act to retard incision by reducing water flow, it is likely instead that rift flank canyon incision records tectonic uplift (regardless of the driving mechanism of this uplift). Provided little or no interfluve degradation has occurred, the depth of incision therefore provides a minimum magnitude of uplift.

3.2.3 Methods for $^{40}Ar/^{39}Ar$ dating

To establish the incision chronology of the west-draining rift flank canyon, the $^{40}Ar/^{39}Ar$ method is utilised (for an overview, see McDougall and Harrison, 1999). A development of the long-established K-Ar dating technique, $^{40}Ar/^{39}Ar$ exploits the ^{40}K-^{40}Ar radioisotope decay system. ^{40}K comprises ~0.01% of all K and has a half life of ~1.25 billion years (Ga); the process of decay to stable ^{40}Ar is dominated by electron capture followed by γ release to ground state. The particular advantage of this radioisotope system is that K is abundant in crustal rocks, including the lavas present on the rift flank. The $^{40}Ar/^{39}Ar$ method is preferred because Ar abundances are determined simultaneously on the same sample. Instead of direct measurement of ^{40}K and ^{40}Ar abundances, which must be performed separately, the $^{40}Ar/^{39}Ar$ method utilises neutron bombardment of the sample to induce ^{39}Ar production from ^{39}K, an isotope which is stable in nature. Knowledge of ^{39}K abundance allows the original abundance of the parent ^{40}K isotope to be determined from the fixed $^{40}K/^{39}K$ ratio. Ar gas

is extracted by laser or resistance furnace step heating until total sample fusion is achieved, analysed by mass spectroscopy, and the $^{40}Ar/^{39}Ar$ age calculated using the equation:

$$t = \frac{1}{\lambda} ln\left(1 + J\frac{^{40}Ar^*}{^{39}Ar_K}\right) \qquad \text{(Equation 3.5)}$$

where t is the sample age; λ is the ^{40}K-^{40}Ar decay constant; $^{40}Ar^*/^{39}Ar_K$ is the measured ratio of radiogenic ^{40}Ar and ^{39}Ar generated by induced decay of ^{39}K, respectively; and J is the irradiation parameter, determined from:

$$J = \frac{(\exp \quad \lambda t) - 1}{^{40}Ar^*/^{39}Ar_K} \qquad \text{(Equation 3.6)}$$

Step-heating, by progressively releasing Ar gas from sample domains sensitive to different temperatures, allows Ar loss to be detected, as more thermally sensitive domains will exhibit anomalous $^{40}Ar/^{39}Ar$ ratios. Domains which have functioned as closed systems since the event of interest will exhibit fixed $^{40}Ar/^{39}Ar$ ratios; plots of apparent $^{40}Ar/^{39}Ar$ ages for successive heating steps will yield flat patterns (plateaux). The presence of well-defined plateaux in such plots enables confident identification of closed-system samples – a further advantage of the $^{40}Ar/^{39}Ar$ method. Age corrections must be made for atmospheric Ar contamination, variations in reactor neutron flux, and mass spectrometer mass bias. The first is done using the $^{40}Ar/^{36}Ar$ ratio of the sample; the second using co-irradiation of mineral standards of known age, which act as fluence monitors; and the third by measurement of air standards, exploiting the fixed $^{40}Ar/^{36}Ar$ atmospheric ratio (Mark et al., 2011). As with any radioisotope dating system, there are several implicit assumptions: that ^{40}K decays at constant rate regardless of physical state; that the $^{40}K/K$ and $^{39}K/K$ ratios are fixed in nature; that radiogenic ^{40}Ar in the sample is produced solely by ^{40}K decay; that any nonradiogenic ^{40}Ar can be detected and corrected for; and that the sample has remained a closed system since the event of interest (typically sample crystallisation and cooling).

Although the $^{40}Ar/^{39}Ar$ technique is commonly used to determine single crystal ages, it is also routinely successfully applied to groundmass sampled from fine-grained lavas. This negates the need to use phenocrysts, which may be absent, and even if present are potential country rock contaminants which may contain excess ^{40}Ar. Although groundmass components can also contain excess ^{40}Ar, as phases which typically formed following eruption they are more likely to have equilibrated with the atmosphere during crystallisation and cooling. ^{40}Ar present in excess of the amount predicted by ^{39}Ar abundance should therefore be explicable by the fixed $^{40}Ar/^{36}Ar$ atmospheric ratio. Detection of non-atmospheric excess ^{40}Ar is therefore an indicator of sample contamination.

3.3 Development of the Loreto segment rift flank

3.3.1 Geology of the Loreto segment rift flank

Although systematic investigation of the pre-rift geology of the rift flank was not a primary aim of this study, very little previous work has been carried out in the area; previous authors have focussed on the area north of the La Purísima canyon (McLean et al., 1987) or to the south around Bahía de La Paz (Hausback, 1984), or on the geochemistry of the volcanic units (Sawlan and Smith, 1984; Bellon et al., 2006). Brief details of the stratigraphy and distribution of the pre-rift units are therefore included here for completeness.

The area between the Comondú and San Javier canyons is dominated by units of the lower and middle Comondú; the upper unit was not observed west of the escarpment, in agreement with reconnaissance observations made by Umhoefer et al. (2001). The middle unit extends ~15-20 km west of the escarpment crest, and chiefly comprises massive to poorly bedded unsorted volcaniclastic breccia. Clasts are typically subangular, and comprise granule to boulder sized pink-purple, grey, and green fragments of andesite lava and dike material, typically hosting euhedral to subhedral phenocrysts of hornblende and plagioclase; exceptional clasts attain lengths of ~1 m. Clasts are supported by a beige matrix of fine to coarse lithic fragments (~30-95%), euhedral crystals

and crystal fragments of hornblende and plagioclase up to ~1 mm in length (~3-15%), and fine-grained tuffaceous material. Lens-like bodies of medium to coarse sand, typically ~1-6 m thick and ~8-40 m wide, are commonly present within the middle unit; these have a similar composition to the breccia matrix, minus the tuffaceous component. At one location on the rift flank, at the base of Mesa de Enmedio, the middle unit hosts ~50 m of andesite lava, which comprised phenocrysts of euhedral plagioclase up to ~10 mm in length (~5-10%), and euhedral hornblende <1mm in length (~1-2%), hosted in fine-grained purple-grey groundmass, which was vesiculated (~15% at upper flow surfaces, decreasing to ~1% in basal parts of flow). Vesicle alignment indicates flow in a WNW direction.

Sawlan and Smith (1984) reported that some breccia clasts displayed flame-like or wispy injections into the surrounding matrix, suggesting they were emplaced at temperatures high enough to permit plastic deformation during transport and deposition; however, such features were not observed in the course of this study. Likewise, although Hausback (1984) reported that breccias in the Bahía de La Paz area had baked underlying sediments, suggesting high-temperature emplacement, the interbedded lenticular sandstones in the area of this study were unaltered by overlaying breccias. This study therefore follows Umhoefer et al. (2001) and McLean (1988) in interpreting the middle Comondú breccias as debris-flow deposits. To the west, the middle unit grades into conglomerates and sandstones of the lower Comondú. Conglomerates are commonly massive to poorly bedded, with matrix-supported subrounded to subangular clasts of andesite lava and dike material, and rare tuffaceous clasts. Clast sizes range from granule to boulder sized; exceptional clasts attain lengths of ~1 m. Matrix materials range in colour from red to beige, and comprise coarse lithic sandstones consisting of ~20-95% lithic fragments, up to ~6% euhedral to subhedral hornblende and plagioclase feldspar crystals and crystal fragments, up to ~2 mm in length, and quartz. Conglomerates are typically interbedded with lenticular and tabular sandstones compositionally and texturally similar to the matrix material; the proportion of conglomerate decreases westwards, such that the conglomeratic component is essentially absent at distances >25-30 km west of the escarpment crest.

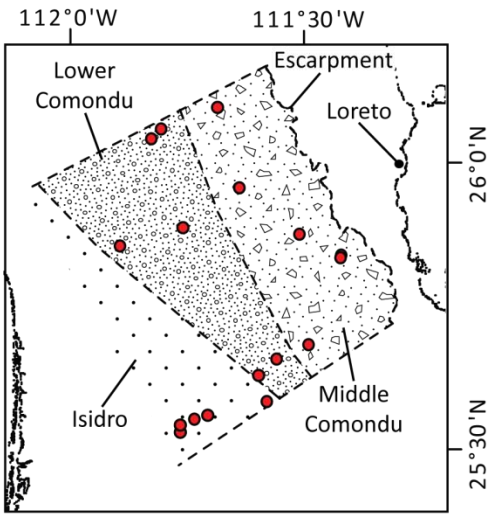

Figure 3.5: Extent of Comondú Group and Isidro Formation units within the study area. *Red dots indicate locations visited during fieldwork.*

The strongly gradational lateral and vertical transitions from middle unit breccias to lower unit conglomerates and then sandstones strongly suggest that all three rock types are components of the same sediment transport system, with clast angularity and size decreasing westwards from an eastern source – consistent with the interpretations of Hausback (1984) and Umhoefer et al (2001) that the Comondú group comprises the westward-migrating eruptive centres of a volcanic arc, and the associated sedimentary apron. Pre-Comondú units were not observed in the study area west of the escarpment, with the exception of the western San Javier canyon. Here, the lower unit lithic sandstones of the Comondú are bounded to the west by poorly bedded white coarse lithic sandstones which are interbedded with white lapilli tuffs typically tens of centimetres to a few metres in thickness, which contain up to ~2% mafic crystal fragments <0.2 mm in length. Lapilli are rounded, range from 1-50 mm in length, contain crystals of hornblende and feldspar, and are hosted in a matrix of fine white ash. Lapilli, crystal fragments, and white ash are frequently reworked into the sandstones, which also contain rare lenses of conglomerate, up to ~2 m thick, which contain rounded to subangular clasts of andesite lava and dike material of pebble to cobble size supported by a matrix of coarse lithic sand. These units, at least ~30 m in thickness, are clearly distinguished from units of the lower Comondú by their distinctive white colouring and tuff content; tuffs are not observed in the Comondú group west of the escarpment, although they are commonly present on the eastern coastal plain (Umhoefer et al., 2001). These units are similar to the Isidro formation as described in the Bahía de La Paz area (Hausback, 1984) and are here assigned to that formation, despite lacking the abundant marine shell hash reported from exposures of the Isidro formation in the western La Purísima canyon (McLean et al., 1987). The extents of the Isidro formation and the formations of the Comondú group in the study area are summarised in Figure 3.5.

3.3.2 The rift flank relict landscape

Across the rift flank study area, units of the Comondú Group and Isidro Formation are incised by a network of west-draining canyons. The summits of the interfluves which separate these canyons

form a series of west-sloping mesas, which can be clearly distinguished on topographic, slope, and relief maps of the rift flank (Figure 3.6). Slope and relief maps are derived from Advanced Spaceborne Thermal Emission and Reflection Radiometer (ASTER) digital elevation models (DEMs), which at the latitude of the study area have a horizontal resolution of ~28 m. Slope is calculated for each pixel using a moving 8-pixel window which returns the greatest slope value, excluding areas of no data; relief is calculated for each pixel using a moving circle of 500 m radius, which returns the maximum relief value – a technique similar to that of Clark (2003), but downscaled to reflect the considerably smaller study area. An indication of the nature of the mesa summits can be obtained from analysis of LANDSAT imagery. Figure 3.7 shows a multiband false-colour composite of bands 1 (absorption peak in visible blue light, displayed in blue), 2 (visible green light, displayed in green), and 7 (mid infra-red, displayed in red), and Figure 3.8 shows an oblique view of the same multiband raster draped over an ASTER DEM. In these images, the post-subduction lavas emit strongly in the mid infra-red band, and can be seen to cap much of the summit area of the interfluve mesas, although they appear absent in some areas, replaced by a smooth dun-coloured surface. A combination of topographic, relief, and slope maps, coupled with LANDSAT imagery, was utilised to visually map out the extent of the low-relief interfluve mesa summits, as shown in Figure 3.7. Median relief of the summit surface is 58 m, with 95% of values falling between 13 m and 209 m. For comparison, median relief of the area bounding the extent of the summit surfaces (excluding the low-relief, low-elevation Magdalena plain west of the 50 m contour, and the coastal plain east of the escarpment crest) is 99 m, with 95% of values falling between 11 m and 349 m (Figure 3.9).

The obvious interruption to this pattern of west-sloping interfluve mesas is the intensely volcanic area in the centre of the peninsular between the Comondú and La Purísima canyons (Figure 3.7), where abundant post-subduction lavas and cinder cones are hosted within a NNW-SSE trending graben, identified by Sawlan and Smith (1984). The extent of this structure was traced out using

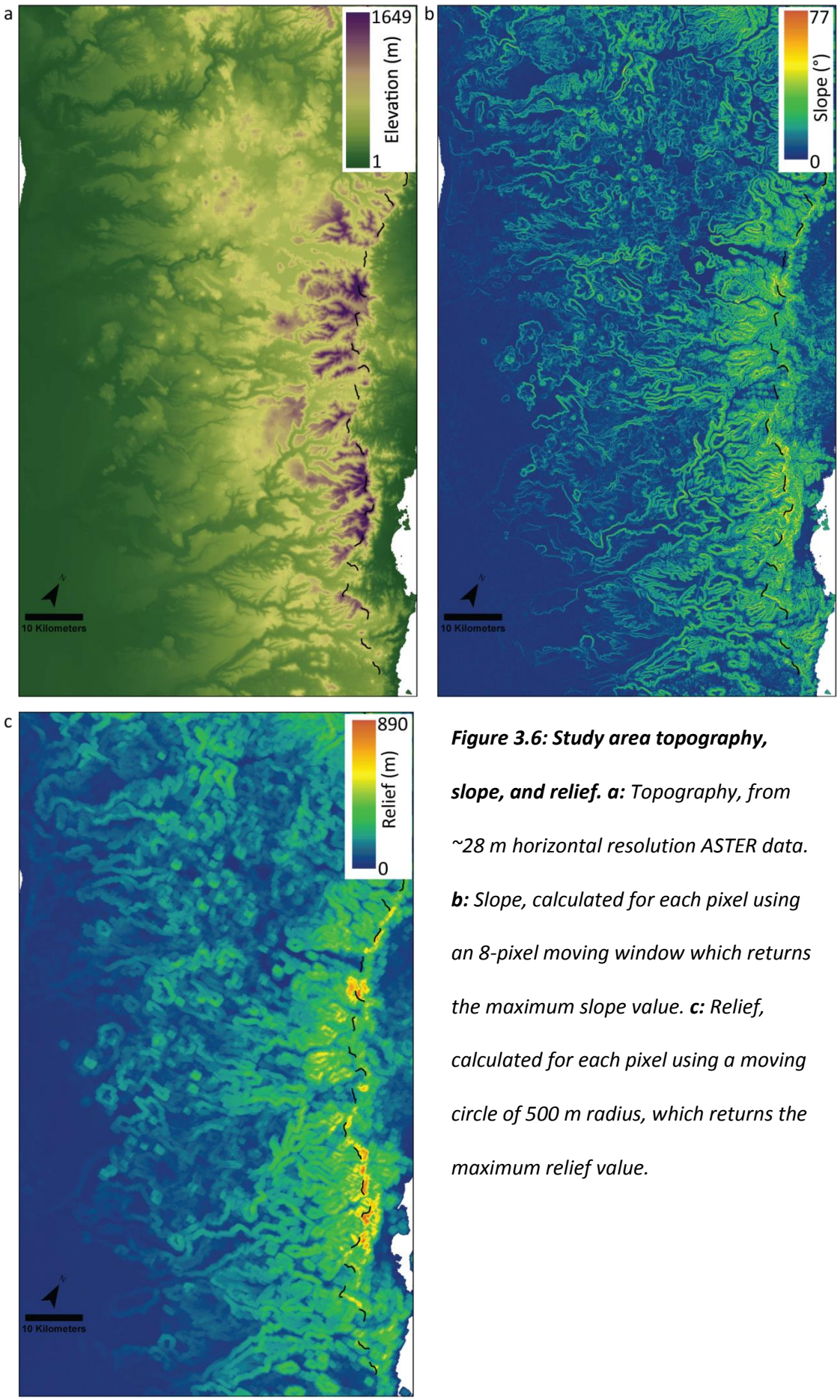

Figure 3.6: Study area topography, slope, and relief. a: *Topography, from ~28 m horizontal resolution ASTER data.* ***b:*** *Slope, calculated for each pixel using an 8-pixel moving window which returns the maximum slope value.* ***c:*** *Relief, calculated for each pixel using a moving circle of 500 m radius, which returns the maximum relief value.*

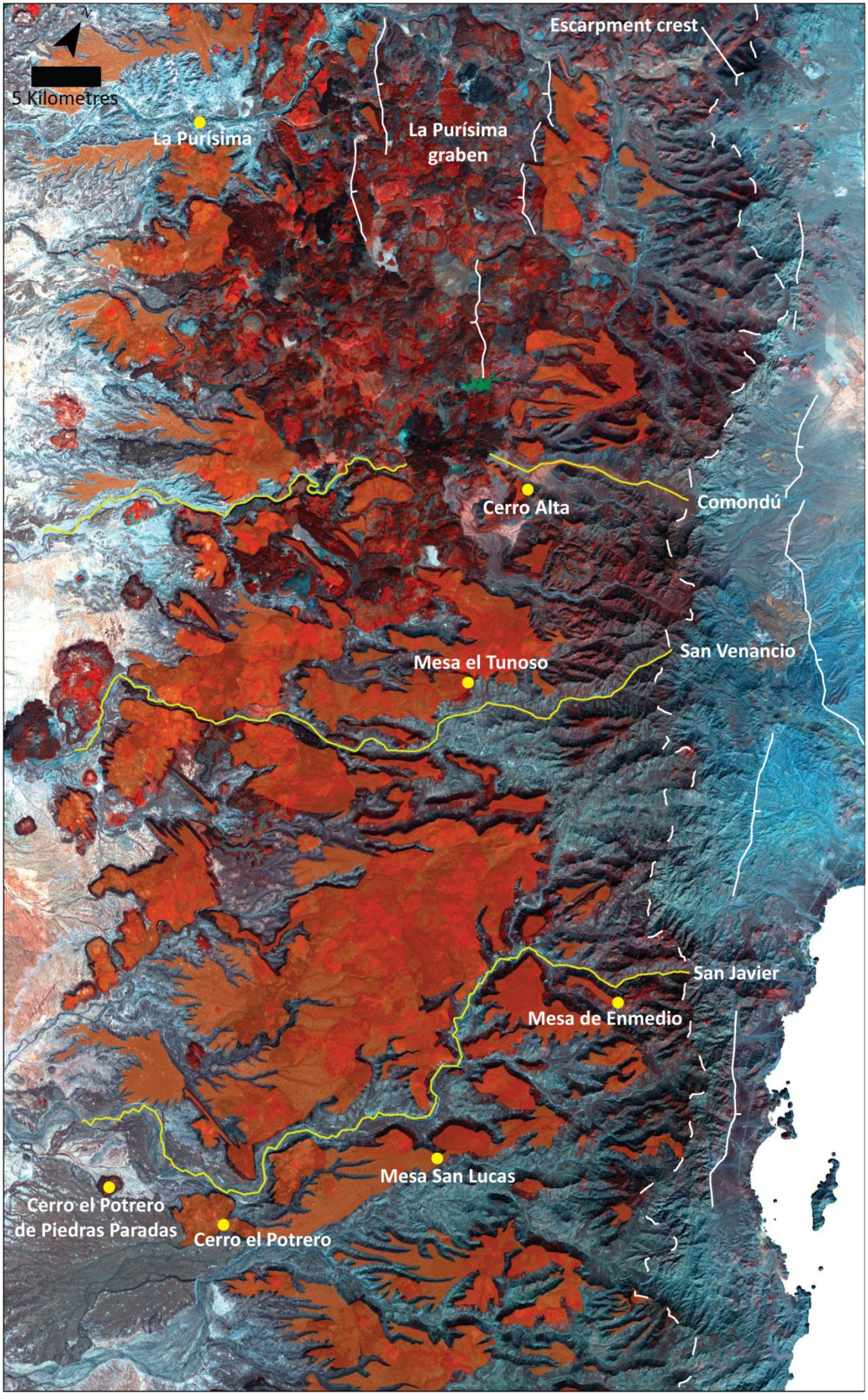
N
5 Kilometres
La Purísima
La Purísima graben
Escarpment crest
Cerro Alta
Comondú
Mesa el Tunoso
San Venancio
San Javier
Mesa de Enmedio
Mesa San Lucas
Cerro el Potrero de Piedras Paradas
Cerro el Potrero

Figure 3.7 (Previous page): LANDSAT image of the study area. *Multi-band false colour LANDSAT image generated from bands 1 (blue), 2 (green), and 7 (red). Rift flank lavas emit strongly in the infra-red band 7. Orange transparency indicates extent of relict landscape preserved atop interfluve mesa summits. Solid white lines indicate fault locations (tick on downthrown side); yellow lines indicate Comondú, San Venancio, and San Javier canyons; dashed white line indicates escarpment crest; yellow dots indicate relict landscape locations discussed in text.*

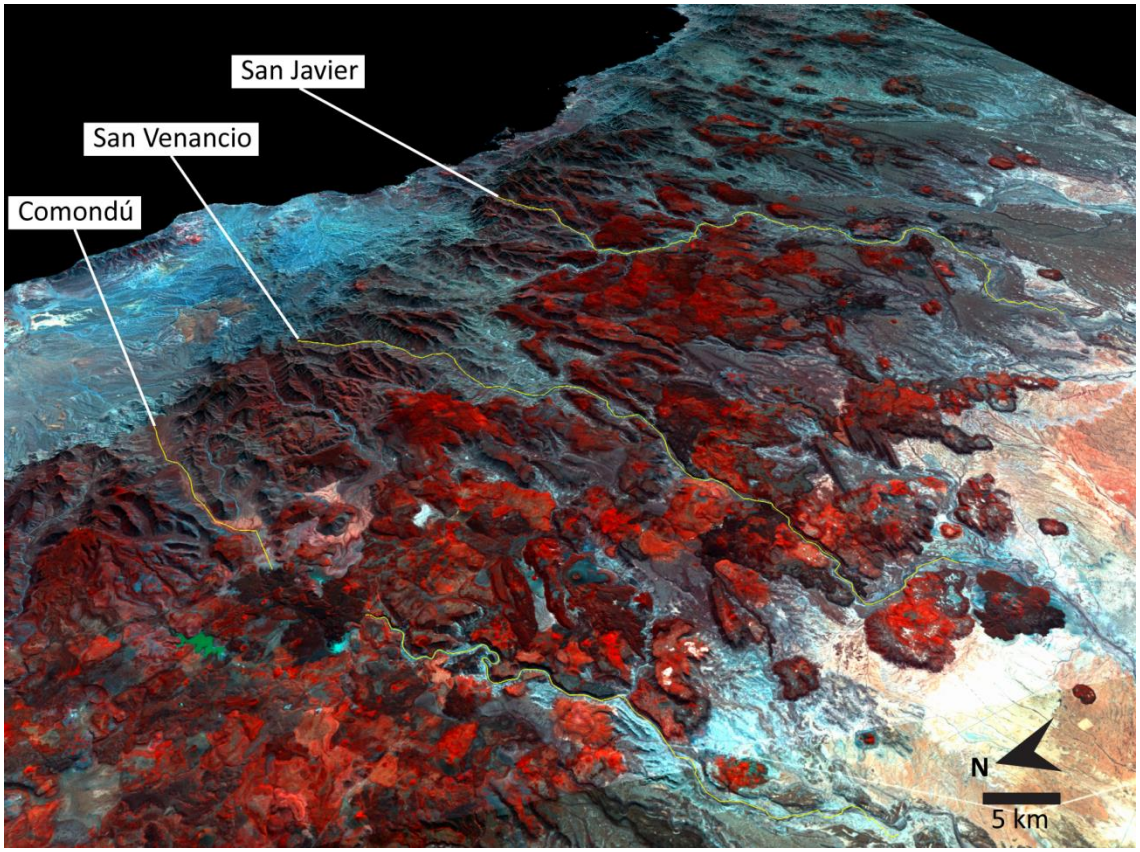

Figure 3.8: Oblique view of study area. *LANDSAT imagery (see Figure 3.7 caption) draped over topography derived from ASTER data; no vertical exaggeration. Yellow lines indicate Comondú, San Venancio, and San Javier canyons. The low-relief relict landscape atop the interfluve mesas is particularly conspicuous.*

LANDSAT imagery and ASTER-derived topography (Figure 3.7); the full extent of the eastern bounding faults can be mapped to their termination ~4 km north of the Comondú canyon, where surface offsets decrease to zero. However, the western bounding faults are concealed beneath lava

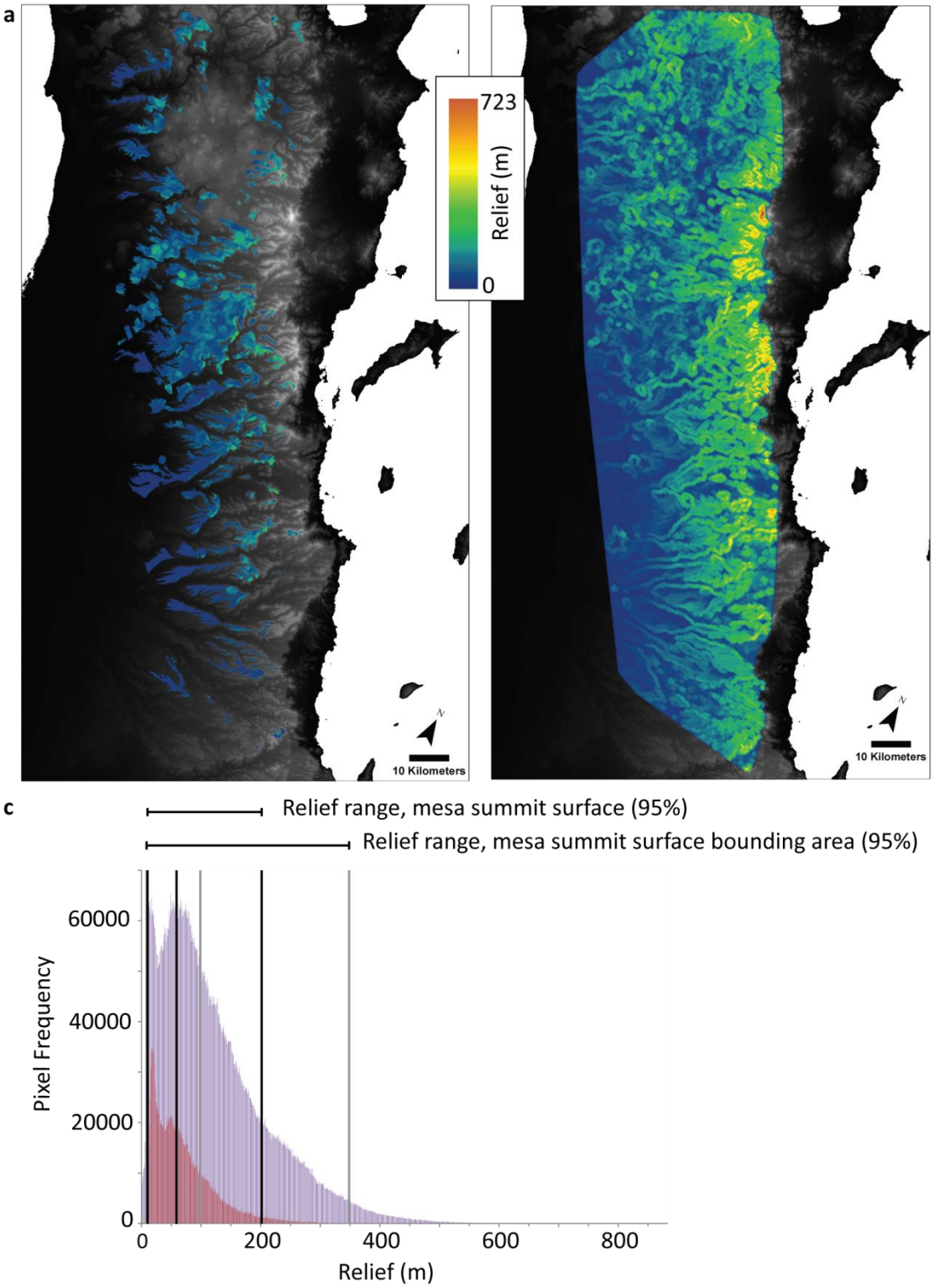

Figure 3.9: Study area and relict landscape relief. *Relief calculated for each pixel using a moving circle of 500 m radius, which returns the maximum relief value.* ***a:*** *Spatial extent used to calculate relict landscape spatial extent.* ***b:*** *Spatial extent used to calculate study area relief.* ***c:*** *Frequency distribution of relict landscape (red) and study area (purple) relief.*

flows which overfill the south-western part of the graben, and the location of their southernmost extent is unclear, although it must be north of the Comondú canyon, as faults are not observed there. The lack of surface offset north of the La Purísima canyon suggest that this marks the northernmost extent of these structures. Bellon et al. (2006) proposed that the graben extended southward as far as the San Javier canyon; however, this study found evidence for faulting to be absolutely lacking on the rift flank south of the Comondú canyon in both remote sensing imagery and at field locations, in agreement with Sawlan and Smith (1984). North of the Comondú canyon, surface offset decreases southwards along the bounding faults, from a maximum of ~325 m at the north-eastern corner of the graben to <20 m at the south-western corner; offset values indicate minimum fault throw, as the depth of infilling post-subduction lava is unclear. The combination of tectonic dissection and intense volcanism have combined to completely obscure the mesa summit surface in this area, and further analysis of the Loreto segment rift flank is therefore limited to the Comondú canyon and the area south.

Field visits were undertaken in order to determine the relationship of the mesa summit surfaces to the underlying Comondú and Isidro units; each field location is briefly described here. At the Mesa de Enmedio, breccia of the middle Comondú is conformably overlain by a post-subduction lava flow at least ~10 m thick; this in turn forms the base of a ~75 m thick succession of lavas and pebble-cobble grade alluvium, the upper boundary of which forms the mesa summit surface (Figure 3.10). The lavas are aphanitic, with the exception of the basal ~1 m of the lowermost flow, which hosts phenocrysts of euhedral plagioclase, hornblende, and spinel ~0.5-3 mm in length. On the surface of the mesa, post-subduction lava flows form narrow ridges up to ~5 m high and ~20-30 m wide above an alluvial cobble surface. The mesa surface lavas are fine-grained and vesiculated (~15-20%), form blocky rubble flows, and are cut by the local tributary canyon of the San Javier – there is no indication that these lavas flowed into the canyon. A sample obtained from one of the mesa summit lavas yielded an $^{40}Ar/^{39}Ar$ age of 6.194 ± 0.014 Ma (see Appendices 1 and 2 for data tables and

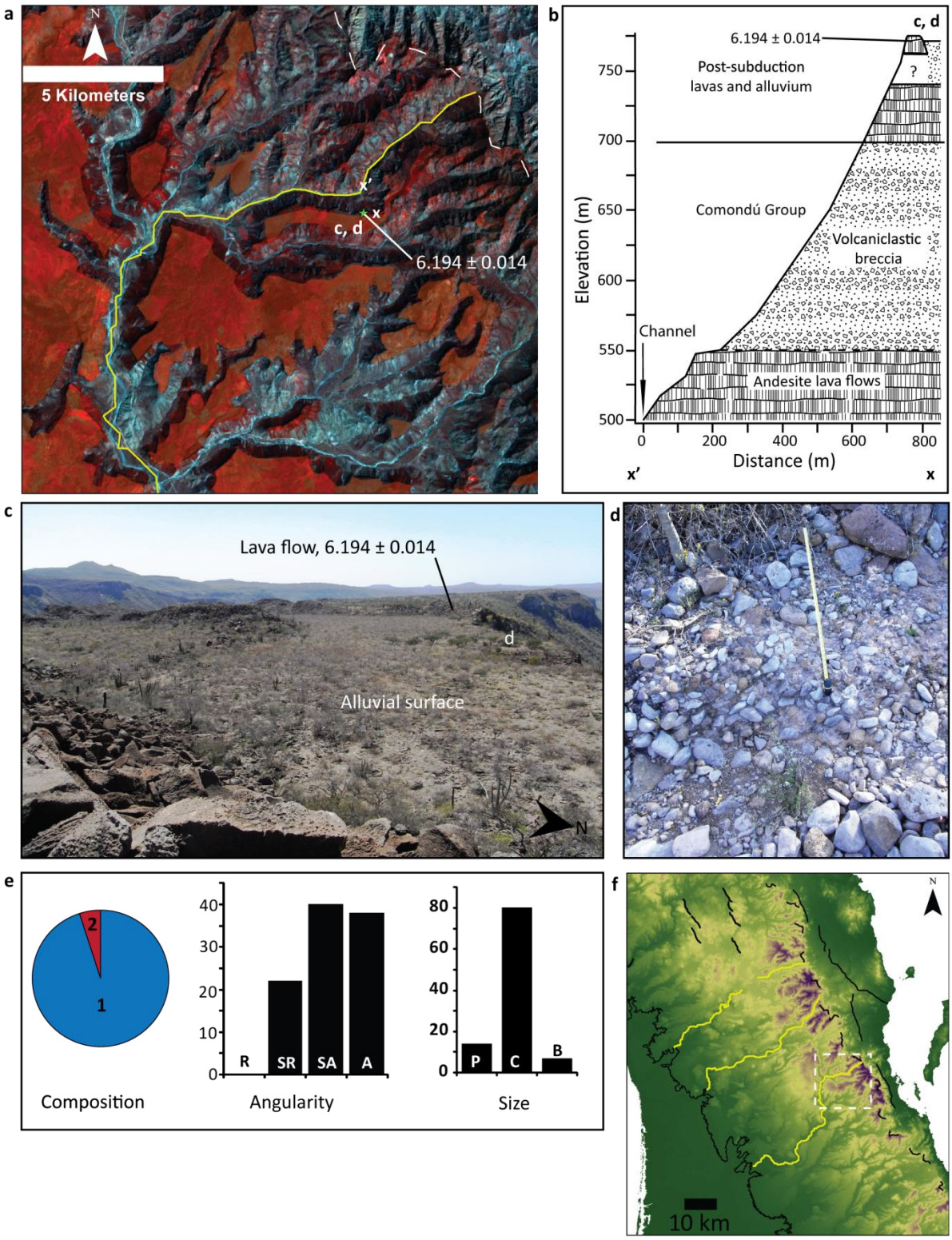
a
N
5 Kilometers
x'
x
c, d
6.194 ± 0.014
b
c, d
6.194 ± 0.014
Post-subduction
lavas and alluvium
?
Comondú Group
Volcaniclastic
breccia
Channel
Andesite lava flows
Elevation (m)
750
700
650
600
550
500
0
200
400
600
800
Distance (m)
x'
x
c
Lava flow, 6.194 ± 0.014
d
Alluvial surface
N
d
e
2
1
40
30
20
10
0
R
SR
SA
A
80
60
40
20
0
P
C
B
Composition
Angularity
Size
f
N
10 km

Figure 3.10 (Previous page): Mesa de Enmedio. a: *Mesa de Enmedio location, showing LANDSAT imagery (see Figure 3.7 caption), extent of relict landscape (orange transparency), San Javier canyon (yellow line), escarpment crest (dashed white line); and location of lava sample for which* $^{40}Ar/^{39}Ar$ *age was obtained (age in Ma).* ***b:*** *Stratigraphic section through Mesa de Enmedio, showing relationship between Comondú group units and post-subduction lavas and alluvial deposits, the uppermost units of which compose the relict landscape atop the mesa summit.* ***c:*** *Image of Mesa de Enmedio summit, showing alluvial surface in the middle distance and post-subduction lava flows transecting the mesa summit in the far distance. Preservation of these surface features require the existence of the relict landscape.* ***d:*** *Image of relict landscape alluvial clasts. 1 m tape shown for scale.* ***e:*** *Relict landscape alluvial clast data. Composition, numbers indicate clast source: 1 – Comondú Group andesite; 2 – post-subduction lavas. Angularity: R – rounded; SR – sub-rounded; SA – sub-angular; A – angular. Size: P – pebble; c – cobble; b – boulder (Wentworth Scale).* ***f:*** *Location map.*

details of methods; $^{40}Ar/^{39}Ar$ ages are quoted to 1σ confidence level, here and throughout). The alluvium is clast-supported, unconsolidated on the mesa surface, and poorly consolidated below (clasts can be dislodged by hand); clasts are subrounded to angular, and are dominantly pebble to cobble sized. Although the majority of clasts comprise Comondú andesite lava, 5% of clasts comprise subrounded post-subduction lava (Figure 3.10).

At the Mesa El Tunoso, breccia of the middle Comondú is overlain by a series of post-subduction lavas, which form an eroding volcanic edifice rising ~100 m above the mesa surface (Figure 3.11). Lavas are fine grained, hosting rare (<5%) phenocrysts of euhedral to subhedral olivine, amphibole, and spinel, 1-2 mm in length; poor exposure due to talus generated by eroding lavas prevented flow thicknesses from being determined, but these were of the order ~10 m. Flows associated with the eroding edifice are cut at the edge of the mesa by the San Venancio canyon; there is no evidence

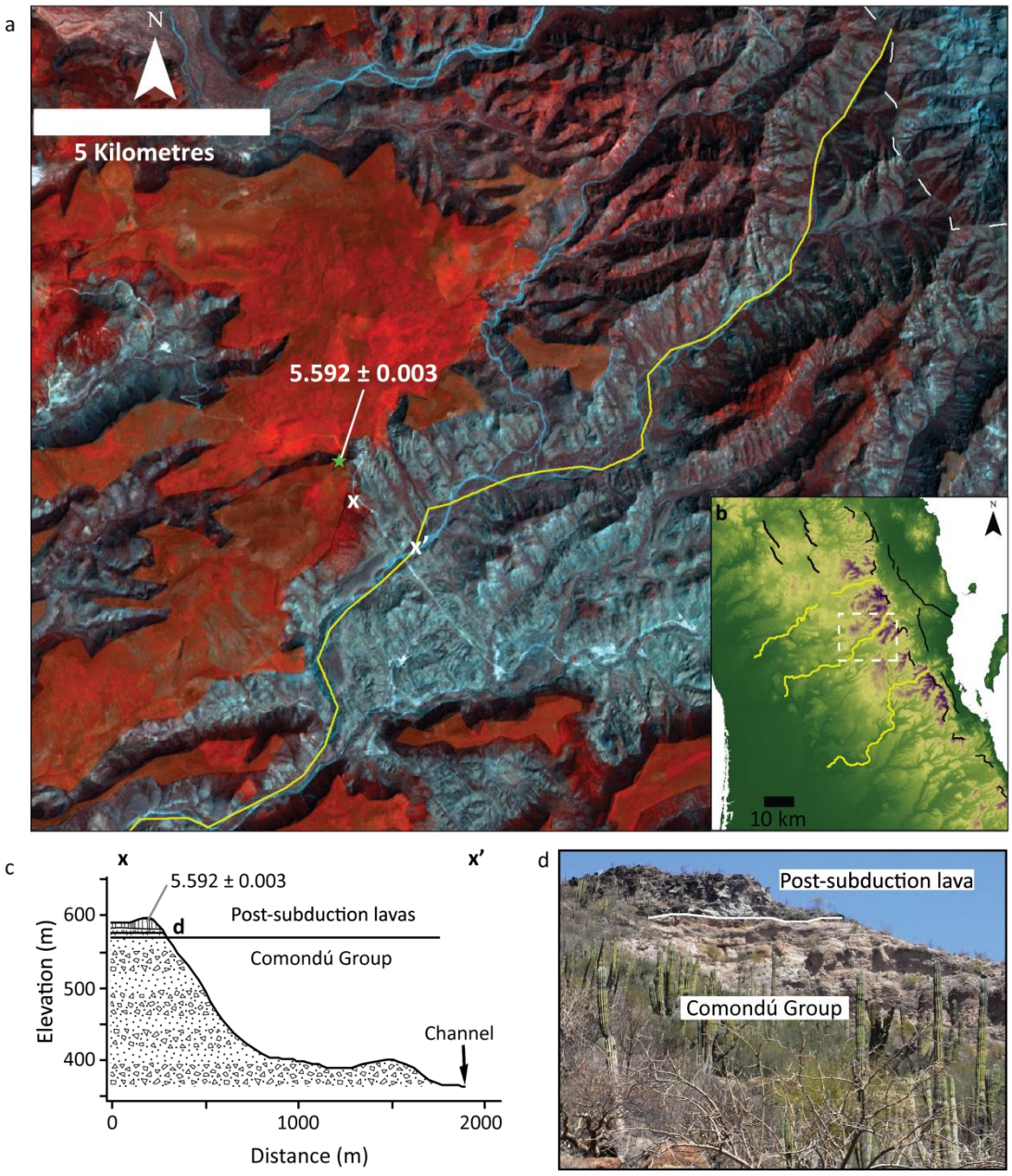

Figure 3.11: Mesa el Tunoso. a: *Mesa el Tunoso location, showing LANDSAT imagery (see Figure 3.7 caption), extent of relict landscape (orange transparency), San Venancio canyon (yellow line), escarpment crest (dashed white line), and location of lava sample for which* $^{40}Ar/^{39}Ar$ *age was obtained (age in Ma).* ***b:*** *Location map.* ***c:*** *Stratigraphic section through Mesa el Tunoso, showing relationship between Comondú group units and post-subduction lavas which compose the relict landscape atop the mesa summit.* ***d:*** *Image of Comondú Group/post-subduction lava boundary in Mesa el Tunoso.*

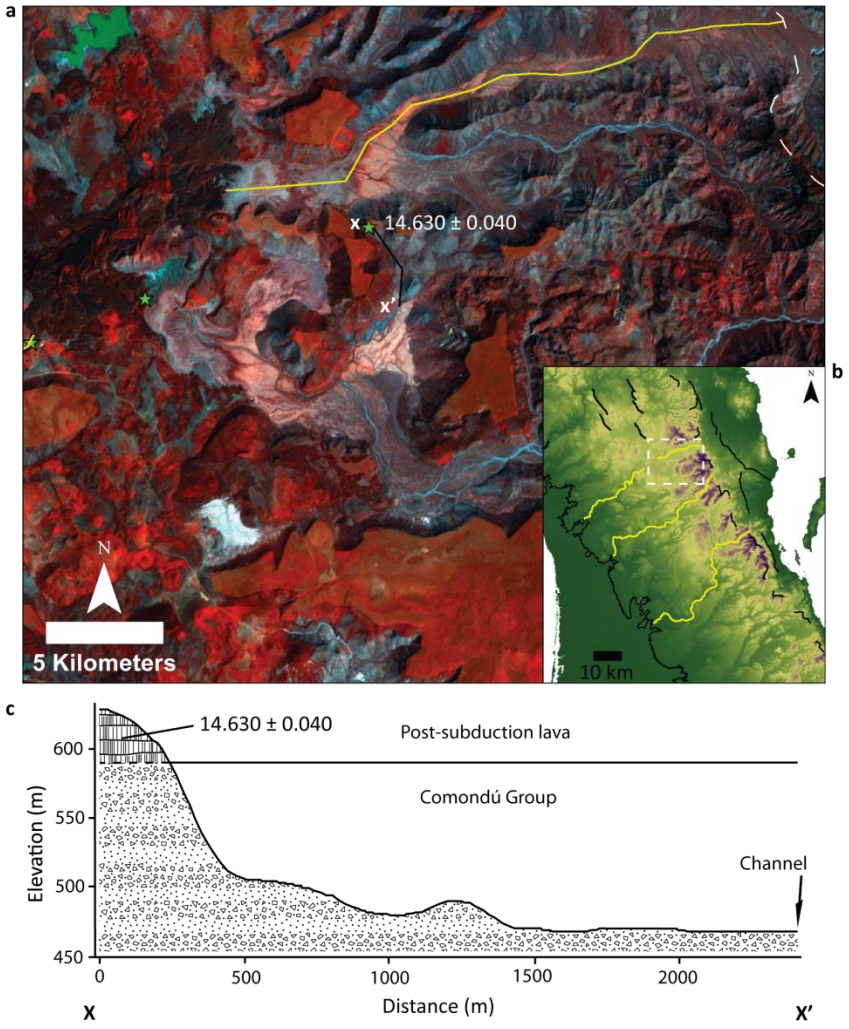

Figure 3.12: Cerro Alta. a: *Cerro Alta location, showing LANDSAT imagery (see Figure 3.7 caption), extent of relict landscape (orange transparency), Comondú canyon (yellow line), escarpment crest (dashed white line), and location of lava sample for which* $^{40}Ar/^{39}Ar$ *age was obtained (age in Ma).* ***b:*** *Location map.* ***c:*** *Stratigraphic section through Cerro Alta, showing relationship between Comondú group units and post-subduction lavas which compose the relict landscape atop the mesa summit.*

that they flowed into the canyon. A sample obtained ~20 m above the base of the edifice yielded an $^{40}Ar/^{39}Ar$ age of 5.592 ± 0.003 Ma. Laterally, these flows are bounded by alluvial cobbles similar to those observed on the Mesa de Enmedio, although here they form a thin deposit <1 m in thickness (Figure 3.11). At Cerro Alta, poorly exposed breccia of the middle Comondú is overlain by ~39 m of fine-grained post-subduction lava, hosting ~1% spinel phenocrysts up to ~0.5 mm in length, which

increase in abundance to ~15-20% near the base of the flow (Figure 3.12). Rare intact exposures indicate the flow was originally emplaced as a coherent unit, but is now erosionally disaggregating into angular boulders and talus. A sample obtained from the top of the exposure yielded an $^{40}Ar/^{39}Ar$ age of 14.630 ± 0.040 Ma (Figure 3.12). Alluvial material was absent from this location.

At the Mesa San Lucas, breccia of the middle Comondú is overlain by ~40 m of unconsolidated rounded to subangular alluvial cobbles, comprising both post-subduction lava clasts (~70%) and Comondú andesite lava (~30%). In-situ post-subduction lava is absent from this location, but present atop the same mesa ~11 km to the west, where ~30-40 m of post-subduction lava conformably overlies lithic sandstones and rare conglomerates of the lower Comondú (Figure 3.13).

At Cerro El Potrero, distinctive white sandstones and tuffs of the Isidro formation are overlain by ~20-30 m of blocky post-subduction lava, which is incised at the mesa edge and laterally bounded by ~1-2 m of unconsolidated alluvial cobbles, comprising clasts of Comondú andesite lava, dyke, and conglomerate material (65%), post-subduction lava (31%), and lapilli tuff of uncertain provenance. Clasts are dominantly pebble to cobble sized, and exhibit a wide range of angularity (Figure 3.13).

Collectively, these field sites indicate that units of the Comondú Group and Isidro Formation are overlain on interfluve mesas by up to several tens of metres of post-subduction lavas and pebble-cobble grade alluvium. The presence of post-subduction lava clasts within this alluvium indicates that these clasts have not simply been remobilised from eroding conglomeratic Comondú units, but record a later phase of fluvial deposition. The significance of both these remote-sensing and field observations is they indicate that the surface of the mesa summits comprise a low-relief relict landscape, which predates canyon incision. The preservation as components of this landscape of lavas ranging in age from ~14.6 to ~5.6 Ma exclude the possibility of significant clastic deposition subsequent to ~15 Ma, followed by widespread bevelling to produce the mesa summit surface. Likewise, the capping of Comondú units solely by unconsolidated coarse alluvial deposits on some mesa summits indicates that the low-relief mesa summit surface did not form by regional

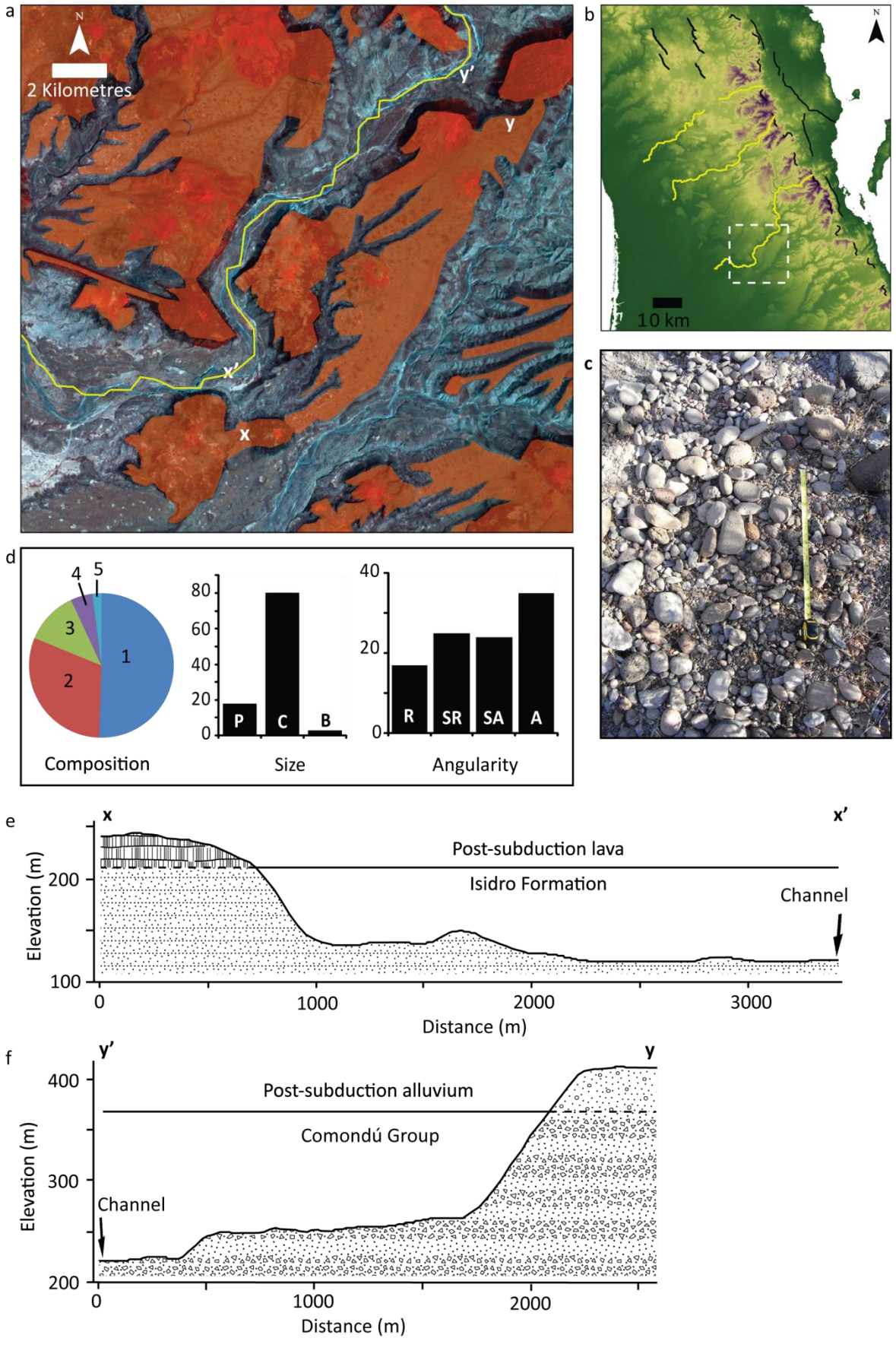
a
N
2 Kilometres
y'
y
x'
x
b
N
10 km
c
d
4
5
3
1
2
Composition
80
60
40
20
0
P
C
B
Size
40
20
0
R
SR
SA
A
Angularity
e
x
x'
Post-subduction lava
Isidro Formation
Channel
Elevation (m)
200
100
0
1000
2000
3000
Distance (m)
f
y'
y
Post-subduction alluvium
Comondú Group
Channel
Elevation (m)
400
300
200
0
1000
2000
Distance (m)

Figure 3.13 (Previous page): Mesa San Lucas. a: *Mesa San Lucas location, showing LANDSAT imagery (see Figure 3.7 caption), extent of relict landscape (orange transparency), and San Javier canyon (yellow line).* ***b:*** *Location map.* ***c:*** *Image of relict landscape alluvial clasts at location y. 1 m tape shown for scale.* ***d:*** *Relict landscape alluvial clast data. Composition, numbers indicate clast source: 1 – Comondú Group andesite; 2 – post-subduction lavas; 3 – Comondú Group andesite dykes; 4 – Comondú Group tuff; 5 – Comondú Group conglomerate. Angularity: R – rounded; SR – sub-rounded; SA – sub-angular; A – angular. Size: P – pebble; C – cobble; B – boulder (Wentworth Scale). Clast counts conducted ~300 m upslope from lava flow to preclude inclusion of talus lava clasts.* ***e-f:*** *Stratigraphic sections of Mesa San Lucas, showing relationship between Comondú group units and post-subduction lavas and alluvial deposits, the uppermost units of which compose the relict landscape atop the mesa summit.*

peneplanation to a resistant layer of capping lava. This relict landscape, where identified, therefore provides a datum from which to measure canyon incision depths, and the ages of the youngest relictlandscape lavas incised by canyons (~6.2 and ~5.6 Ma) provide a maximum limit to the timing of incision onset.

3.3.3 Rift flank canyon incision

The low-relief landscape preserved atop interfluve mesas which characterised the rift flank prior to uplift is dissected by west-draining canyons which attain maximum incision depths of ~400-600 m at the escarpment crest. Post-subduction lavas which flowed into these canyons after the onset of incision provide minimum ages for incision to the depth of each lava flow. The Comondú canyon preserves the most complete record of incision (Figure 3.14). The canyon has been completely dammed ~15 km west of the escarpment crest by the ~6 km long La Joya lava flow complex; the basal flow of this complex, which extends across the width of the canyon and lies ~290 m below the ~14.6-5.6 Ma relict landscape, yields an $^{40}Ar/^{39}Ar$ age of 3.180 ± 0.011 Ma. The flow is at least 9 m thick, and comprises slightly (~2%) vesiculated aphanitic lava. Following emplacement of the lava

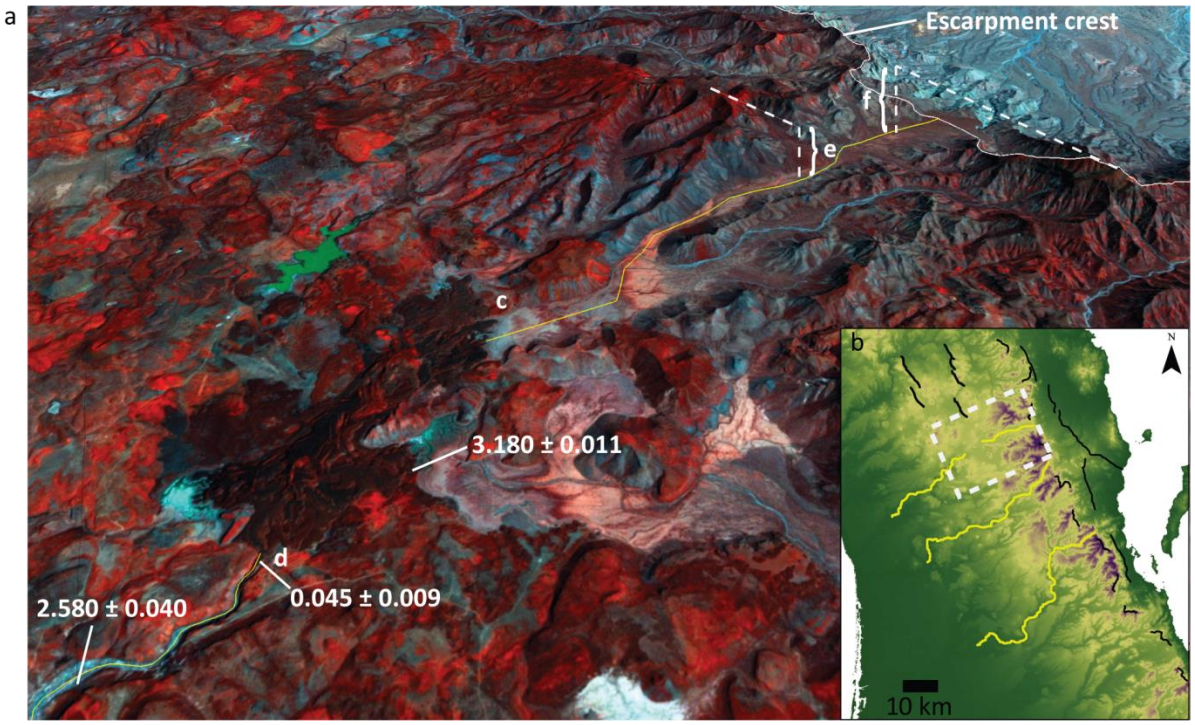
a
Escarpment crest
f
e
c
b
N
3.180 ± 0.011
d
2.580 ± 0.040
0.045 ± 0.009
10 km

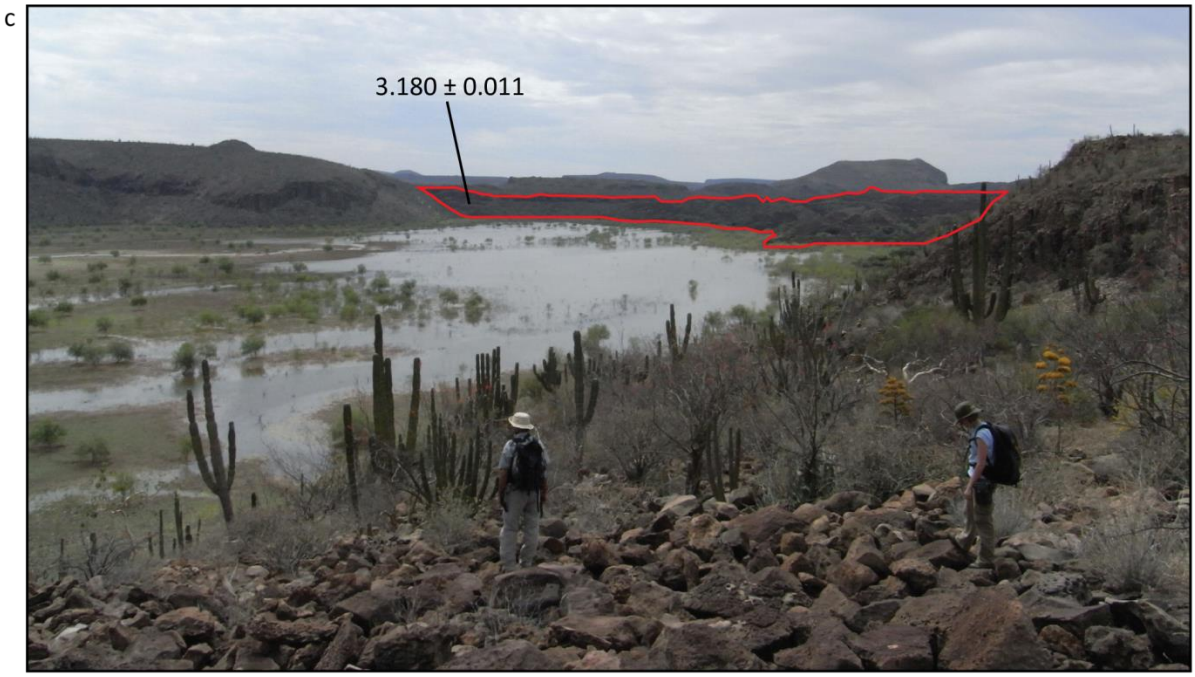
c
3.180 ± 0.011


d
0.045 ± 0.009

Figure 3.14 (Previous page): Canyon-filling lavas in the Comondú canyon. a: *Oblique view of the Comondú canyon (see Figures 4.7 and 4.8 captions), showing locations of lava samples for which $^{40}Ar/^{39}Ar$ ages were obtained (ages in Ma).* ***b:*** *Location map.* ***c:*** *Image showing ~3.2 Ma lava dam (red outline) blocking westward drainage.* ***d:*** *Panoramic image of ~0.045 Ma lava flowing into Comondú canyon, which runs downstream to left of image.* ***e:*** *Location of highest elevation atop interfluves bounding Comondú canyon at which relict landscape can be identified.* ***f:*** *Location of highest elevation atop interfluves bounding Comondú canyon; possibly the remains of an upper Comondú volcanic edifice.*

dam, the upstream section of the Comondú canyon ceased to drain to the Pacific; as a result, vertical incision ceased upstream of the dam, and upstream canyon incision predates ~3.2 Ma. Vertical incision prior to this time totals ~600 m at the easternmost occurrence of the relict surface in the Comondú canyon, ~6 km west of the escarpment crest; however, the southern interfluve of the Comondú canyon attains a maximum elevation of ~1650 m asl and ~1110 m above the modern stream at the escarpment crest, although the relict landscape cannot be identified atop the interfluve here (Figure 3.14). The possibility that this location represents an isolated occurrence of significant topography on the otherwise low-relief relict landscape cannot be excluded; Sawlan (1991) interpreted prominent topographic peaks at the escarpment crest as volcanic edifices of the upper Comondú. The inaccessibility of the area prevented field investigation during this study.

Approximately 3 km downstream of the ~3.2 Ma dam, the base of a poorly exposed lava yielding an $^{40}Ar/^{39}Ar$ age of 2.585 ± 0.040 Ma is situated ~7 m above the modern Comondú stream elevation (Figure 3.14). The flow comprises non-vesiculated aphanitic grey lava visually similar to the ~3.2 Ma flow from the base of the lava dam upstream. The flow base is ~240 m below the ~14.6-5.6 Ma relict landscape; however, some fraction of this incision occurred prior to the emplacement of the ~3.2 Ma lava dam. As the resistant lava dam prevented subsequent upstream vertical incision, the canyon floor upstream of the dam can be projected downstream, indicating that only ~100 m of vertical

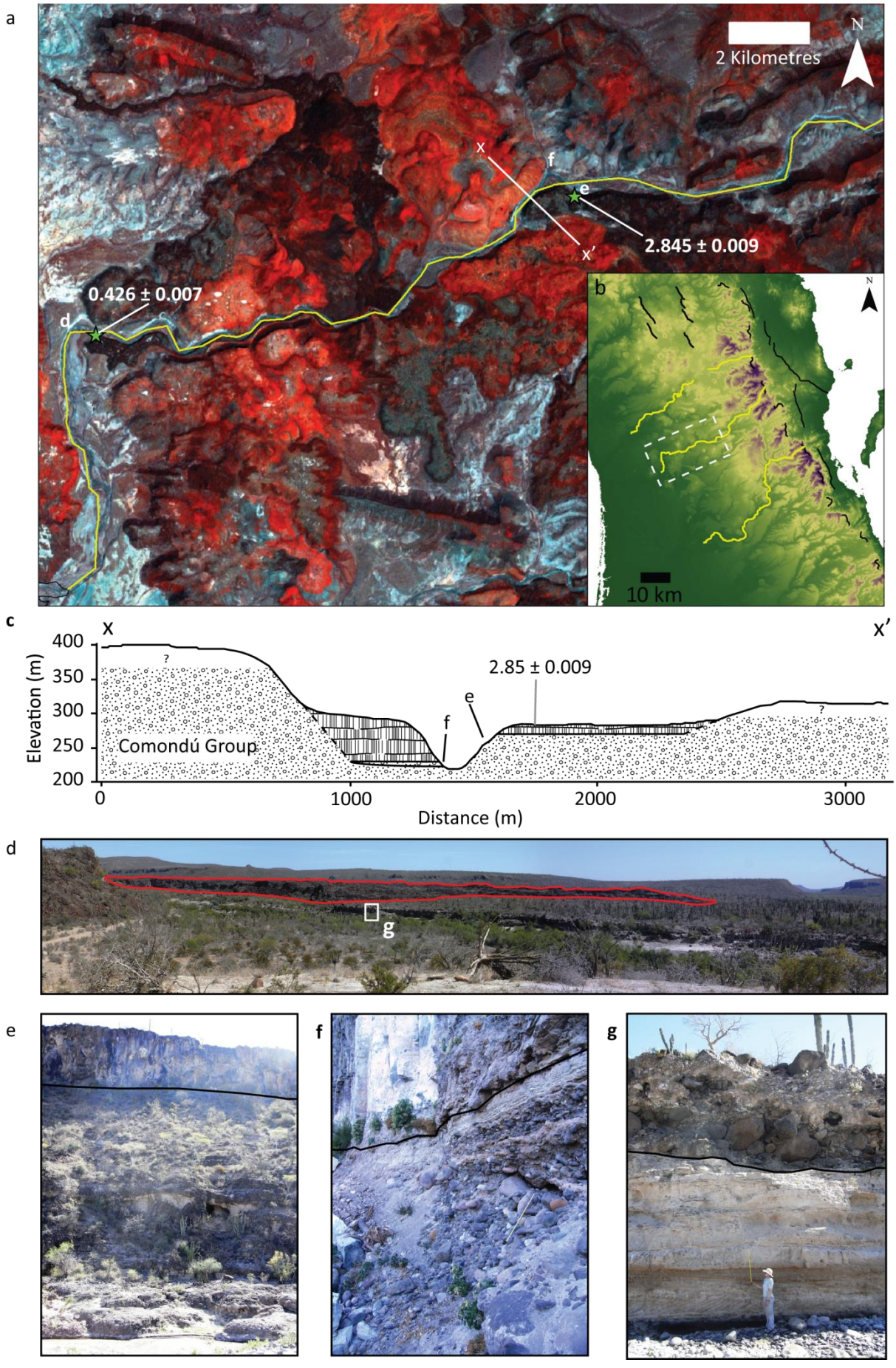
a
2 Kilometres
N
x
x'
f
e
2.845 ± 0.009
0.426 ± 0.007
d
b
N
10 km
c
x
x'
400
350
300
250
200
Elevation (m)
?
Comondú Group
2.85 ± 0.009
e
f
?
0
1000
2000
3000
Distance (m)
d
g
e
f
g

Figure 3.15 (Previous page): Canyon-filling lavas in the San Venancio canyon. a: *Location map showing LANDSAT imagery (see Figure 3.7 caption), San Venancio canyon (yellow line), and locations of lava samples for which $^{40}Ar/^{39}Ar$ ages were obtained (ages in Ma).* ***b:*** *Location map.* ***c:*** *Stratigraphic section across the San Venancio canyon, showing bench formed by continued incision following eruption of ~2.85 Ma lava, and younger undated lava covering canyon floor.* ***d:*** *Image showing ~0.426 Ma lava (red transparency) within the San Venancio canyon mouth.* ***e:*** *Image showing ~2.85 Ma lava atop Comondú Group units in south wall bench of the San Venancio canyon; solid black line indicates lava/ Comondú boundary. The base of the lava flow is ~40 m above the canyon floor in foreground.* ***f:*** *Image showing undated canyon-filling lava overlaying unconsolidated alluvial deposits ~5 m above the floor of the San Venancio canyon; solid black line indicates lava/alluvium boundary. 1 m tape shows scale.* ***g:*** *Image showing incision in the San Venancio canyon beneath the ~0.426 Ma lava. Massive unconsolidated alluvial deposits overlay well-consolidated Comondú Group sandstones. Solid black line indicates Comondú /alluvium boundary. Geologist holds 1 m tape for scale.*

incision occurred between ~3.2-2.6 Ma; ~67% of incision occurred prior to ~3.2 Ma. The proximity of the ~2.6 Ma lava to the modern stream elevation indicates that the canyon has subsequently experienced negligible incision. This is consistent with the presence of a lava situated in the modern stream channel immediately downstream of the ~3.2 Ma lava dam, which yields an $^{40}Ar/^{39}Ar$ age of 0.045 ± 0.009 Ma. This flow is also aphanitic, but is densely (~60%) vesiculated (Figure 3.14).

These timings are corroborated in the two other canyons studied. In the San Venancio canyon, an aphanitic, moderately vesiculated (~10%) lava flow ~30 km west of the escarpment crest yields an $^{40}Ar/^{39}Ar$ age of 2.845 ± 0.009 Ma (Figure 3.15). The flow is a channelized offshoot from a larger flow complex to the south, which has overtopped the canyon wall and flowed westward within the canyon for ~4 km. The base of the flow lies ~100 m below the ~14.6-5.6 Ma relict landscape and ~40 m above the modern stream, constraining ~71% of the incision here to before ~2.8 Ma ago (Figure

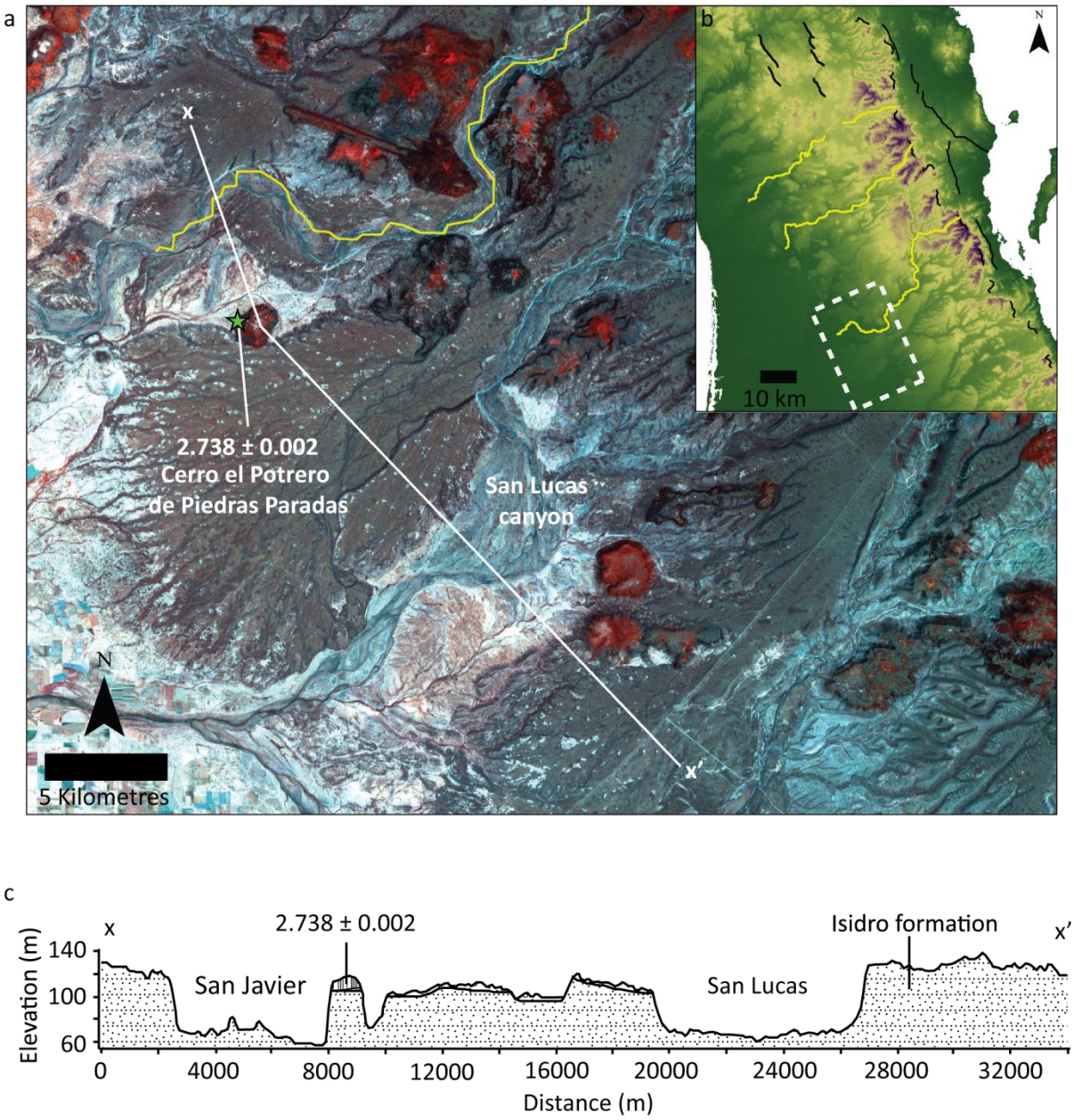

Figure 3.16: Canyon filling lava in the San Javier canyon. a: *Location map showing LANDSAT imagery (see Figure 3.7 caption), San Javier canyon (yellow line), and location of lava sample for which* $^{40}Ar/^{39}Ar$ *age was obtained (age in Ma).* ***b:*** *Location map.* ***c:*** *Stratigraphic section across the San Javier canyon and the San Lucas canyon to the south, showing incision following eruption of ~2.7 Ma lava.*

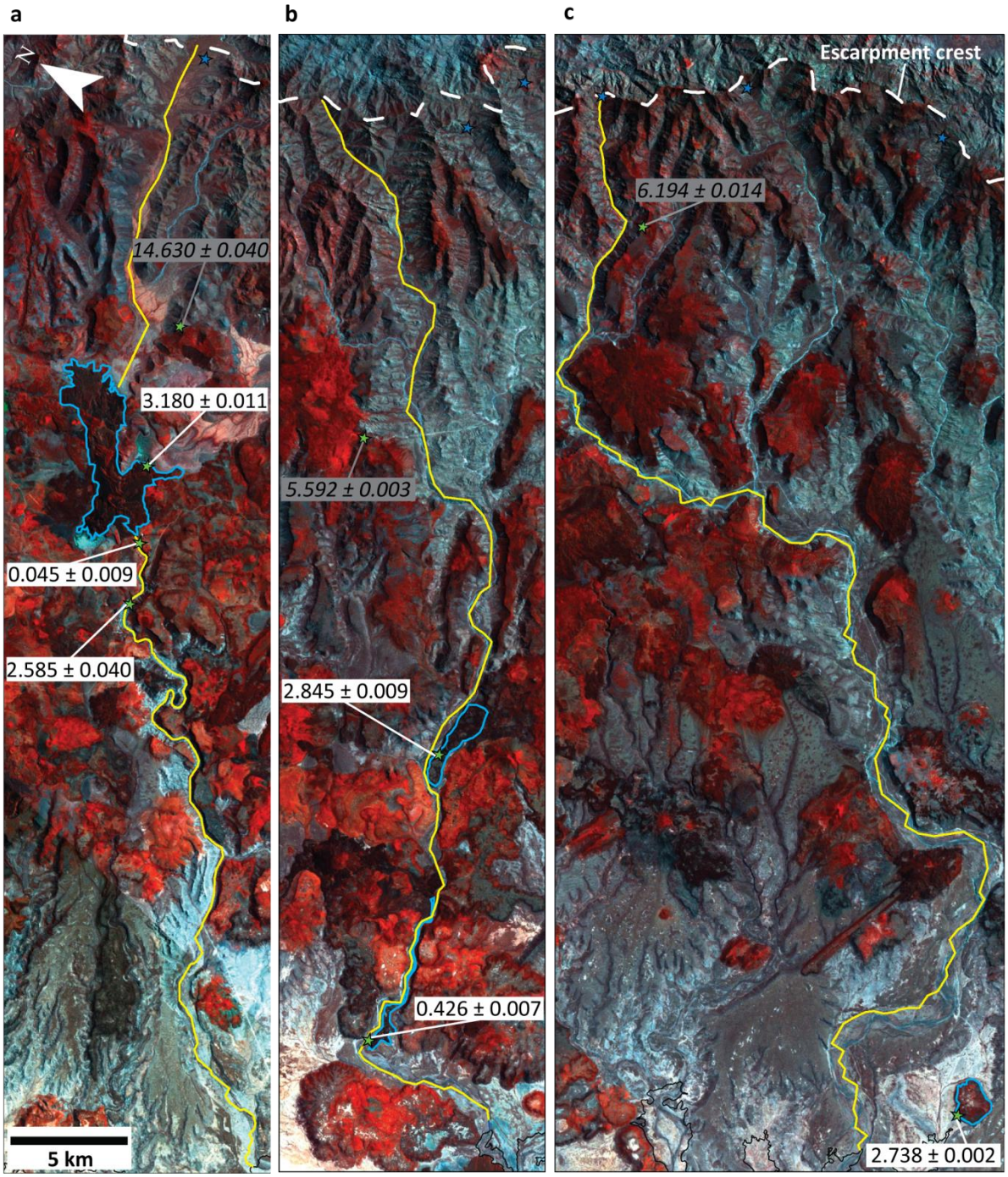

Figure 3.17: Summary of all lava samples for which $^{40}Ar/^{39}Ar$ ages were obtained. *LANDSAT imagery showing locations (see Figure 3.7 caption).* ***a:*** *Comondú canyon.* ***b:*** *San Venancio canyon.* ***c:*** *San Javier canyon. Post-subduction lavas are red; mesa-capping relict landscape alluvial deposits are grey. Modern streams shown by yellow lines. Lava sample locations shown by green stars; $^{40}Ar/^{39}Ar$ ages in Ma; incised relict landscape lava ages italicised in grey boxes; canyon-filling lavas in white boxes.*

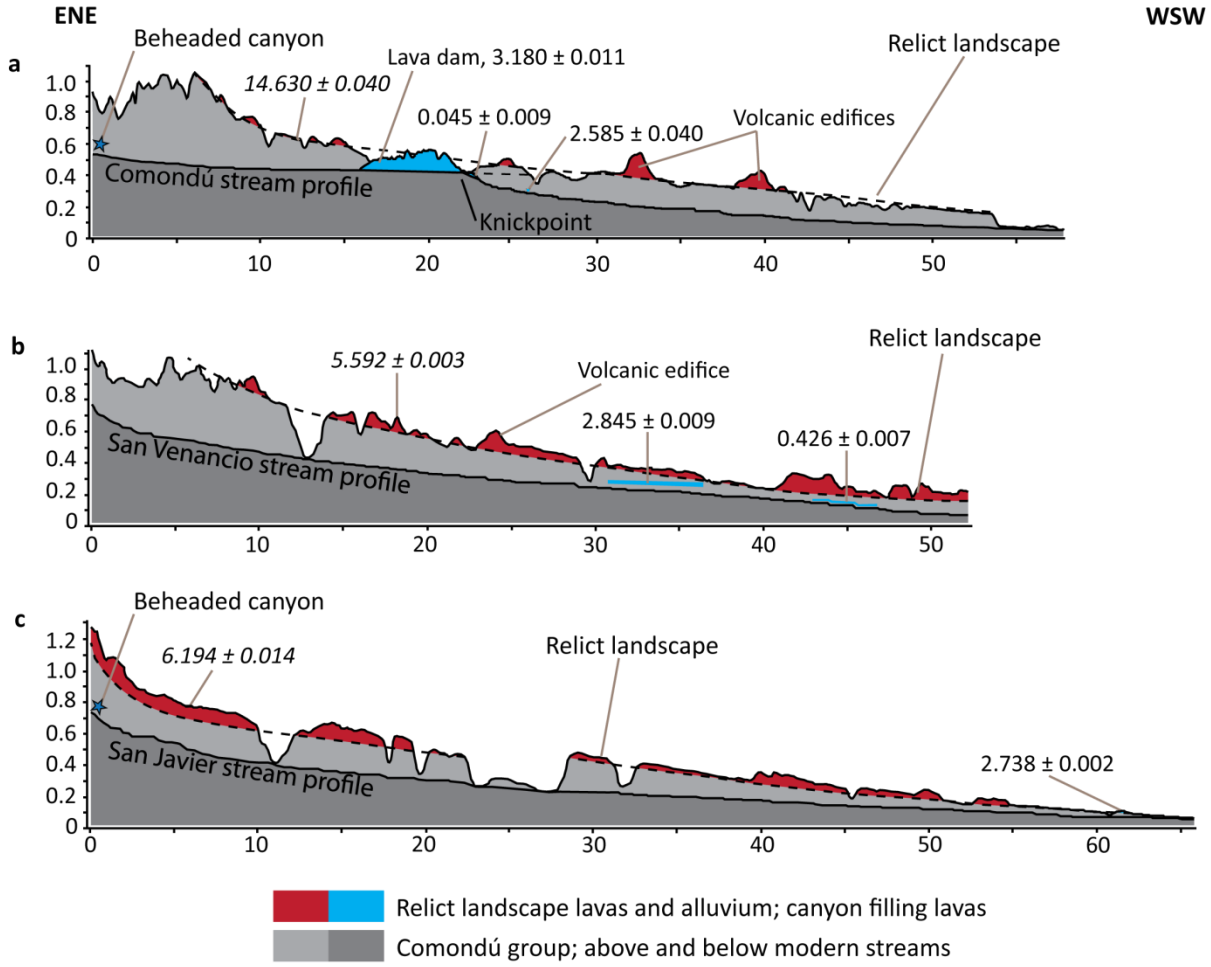

Figure 3.18: *Modern stream elevation changes downstream from escarpment crest (drainage divide) to 50 m contour.* ***a:*** *Comondú canyon.* ***b:*** *San Venancio canyon.* ***c:*** *San Javier canyon. See Figure 3.17 for locations. Upper profile on each plot shows interfluve mesa elevations; dashed black line shows top of Comondú group units. Overlying relict landscape alluvial deposits and lava flows shown in red; canyon-filling lavas shown in blue.* $^{40}Ar/^{39}Ar$ *ages are in Ma.*

3.15). Approximately 14 km downstream, a second lava has entered the canyon from the north, and flowed westward for ~7 km; this aphanitic, moderately vesiculated (~25%) flow yields an $^{40}Ar/^{39}Ar$ age of 0.426 ± 0.007 Ma. The base lies ~60 m below the relict surface, and ~5 m above the modern stream, constraining ~92% of incision to before ~0.4 Ma (Figure 3.15). Within the San Javier canyon, a ~9 m thick aphanitic, moderately (~15%) vesiculated lava which caps the ~60 m high mesa Cerro Potrero de Piedras Paradas, situated in the canyon ~40 km west of the escarpment, yields an

$^{40}Ar/^{39}Ar$ age of 2.738 ± 0.002 Ma (Figure 3.16). The flow base is ~20 m below the ~14.6-5.6 Ma relict landscape and ~50 m above the modern stream; although the onset of incision at this location predates ~2.7 Ma, ~71% of incision occurred subsequent to this time (Figure 3.16). Figure 3.17 summarises the locations and $^{40}Ar/^{39}Ar$ ages of sampled lavas. Estimation of vertical incision rates is complicated by the spatial variation of incision depth due to the asymmetric uplift of the rift flank (Figure 3.18). Upstream of the ~3.2 Ma Comondú lava dam, at the easternmost occurrence of the relict landscape in the Comondú canyon, our data imply minimum vertical incision rates of ~250 m Ma^{-1} between ~5.6-3.2 Ma; at the point of maximum interfluve elevation, vertical incision rates during this time may have exceeded ~460 m Ma^{-1}. Following lava dam formation, incision rates ~3 km downstream decreased to ~170 m Ma^{-1} until ~2.6 Ma, and were subsequently negligible. In the San Venancio and San Javier canyons, minimum vertical incision rates after incision onset at ~5.6 Ma range from ~36 to ~7 m Ma^{-1}. These low incision rates partly reflect the greater distance of these samples from the zone of maximum uplift at the Loreto segment faults; however, these lavas are all younger than ~2.8 Ma, and lower rates are consistent with the decrease in incision rates after ~3.2 Ma observed in the Comondú canyon.

3.4 Discussion

3.4.1 Chronology of rift flank landscape development

Collectively, these data record the post-subduction development of the rift flank. Subduction of the Farallon plate beneath North America ceased between ~15-14 Ma, as indicated by seafloor magnetic lineations generated by the Pacific-Farallon spreading centres preserved offshore southern Baja California. These indicate fragmentation of the local remnant of the Farallon plate (the Magdalena microplate) and subsequent clockwise rotation (by 45-60°) of these fragments, likely in response to a combination of slab detachment and loss of slab pull (Lonsdale, 1991; Tian et al., 2011). Limited spreading at rates of ~14-16 mm a^{-1} roughly parallel to the continental margin continued until ~12-11.5 Ma (Lonsdale, 1991; Tian et al., 2011) or possibly as late as 8-7 Ma at rates of ~6 mm a^{-1} (Michaud et al., 2006). The onset of this fragmentation, at ~15 Ma, closely coincides with the shift in

deposition style of the Comondú Group reported by Umhoefer et al. (2001) at ~15 Ma, from widespread volcaniclastic sedimentation to calc-alkaline volcanism localised on the coastal plain east of the escarpment. The cessation of Comondú deposition on the rift flank was marked by the abrupt, but seemingly conformable onset of post-subduction lava emplacement, reflected by the oldest $^{40}Ar/^{39}Ar$ age obtained by this study of 14.630 ± 0.040 Ma. This is consistent with the oldest previously reported K-Ar ages from these lavas, of 15.0 ± 0.4 Ma (Bellon et al., 2006), and 14.7 ± 0.7 Ma (McLean et al., 1987), although some caution is appropriate in making this comparison as the K-Ar method does not easily permit identification of samples which have suffered Ar contamination from atmospheric or other sources (see Section 3.2.3). Cessation of rift flank volcaniclastic Comondú Group deposition may have been caused by the construction of Comondú Group volcanic edifices on the coastal plain, identified by the presence of upper Comondú Group lavas and associated dike swarms (Zanchi, 1994; Umhoefer et al., 2001); these may have formed a topographic barrier intercepting westward sediment transport. Alternatively, limited extension has been reported from the northern Gulf as early as ~15 Ma (Lee et al., 1996); the onset of extension in the southern Gulf at this time could also have acted to intercept sediment, although there is no evidence of southern Gulf extension prior to ~11-10 Ma (Henry and Aranda-Gomez, 2000).

Following the cessation of Comondú Group deposition and the onset of post-subduction lava emplacement at ~15 Ma, a low-relief landscape developed on the rift flank. This persisted until at least ~6.2-5.6 Ma, the ages of the youngest lavas incised by the canyon systems which subsequently developed (Figures 3.17 and 3.18), and comprises laterally variable thicknesses of up to a few tens of metres of post-subduction lavas and coarse alluvium. Subsequent to ~5.6 Ma, this landscape was incised by a series of west-draining canyons; in the Comondú canyon, two-thirds of vertical incision occurred prior to ~3.2 Ma, and the remaining third was essentially complete by ~2.6 Ma. Likewise, in the San Venancio canyon, ~71% of incision occurred prior to ~2.8 Ma. The modern canyon network therefore seems to have developed in <3 Ma, between ~5.6 and ~2.6 Ma, with the majority of incision occurring prior to ~3.2 Ma. As previously described (see Section 3.2.2, this chapter), regional

palaeoclimate proxy records indicate increasing aridity during this time, which should act to retard rather than promote fluvial incision. Canyon incision in the study area is therefore attributed to surface uplift and tilting, the asymmetry of which is shown by the swath profiles of Figure 3.2. The erosional response to uplift was strongly partitioned; despite removal of depths of material of up to ~600 m – and possibly as much as ~1110 m – during canyon formation, interfluve summit erosion was negligible, resulting in the preservation of the pre-incision low relief surface as a relict landscape atop the canyon interfluves. The minimum vertical incision rates associated with canyon formation – ranging from ~250 m Ma^{-1} to as high as ~460 m Ma^{-1} at <10 km from the escarpment crest, and decreasing to ~36-7 m Ma^{-1} at >30 km from the escarpment crest – display a striking spatial gradient due to the asymmetric distribution of uplift, which decreases sharply with increasing distance from the Loreto segment faults.

3.4.2 Determining the mechanism of surface uplift

Incision of the west-draining rift flank canyons, used in this study as a proxy for surface uplift, began after ~5.6 Ma and was largely complete by ~3.2 Ma. Assuming that the onset of incision did not significantly lag the onset of uplift, uplift likely began at ~6-5 Ma, and was largely complete by ~3.2 Ma. This post-dates by ~10-8 Ma the timing of slab detachment at ~15-13 Ma, when Pacific/Farallon spreading centres west of Baja California rotated ~45-60° clockwise in response to a loss of slab pull following detachment of the Farallon slab (Lonsdale, 1991; Tian et al., 2011; see also Section 2.1.2). Assuming a likely response time of ~2 Ma (see Section 3.1.2, this chapter) for the onset of asthenospheric flow through the resultant slab window, rift flank surface uplift occurred ~8-6 Ma later than expected if asthenospheric upwelling provided the driving force.

The timing of rift flank uplift is therefore inconsistent with active asthenospheric upwelling as a driver of uplift. However, the timing of uplift is coeval with the timing of active faulting and escarpment development at Loreto (see Chapter 2), and more broadly with the timing of lithospheric rupture and the onset of oceanic spreading between ~6-3 Ma ago in the southern and central Gulf

(Lizarralde et al., 2007). This indicates that rift flank uplift did not occur as a result of pre-rift topographic doming; rather, rifting and rift flank uplift have occurred synchronously. The lack of surface uplift associated with slab window opening may be explained by numerical modelling of slab detachment which indicates that asthenospheric flow through the window is entrained and pulled downwards by the sinking slab, rather than ascending to the base of the crust (Burkett and Billen, 2009).

Synchronous occurrence of rift flank uplift and lithospheric rupture are predicted by models of rift flank uplift which invoke as driving mechanisms either the flexurally distributed isostatic response to rift-related lithospheric unloading, or induced asthenospheric upwelling due to small-scale convection. Small-scale asthenospheric convection is proposed to operate beneath rift margins as a result of the lateral thermal gradient beneath thinned or ruptured lithosphere in the rift zone and nonextended surrounding continental lithosphere (Buck, 1986; Boutilier and Keen, 1999; Simon et al., 2009). The asthenospheric flow caused by this convection should generate partial melting due to decompression, and also crystal fabric realignment such that crystal long axes are parallel to flow direction. Both of these processes should cause seismic shear wave velocity anomalies, permitting the detection of asthenospheric flow. Recent analyses of shear wave velocity anomalies beneath the Gulf indicate convective upwelling beneath the northern Gulf but infer the presence of a lodged slab fragment(s) beneath southern Baja California and the southern Gulf, which prevents convection by inhibiting return flow (Wang et al., 2009; Zhang et al., 2009; Long, 2010; Zhang and Paulssen, 2012). If this interpretation is correct, then small-scale asthenospheric convection can be excluded as a mechanism of rift flank uplift at the southern Gulf, including the area of this study, although it may play a role further north.

However, flexural rift flank uplift in response to lithospheric unloading remains a candidate uplift mechanism. It is therefore necessary to explore whether the magnitude of observed mechanical and erosional unloading can generate sufficient flexural uplift to match the observed uplift. To do this,

the model of Jordan (1981) is used, as modified by Allen and Allen (2005), in which the crust is approximated by a semi-infinite (continuous) elastic plate of uniform rigidity which rests on a viscous fluid substrate of zero strength. The volume of erosional and mechanical unloading between the escarpment crest and approximate continent-ocean transition (Lonsdale, 1991; Lizarralde et al., 2007) was estimated using a combined topographic and bathymetric profile obtained from Global Multi-Resolution Topography (GMRT) data, which has a horizontal resolution of ~100 m (Ryan et al., 2009). The (negative) load generated by erosional and mechanical unloading is calculated from the area between the topographic and bathymetric profile, and the modern elevation of the escarpment crest on the profile. Implicit in this methodology is the assumption that the relative elevations of the modern escarpment crest and the unloaded area east of the crest were the same prior to crustal unloading. However, as discussed in Section 3.4.1, the pre-rift landscape of the rift flank was characterised by west-draining rivers during and likely also after Comondú Group deposition. Therefore, the area east of the modern escarpment crest was presumably situated at a greater relative elevation than the area of the modern rift flank, although by what magnitude is unknown. The estimated volume of unloaded material must therefore be regarded as a minimum estimate. In addition, the minor effect of the unloading of the rift flank itself by incision of the west-draining canyons is not considered.

Unloaded material was approximated by a series of columns, with widths of 0.5 km. Deflection produced by each column load *i* was calculated using:

$$w_i = \frac{h}{2}\frac{\rho_c - \rho_w}{\rho_m - \rho_w}\{\exp(-\lambda(-x+s-a))\cos(\lambda(-x+s-a)) - \exp(-\lambda(-x+s+a))\cos(\lambda(-x+s+a))\}$$

[Equation 3.7]

where h is load height, ρ_c is the density of continental crust (2700 kg m^{-3}), ρ_w is the density of seawater (1025 kg m^{-3}), ρ_m is the density of the mantle (3300 kg m^{-3}), x is horizontal distance, s is the

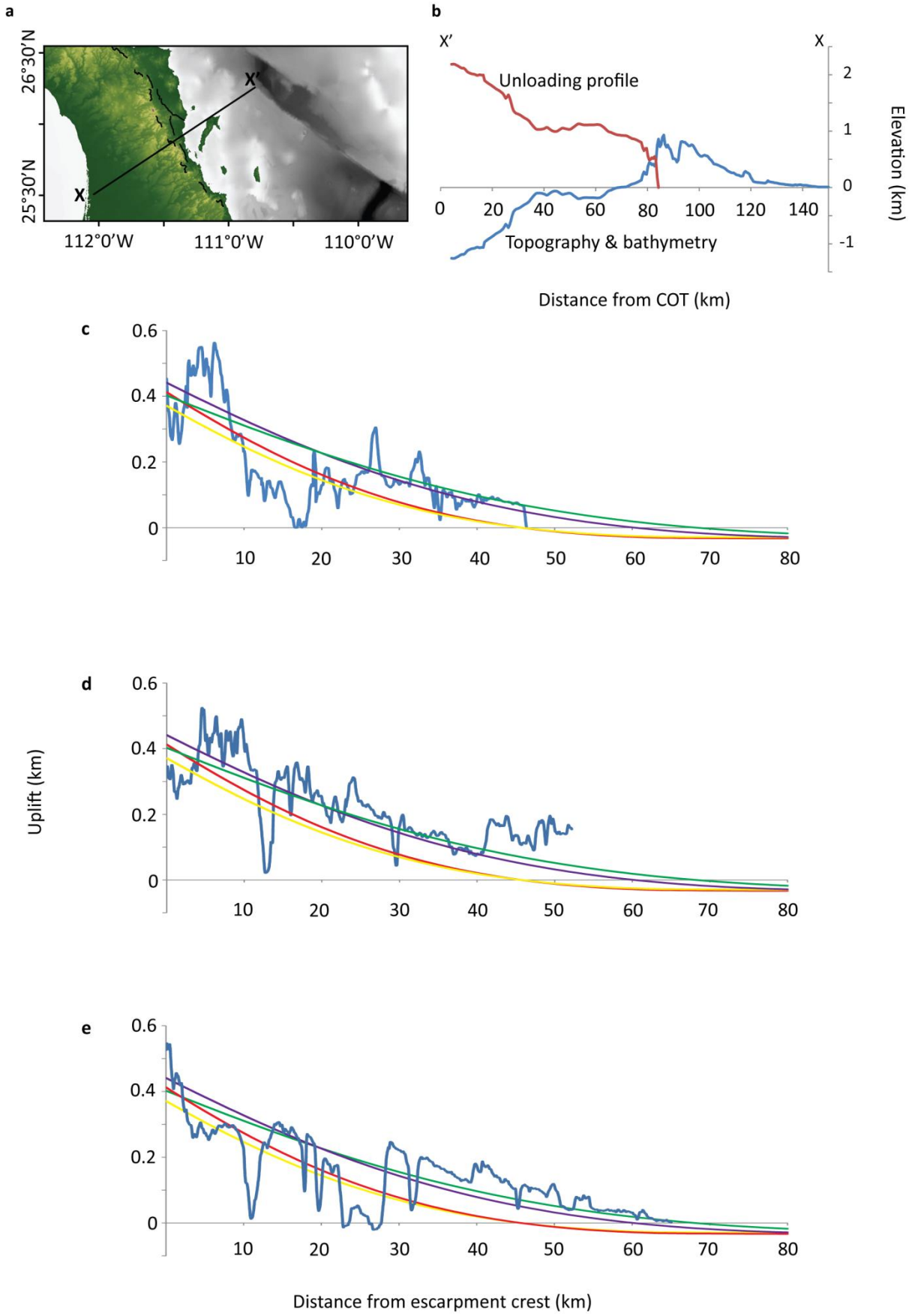
a
26°30'N
25°30'N
112°0'W
111°0'W
110°0'W
X
X'
b
X'
X
Unloading profile
Topography & bathymetry
Elevation (km)
2
1
0
-1
0
20
40
60
80
100
120
140
Distance from COT (km)
c
d
e
Uplift (km)
0.6
0.4
0.2
0
10
20
30
40
50
60
70
80
Distance from escarpment crest (km)

Figure 3.19 (Previous page): Flexure modelling results. a: *location of combined topographic & bathmetric profile obtained from GMRT data.* ***b:*** *topographic & bathymetric profile (blue line) used to obtain unloading profile (red line). Horizontal scale shows distance from continent-ocean transition (COT), as located by Lonsdale (1991) and Lizarralde et al. (2007).* ***c-e:*** *uplift profiles for the Comondú, San Venancio, and San Javier canyons respectively, obtained by subtracting stream elevations from interfluve elevations (see Figure 3.18). Horizontal scale shows distance from escarpment crest. Flexural responses to unloading are shown, assuming T_e of 10 km, crustal replacement by seawater (blue line) and air infill (red line), and T_e of 15 km, crustal replacement by seawater (green line), and air (purple line).*

position of the centre of the load, a is the load half-width, and λ is the inverse flexural parameter $1/\alpha$, calculated from

$$\alpha = \left(\frac{4D}{(\rho_m - \rho_w)g}\right)^{0.25} \quad \text{[Equation 3.8]}$$

where g is gravitational acceleration (9.81 m s^{-2}), and D is the flexural rigidity parameter, calculated from

$$D = \frac{E{T_e}^3}{12(1-\nu^2)} \quad \text{[Equation 3.9]}$$

where E is Young's modulus (70 GPa), T_e is effective elastic thickness, and v is Poisson's ratio (0.25). Total deflection is the sum of deflections from all column loads. The above calculation assumes total replacement of crust by seawater; for replacement by air, ρ_a (1.23 kg m^{-3}) was substituted for ρ_w throughout. The effect of post-rift sediment loading was ignored, as the southern Gulf contains little post-rift sediment (Lizarralde et al., 2007). Effective elastic thicknesses of 10-15 km give the best matches to observed minimum uplift magnitudes, obtained from canyon incision depths (interfluve elevation minus stream elevation; see Figure 3.19); these values are slightly lower than previously published T_e estimates from northern Baja California of ~15-20 km (Mueller et al., 2009). However,

in southern Baja California these T_e values would produce uplift of greater wavelength than observed. T_e of 20 km, for example, generates uplift which extends ~90 km west of the escarpment, but observed uplift decreases to zero ~55-65 km west of the escarpment crest. This discrepancy may be due to the fact that Mueller et al. (2009) estimate T_e with respect to modern topography as opposed to minimum uplift magnitudes; if, as in the area of this study, modern elevations include a contribution from pre-rift topography, then fitting of flexural profiles to modern topography will overestimate T_e values.

The flexurally distributed response to lithospheric unloading during rifting is therefore sufficient to generate the observed magnitude of rift flank uplift, and is consistent with the synchronous timing of rift flank uplift and crustal extension. However, although flexural uplift can explain all of the observed uplift, contributions from other syn- and post-rift processes cannot be entirely excluded. These include the effects of conductive heating of the lithosphere beneath Baja California from the juxtaposed thinned lithosphere of the Gulf; however, numerical modelling of other rifts indicates that this effect is likely limited, resulting in maximum uplift magnitudes of ~250 m attained ~50 Ma after the onset of rifting (Leroy et al., 2008). Likewise some models of depth dependent stretching, in which extension increases with depth such that warmer lower crust and/or lithospheric mantle are emplaced beneath non-extended brittle upper crust, predict rift flank uplift occurring near-synchronously with extension. Depth-dependent stretching models fall into two categories: discontinuous, where the lithospheric mantle and crust decouple across the Moho during extension (Royden and Keen, 1980), and continuous, where the increase of extension with depth does not occur as an abrupt transition (Rowley and Sahagian, 1986). In the southern Gulf, seismic imaging of the crust/mantle boundary indicate that the lateral extent of lower crustal extension does not depart significantly from the surface distribution of faulting, which is inconsistent with continuous models of depth-dependent stretching (Lizarralde et al., 2007; Savage and Wang, 2012). Discontinuous depth-dependent stretching cannot be excluded in the southern Gulf, as the depth and lateral variation of the lithosphere/asthenosphere boundary is unknown; however, in the Salton

Trough – the northernmost part of the Gulf of California rift system – the extent of extension in the mantle lithosphere appears only slightly (<~20 km) wider than the extent of surface crustal extension (Lekic et al., 2011), suggesting extension magnitude varies little with depth. It should also be noted that recent numerical modelling of discontinuous depth-dependent stretching indicates that the process does not generate significant rift flank uplifts (Huismans and Beaumont, 2008). In any case, it would be remarkably fortuitous if depth-dependent stretching generated rift flank uplift with a wavelength and magnitude so closely matching that expected for the isostatic response to crustal unloading.

3.5 Conclusions

This study has investigated the timing of rift flank uplift west of the Loreto rift segment of the Gulf of California. Here, widespread volcaniclastic sedimentation ceased synchronously with the cessation of subduction west of Baja California at ~15 Ma (Lonsdale, 1991; Tian et al., 2011), leading to the development of a low-relief landscape which persisted until ~5.6 Ma. Subsequently, this surface was uplifted and incised by a series of west draining canyons; the majority of incision was complete by ~3.2 Ma (Figure 3.20). Uplift was coeval with active faulting at Loreto (Chapter 2) and also with the timing of lithospheric rupture and the onset of oceanic spreading in the Gulf of California (Lizarralde et al., 2007), consistent with models of rift flank uplift driven by isostatic flexure (Weissel and Karner, 1989; Braun and Beaumont, 1989; Kooi et al., 1992), but inconsistent with models of uplift driven by asthenospheric flow triggered by the opening of a slab window beneath the southern Gulf (Ferrari et al., 2002; Fletcher et al., 2007; Castillo, 2008). Previously published analyses of shear wave velocity anomalies indicate that rift-induced small scale convection is absent from the asthenosphere beneath the southern Gulf and therefore does not contribute to rift flank uplift (Wang et al., 2009; Zhang et al., 2009; Zhang and Paulssen, 2012). A contribution from other proposed uplift mechanisms – thermal convection and depth-dependent stretching – cannot be wholly excluded, but simple 2D modelling performed in this study indicates that the flexurally-distributed isostatic response to the mechanical and erosional unloading caused by rifting is

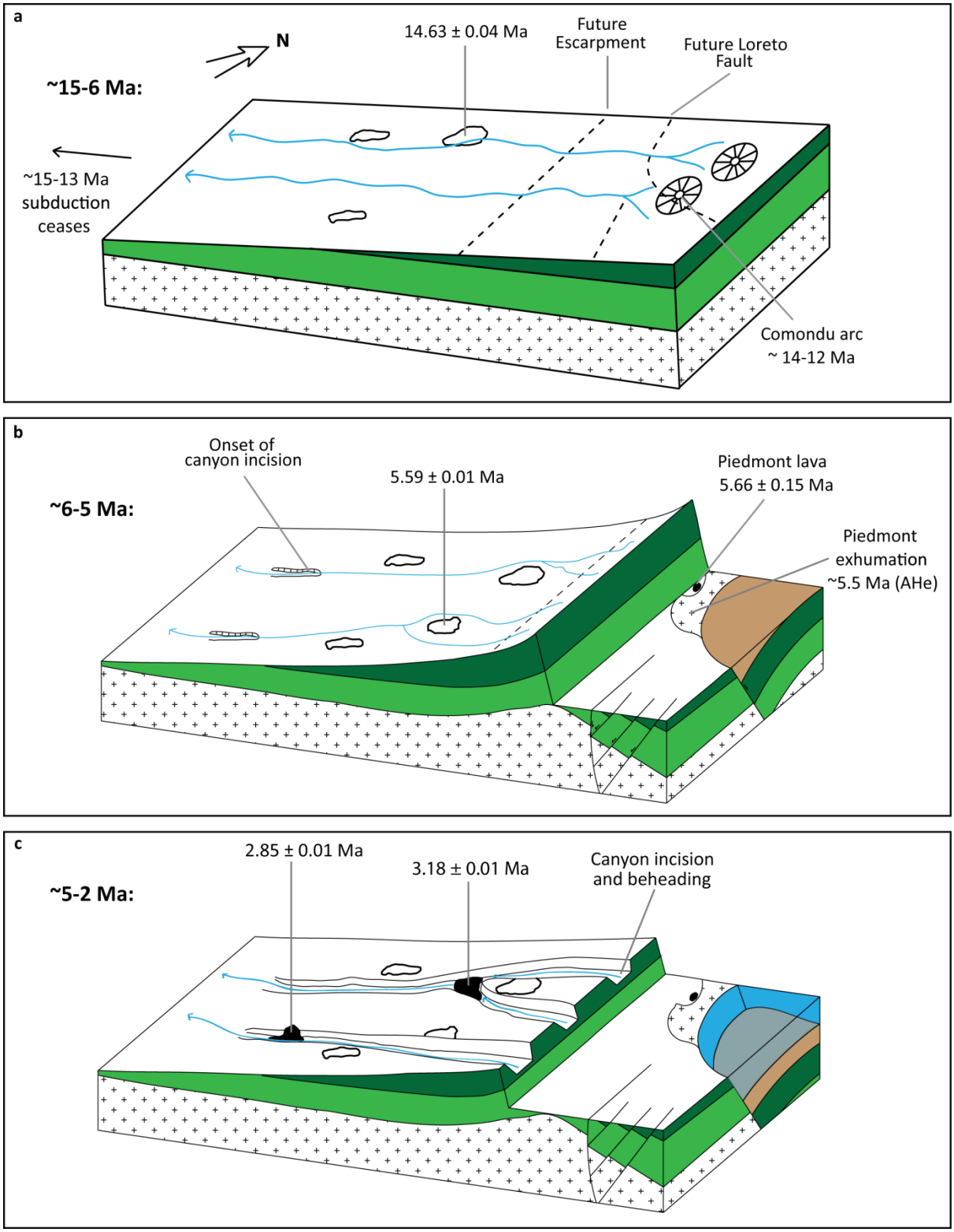

sufficient to explain the magnitude and extent of the observed uplift; there is no need to invoke additional mechanisms.

Figure 3.20 (Previous page): Cartoon showing rift flank development at the Loreto rift segment. a: *Following cessation of Comondú Group deposition on the rift flank at ~15 Ma, a low-relief landscape developed, composed of thin alluvial deposits and post-subduction lavas. Comondú volcanic centres developed along the future coastal plain, and possibly also along the future escarpment crest.* ***b:*** *Between ~8-6 Ma, the onset of slip on the Loreto fault drove denudation of the basement piedmont west of the fault, as indicated by the AHe ages reported in Chapter 2. The piedmont was exhumed as far west as the location of the Cerro Papini lava by ~5.7 Ma (see Chapter 2). The Nopolo monocline is assumed to have also developed at this time, although the age of this structure is not directly constrained; it may be younger (Willsey et al., 2002). On the rift flank, incision of west-draining canyons began after ~5.6 Ma – the $^{40}Ar/^{39}Ar$ age of the youngest relict landscape lava incised by the rift flank canyons; rift flank uplift therefore began no earlier than ~5.6 Ma.* ***c:*** *Canyon incision continued on the rift flank until ~2.8 Ma, although it was largely complete by ~3.2 Ma, as indicated by the $^{40}Ar/^{39}Ar$ ages of lavas which flowed into rift flank canyons during incision. Rift flank uplift was therefore complete no later than ~2.8 Ma, and likely prior to ~3.2 Ma.*

3.6 References

Allen, P.A., and Allen, J.R., 2005, Basin Analysis: Blackwell Publishing, Malden, USA.

Applegate, S., 1986, The El Cien formation strata of Oligocene and early Miocene age in Baja California Sur: Universita Nacional Autonoma Mexico Instituto Geologia Revista, v. 6, no. 2, p. 145–162.

Atwater, T., 1970, Implications of Plate Tectonics for the Cenozoic Tectonic Evolution of Western North America: GSA Bulletin, v. 81, p. 3513–3536.

Ballog, R.A., and Malloy, R.E., 1981, Neogene palynology from the southern California continental borderland, site 467, Deep Sea Drilling Project leg 63: Initial Reports of the Deep Sea Drilling Project, v. 63, p. 565-576.

Beal, C., 1948, Reconnaissance of the geology and oil possibilities of Baja California, Mexico: GSA Memoir 31.

Bellon, H., Aguillon-Robles, A., Calmus, T., Maury, R.C., Bourgois, J., and Cotten, J., 2006, La Purisima volcanic field, Baja California Sur (Mexico): Miocene to Quaternary volcanism related to subduction and opening of an asthenospheric window: Journal of Volcanology and Geothermal Research, v. 152, p. 253 – 272.

Bialas, R.W., and Buck, W.R., 2009, How sediment promotes narrow rifting: Application to the Gulf of California: Tectonics, v. 28, no. 4, DOI: 10.1029/2008TC002394.

Bohannon, R.G., Naeser, C.W., Schmidt, D.L., and Zimmerman, R.A., 1989, The timing of uplift, volcanism, and rifting peripheral to the Red Sea: a case for passive rifting?: Journal of Geophysical Research, v. 94, p. 1683–1701.

Bonini, J.A., and Baldwin, S.L., 1998, Mesozoic metamorphic and middle to late Tertiary magmatic events on Mesozoic metamorphic and middle to late Tertiary magmatic events on Magdalena and Santa Margarita Islands, Baja California Sur, Mexico: Implications for the tectonic evolution of the Baja: GSA Bulletin, v. 110, no. 8, p. 1094–1104.

Boutilier, R.R., and Keen, C.E., 1999, Small-scale convection and divergent plate boundaries: Journal of Geophysical Research, v. 104, no. B4, p. 7389–7403.

Braun, J., and Beaumont, C., 1989, A physical explanation of the relation between flank uplifts and the breakup unconformity at rifted continental margins: Geology, v. 17, no. 8, p. 760-764.

Buck, W.R., 1986, Small-scale convection induced by passive rifting: the cause for uplift of rift shoulders: Earth and Planetary Science Letters, v. 77, p. 362–372.

Burbank, D.W., and Anderson, R.S., 2012, Tectonic Geomorphology: Wiley-Blackwell, Chichester, UK.

Burkett, E.R., and Billen, M.I., 2009, Dynamics and implications of slab detachment due to ridge-trench collision: Journal of Geophysical Research, v. 114, no. B12, DOI: 10.1029/2009JB006402.

Calmus, T., Pallares, C., Maury, R.C., Aguillón-Robles, A., Bellon, H., Benoit, M., and Michaud, F., 2011, Volcanic Markers of the Post-Subduction Evolution of Baja California and Sonora, Mexico: Slab Tearing Versus Lithospheric Rupture of the Gulf of California: Pure and Applied Geophysics, v. 168, no. 8-9, p. 1303–1330.

Carreno, A.L., Ledesma-Vazquez, J., and Guerrero-Arenas, R., 2000, Biostratigraphy and depositional history of the Tepetate formation at Arroyo Colorado (early-middle Eocene), Baja California Sur, Mexico: Ciencias Marinas, v. 26, no. 1, p. 177–200.

Castillo, P.R., 2008, Origin of the adakite-high-Nb basalt association and its implications for postsubduction magmatism in Baja California, Mexico: GSA Bulletin, v. 120, no. 3-4, p. 451–462.

Chatelain, J.-L., Molnar, P., Prevot, R., and Isacks, B., 1992, Detachment of part of the downgoing slab and uplift of the New Hebrides (Vanuatu) islands: Geophysical Research Letters, v. 19, no. 14, p. 1507–1510.

Clark, M.K., 2003, Late Cenozoic uplift of southeastern Tibet: PhD thesis, Massachusetts Institute of Technology.

Cox, K., 1989, The role of mantle plumes in the development of continental drainage patterns: Nature, v. 342, no. 21, p. 873–877.

Dorsey, R.J., and Burns, B., 1994, Regional stratigraphy, sedimentology, and tectonic significance of Oligocene-Miocene sedimentary and volcanic rocks, northern Baja California, Mexico: Sedimentary Geology, v. 88, p. 231–251.

Dorsey, R.J., and Umhoefer, P.J., 2000, Tectonic and eustatic controls on sequence stratigraphy of the Pliocene Loreto basin, Baja California Sur, Mexico: GSA Bulletin, v. 112, no. 2, p. 177–199.

Duretz, T., Gerya, T.V., and May, D.A., 2011, Numerical modelling of spontaneous slab breakoff and subsequent topographic response: Tectonophysics, v. 502, p. 244–256.

Duretz, T., Schmalholz, S.M., and Gerya, T., 2012, Dynamics of slab detachment: Geochemistry Geophysics Geosystems, v. 13, no. 3, DOI: 10.1029/2011GC004024.

Ebinger, C.J., Bechtel, T.D., Forsyth, D.W., and Bowin, C.O., 1989, Effective elastic plate thickness beneath the East african and Afar Plateax and dynamic compensation of the uplifts: Journal of Geophysical Research, v. 94, no. B3, p. 2883–2901.

Ferraccioli, F., Finn, C.A., Jordan, T.A., Bell, R.E., Anderson, L.M., and Damaske, D., 2011, East Antarctic rifting triggers uplift of the Gamburtsev Mountains.: Nature, v. 479, no. 7373, p. 388–392.

Ferrari, L., Lopez-Martinez, M., Aguirre-Diaz, G., and Carrasco-Nunez, G., 1999, Space-time patterns of Cenozoic arc volcanism in central Mexico: from the Sierra Madre Occidental to the Mexican Volcanic Belt: Geology, v. 27, no. 4, p. 303–306.

Ferrari, L., Lopez-Martinez, M., and Rosas-Elguera, J., 2002, Ignimbrite flare-up and deformation in the southern Sierra Madre Occidental, western Mexico: Implications for the late subduction history of the Farallon plate: Tectonics, v. 21, no. 4, DOI: 10.1029/2001TC001302.

Fletcher, J.M., Grove, M., Kimbrough, D., Lovera, O., and Gehrels, G.E., 2007, Ridge-trench interactions and the Neogene tectonic evolution of the Magdalena shelf and southern Gulf of California: Insights from detrital zircon U-Pb ages from the Magdalena fan and adjacent areas: GSA Bulletin, v. 119, no. 11-12, p. 1313–1336.

Gastil, R.G., Phillips, R., and Allison, E.C., 1975, Reconnaissance geology of the state of Baja California: GSA Memoir 140.

Gerya, T.V., Yuen, D.A., and Maresch, W.V., 2004, Thermomechanical modelling of slab detachment: Earth and Planetary Science Letters, v. 226, no. 1-2, p. 101–116.

Grimm, K., and Foellmi, K., 1994, Doomed pioneers: allochthonous crustacean tracemakers in anaerobic basinal strata, Oligo-Miocene San Gregorio formation, Baja California Sur, Mexico: Palaios, v. 9, p. 313–334.

Groome, W.G., and Thorkelson, D.J., 2009, The three-dimensional thermo-mechanical signature of ridge subduction and slab window migration: Tectonophysics, v. 464, no. 1-4, p. 70–83.

Guillaume, B., Martinod, J., Husson, L., Roddaz, M., and Riquelme, R., 2009, Neogene uplift of central eastern Patagonia: Dynamic response to active spreading ridge subduction? Tectonics, v. 28, no. 2, DOI: 10.1029/2008TC002324.

Guillaume, B., Moroni, M., Funiciello, F., Martinod, J., and Faccenna, C., 2010, Mantle flow and dynamic topography associated with slab window opening: Insights from laboratory models: Tectonophysics, v. 496, no. 1-4, p. 83–98.

Hausback, B., 1984, Cenozoic volcanic and tectonic evolution of Baja California Sur, Mexico, *in* Frizzell, V.A., ed., Geology of the Baja California Peninsula, Pacific Section SEPM, p. 219–236.

Heim, A., 1922, Notes on the Tertiary of southern Lower California: Geological Magazine, v. 59, p. 529–547.

Henry, C.D., and Aranda-Gomez, J.J., 2000, Plate interactions control middle – late Miocene, proto-Gulf and Basin and Range extension in the southern Basin and Range: Tectonophysics, v. 318, p. 1–26.

House, M.A., Kelley, S.A., and Roy, M., 2003, Refining the footwall cooling history of a rift flank uplift, Rio Grande rift, New Mexico: Tectonics, v. 22, no. 5, DOI: 10.1029/2002TC001418.

Huismans, R.S., and Beaumont, C., 2008, Complex rifted continental margins explained by dynamical models of depth-dependent lithospheric extension: Geology, v. 36, no. 2, p. 163-166.

Huismans, R., Podladchikov, Y.Y., and Cloetingh, S., 2001, Transition from passive to active rifting: relative importance of asthenospheric doming and passive extension of the lithosphere: Journal of Geophysical Research, v. 106, no. B6, p. 11,271–11,291.

Japsen, P., Bonow, J.M., Green, P.F., and Chalmers, J.A., 2009, Formation, uplift and dissection of planation surfaces at passive continental margins – a new approach: Earth Surface Processes and Landforms, v. 34, p. 683–699.

Jordan, T.E., 1981, Thrust loads and foreland basin evolution, Cretaceous, western United States: AAPG Bulletin, v. 65, no. 12, p. 2506–2520.

Kooi, H., Cloetingh, S., and Burrus, J., 1992, Lithospheric necking and regional isostasy at extensional basins 1. Subsidence and gravity modeling with an application to the Gulf of Lions margin (SE france): Journal of Geophysical Research, v. 97, p. 17,553–17,571.

Kusznir, N.J., and Karner, G.D., 2007, Continental lithospheric thinning and breakup in response to upwelling divergent mantle flow: application to the Woodlark, Newfoundland and Iberia margins: Special Publications of the Geological Society of London, v. 282, p. 389–419.

Langenheim, V.E., and Jachens, R., 2003, Crustal structure of the Peninsular Ranges batholith from magnetic data: Implications for Gulf of California rifting: Geophysical Research Letters, v. 30, no. 11, DOI: 10.1029/2003GL017159.

Lee, J., Miller, M.M., Crippen, R., Hacker, B., and Ledesma-Vazquez, J., 1996, Middle Miocene extension in the Gulf Extensional Province, Baja California: Evidence from the southern Sierra Juarez: GSA Bulletin, v. 108, no. 5, p. 505–525.

Lekic, V., French, S.W., and Fischer, K.M., 2011, Lithospheric thinning beneath rifted regions of Southern California.: Science, v. 334, no. 6057, p. 783–787.

Leroy, M., Gueydan, F., and Dauteuil, O., 2008, Uplift and strength evolution of passive margins inferred from 2-D conductive modelling: Geophysical Journal International, v. 172, no. 1, p. 464–476.

Lizarralde, D., Axen, G.J., Brown, H.E., Fletcher, J.M., González-Fernández, A., Harding, A.J., Holbrook, W.S., Kent, G.M., Paramo, P., Sutherland, F., and Umhoefer, P.J., 2007, Variation in styles of rifting in the Gulf of California: Nature, v. 448, p. 466–469.

Long, M.D., 2010, Frequency-dependent shear wave splitting and heterogeneous anisotropic structure beneath the Gulf of California region: Physics of the Earth and Planetary Interiors, v. 182, no. 1-2, p. 59–72.

Lonsdale, P.F., 1991, Structural patterns of the Pacific floor offshore of Peninsular California, *in* Dauphin, J.P. and Simoneit, R.T. eds., The Gulf and Peninsular Province of the Californias, AAPG Memoir 47, p. 87–125.

Mark, D.F., Stuart, F.M., and de Podesta, M., 2011, New high-precision measurements of the isotopic composition of atmospheric argon: Geochimica et Cosmochimica Acta, v. 75, no. 23, p. 7494–7501.

McDougall, I., and Harrison, T.M., 1999, Geochronology and Thermochronology by the 40Ar/39Ar method, Oxford University Press, Oxford, UK.

McLean, H., 1988, Reconnaissance geologic map of the Loreto and part of the San Javier quadrangles, Baja California Sur, Mexico: Map MF1799, USGS.

McLean, H., Hausback, B., and Knapp, J., 1987, The geology of west central Baja California Sur Mexico: USGS Bulletin 1579.

Michaud, F., Royer, J.Y., Bourgois, J., Dyment, J., Calmus, T., Bandy, W., Sosson, M., Mortera-Gutiérrez, C., Sichler, B., Rebolledo-Viera, M., and Pontoise, B., 2006, Oceanic-ridge subduction vs. slab break off: Plate tectonic evolution along the Baja California Sur continental margin since 15 Ma: Geology, v. 34, p. 13–16.

Miller, M.S., and Agostinetti, N.P., 2011, Erosion of the continental lithosphere at the cusps of the Calabrian arc: Evidence from S receiver functions analysis: Geophysical Research Letters, v. 38, no. 23, DOI: 10.1029/2011GL049455.

Morgan, P., 1983, Constraints on rift thermal processes from heat flow and uplift: Tectonophysics, v. 94, p. 277–298.

Moucha, R., and Forte, A.M., 2011, Changes in African topography driven by mantle convection: Nature Geoscience, v. 4, no. 8, p. 707–712.

Mueller, K., Kier, G., Rockwell, T., and Jones, C.H., 2009, Quaternary rift flank uplift of the Peninsular Ranges in Baja and southern California by removal of mantle lithosphere: Tectonics, v. 28, DOI: 10.1029/2007TC002227.

Negrete-Aranda, R., and Cañón-Tapia, E., 2008, Post-subduction volcanism in the Baja California Peninsula, Mexico: The effects of tectonic reconfiguration in volcanic systems: Lithos, v. 102, p. 392 – 414.

Nielsen, C., and Thybo, H., 2009, No Moho uplift below the Baikal Rift Zone: Evidence from a seismic refraction profile across southern Lake Baikal: Journal of Geophysical Research, v. 114, no. B8, DOI: 10.1029/2008JB005828.

Oskin, M., Stock, J., and Martín-Barajas, A., 2001, Rapid localization of Pacific–North America plate motion in the Gulf of California: Geology, v. 29, no. 5, p. 459-462.

Pallares, C., Maury, R.C., Bellon, H., Royer, J.-Y., Calmus, T., Aguillón-Robles, A., Cotten, J., Benoit, M., Michaud, F., and Bourgois, J., 2007, Slab-tearing following ridge-trench collision: Evidence from Miocene volcanism in Baja California, México: Journal of Volcanology and Geothermal Research, v. 161, p. 95 – 117.

Peryam, T.C., Dorsey, R.J., and Bindeman, I., 2011, Plio-Pleistocene climate change and timing of Peninsular Ranges uplift in southern California: Evidence from paleosols and stable isotopes in the Fish Creek–Vallecito basin: Palaeogeography, Palaeoclimatology, Palaeoecology, v. 305, no. 1-4, p. 65–74.

Pik, R., Marty, B., Carignan, J., Yirgu, G., and Ayalew, T., 2008, Timing of East African Rift development in southern Ethiopia: Implication for mantle plume activity and evolution of topography: Geology, v. 36, p. 167–170.

Raymo, M.E., Mitrovica, J.X., O'Leary, M.J., DeConto, R.M., and Hearty, P.J., 2011, Departures from eustasy in Pliocene sea-level records: Nature Geoscience, v. 4, no. 5, p. 328–332.

Rogers, R.D., Kárason, H., and Hilst, R.D.V.D., 2002, Epeirogenic uplift above a detached slab in northern Central America: Geology, v. 30, p. 1031–1034.

Rogers, G., Saunders, A., Terrell, D., Verma, S., and Marriner, G., 1985, Geochemistry of Holocene volcanic rocks associated with ridge subduction in Baja California, Mexico: Nature, v. 315, p. 389–392.

Rowley, D.B., and Sahagian, D., 1986, Depth-dependent stretching: A different approach: Geology, v. 14, p. 32–35.

Royden, L., and Keen, C.E., 1980, Rifting processes and thermal evolution of the continental margin of eastern Canada determined from subsidence curves: Earth and Planetary Science Letters, v. 51, p. 343–361.

Ruppel, C., 1995, Extensional processes in continental lithosphere: Journal of Geophysical Research, v. 100, no. B12, p. 24187–24215.

Ryan, W.B.F., Carbotte, S.M., Coplan, J.O., O'Hara, S., Melkonian, A., Arko, R., Weissel, R.A., Ferrini, V., Goodwillie, A., Nitsche, F., Bonczkowski, J., and Zemsky, R., 2009, Global Multi-Resolution Topography synthesis: Geochemistry Geophysics Geosystems, v. 10, no. 3, DOI: 10.1029/2008GC002332.

Savage, B., and Wang, Y., 2012, Integrated Model of the Crustal Structure in the Gulf of California Extensional Province: Bulletin of the Seismological Society of America, v. 102, no. 2, p. 878–885.

Sawlan, M.G., 1991, Magmatic evolution of the Gulf of California rift, *in* Dauphin, J. and Simoneit, B. eds., The Gulf and Peninsular Province of the Californias, American Association of Petroleum Geologists, p. 301–369.

Sawlan, M.G., and Smith, J.G., 1984, Petrological characteristics, age, and tectonic setting of Neogene volcanic rocks in northern Baja California Sur, Mexico, *in* Frizzel, V.A., ed., Geology of the Baja California Peninsula, Pacific Section, SEPM, p. 237–251.

Schildgen, T.F., Cosentino, D., Bookhagen, B., Niedermann, S., Yıldırım, C., Echtler, H., Wittmann, H., and Strecker, M.R., 2012, Multi-phased uplift of the southern margin of the Central Anatolian plateau, Turkey: A record of tectonic and upper mantle processes: Earth and Planetary Science Letters, v. 317-318, p. 85–95.

Schildgen, T.F., Hodges, K.V., Whipple, K.X., Pringle, M.S., van Soest, M., and Cornell, K., 2009, Late Cenozoic structural and tectonic development of the western margin of the central Andean Plateau in southwest Peru: Tectonics, v. 28, DOI: 10.1029/2008TC002403.

Schweitzer, C.E., Feldmann, R.M., González-Barba, G., and Ćosović, V., 2007, Decapod crustaceans (Brachyura) from the Eocene Tepetate formation, Baja California Sur, Mexico: Annals of Carnegie Museum, v. 76, no. 1, p. 1–14.

Schwennicke, T., and Plata-Hernandez, E., 2003, Stratigraphy and age of the Comondú Group near Timbabichi, Baja California Sur, Mexico, *in* 99th Annual Meeting GSA Cordilleran Section Abstracts.

Seiler, C., Fletcher, J.M., Kohn, B.P., and Gleadow, A.J.W., 2011, Low-temperature thermochronology of northern Baja California, Mexico: Decoupled slip-exhumation gradients and delayed onset of oblique rifting across the Gulf of California: Tectonics, v. 30, DOI: 10.1029/2009TC002649.

Sengor, A.M.C., and Burke, K., 1978, Relative timing of rifting and volcanism on Earth and its tectonic implications: Geophysical Research Letters, v. 5, no. 6, p. 419–421.

Sepulchre, P., Ramstein, G., Fluteau, F., Schuster, M., Tiercelin, J.J., and Brunet, M., 2006, Tectonic uplift and eastern Africa aridification: Science, v. 313, no. 5792, p. 1419-1423.

Simon, K., Huismans, R.S., and Beaumont, C., 2009, Dynamical modelling of lithospheric extension and small-scale convection: implications for magmatism during the formation of volcanic rifted margins: Geophysical Journal International, v. 176, no. 1, p. 327–350.

Spiegel, C., Kohn, B.P., Belton, D.X., and Gleadow, A.J.W., 2007, Morphotectonic evolution of the central Kenya rift flanks: Implications for late Cenozoic environmental change in East Africa: Geology, v. 35, p. 427-430.

Steckler, M.S., 1985, Uplift and extension at the Gulf of Suez: indications of induced mantle convection: Nature, v. 317, no. 12, p. 135–139.

Stock, J.M., and Hodges, K.V., 1989, Pre-Pliocene extension around the Gulf of California and the transfer of Baja California to the Pacific plate: Tectonics, v. 8, p. 99–115.

Thouret, J., Worner, G., Gunnell, Y., Singer, B., Zhang, X., and Souriot, T., 2007, Geochronologic and stratigraphic constraints on canyon incision and Miocene uplift of the Central Andes in Peru: Earth and Planetary Science Letters, v. 263, no. 3-4, p. 151–166.

Tian, L., Castillo, P.R., Lonsdale, P.F., Hahm, D., and Hilton, D.R., 2011, Petrology and Sr-Nd-Pb-He isotope geochemistry of postspreading lavas on fossil spreading axes off Baja California Sur, Mexico: Geochemistry Geophysics Geosystems, v. 12, no. 2, DOI: 10.1029/2010GC003319.

Umhoefer, P.J., 2011, Why did the Southern Gulf of California rupture so rapidly?—Oblique divergence across hot, weak lithosphere along a tectonically active margin: GSA Today, v. 21, no. 11, p. 4–10.

Umhoefer, P.J., Dorsey, R.J., and Renne, P., 1994, Tectonics of the Pliocene Loreto basin, Baja California Sur, Mexico, and Evolution of the Gulf of California: Geology, v. 22, p. 649–652.

Umhoefer, P.J., Dorsey, R.J., Willsey, S., Mayer, L., and Renne, P., 2001, Stratigraphy and geochronology of the Comondú Group near Loreto, Baja California Sur, Mexico: Sedimentary Geology, v. 144, p. 125–147.

Umhoefer, P.J., Mayer, L., and Dorsey, R.J., 2002, Evolution of the margin of the Gulf of California near Loreto, Baja California Peninsula, Mexico: GSA Bulletin, v. 114, no. 7, p. 849–868.

Underhill, J.R., and Partington, M.A., 1993, Jurassic thermal doming and deflation in the North Sea: implications of the sequence stratigraphic evidence, *in* Parker, J.R. ed., Petroleum Geology of Northwest Europe: Proceedings of the 4th Conference, The Geological Society, London, p. 337–345.

Wang, Y., Forsyth, D.W., and Savage, B., 2009, Convective upwelling in the mantle beneath the Gulf of California: Nature, v. 462, p. 499–502.

Watts, A., 2001, Isostasy and Flexure of the Lithosphere: Cambridge University Press, Cambridge, UK.

Weissel, J.K., and Karner, G.D., 1989, Flexural uplift of rift flanks due to mechanical unloading of the lithosphere during extension: Journal of Geophysical Research, v. 94, no. B10, p. 13919–13950.

van Wijk, J.W., Lawrence, J.F., and Driscoll, N.W., 2008, Formation of the Transantarctic Mountains related to extension of the West Antarctic Rift system: Tectonophysics, v. 458, no. 1-4, p. 117–126.

Willsey, S.P., Umhoefer, P.J., and Hilley, G.E., 2002, Early evolution of an extensional monocline by a propagating normal fault: 3-D analysis from combined field study and numerical modeling: Journal of Structural Geology, v. 24, p. 651–669.

Wobus, C.W., Tucker, G.E., and Anderson, R.S., 2010, Does climate change create distinctive patterns of landscape incision? Journal of Geophysical Research, v. 115, no. F4, DOI: 10.1029/2009JF001562.

Zanchi, A., 1994, The opening of the Gulf of California near Loreto, Baja California, Mexico: from basin and range extension to transtensional tectonics: Journal of Structural Geology, v. 16, no. 12, p. 1619–1639.

van de Zedde, D.M.A., and Wortel, M.J.R., 2001, Shallow slab detachment as a transient source of heat at midlithospheric depths: Tectonics, v. 20, no. 6, p. 868–882.

Zhang, X., and Paulssen, H., 2012, Geodynamics of the Gulf of California from surface wave tomography: Physics of the Earth and Planetary Interiors, v. 192-193, p. 59–67.

Zhang, X., Paulssen, H., Lebedev, S., and Meier, T., 2009, 3D shear velocity structure beneath the Gulf of California from Rayleigh wave dispersion: Earth and Planetary Science Letters, v. 279, p. 255–262.

Ziegler, P.A., 1992, Plate tectonics, plate moving mechanisms and rifting: Tectonophysics, v. 215, no. 1-2, p. 9–34.

Ziegler, P.A., and Cloetingh, S., 2004, Dynamic processes controlling evolution of rifted basins: Earth-Science Reviews, v. 64, no. 1-2, p. 1–50.

4. Response of the rift flank catchments to transient uplift at Loreto

"Rivers carve the country, a landscape shaped by a stream."

Frank Turner, *The Fastest Way Back Home.*

4.1 Introduction

4.1.1 Statement of the problem

The topography of mountainous non-glaciated landscapes primarily reflects the development of fluvial relief: the extent to which streams incise their bedrock, in response to variations in uplift rate and magnitude, climate, and lithology (Whipple and Tucker, 1999; Ouimet et al., 2009). An implication of this observation is that a thorough understanding of the complex feedbacks between these input environmental variables, the fluvial response, and topographic outcomes is required in order to develop conceptual models of landscape evolution. Unfortunately, a further implication of this relationship is that bedrock streams will tend to adjust over time to prevailing tectonic, climatic, and lithologic conditions; the resultant smooth concave-up channel profiles are non-unique, and cannot easily be exploited to reconstruct the nature of the fluvial response. Therefore, numerous studies have focussed on identifying upland streams still in the process of adjustment to perturbations in tectonic and climatic conditions or changes in lithology, such as the unroofing of resistant basement (e.g. Snyder et al., 2000; Duvall et al., 2004; Oskin and Burbank, 2007; Whittaker et al., 2008; Berlin and Anderson, 2009; Wobus et al., 2010; Walsh et al., 2012). However, studies of established large-scale upland landscapes experiencing departures from steady-state have the drawback that the observed transient topography may include a significant component of inherited relief. This complicates attempts to constrain the magnitude and distribution of topographic changes.

In this study, the response of a low-relief landscape to an episode of transient uplift and tilting is examined. Rather than focus solely on two-dimensional stream profiles, an attempt is made to document the response to uplift across catchment areas. Preservation of the pre-uplift landscape atop channel interfluves provides a datum from which the magnitude of surface uplift can be measured, through the use of fluvial incision depth as a proxy for uplift. Although trunk streams

draining this landscape exhibit smooth elevation profiles which lack convexities, suggesting that these channels have adjusted to uplift, this study shows that the extent to which each catchment area has responded to uplift varies considerably. This variation consists of the extent of destruction of prominent interfluve mesas which are capped by the pre-uplift landscape. This study concludes that the observed extent of interfluve destruction, and thus the extent of catchment response to uplift, is mediated by lithological variation: the spatial distribution of resistant lavas which are a component of the pre-uplift landscape.

4.1.2 The study area

This study focuses on the south-central Baja California Peninsula, which forms the western margin of the Gulf of California (Figure 4.1). A highly oblique transtensional rift, the Gulf is thought to have initiated in the mid-Neogene to accommodate divergent Pacific-North America motion subsequent to cessation of Pacific-Farallon spreading and foundering of the oceanic Farallon plate beneath North America (Atwater, 1970; Stock and Hodges, 1989). Rifting has resulted in the near-complete transfer of Baja California from North America to the Pacific plate; the peninsula currently exhibits ~90% of Pacific plate motion, with the remainder accommodated by a transtensional shear zone west of the peninsular (Dixon et al., 2000; Plattner et al., 2009). Throughout this major plate boundary reorganisation, the Baja California Peninsula has acted largely as a rigid block, experiencing only minor deformation; there are no peninsula-transecting faults south of the Agua Blanca fault, near the head of the Gulf. Rift-bounding faults are restricted to a narrow eastern coastal plain, typically less than ~20 km wide, which is separated from the unextended rift flank by a prominent east-facing rift escarpment, the Main Gulf Escarpment (MGE), which runs the length of the peninsula. In common with many rifts, the rift-bounding faults define distinct rift segments exhibiting similar structural styles, separated by accommodation zones (Axen, 1995). West of the Loreto and Timbabichi segments, and the intervening Bahía Agua Verde accommodation zone (Umhoefer et al., 2002), the unextended rift flank comprises a remarkably uniform west-sloping

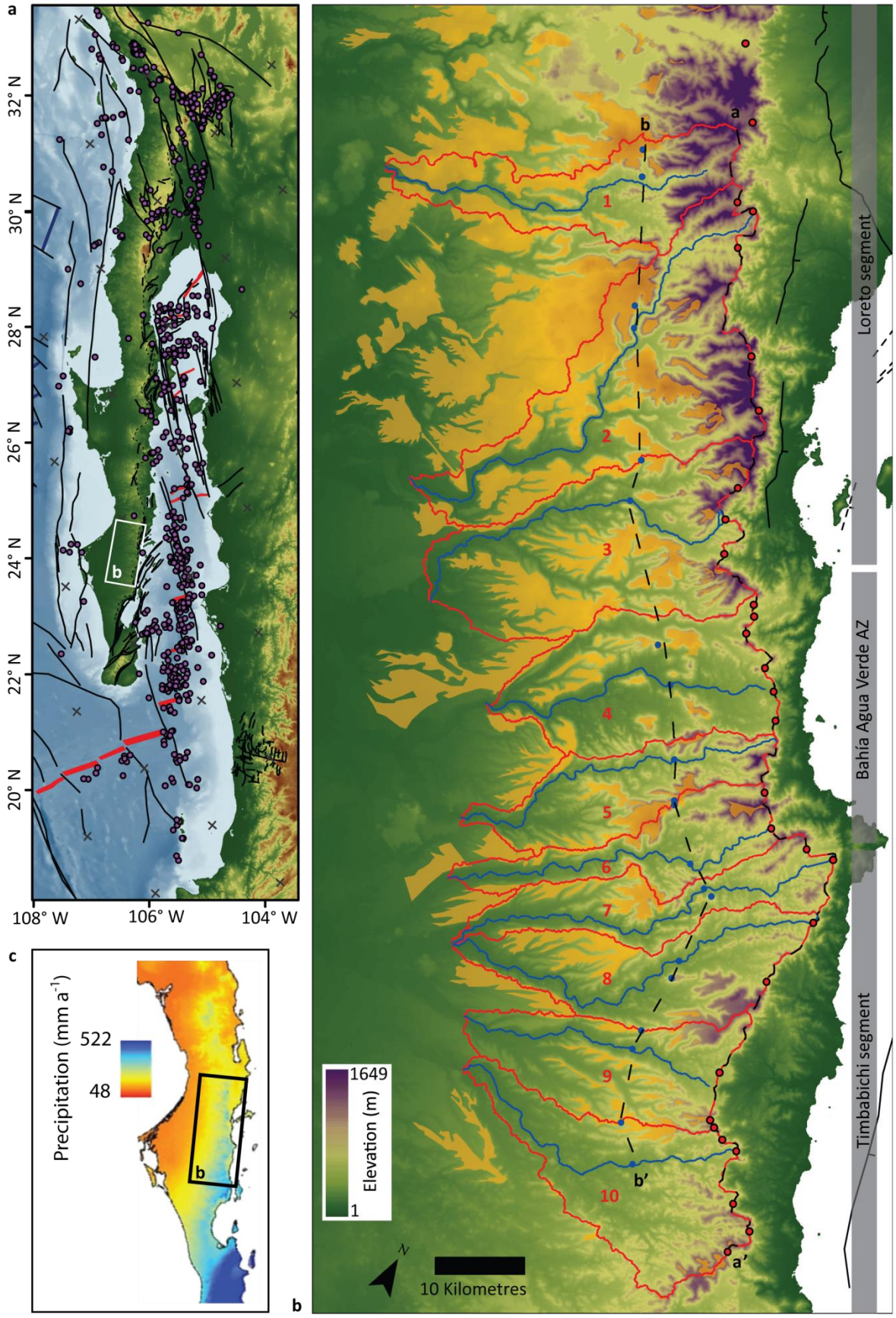
a
32° N
30° N
28° N
26° N
24° N
22° N
20° N
108° W
106° W
104° W
b
c
Precipitation (mm a-1)
522
48
b
b
a
b
1
2
3
4
5
6
7
8
9
10
b'
a'
Loreto segment
Bahía Agua Verde AZ
Timbabichi segment
1649
Elevation (m)
1
N
10 Kilometres

Figure 4.1 (Previous page): Overview of the Gulf of California and study area. a: *Topography and bathymetry of the Gulf of California, from the Global Multi-Resolution Topography (GMRT) synthesis (Ryan et al., 2009), showing major structures (black lines), abandoned (blue) and active (red) spreading centres, and epicentre locations for earthquakes >Mw 4.5 during the period 1973-2009 (USGS National Earthquake Information Centre archive).* ***b:*** *Rift flank study area topography, from the Advanced Spaceborne Thermal Emission and Reflection Radiometer (ASTER) dataset; horizontal resolution ~28 m. Orange transparency indicates extent of rift flank relict landscape; solid black lines indicate faults (tick indicates downthrown block); red lines delineate catchment areas included in this study; blue lines indicate trunk streams; blue dots indicate locations of spot incision depths below relict landscape; red dots indicate locations of beheaded canyons; dashed black lines indicate transects* ***a***-***a'*** *and* ***b***-***b'****. Grey bars indicate extents of Timbabichi and Loreto rift segments, separated by the inferred Bahia Agua Verde accommodation zone* (Axen, 1995; Umhoefer et al., 2002). ***c:*** *Study area mean annual precipitation distribution, from Holmgren et al. (2011).*

low-relief landscape, dissected by a network of west-draining canyons which typically attain depths of ~400-600 m near the escarpment crest (Figure 4.1). This area is bounded to the north by the core of the La Purísima volcanic field, where the landscape has been disrupted by intense volcanism and minor extensional faulting, and to the south by the Isla San Jose accommodation zone (Axen, 1995; Drake, 2005; Umhoefer et al., 2007) and the major structural embayment of Bahía de la Paz, which has dissected the uplifted rift flank (Busch et al., 2011). As demonstrated in Chapter 3, the low-relief landscape preserved atop the interfluve mesas between the rift flank canyons developed subsequent to ~15 Ma, following the cessation of deposition of the volcaniclastic Comondú Group. The dominant geological unit of Baja California Sur, the Comondú Group comprises a westward-thinning wedge of volcaniclastic sediment attaining thicknesses of ~1.5-2 km near the eastern coast of the peninsula, and which blanketed south-central Baja California during the Early and Middle Miocene (Hausback, 1984; Umhoefer et al., 2001). On the rift flank, the youngest Comondú units are discontinuously overlain by mafic lavas of the La Purísima volcanic field (Sawlan and Smith, 1984;

McLean et al., 1987; Bellon et al., 2006), which interfinger laterally with unconsolidated alluvial deposits which are up to ~40 m thick. As discussed in Chapter 3, these post-Comondú units are together interpreted as comprising a low-relief relict landscape, now preserved atop the rift flank interfluve mesas; the $^{40}Ar/^{39}Ar$ age of the youngest relict landscape lava incised by the canyon network indicates this landscape persisted until ~5.6 Ma. $^{40}Ar/^{39}Ar$ ages yielded by syn- and post-incision lavas which have flowed into canyons and are situated at or near modern stream channel elevations indicate that incision occurred largely between ~6-5 and ~3.2 Ma, and was likely complete by ~2.6 Ma. Canyon incision occurred in response to westward tilting of the unextended rift flank; therefore, although the stable rift flank has not experienced significant internal deformation during development of the Gulf of California rift, neither has it remained entirely tectonically quiescent. The temporal coincidence of rift flank tilting and surface uplift, as recorded by canyon incision, and crustal extension, as recorded by the timing of footwall exhumation west of the rift-bounding Loreto fault, indicate that rift flank tilting and uplift was driven by the flexurally distributed isostatic response of the lithosphere to lithospheric unloading during rifting (see Chapter 3). This interpretation is also consistent with the onset of seafloor spreading in the southern Gulf between ~3-6 Ma (Lizarralde et al., 2007). The crucial implication of rift flank surface uplift driven by isostatic flexure in response to lithospheric unloading is that the uplift was likely transient; lithospheric thinning and the associated isostatic response should cease once the rift has progressed to full lithospheric rupture and seafloor spreading has initiated, provided the rate of igneous crust generation is sufficient to accommodate the crustal extension rate imposed on the rift by Pacific/North America divergence. Assuming this is the case, further lithospheric thinning should occur only through erosional unloading of the uplifted rift flank itself; the isostatic response to this unloading could result in additional uplift of the rift flank interfluves, although major (kilometre-scale) increases in relief are thought necessary for this process to be significant (Montgomery, 1994; Whipple et al., 1999). A few caveats exist to the presumption that the rift flank has experienced only transient uplift; these include failure of seafloor spreading rates to match Pacific/North American

divergence rates, which could lead to continued slip on rift-bounding faults, potentially resulting in coseismic and isostatic uplift of the rift flank, and a number of possible rift-related thermal processes, including lateral conduction within the lithosphere and small-scale induced asthenospheric convection (e.g. Buck, 1986; Huismans et al., 2001; Leroy et al., 2008). Therefore, the first part of this study briefly reviews the evidence supporting the presumption that the rift flank has experienced only transient rift-related surface uplift, which has now ceased, and that this tectonic forcing was relatively uniform across the study area.

If this presumption is correct, then the south-central Baja California rift flank provides an opportunity to examine drainage network development in response to transient surface uplift and tilting, and in particular to isolate the extent to which this response is controlled by lithological variation. Burial of antecedent topography beneath the Comondú Group, resulting in low-relief landscape development prior to uplift, means that the current topography is derived solely from well-constrained rift-related uplift, and lacks complications associated with inherited topography (e.g. Densmore et al., 2004). Subsequently, landscape development has been mediated principally by fluvial processes; in contrast to many well-studied high-elevation areas, topography has not been influenced by Cenozoic glaciations (e.g. Clark et al., 2005). Although long term, high-resolution climatic data are lacking, modern mean annual precipitation is evenly distribution across the study area (Figure 4.1) (Hastings and Turner, 1965; Holmgren et al., 2011). In contrast to the rift flank of northern Baja California, which attains higher elevations (Peryam et al., 2011), rift flank uplift in south-central Baja California has been insufficient to generate orographic precipitation and the associated feedback into fluvial incision effectiveness.

The study area therefore fulfils many of the key criteria listed by Tucker (2009) as necessary to define a natural experiment in landscape evolution. The rift flank canyon systems developed on a low relief surface, the product of topographic resetting through prolonged sedimentation, and thus lack inherited topography; exhibit negligible climatic variation; and have likely experienced similar

tectonic histories of transient rift-related uplift and tilting followed by quiescence, as discussed further below. The only significant variation across the study area is therefore lithological: the distribution of resistant lavas associated with the La Purísima volcanic field, which discontinuously cap the friable underlying volcaniclastic sediments of the Comondú Group. The study area therefore provides an excellent opportunity to examine the effects of spatially variable lithology on catchment development in response to transient surface uplift and tilting.

4.2 Tectonic history

4.2.1 Is the rift flank still uplifting?

The study area comprises ten catchments, which drain westward from the escarpment crest (Figure 4.1). Numerous lines of evidence point to these catchments having experienced tectonic quiescence following rift flank uplift. As discussed in Chapter 3, the presence of lavas yielding $^{40}Ar/^{39}Ar$ ages of ~2.6 Ma or less situated at or near modern stream elevations in the two northernmost catchments – the San Venancio and the San Javier, respectively catchments 1 and 2 – strongly suggest that uplift and the resulting vertical incision ceased prior to this time. However, as lava sampling did not extend to the remaining catchments, it is necessary to consider other evidence to support a similar tectonic history for the eight catchments to the south.

Bedrock streams experiencing increased uplift rates typically adjust by formation of steepened reaches, termed knickzones or knickpoints, immediately upstream of the boundary of the uplifting area. These knickpoints then propagate upstream, facilitating catchment adjustment to the new equilibrium state within a characteristic response time, thought to be typically on the scale of ~10^5-10^7 a (Whittaker, 2012). Identification of knickpoints therefore serves to identify streams still in the process of adjusting to tectonic perturbations, although this can be complicated by the presence of knickpoints generated by non-tectonic changes in substrate erosivity – for example, lithological changes or climatic boundaries. As can be seen in Figure 4.2, the rift flank trunk streams all exhibit smooth longitudinal profiles free of convexities. Note that this absence of knickpoints may indicate

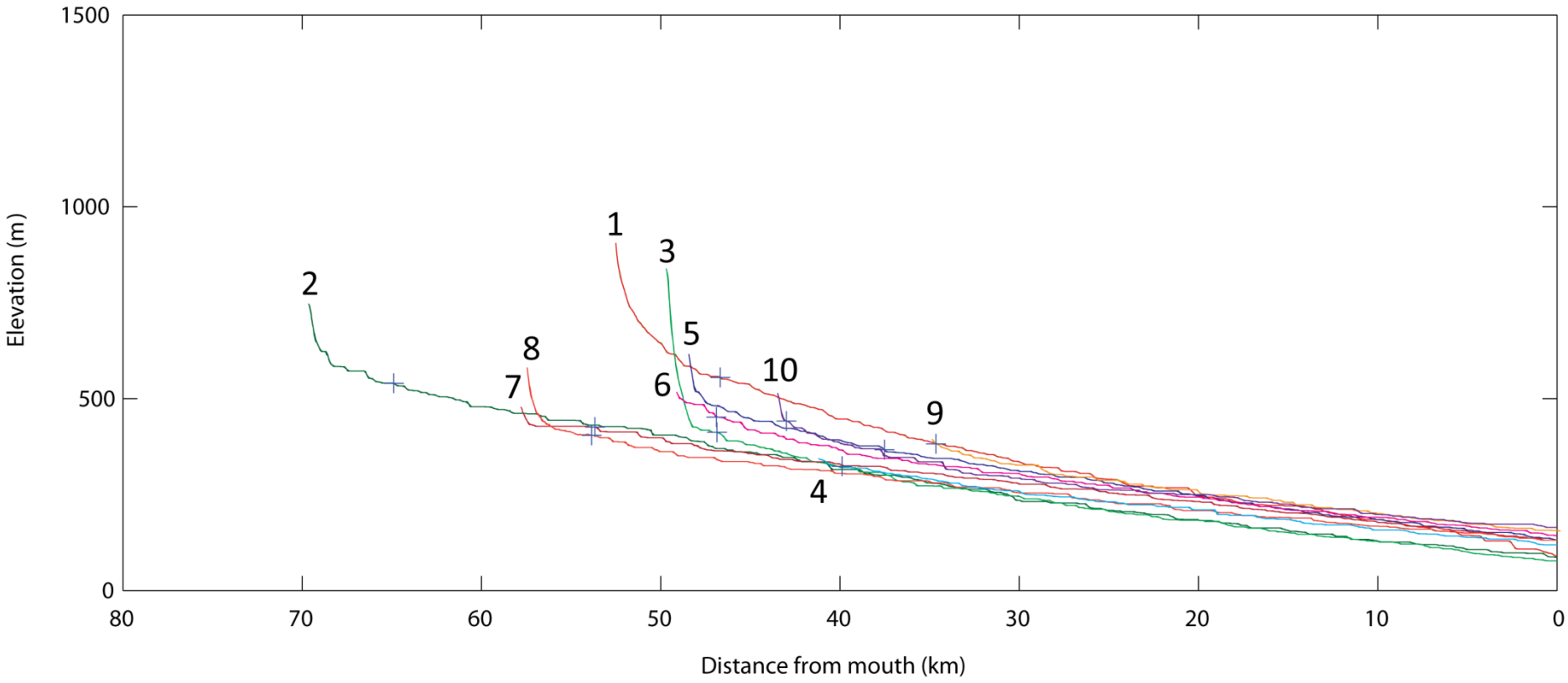

Figure 4.2: Trunk stream elevation profiles. *Numbers correspond to catchments in Figure 4.1. Crosses indicate upstream regression limits for k_{sn} calculations.*

either the cessation of transient uplift, or merely that channels have fully adjusted to a steady uplift rate. Determining whether the rift flank has experienced significant absolute surface uplift since the inferred end of rift-related uplift prior to ~2.6 Ma is not straightforward. Some previous studies have exploited the elevations of datable emergent marine terraces to constrain uplift rates of coast-draining catchments (e.g., Snyder et al., 2000). However, some caution is appropriate when extrapolating coastal uplift rates to infer regional tectonic motions. East of the study area, ages of coastal terraces located between Timbabichi and Loreto obtained from amino-acid racemisation and U-series geochronologic studies of marine fossils suggest that these locations have experienced only ~30-40 m of uplift since marine isotope stages 11-13 (~0.4-0.5 Ma); older terraces are lacking (Ortlieb, 1991; Mayer, 1999). However, given that the Gulf coastline is intensely faulted, uplift magnitudes derived from marine terraces may reflect only localised coseismic uplift of individual fault blocks, which is unlikely to have affected the entire rift flank, particularly at such small magnitudes. For example, much greater uplift of the coastal plain around Loreto is indicated by the uplift and emergence of marine units of the Loreto basin since ~2 Ma as a consequence of slip on offshore faults east of the Sierra la Sierrita; these units are now situated at elevations of ~100-200 m asl (Dorsey and Umhoefer, 2000). However, as discussed previously, the Comondú, San Venancio, and San Javier rift flank catchments west of the Loreto basin have all undergone vertical incision of <10 m since ~2.6 Ma, implying that the rift flank west of the Loreto basin experienced little uplift during this time. This suggests that even apparently significant uplift of the coastal plain may not be transmitted as far west as the rift flank. Therefore, this study does not utilise the uplift estimates derived from emergent marine terraces to constrain the uplift history of the rift flank catchments not included in the lava study described in Chapter 3.

However, the coastal terrace data does provide information on the extent of rift-bounding and coastal fault activity. The low uplift rates (~0.1 m ka^{-1}) implied by terrace elevations suggest that these faults are active only at low rates. This is in agreement with the distribution of modern seismic activity in the Gulf region (Figure 4.1); in particular, the rift bounding faults of the southern Gulf

exhibit virtually no activity. Instead, slip is strongly concentrated around the system of spreading centres and transform structures along the midline of the Gulf. Such a distribution lends qualitative support to the hypothesis that, at least in the southern Gulf, relative Pacific/North America motion is largely accommodated by seafloor spreading, in conjunction with limited slip on shear zones west of Baja California, which in turn suggests lithospheric thinning by means of mechanical crustal extension has ceased. As the isostatic response to lithospheric thinning was likely the driving mechanism for rift flank uplift (see Chapter 3), it can be reasonably concluded that rift flank uplift has ceased. In principle, lower lithospheric erosion driven by asthenospheric processes could still require isostatic adjustment and drive further uplift, but evidence for this is lacking, as discussed in Chapter 3.

In summary, three separate observations indicate that the rift flank is not currently experiencing surface uplift. Firstly, the lack of convexities in rift flank stream profiles indicates that there has been no increase in rift flank uplift rate within the trunk stream response times, and is consistent with tectonic quiescence. Second, the presence of lavas yielding $^{40}Ar/^{39}Ar$ ages of ~2.6 Ma or less situated at or near modern stream elevations in the northern catchments suggests little uplift has occurred since this time. Thirdly, evidence for ongoing low rates of coseismic uplift at coastal plain and offshore faults during this time suggests that such uplift is minor, localised, and has negligible impact on the rift flank, consistent with a distribution of recent seismic activity across the Gulf which suggests that brittle lithospheric thinning and the resultant isostatic uplift has largely ceased. This study therefore proceeds on the assumption that the rift flank study area has experienced negligible uplift since at least ~2.6 Ma.

4.2.2 Did rift flank uplift vary along strike?

In reviewing the rift flank uplift history, it is also necessary to consider briefly whether uplift varied significantly in magnitude across the study area. Identification of the relict landscape atop the

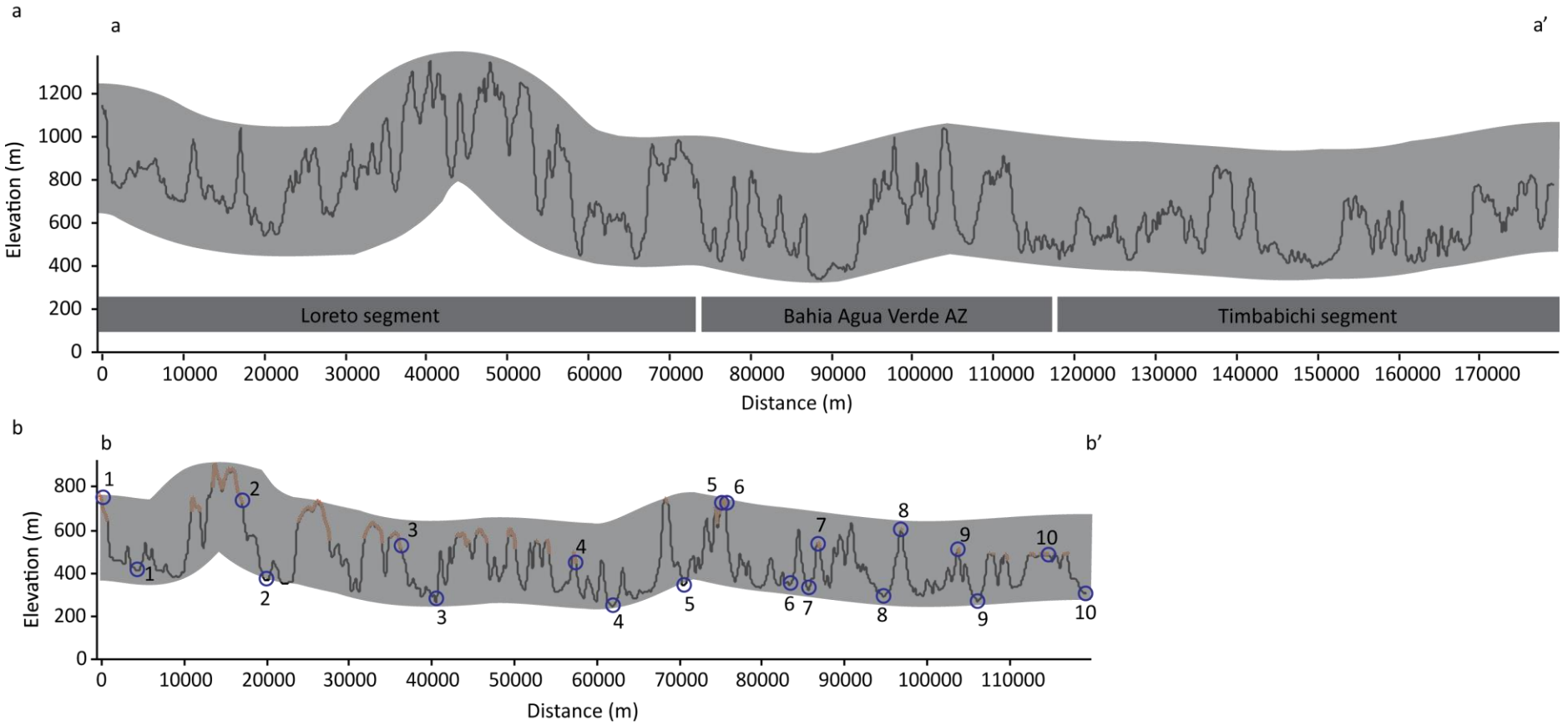

Figure 4.3: Rift flank topographic profiles. a: *Profile **a**-**a'** in Figure 4.1, along the escarpment crest. Extent of grey background indicates maximum relief of 600 m at the escarpment crest; canyon incision depths at the escarpment crest therefore do not exceed ~600 m.* ***b:*** *Profile **b**-**b'** in Figure 4.1, along a transect ~10 km west of the escarpment crest. Note that transect **b**-**b'** is considerably shorter than transect **a**-**a'** due to highly irregular nature of escarpment crest. Orange overlays identify areas of relict landscape. Blue circles indicate spot incision depths in Figure 4.1; numbers indicate catchments in Figure 4.1. Extent of grey background indicates maximum relief of 400 m ~10 km west of the escarpment crest.*

interfluve mesas of the study area permits the magnitude of surface uplift to be more closely constrained. The escarpment crest has experienced the highest uplift; here, interfluve elevations of ~800-1000 m asl are typical, with the exception of the area west of the northern Escondido fault which comprises the headwaters of catchments 2 and 3. Here, the escarpment crest rises to ~1200 m asl (Figure 4.3). Superficially, this suggests enhanced uplift in this area. However, as the rift flank canyons have developed in response to uplift, and as the absence of long profile convexities suggests they have adjusted to uplift, the depth of canyon incision is likely a better indicator of uplift magnitude. As can be seen in Figure 4.3, incision depths at the escarpment crest are typically ~400-600 m; this relatively low variation in incision depths is also observed west of the escarpment crest. Here, where interfluves widen to form mesas, the relict landscape can be more confidently identified and exploited as a datum to track variation in canyon incision. Incision depths of ~200-400 m are typical (Figure 4.3). Based on these canyon incision depths, uplift appears to have been relatively uniform along the strike of the study area. The absence of deeper incision west of the higher elevation area west of the Escondido fault suggests that the higher elevation is not the result of greater rift-related uplift. Instead, the elevation of the relict landscape appears to have been as much as ~400 m greater in this area prior to uplift and incision. Possibly this area hosted volcanic edifices generated by late-stage volcanism of the Comondú Group, as proposed north of the study area by Sawlan (1991); confirmation of this requires detailed field investigation, but access to this remote, high relief zone close to the escarpment is challenging.

In summary, the magnitude of rift-related uplift experienced by the study area is relatively consistent, decreasing westwards from maxima of ~400-600 m at the escarpment crest; the limit of uplift is defined by the western limit of incision.

4.3 Catchment analysis

The 10 catchments which drain westwards across the study area from the escarpment crest are incised into a low-relief landscape comprising thin alluvial deposits and discontinuous resistant lavas, underlain by units of the volcaniclastic Comondú Group. Defining a western boundary to the study

Figure 4.4: Image of catchment 1 trunk stream. *Note mixed nature of stream substrate, with alluvium (grey) in the middle distance and exposed bedrock straths in foreground (white). Dirt road is ~2.5 m wide.*

area in the absence of a fault-bounded mountain front is not straightforward. The catchments are bounded to the west by the low-relief alluvial Magdalena Plain, which is not incised. The plain ranges in width from ~20 km in the north to ~80 km in the south, but largely lies at elevations of less than 50 m asl. The absence of incision strongly suggests that the plain acts as the base level to which the west-draining rift flank streams are graded; moreover, the tendency for the unconfined streams on the plain to amalgamate renders catchment analysis difficult. For the purposes of this study, the western boundary of the study area is identified as the location where the incision depth of the canyons decreases to 50 m. This occurs at a distance of ~30-40 km west of the escarpment crest; within this area, catchment sizes range from 211-599 km^2.


d

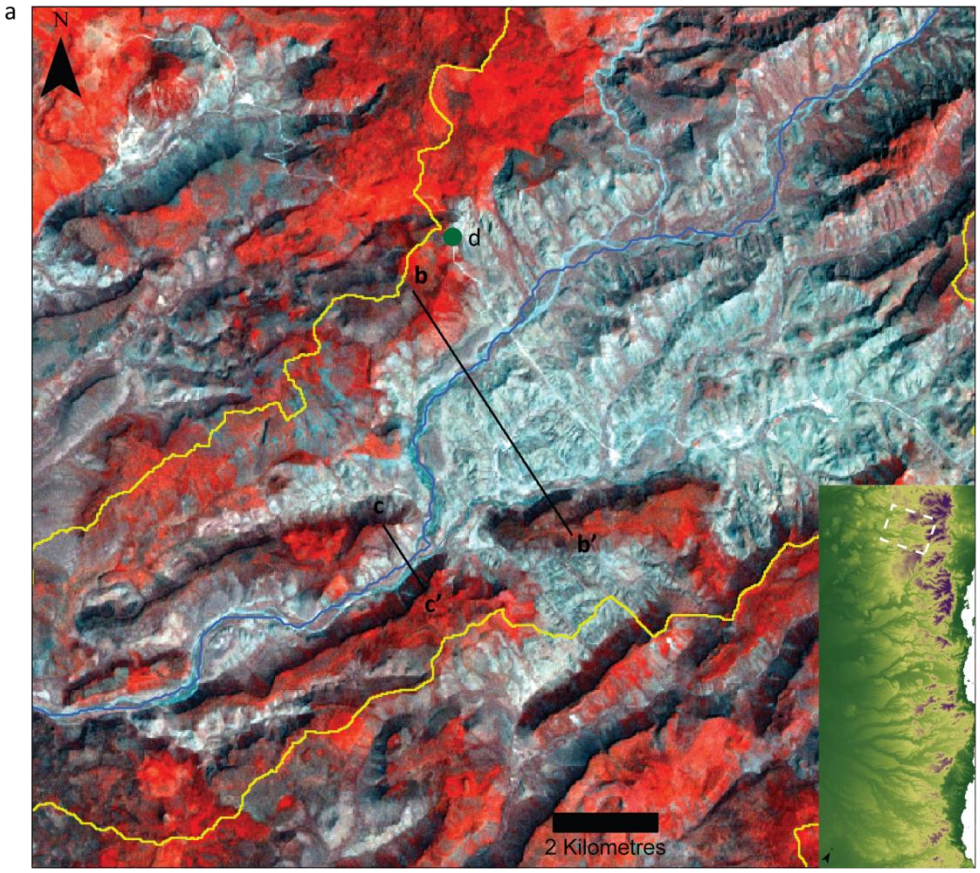
a
N
d
b
b′
c
c′
2 Kilometres

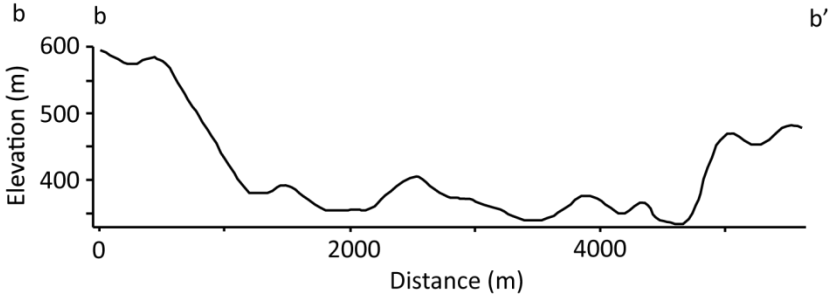
b
b′
600
500
400
Elevation (m)
0
2000
4000
Distance (m)

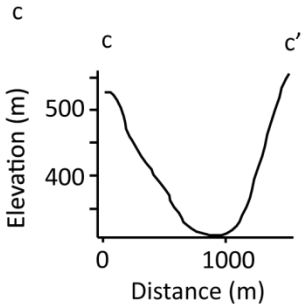
c
c
c′
500
400
Elevation (m)
0
1000
Distance (m)

Figure 4.5 (Previous page): Catchment 1. a: *False-colour multi-band LANDSAT image comprising bands 1 (blue), 2 (green) and 7 (red); 15 m horizontal resolution. Yellow line indicates catchment boundaries; blue line indicates trunk stream; black lines indicate topographic profiles, green dot indicates viewpoint for photograph* ***d****.* ***b:*** *Topographic profile* ***b****-****b'****.* ***c:*** *Topographic profile* ***c****-****c'****.* ***d:*** *Panoramic photograph looking NE to SE from point* ***d*** *in* ***a****; right-hand side of image looking parallel to profile* ***b****-****b'****. Note broad, low-relief canyon floor, and low-relief mesa summits.*

Field examination of the two northernmost catchments indicates that the canyon channels are characterised by exposed bedrock straths discontinuously mantled by coarse alluvial deposits (Figure 4.4). Significant alluvial fills are absent from the study area canyons, although present in the upper reaches of the Comondú canyon north of the study area, where ponded alluvium completely conceals bedrock east of a major lava dam (Chapter 3). A key feature of the study area topography is that fluvial dissection of the relict landscape in response to rift flank uplift is occurring not only by vertical incision, but also by lateral canyon widening through destruction of interfluve mesas (Figure 4.1). The degree of interfluve destruction varies considerably downstream within each catchment. In catchment 1, interfluve destruction ~15 km west of the escarpment crest has produced a ~3.4 km wide area in which relief does not exceed ~50 m, which contains the trunk stream and a major tributary (Figure 4.5, profile b-b'). However, ~4.5 km downstream, after the trunk stream and tributary merge, the resulting stream is confined within a canyon only ~1.3 km wide from canyon wall crest to canyon wall crest; the low-relief canyon floor area is only ~200 m in width (Figure 4.5, profile c-c'). In catchment 3, ~15 km west of the escarpment crest, the low-relief canyon floor area attains a width of ~3 km (Figure 4.6, profile b-b'), which decreases ~7.7 km downstream to ~0.4 km (Figure 4.6, profile c-c'). In catchment 4, the low-relief canyon floor area, although occupied by several tributary streams in addition to the trunk stream, attains a width of ~4.7 km at a distance of ~6 km from the escarpment crest; the canyon wall crest to wall crest distance is ~7.8 km (Figure 4.7, profile b-b'). This broad low-relief area extends downstream almost the entire length of the catchment, occasionally interrupted by isolated buttes which are the remnants of interfluves (Figure

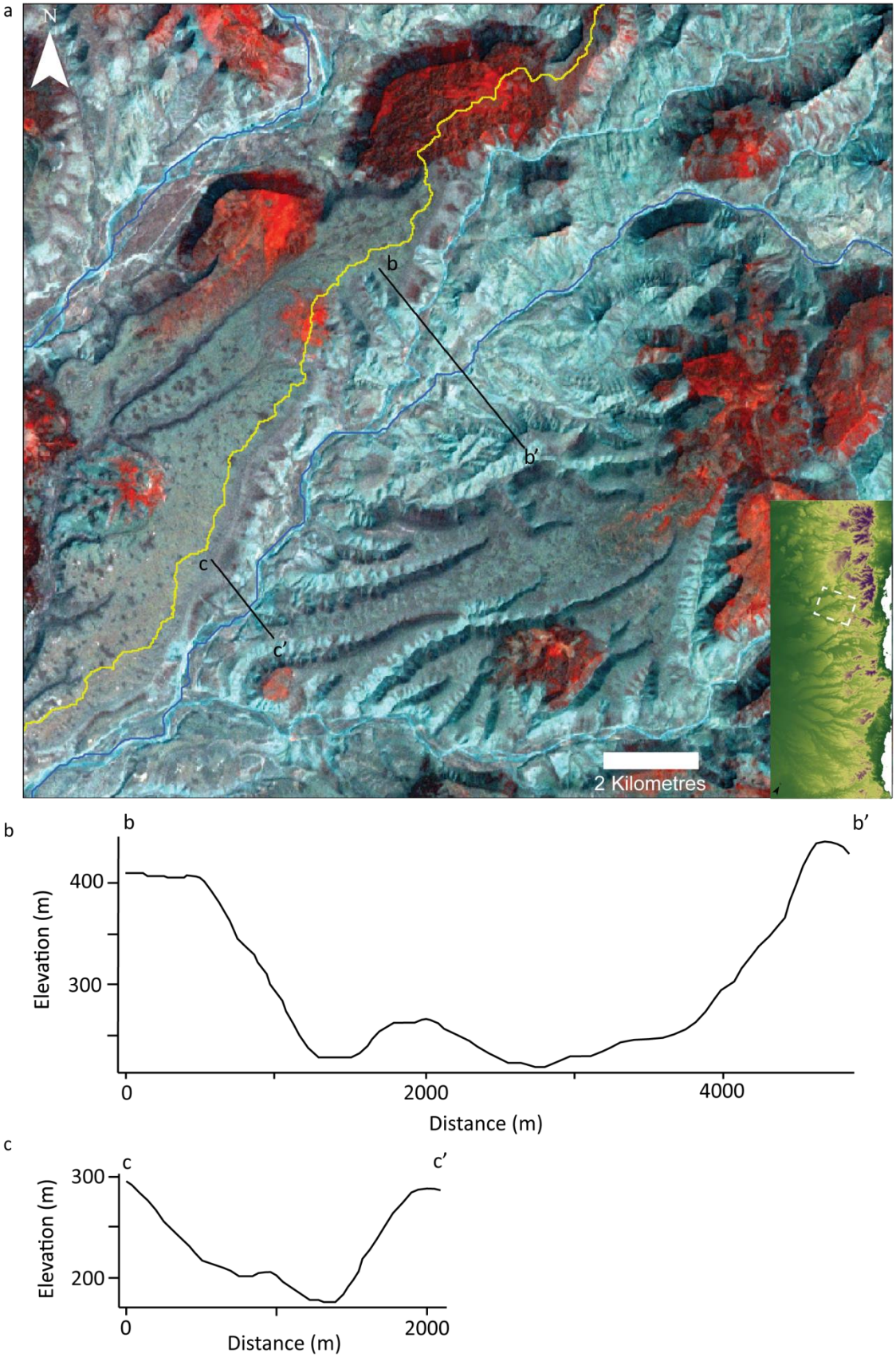

Figure 4.6: Catchment 3. a: *See Figure 4.5 caption.* ***b:*** *Topographic profile b-b'.* ***c:*** *Topographic profile c-c'.*

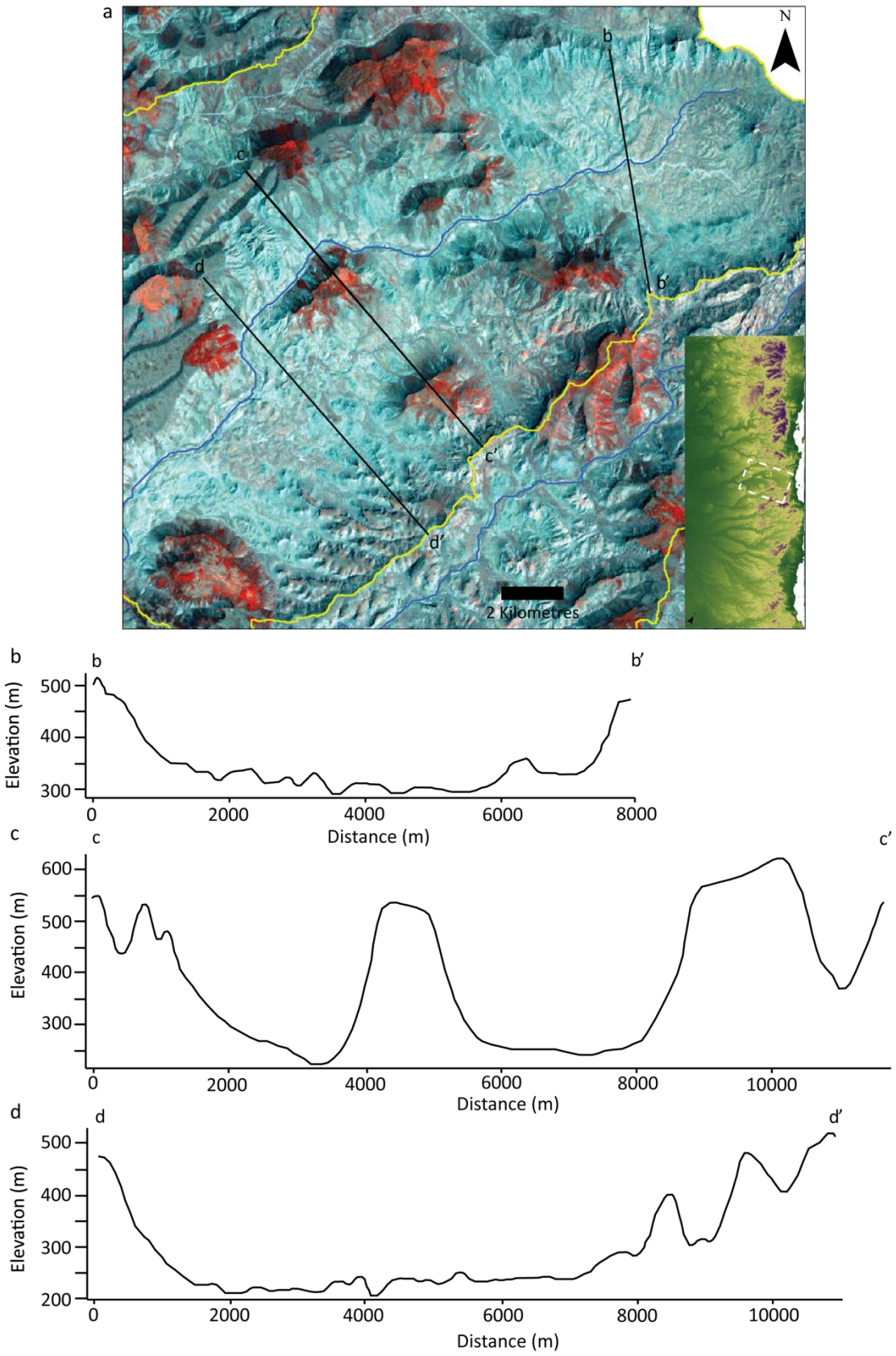

Figure 4.7: Catchment 4. a: *See Figure 4.5 caption.* ***b:*** *Topographic profile b-b'.* ***c:*** *Topographic profile c-c'.* ***d:*** *Topographic profile d-d'.*

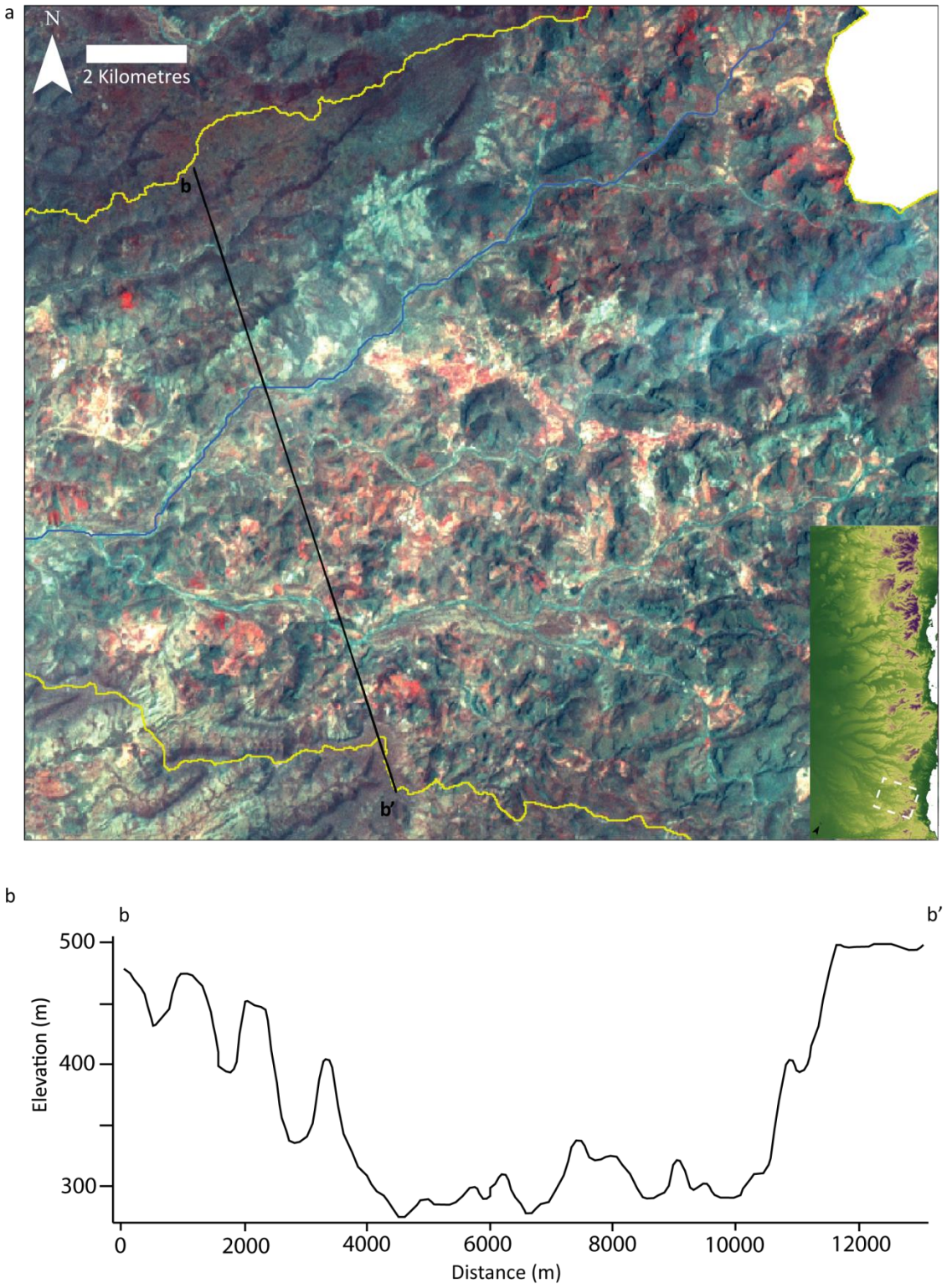

Figure 4.8: Catchment 10. a: *See Figure 4.5 caption.* ***b:*** *Topographic profile b-b'.*

4.7, profile c-c'). Approximately 17 km west of the escarpment crest, the low-relief canyon floor broadens to as wide as ~5.5 km; the canyon wall crest to wall crest distance is ~8.7 km (Figure 4.7,

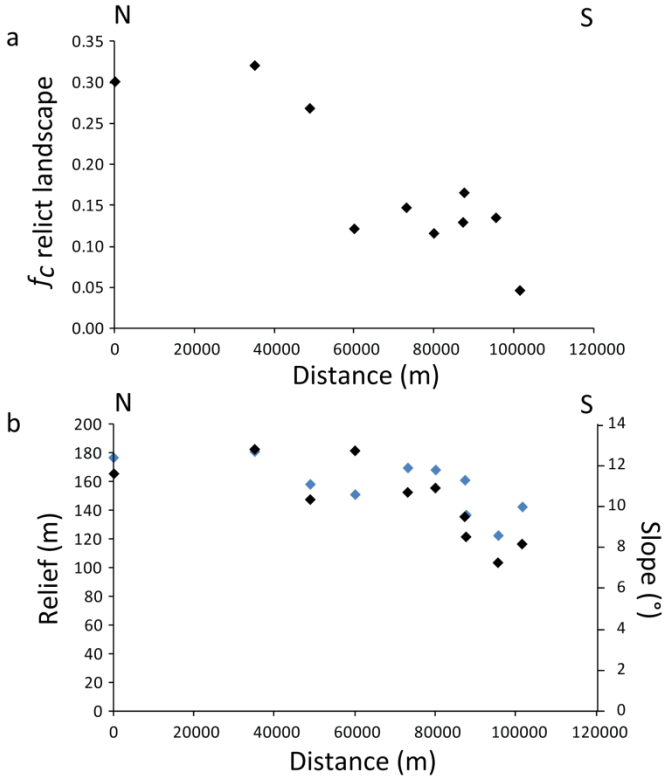

Figure 4.9: Catchment topographic metrics. a: *Fraction of each catchment (f_c) comprised of mesa-capping relict landscape; note that f_c decreases southward across the study area.* ***b:*** *Relief (black) and slope (blue); note that both decrease southward across the study area.*

profile d-d'). In catchment 10, the southernmost catchment area, major interfluves are virtually absent; ~12 km west of the escarpment crest, the low-relief canyon floor extends to a width of ~5.8 km (Figure 4.8, profile b-b').

Although interfluve destruction is observed across the study area, the extent to which it has occurred varies. Therefore, in order to determine the extent of the relict landscape remaining in each catchment, slope and relief maps were generated from a ~28 m horizontal resolution Advanced Spaceborne Thermal Emission and Reflection Radiometer (ASTER) digital elevation model (DEM), coupled with ~15 m resolution pan-sharpened multiband LANDSAT imagery (see Chapter 3). The proportion of each catchment which is comprised of mesa-capping relict landscape ranges from 5-32%. This reflects the fact that the degree of interfluve mesa destruction within each catchment increases from north to south across the study area (Figure 4.9). Interfluve destruction is also reflected in catchment mean slope and relief, calculated as described in Chapter 3. These also display a general decrease from north to south (Figure 4.9). Note that study area distances along strike are obtained by projecting canyon mouth locations onto a transect roughly parallel to the trend of the escarpment crest.

Figure 4.10: Study area LANDSAT. *False colour multi-band LANDSAT image comprising bands 1 (blue), 2 (green) and 7 (red); 15 m horizontal resolution. Eastern limit is escarpment crest, western limit is a line joining catchment mouths. Orange overlay indicates relict landscape areas composed of alluvial deposits; purple overlay indicates relict landscape areas composed of lava. Red lines indicate catchment areas, blue lines indicate trunk streams.*

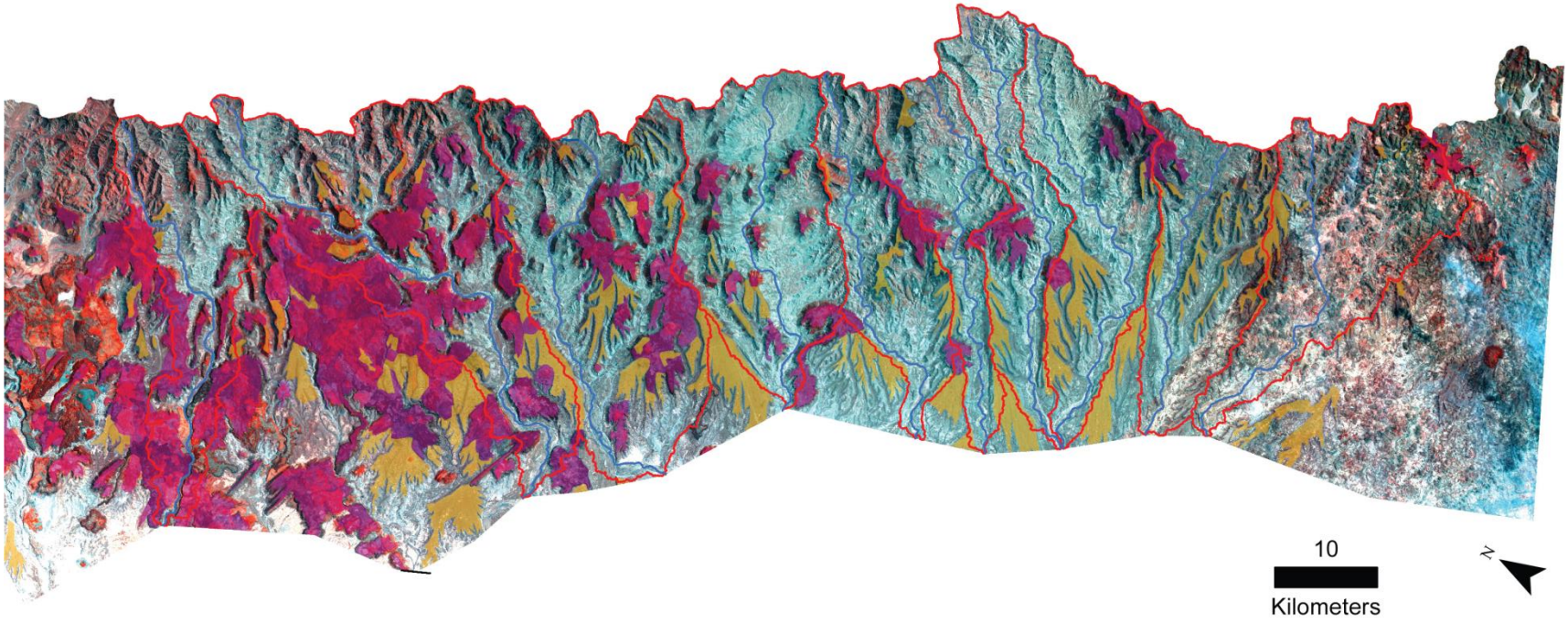

4.3.1 Evaluating the role of lithology in catchment development

The study area exhibits a systematic lithological variation; the abundance of post-subduction lavas, associated with the La Purísima volcanic field, decreases southward across the study area (Figure 4.10). As described in Chapter 3, these lavas emit strongly in the LANDSAT mid infra-red band 7, which can be exploited to map their extent. The proportion of the relict landscape in each catchment composed of lava decreases systematically from north to south within the study area from ~96% in the northernmost catchment to ~23-21% in the two southernmost catchments (Figure 4.11). The extent to which the study area catchments are armoured by resistant relict landscape lavas therefore appears to control the variation in catchment response to uplift.

To more fully characterise canyon response to uplift, and to facilitate comparisons between canyons, this study exploits the widely observed slope-area relationship

$$S = k_s A^{-\theta} \quad \text{(Equation 4.1)}$$

where S is channel slope; A is the contributing drainage area; and k_s and θ are the steepness and concavity indices (Flint, 1974). Both k_s and θ can be readily estimated from log-log plots of observed stream gradient and area; a linear regression to these data yields k_s from the y-axis intercept and θ from the negative slope of the regression. This relationship holds for bedrock rivers in steady-state dominated by fluvial processes; this is generally the case once contributing drainage areas exceed a critical area of ~10^6-10^7 m^2, at which point upper-reach debris-flow processes cease to dominate (Stock and Dietrich, 2003). Because k_s and θ covary, a normalised steepness index value, k_{sn}, is commonly obtained by substitution of a reference θ value, θ_{ref}. The advantage of k_{sn} indices is that they facilitate comparison between different channels or reaches with different contributing drainage areas. By convention, the θ_{ref} value used is 0.45, a reasonable mean value given that observed θ values can range from ~0.3-1.2, but are more typically found in the range ~0.3-0.6 (Whipple, 2004). In principle, however, θ_{ref} can be set to any value within this range. k_{sn} values therefore scale such that channels with higher k_{sn} exhibit steeper slopes, regardless of drainage area.

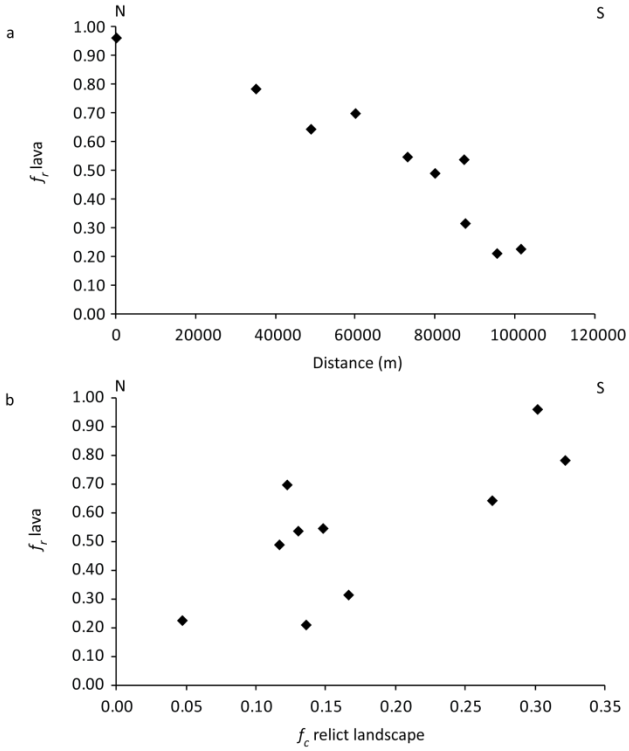

Figure 4.11: Relict landscape lava metrics. a: *Fraction of relict landscape within each catchment which is composed of lava (f_r); note that f_r decreases southward across the study area.* ***b:*** *Variation of f_r with f_c; note that the greater the proportion of relict landscape composed of lava within a catchment, the greater the proportion of relict landscape which is preserved within that catchment.*

Normalised channel steepness has been shown to be a function of uplift rate, substrate erosivity, and climate (e.g., Snyder et al., 2000; Duvall et al., 2004; Whipple, 2004; VanLaningham et al., 2006; Wobus et al., 2006; Whittaker et al., 2008). k_{sn} values were obtained from ~28 m resolution ASTER DEMs utilising the Stream Profiler extension for ArcMap and MatLab developed by Snyder et al. (2000) and Wobus et al. (2006). Use of this tool avoids generation of stream profiles exhibiting multiple stepped flat segments of zero slope which cannot be handled by log-log slope-area plots, a common problem with stream profiles derived directly from DEM raw pixel data due to elevation averaging associated with lower pixel resolution (Wobus et al., 2006). Instead, stream profiles are generated by sampling at equal vertical intervals – this study utilises a value of 20 m, the approximate vertical resolution of ASTER data – and then smoothed using a 280 m moving-window average, approximately ten times the ASTER pixel horizontal resolution. Slope-area data are then calculated both from the resulting smoothed profile, and by averaging the logarithm of unsmoothed slopes over log-bins in the drainage area. Comparison of slope-area data produced by these two methods permits detection of

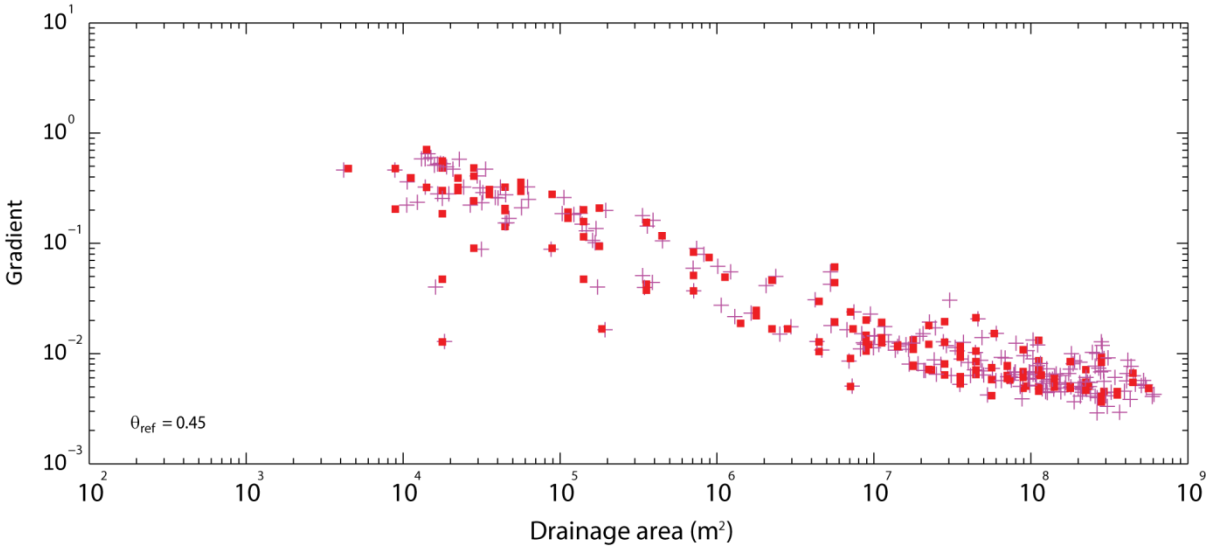

Figure 4.12: Slope-area values for all study area trunk streams. *Squares are slope-area data measured from DEM-derived stream profiles using the log-bin averaging method; crosses are data obtained using a 400 m smoothing window (Wobus et al., 2006).*

any systematic bias associated with each method; the use of a smoothing window will tend to reduce apparent steepness as the profile locally flattens, while log-bin averaging is susceptible to outliers (Wobus et al., 2006). Slope-area plot regression limits for calculation of k_{sn} utilising Equation 4.1 were set upstream at the location of the critical area threshold for fluvial process dominance (Figure 4.1), identified by the break in trend of slope-area data, and downstream at the canyon mouths, downstream from which alluvial processes dominate. As the rift flank streams lack knickpoints, each stream was analysed as a single segment within the identified regression limits. Values of k_{sn} obtained from the slope-area data (Figure 4.12) range from 39-17 $m^{0.9}$, and decrease from north to south within the study area (Figure 4.13); note that the units of k_{sn} arise from dimensional analysis of the slope-area relationship and are dependent on the value of θ_{ref} (Wobus et al., 2006). As previously discussed, k_{sn} values are thought to be dependent primarily on uplift rate and history, climate, and lithological variation. There are no climatic variations between study area catchments (Figure 4.1), and measured k_{sn} values show no relationship to surface uplift magnitude, as measured by canyon incision depth 10 km west of the escarpment crest (Figure 4.13). However, a

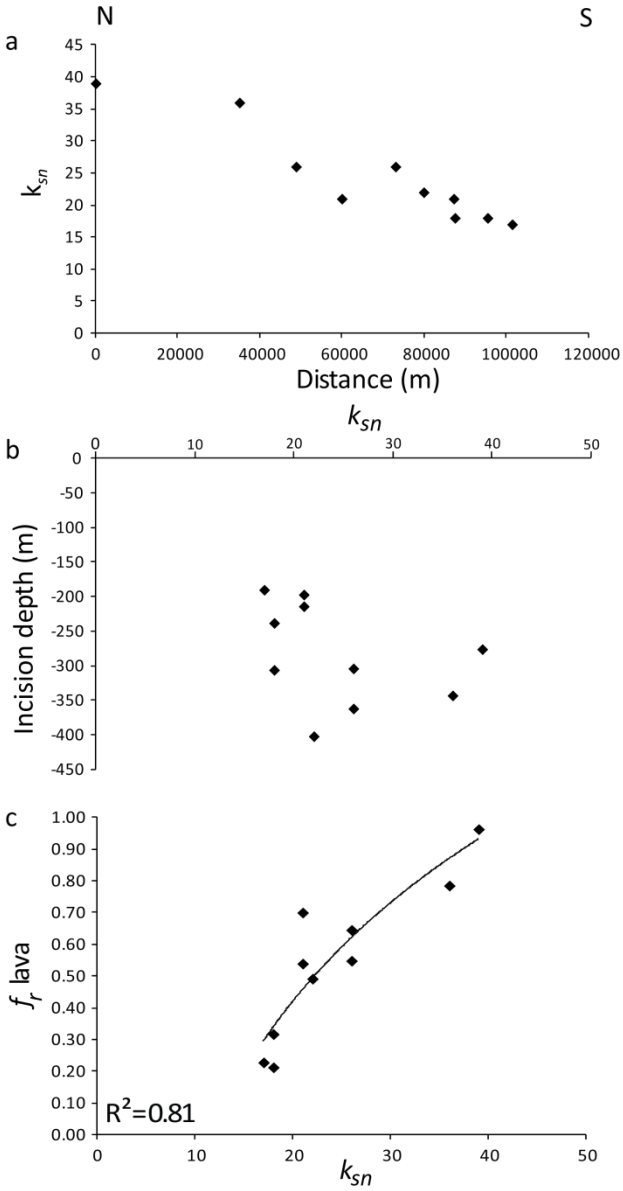

Figure 4.13: k_{sn} metrics. a: *Variation of k_{sn} across the study area.* ***b:*** *Variation of k_{sn} with spot incision depths for each catchment (see Figure 4.3); note that there is no relationship between k_{sn} and incision depth.* ***c:*** *Variation of f_r lava with k_{sn}.*

strong relationship (R^2 = 0.81) is observed between k_{sn} and the fraction of the relict landscape within each catchment composed of resistant lava (Figure 4.13).

4.4 Discussion

The observed variation of interfluve destruction across the study area indicates the response of the study area catchments to transient uplift and tilting. Because the fraction of each catchment armoured by resistant lava controls the extent of catchment adjustment, spatial substitution can be used to examine the manner in which catchment adjustment occurs. As shown in Figure 4.14, well-armoured catchments preserve extensive interfluve mesas capped by the pre-incision relict landscape. Less well armoured catchments, which have responded faster to uplift, exhibit greater interfluve degradation; this has produced lower-elevation ridge-like interfluves, which lack summit mesa surfaces, although these are discontinuously preserved on isolated buttes. In the least armoured catchment, catchment 10, the ridge-like interfluves have been further degraded to produce linear chains of low-relief hills across much of the catchment area. Thus although rift flank trunk streams exhibit profiles free of convexities, indicating they have adjusted to uplift, the ongoing process of

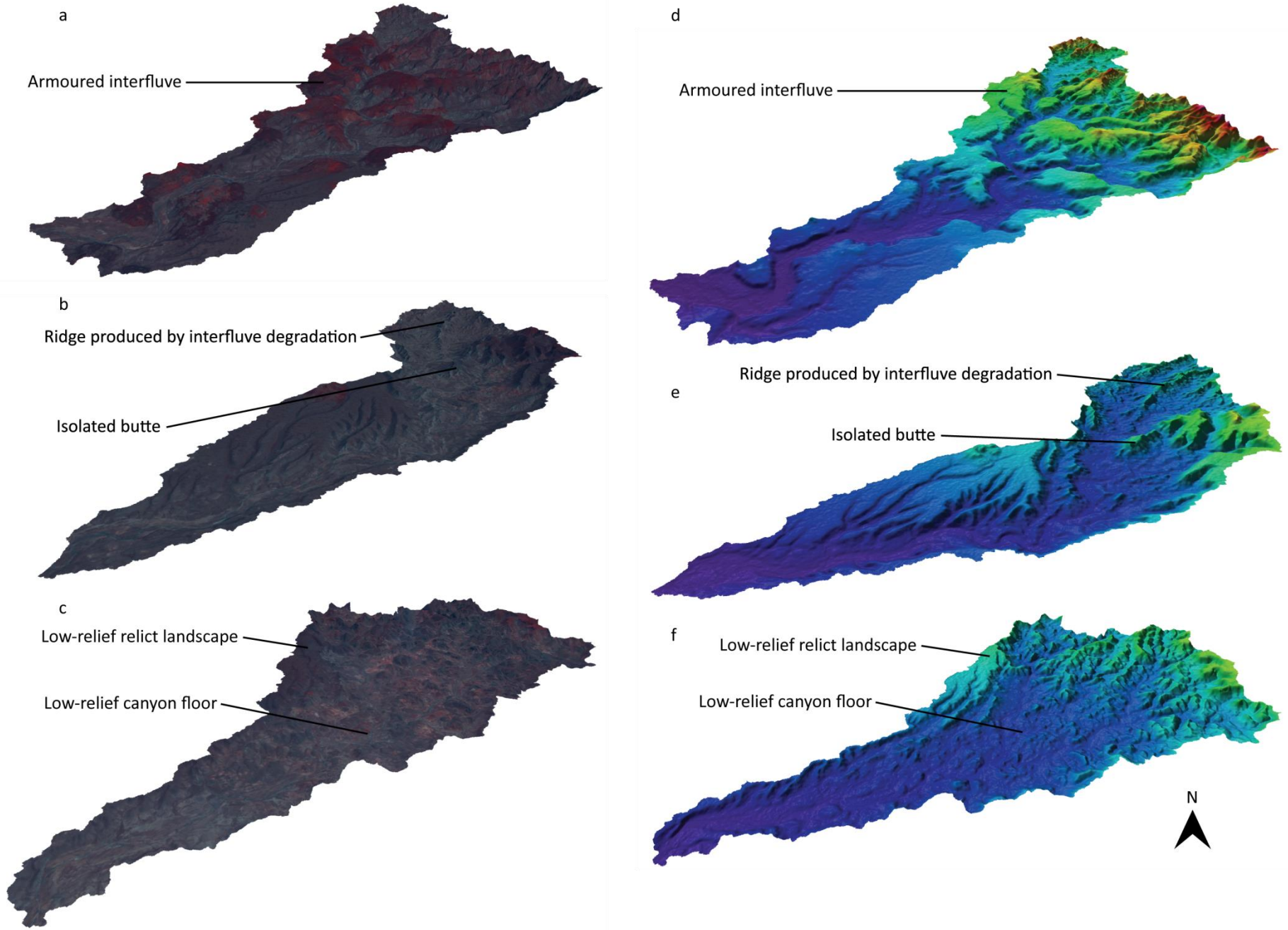
a
Armoured interfluve
b
Ridge produced by interfluve degradation
Isolated butte
c
Low-relief relict landscape
Low-relief canyon floor
d
Armoured interfluve
e
Ridge produced by interfluve degradation
Isolated butte
f
Low-relief relict landscape
Low-relief canyon floor
N

Figure 4.14 (Previous page): Oblique views of catchment topography. a-c: *False colour multi-band LANDSAT imagery (band 1, blue; band 2, green; band 7, red) draped over topography derived from ASTER DEM.* ***a:*** *Catchment 2.* ***b:*** *Catchment 8.* ***c:*** *Catchment 10.* ***d-f:*** *Topography derived from ASTER DEM.* ***d:*** *Catchment 2.* ***e:*** *Catchment 8.* ***f:*** *Catchment 10. No vertical exaggeration.*

interfluve mesa destruction indicates the catchments as a whole have yet to complete their adjustment. The current rift flank landscape is therefore transient; in the absence of further uplift, continuing interfluve destruction will generate a low-relief landscape. The rate at which this occurs is mediated by the extent to which catchments are armoured by resistant lava. Lithospheric unloading associated with rift flank erosion will provoke an isostatic response, but the relatively small scale of the incision suggests the additional relief formed by the resultant uplift and incision will be minor (Montgomery, 1994; Whipple et al., 1999).

The continued destruction of interfluves following degradation from mesas to narrow ridges is particularly striking. The ability of even the small catchments connecting the crests of these ridges to the canyon floors to degrade and remove the interfluve ridges suggests that this process may also have operated at the escarpment crest, where narrow headwalls separate west-draining rift flank canyons from the east-facing escarpment. At numerous locations along the escarpment, the removal of canyon headwalls has resulted in canyon beheading (Figure 4.1). The presence of beheaded streams – often termed wind gaps – atop the crests of uplifted fault or tilt blocks is commonly interpreted to indicate that the drainage atop the uplifted block was antecedent to the uplift, and that beheaded footwall streams originally drained areas which later subsided. This observation has been used in the Sierra Nevada to assign relative ages to surface uplift, as recorded by stream incision, and faulting (Wakabayashi and Sawyer, 2001; Schweickert, 2009). However, the development of the study area catchments suggests this technique may not be reliable. Here, small subordinate catchments, presumably debris-flow dominated, have destroyed canyon interfluve mesas and are thus also presumably capable of removing the narrow headwalls which form the interfluves between west-draining rift flank canyons and east-draining escarpment streams.

Independent dating of the timing of the rift flank canyon incision and escarpment development indicate that canyons formed synchronously with rift flank surface uplift and tilting, and thus do not represent a phase of incision antecedent to rift-related extensional faulting (Chapters 2 and 3).

The correlation of trunk stream normalised steepness with the fraction of the relict landscape armoured by resistant lava is unexpected. Although a considerable number of studies relate k_{sn} values to changes in stream bed lithology (e.g. Duvall et al., 2004; Jansen, 2006; VanLaningham et al., 2006; Goode and Wohl, 2010), the lithological variation exhibited by the study area directly affects not the stream bed, but the summits of the interfluve mesas. Intuitively, stream steepness should be independent of the susceptibility of interfluve summits to erosion; note that the studied trunk streams do not flow across interfluve surfaces. The correlation is not due to trunk canyons capturing areas which previously drained westwards across mesa summits. If interfluve destruction delivered additional drainage area to trunk streams, increasing stream power and facilitating incision, then trunk streams of catchments which exhibit greater interfluve loss should exhibit proportionally greater drainage area in their higher reaches, compared to catchments which have experienced less interfluve loss. However, as Figure 4.15 shows, this is not the case; the distance downstream at which the study area canyons attain the first, second and third quartile of their total drainage area varies considerably across the study area, but there is no tendency for the less armoured southern catchments to display proportionally greater drainage area in their upper reaches.

Instead, the observed relationship between k_{sn} values and the extent of catchment armouring may reflect processes of fluvial incision. Bedrock streams incise their beds by performing work on them, the efficiency of which depends fundamentally not only on the rate of clear water flow, but also on the availability of sediment. The relationship between sediment availability and incision is complex; entrained clasts promote incision, through tool effects of saltation impacts and abrasion, but also act to retard incision by transiently shielding bedrock surfaces as alluvial cover (Sklar and Dietrich, 2001; Sklar and Dietrich, 2006; Johnson and Whipple, 2010).

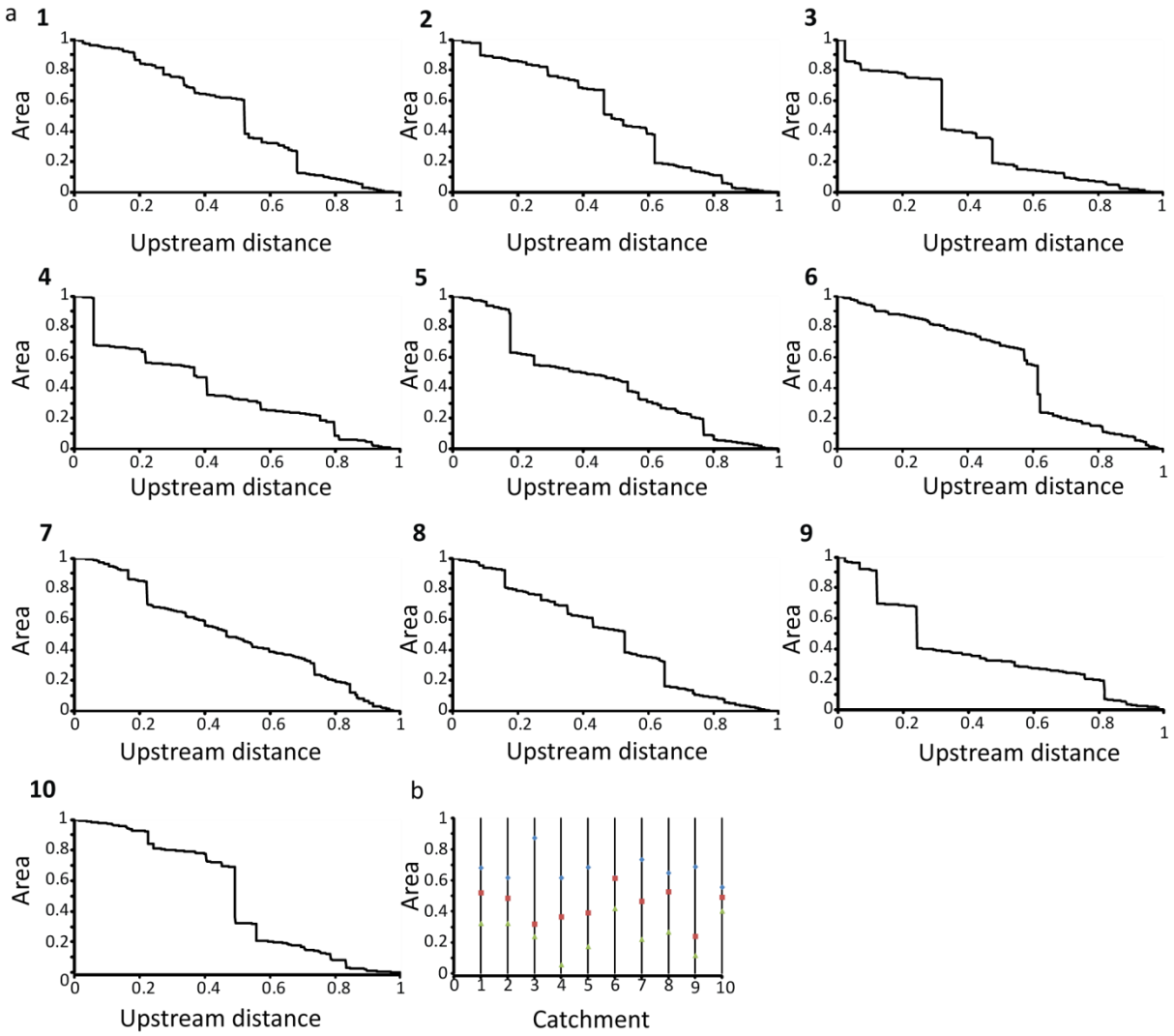

Figure 4.15: Normalised distance-area data for catchment trunk streams. a: *Distance-area plots for trunk streams of catchments 1-10.* ***b:*** *Normalised distances upstream from canyon mouths at which each trunk stream attains 25% (blue dot), 50% (red square), and 75% (green triangle) of its total drainage area.*

Because lava armouring controls the rate of interfluve destruction, it must also strongly modulate the rate of sediment supply to each trunk stream. The observed decrease in normalised steepness with greater interfluve destruction suggests that here, the incision-promoting tool effects dominate incision-retarding cover effects; enhanced incision rates permit faster reduction of stream slope. However, this statement is at variance with previous theoretical and field-based studies, which support variation of stream bed erosion rate as a broadly parabolic function of increasing sediment

supply (Sklar and Dietrich, 2006; Turowski et al., 2007; Johnson et al., 2009; Hobley et al., 2011). Such a relationship requires increasing dominance of cover effects with higher rates of sediment supply. Possibly the study area catchments fall on the ascending limb of this curve, where increasing rates of sediment supply lead to increased erosion rates but are insufficient to cause significant cover effects, but such a fortuitous arrangement seems unlikely. A speculative explanation is provided by an analogue modelling study conducted by Johnson and Whipple (2010), which investigated the effects of varying sediment and water fluxes on a flume uniformly lined with weak concrete. Following the early development of a more deeply incised channel along the flume centreline, increasing sediment fluxes generated the expected cover effect along the centreline channel. However, this was compensated by a widening of the zone of erosion beyond the active channel, in response to increased channel sedimentation. In this case, an increased sediment flux led to an overall increase in erosion rate across the flume surface, accompanied by a decrease in erosion of the channel due to sediment cover effects. A similar process is reported from a field study by Turowski et al. (2008), where lateral erosion rates of the channel walls of a bedrock river in Taiwan increased during transient alluviation of the channel bed during large flood events, which exposed the channel walls to enhanced erosion driven by tool effects. Similar processes may have influenced the catchments in this study; catchments less extensively armoured by lava would have experienced higher sediment fluxes as a result of faster interfluve destruction. The resultant alluviation of active channels could have promoted lateral incision, resulting in broader channels with more scope to expose bedrock and permit channel slope decrease. This process would, however, require alternating cycles of rapid alluviation and lateral incision followed by removal of sediment from the main channel to facilitate vertical incision, with the rate of sediment supply mediated by the extent of interfluve lava armouring. Evidence of the systematic variation in channel width implicit in this hypothesis could be provided by future field investigation.

4.5 Conclusions

This study has documented the spatial variation in catchment response to transient rift flank uplift in south-central Baja California, which forms part of the western margin of the Gulf of California rift. Uplift and tilting of the original low-relief study area surface has led to the incision of west-draining canyons. The trunk streams of these canyon networks exhibit smooth elevation profiles free from convexities, suggesting they have adjusted to uplift; this observation supports a model of rift flank tectonic quiescence since ~2.6 Ma, based on $^{40}Ar/^{39}Ar$ ages yielded by lavas situated on canyon floors at or near modern stream elevations (Chapter 3). However, ongoing destruction of canyon interfluve mesas suggests that the catchment response to uplift is incomplete; continued interfluve removal will eventually produce a new low-relief rift flank landscape. The process of interfluve degradation has already produced several kilometre-scale low-relief areas across the rift flank, bounded by persistent interfluve mesas; these low-relief areas are characterised by irregular topography, often consisting of linear ridges or chains of low hills which are the remnants of degraded interfluves. The summits of isolated buttes also discontinuously preserve fragments of the relict landscape. The extent of interfluve degradation varies systematically across the study area, concordantly with the fraction of the relict landscape within each catchment which is composed of resistant lava. This relationship strongly suggests that the rate of catchment adjustment by interfluve degradation is controlled by the extent to which the interfluve summits within each catchment are armoured by resistant lava. A more complex relationship between fluvial adjustment and interfluve erosivity is suggested by the strong correlation between trunk canyon normalised steepness and the extent of interfluve lava armouring. This may reflect variations in sediment supply between catchments; greater interfluve degradation provides higher sediment fluxes, which may facilitate incision by providing tools for saltation impacts and abrasion. However, further investigation is necessary to determine why higher sediment fluxes do not result in increased bedrock shielding.

4.6 References

Atwater, T., 1970, Implications of plate tectonics for the Cenozoic tectonic evolution of western North America: Geological Society of America Bulletin, v. 81, p. 3513–3536.

Axen, G., 1995, Extensional segmentation of the Main Gulf Escarpment, Mexico and United States: Geology, v. 23, no. 6, p. 515–518.

Bellon, H., Aguillon-Robles, A., Calmus, T., Maury, R.C., Bourgois, J., and Cotten, J., 2006, La Purisima volcanic field, Baja California Sur (Mexico): Miocene to Quaternary volcanism related to subduction and opening of an asthenospheric window: Journal of Volcanology and Geothermal Research, v. 152, p. 253 – 272.

Berlin, M.M., and Anderson, R.S., 2009, Steepened channels upstream of knickpoints: controls on relict landscape response: Journal of Geophysical Research, v. 114, DOI: 10.1029/2008JF001 148.

Buck, W.R., 1986, Small-scale convection induced by passive rifting: the cause for uplift of rift shoulders: Earth and Planetary Science Letters, v. 77, p. 362–372.

Busch, M.M., Arrowsmith, J.R., Umhoefer, P.J., Coyan, J. A., Maloney, S.J., and Gutierrez, G.M., 2011, Geometry and evolution of rift-margin, normal-fault-bounded basins from gravity and geology, La Paz-Los Cabos region, Baja California Sur, Mexico: Lithosphere, v. 3, no. 2, p. 110–127.

Clark, M.K., Maheo, G., Saleeby, J., and Farley, K.A., 2005, The non-equilibrium landscape of the southern Sierra Nevada, California: GSA Today, v. 15, no. 9, p. 4–10.

Densmore, A.L., Dawers, N.H., Gupta, S., Guidon, R., and Goldin, T., 2004, Footwall topographic development during continental extension: Journal of Geophysical Research, v. 109, DOI: 10.1029/2003JF000115.

Dixon, T., Farina, F., DeMets, C., and Suarez-Vidal, F., 2000, New kinematic models for Pacific-North America motion from 3 Ma to present, II: Evidence for a “Baja California shear zone” Geophysical Research Letters, v. 27, no. 23, p. 3961–3964.

Dorsey, R.J., and Umhoefer, P.J., 2000, Tectonic and eustatic controls on sequence stratigraphy of the Pliocene Loreto basin, Baja California Sur, Mexico: GSA Bulletin, v. 112, no. 2, p. 177–199.

Drake, W.R., 2005, Structural analysis, stratigraphy, and geochronology of the San Jose island accommodation zone, Baja California Sur, Mexico: MSc thesis, Northern Arizona University, US.

Duvall, A., Kirby, E., and Burbank, D., 2004, Tectonic and lithologic controls on bedrock channel profiles and processes in coastal California: Journal of Geophysical Research, v. 109.

Flint, J.J., 1974, Stream gradient as a function of order, magnitude, and discharge: Water Resources Research, v. 10, no. 5, p. 969–973.

Goode, J.R., and Wohl, E., 2010, Substrate controls on the longitudinal profile of bedrock channels: Implications for reach-scale roughness: Journal of Geophysical Research, v. 115, DOI: 10.1029/ 2008JF001188.

Hastings, J.R., and Turner, R.M., 1965, Seasonal precipitation regimes in Baja California Mexico: Geografiska Annaler, v. 47A, no. 4, p. 204–223.

Hausback, B., 1984, Cenozoic volcanic and tectonic evolution of Baja California Sur, Mexico, *in* Frizzell, V. ed., Geology of the Baja California Peninsula, Pacific Section SEPM, p. 219–236.

Hobley, D.E.J., Sinclair, H.D., Mudd, S.M., and Cowie, P.A., 2011, Field calibration of sediment flux dependent river incision: Journal of Geophysical Research, v. 116, DOI: 10.1029/2010JF001935.

Holmgren, C.A., Betancourt, J.L., and Rylander, K.A., 2011, Vegetation history along the eastern, desert escarpment of the Sierra San Pedro Mártir, Baja California, Mexico: Quaternary Research, v. 75, no. 3, p. 647–657.

Huismans, R., Podladchikov, Y.Y., and Cloetingh, S., 2001, Transition from passive to active rifting: relative importance of asthenospheric doming and passive extension of the lithosphere: Journal of Geophysical Research, v. 106, no. B6, p. 11,271–11,291.

Jansen, J.D., 2006, Flood magnitude–frequency and lithologic control on bedrock river incision in post-orogenic terrain: Geomorphology, v. 82, no. 1-2, p. 39–57.

Johnson, J.P.L., and Whipple, K.X., 2010, Evaluating the controls of shear stress, sediment supply, alluvial cover, and channel morphology on experimental bedrock incision rate: Journal of Geophysical Research, v. 115, DOI: 10.1029/2009JF001335.

Johnson, J.P.L., Whipple, K.X., Sklar, L.S., and Hanks, T.C., 2009, Transport slopes, sediment cover, and bedrock channel incision in the Henry Mountains, Utah: Journal of Geophysical Research, v. 114, DOI: 10.1029/2007JF000862.

Leroy, M., Gueydan, F., and Dauteuil, O., 2008, Uplift and strength evolution of passive margins inferred from 2-D conductive modelling: Geophysical Journal International, v. 172, no. 1, p. 464–476.

Lizarralde, D., Axen, G.J., Brown, H.E., Fletcher, J.M., González-Fernández, A., Harding, A.J., Holbrook, W.S., Kent, G.M., Paramo, P., Sutherland, F., and Umhoefer, P.J., 2007, Variation in styles of rifting in the Gulf of California: Nature, v. 448, p. 466–469.

Mayer, L., 1999, Active tectonics of the Loreto area, Baja California Sur, Mexico: Geomorphology, v. 27, no. 3-4, p. 243–255.

McLean, H., Hausback, B., and Knapp, J., 1987, The geology of west central Baja California Sur Mexico: USGS Bulletin 1579.

Montgomery, D.R., 1994, Valley incision and the uplift of mountain peaks: Journal of Geophysical Research, v. 99, no. B7, p. 13913–13921.

Ortlieb, L., 1991, Quaternary Vertical Movements Along the Coasts of Baja California and Sonora, *in* Dauphin, J.P. and Simoneit, B.T. eds., The Gulf and Peninsular Province of the Californias, American Association of Petroleum Geologists, Memoir 47, p. 447–480.

Oskin, M.E., and Burbank, D., 2007, Transient landscape evolution of basement-cored uplifts: Example of the Kyrgyz Range, Tian Shan: Journal of Geophysical Research, v. 112, DOI: 10.1029/2006JF000563.

Ouimet, W.B., Whipple, K.X., and Granger, D.E., 2009, Beyond threshold hillslopes: channel adjustment to base-level fall in tectonically active mountain ranges: Geology, v. 37, no. 7, p. 579–582.

Peryam, T.C., Dorsey, R.J., and Bindeman, I., 2011, Plio-Pleistocene climate change and timing of Peninsular Ranges uplift in southern California: Evidence from paleosols and stable isotopes in the Fish Creek–Vallecito basin: Palaeogeography, Palaeoclimatology, Palaeoecology, v. 305, no. 1-4, p. 65–74.

Plattner, C., Malservisi, R., and Govers, R., 2009, On the plate boundary forces that drive and resist Baja California motion: Geology, v.37, no. 4, p. 359-362.

Ryan, W.B.F., Carbotte, S.M., Coplan, J.O., O'Hara, S., Melkonian, A., Arko, R., Weissel, R.A., Ferrini, V., Goodwillie, A., Nitsche, F., Bonczkowski, J., and Zemsky, R., 2009, Global Multi-Resolution Topography synthesis: Geochemistry Geophysics Geosystems, v. 10, no. 3, DOI: 10.1029/2008 GC002332.

Sawlan, M.G., 1991, Magmatic evolution of the Gulf of California rift, *in* Dauphin, J. and Simoneit, B. eds., The Gulf and Peninsular Province of the Californias, American Association of Petroleum Geologists, p. 301–369.

Sawlan, M.G., and Smith, J.G., 1984, Petrological characteristics, age, and tectonic setting of Neogene volcanic rocks in northern Baja California Sur, Mexico, *in* Frizzel, V.A. ed., Geology of the Baja California Peninsula, Pacific Section, Society of Economic Paleontologists and Mineralogists, p. 237–251.

Schweickert, R., 2009, Beheaded west-flowing drainages in the Lake Tahoe region, northern Sierra Nevada: implications for timing and rates of normal faulting, landscape evolution and mechanism of Sierran uplift: International Geology Review, v. 51, no. 9, p. 994–1033.

Sklar, L.S., and Dietrich, W.E., 2001, Sediment and rock strength controls on river incision into bedrock: Geology, v. 29, no. 12, p. 1087–1090.

Sklar, L.S., and Dietrich, W.E., 2006, The role of sediment in controlling steady-state bedrock channel slope: Implications of the saltation–abrasion incision model: Geomorphology, v. 82, p. 58–83.

Snyder, N.P., Whipple, K.X., Tucker, G.E., and Merritts, D.J., 2000, Landscape response to tectonic forcing: Digital elevation model analysis of stream profiles in the Mendocino triple junction region, northern California: GSA, v. 112, no. 8, p. 1250–1263.

Stock, J., and Dietrich, W.E., 2003, Valley incision by debris flows: Evidence of a topographic signature: Water Resources Research, v. 39, no. 4, DOI: 10.1029/2001WR001057.

Stock, J.M., and Hodges, K.V., 1989, Pre-Pliocene extension around the Gulf of California and the transfer of Baja California to the Pacific Plate: Tectonics, v. 8, no. 1, p. 99–115.

Tucker, G.E., 2009, Natural experiments in landscape evolution: Earth Surface Processes and Landforms, v. 34, p. 1450–1460.

Turowski, J.M., Hovius, N., Meng-Long, H., Lague, D., and Men-Chiang, C., 2008, Distribution of erosion across bedrock channels: Earth Surface Processes and Landforms, v. 33, p. 353–363.

Turowski, J.M., Lague, D., and Hovius, N., 2007, Cover effect in bedrock abrasion: A new derivation and its implications for the modeling of bedrock channel morphology: Journal of Geophysical Research, v. 112, DOI: 10.1029/2006JF000697.

Umhoefer, P.J., Dorsey, R.J., Willsey, S., Mayer, L., and Renne, P., 2001, Stratigraphy and geochronology of the Comondú Group near Loreto, Baja California Sur, Mexico: Sedimentary Geology, v. 144, p. 125–147.

Umhoefer, P.J., Mayer, L., and Dorsey, R.J., 2002, Evolution of the margin of the Gulf of California near Loreto, Baja California Peninsula, Mexico: GSA Bulletin, v. 114, no. 7, p. 849–868.

Umhoefer, P.J., Schwennicke, T., Margo, T.D., Ruiz-Geraldo, G., Ingle, J.C., and McIntosh, W., 2007, Transtensional fault-termination basins: an important basin type illustrated by the Pliocene San Jose Island basin and related basins in the southern Gulf of California, Mexico: Basin Research, v.19, p. 297–322.

VanLaningham, S., Meigs, A., and Goldfinger, C., 2006, The effects of rock uplift and rock resistance on river morphology in a subduction zone forearc, Oregon, USA: Earth Surface Processes and Landforms, v. 31, no. 10, p. 1257–1279.

Wakabayashi, J., and Sawyer, T.L., 2001, Stream Incision , Tectonics , Uplift , and Evolution of Topography of the Sierra Nevada , California: The Journal of Geology, v. 109, p. 539–562.

Walsh, L.S., Martin, A.J., Ojha, T.P., and Fedenczuk, T., 2012, Correlations of fluvial knickzones with landslide dams, lithologic contacts, and faults in the southwestern Annapurna Range, central Nepalese Himalaya: Journal of Geophysical Research, v. 117, DOI: 10.1029/2011JF001984.

Whipple, K.X., 2004, Bedrock Rivers and the Geomorphology of Active Orogens: Annual Review of Earth and Planetary Sciences, v. 32, p. 151–185.

Whipple, K.X., Kirby, E., and Brocklehurst, S.H., 1999, Geomorphic limits to climate-induced increases in topographic relief: Nature, v. 401, p. 39–43.

Whipple, K.X., and Tucker, G.E., 1999, Dynamics of the stream-power incision model: implications for height limits of mountain ranges, landscape response timescales, and research needs: Journal of Geophysical Research, v. 104, no. B8, p. 17661–17674.

Whittaker, A.C., 2012, How do landscapes record tectonics and climate? Lithosphere, v. 4, no. 2, p. 160–164.

Whittaker, A.C., Cowie, P.A., Tucker, G.E., and Roberts, G., 2008, Decoding temporal and spatial patterns of fault uplift using transient river long profiles: Geomorphology, v. 100, p. 506 – 526.

Wobus, C.W., Tucker, G.E., and Anderson, R.S., 2010, Does climate change create distinctive patterns of landscape incision? Journal of Geophysical Research, v. 115, no. F4, DOI: 10.1029/2009JF001562.

Wobus, C.W., Whipple, K.X., Kirby, E., Snyder, N.P., Johnson, J., Spyropolou, K., Crosby, B., and Sheehan, D., 2006, Tectonics from topography: procedures, promises, and pitfalls, *in* Willett, S.D., Hovius, N., Brandon, M.T., and Fisher, D.M. eds., Tectonics, Climate, and Landscape Evolution, GSA Special Paper 398, p. 55–74.

5. Conclusions and future work

“What I’ve felt, what I’ve known, turn the pages, turn the stone”

Metallica, *Unforgiven II.*

5.1 Conclusions

At the Loreto fault, low-temperature thermochronometers indicate that ~1.5 km of rift-related footwall exhumation occurred at ~8-6 Ma, causing resetting of AHe ages and resulting in the development of a low-elevation basement piedmont west of the fault. The timing of this exhumation is corroborated by the presence of a lava yielding an $^{40}Ar/^{39}Ar$ age of ~5.7 Ma which overlays the piedmont. However, piedmont exhumation was insufficient to reset AFT ages, which reflect either Late Cretaceous post-emplacement cooling or Early Miocene reheating. Stratigraphic evidence that the piedmont basement was situated close to the surface in the Early Miocene suggests this reheating was likely due to hydrothermal processes. The episode of piedmont exhumation at ~8-6 Ma records westward erosional retreat of the escarpment, driven by slip on the Loreto fault. The onset of significant extension at Loreto at ~8-6 Ma thus post-dates the cessation of Pacific/Farallon spreading offshore at ~12.5-11.5 Ma by ~6.5-3.5 Ma, consistent with the delay in the onset of extension reported by Seiler et al. (2011) from northern Baja California. A delay in the onset of crustal extension after foundering of the Farallon plate may be characteristic of the eastern margin of Baja California, as suggested by Seiler et al. (2011).

On the rift flank west of the Loreto rift segment, widespread deposition of volcaniclastic sediment shed from the Comondú subduction arc ceased at ~15 Ma, synchronously with the cessation of subduction west of Baja California between ~15-13 Ma. Subsequently, a low relief landscape developed, composed of thin alluvial deposits interfingered with discontinuous lava flows. Dating of these lavas using the $^{40}Ar/^{39}Ar$ technique reveal that this landscape persisted until ~6.2-5.6 Ma, when the incision of west-draining canyons began. Canyon incision continued until ~2.6 Ma, but was largely complete by ~3.2 Ma. Synchroneity of the surface uplift and westward tilting recorded by this incision with the timing of onset of significant extension on the Loreto fault indicates that the driving

mechanism for rift flank uplift was the flexurally distributed isostatic response to crustal thinning and lithospheric rupture in the southern Gulf of California. Simple two-dimensional flexural modelling indicates that this mechanism is sufficient to explain the observed uplift; there is no need to invoke additional mechanisms.

The transient uplift experienced by the rift flank as a result of lithospheric unloading is reflected in the development of the west-draining rift flank canyons. Although the trunk streams of these canyon networks exhibit smooth, concave-up elevation profiles, suggesting they have adjusted to uplift, the interfluves between the canyons exhibit a variety of morphologies. These record a process of progressive interfluve degradation from flat-topped mesas capped by relics of the pre-incision landscape, to linear ridges, and ultimately to chains of low hills and widespread kilometre-scale low-relief canyon floors. The extent of interfluve destruction decreases from north to south across the rift flank study area, and is likely controlled by the extent of post-subduction lavas which discontinuously cap the interfluve mesas and resist erosion.

5.2 Future work

Despite widespread recognition of the value of the Gulf of California as a natural laboratory to investigate processes of continental rifting and passive margin development (e.g. Moore and Buffington, 1968; Lizarralde et al., 2007; Seiler et al., 2011; Umhoefer, 2011), the development mechanisms and age of many of the major landscape features around the Gulf remain unclear. In particular, three key questions can be identified which require future study:

· *Was flooding of the Gulf of California controlled by rift flank development?*

In contrast to the sediment-starved southern Gulf of California, the area of the Gulf north of Isla Tiburon and Isla Angel de la Guarda has been plentifully supplied with sediment due to capture of the Colorado River by the Gulf rift at ~5.3 Ma (Moore, 1973; Dorsey et al., 2007; Dorsey, 2010). This

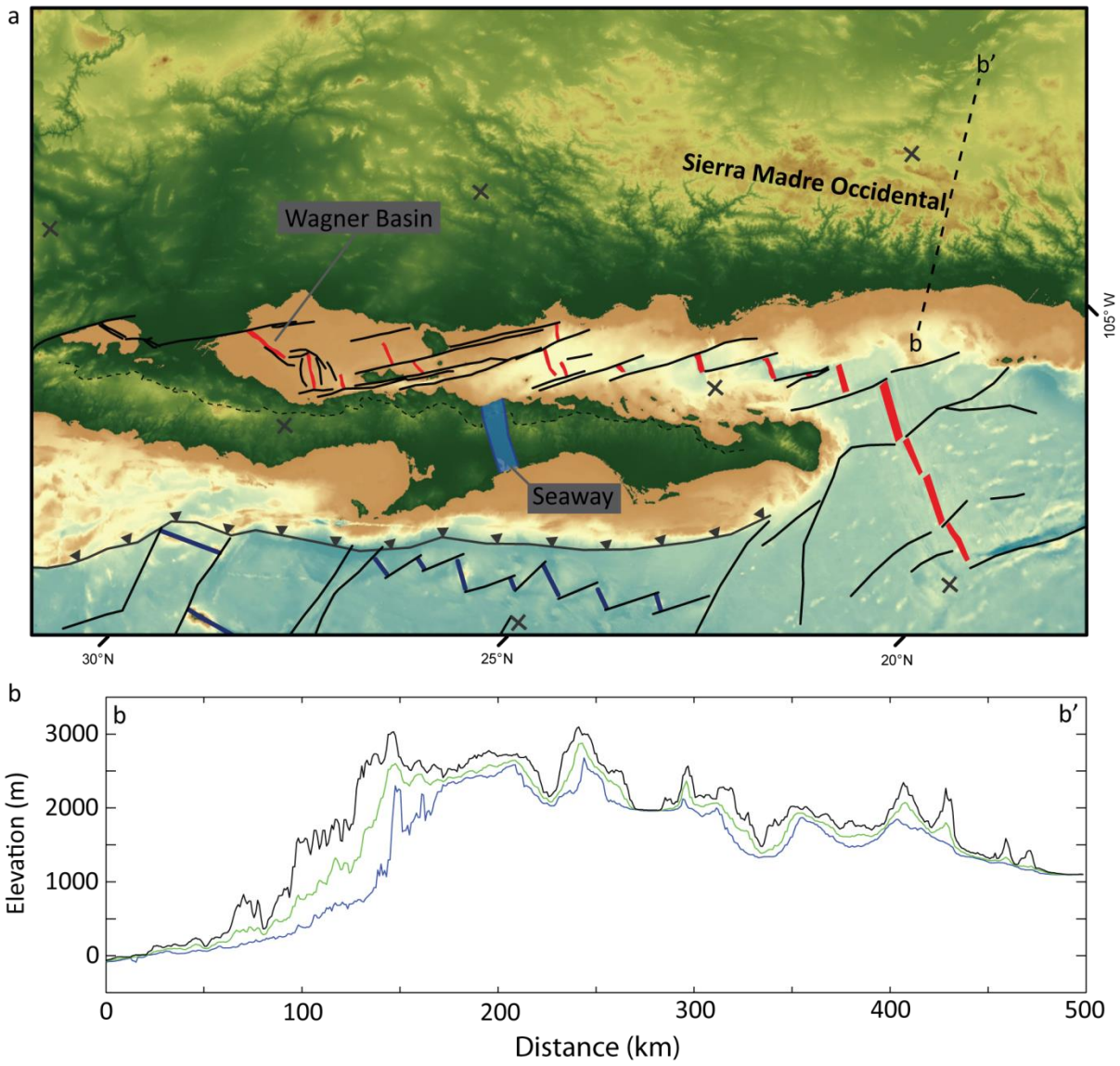

Figure 5.1: Future work locations. a: *Overview of Gulf of California topography and bathymetry, from ASTER and GMRT data, respectively (Ryan et al., 2009). Showing major structures (solid black lines), abandoned (blue lines) and active (red lines) spreading centres, and Baja California escarpment (dotted black line). Locations of Wagner basin, proposed Mid-Miocene seaway at San Ignacio (Helenes and Carreño, 1999), and Sierra Madre Occidental are shown.* ***b:*** *Topographic profile from a 10 km wide swath centred on* ***b-b'****; maximum (black), mean (green), and minimum (blue) topography shown.*

sediment has filled the rift basins of the northern Gulf to depths of up to ~6 km (Helenes et al., 2009). However, micropalaeontological analysis of sediments recovered from the base of a ~5.4 km

deep exploratory well in the Wagner basin suggests that marine conditions may have existed in the northern Gulf as early as the Middle Miocene, prior to ~11.6 Ma (Helenes and Carreño, 1999; Helenes et al., 2009). This is controversial, because significant rift-related extension around the northern Gulf is not thought to have begun earlier than ~9-7 Ma (Seiler et al., 2011), and the Gulf is not thought to have flooded until ~6 Ma (Oskin and Stock, 2003), shortly prior to the onset of oceanic spreading in the southern Gulf at ~6-3 Ma (Lizarralde et al., 2007). In the absence of a Middle Miocene connection to the Pacific Ocean via the southern Gulf, flooding of the northern Gulf is proposed to have occurred via a marine seaway which cut across the central Baja California Peninsula approximately at the latitude of the well-documented Late Miocene Santa Rosalía basin (Helenes et al., 1999). This area is characterised by west-draining rift flank canyons and post-subduction lavas similar to those west of Loreto (Sawlan and Smith, 1984; Sawlan, 1991), permitting a test of the seaway hypothesis by analysis of the timing of rift flank uplift.

· *When did uplift of the Sierra Madre Occidental occur?*

The eastern margin of the Gulf of California does not exhibit a tilted rift flank similar to that which characterises the western margin. Instead, the eastern margin is bounded by the non-extended Sierra Madre Occidental, which forms a low-relief plateau ~500 km in length, typically attaining elevations of ~2500 m asl. The plateau forms the core of the larger Sierra Madre Occidental ignimbrite province, the world's largest silicic ignimbrite province, which was largely erupted between ~32-23 Ma and has subsequently been partially tectonically dissected by Basin and Range faulting occurring from ~30 to as late as ~12 Ma, and by faulting related to the Gulf since ~10 Ma (Nieto-Samaniego et al., 1999; Henry and Aranda-Gomez, 2000; Aguirre-Díaz and Labarthe-Hernández, 2003). However, the timing and mechanism of plateau surface uplift is unknown; proposed mechanisms include the emplacement of the source batholith for the ignimbrites, or an Early Miocene slab detachment event affecting part of the subducting Farallon plate (Ferrari et al., 2002). The western margin of the Sierra Madre Occidental plateau has been incised by prominent

canyons which drain to the Gulf of California and attain depths of ~1.5-2 km below the plateau surface (Montgomery and Lopez-Blanco, 2003). Such incision depths make these canyons a plausible target for a study utilising low-temperature thermochronometers. These could be used to reconstruct the timing of incision, which would provide a minimum age for the timing of plateau uplift.

· *Why was there no surface response to slab detachment?*

This study has examined the possibility that surface uplift in southern Baja California was driven by asthenospheric upwelling through a proposed slab window, which opened as the subducting Farallon slab detached from the stalled Magdalena ridge (Ferrari et al., 2002; Fletcher et al., 2007; Castillo, 2008). The results of this study show that the timing of uplift is inconsistent with this model. However, several numerical models of slab detachment indicate that surface uplift is also expected as a result of the loss of slab pull which occurs during slab detachment (Gvirtzman and Nur, 1999; Buiter et al., 2002; Burkett and Billen, 2010). Estimates of the likely scale and distribution of detachment-driven uplift vary. Numerical modelling by Buiter et al. (2002) suggests uplift of 2-6 km with a width of ~300 km; in contrast, Burkett and Billen (2010) propose uplift of similar magnitude, but limited to the trench, which is eliminated as a topographic feature. However, there is no evidence for uplift of Baja California at the likely time of slab detachment, inferred to be ~15-13 Ma based on the clockwise rotation of spreading centres recorded by magnetic lineations (Lonsdale, 1991; Tian et al., 2011). It is unclear why the proposed slab detachment did not generate the expected surface uplift; perhaps the slab fragment identified beneath the southern Baja California Peninsula by Zhang et al. (2009) and Zhang and Paulssen (2012) indicates that the detachment depth beneath the southern Gulf was deep enough to preclude the expected surface uplift response. In this context, the higher elevations of the Sierra San Pedro Martír and the Sierra Juarez in northern Baja California, at latitudes where the Farallon spreading ridge was subducted, are particularly significant: could shallow slab detachment beneath northern Baja California have contributed to

greater uplift than observed in southern Baja California, where detachment was deeper? Further field study of the timing of rift flank uplift in the northern Gulf may resolve this question, and could provide new insights into the subduction dynamics of the region.

5.3 References

Aguirre-Díaz, G.J., and Labarthe-Hernández, G., 2003, Fissure ignimbrites: Fissure-source origin for voluminous ignimbrites of the Sierra Madre Occidental and its relationship with Basin and Range faulting: Geology, v. 31, no. 9, p. 773.

Buiter, S.J.H., Govers, R., and Wortel, M.J.R., 2002, Two-dimensional simulations of surface deformation caused by slab detachment: Tectonophysics, v. 354, no. 3-4, p. 195–210.

Burkett, E.R., and Billen, M.I., 2010, Three-dimensionality of slab detachment due to ridge-trench collision: Laterally simultaneous boudinage versus tear propagation: Geochemistry Geophysics Geosystems, v. 11, no. 11, DOI: 10.1029/2010GC003286.

Castillo, P.R., 2008, Origin of the adakite-high-Nb basalt association and its implications for postsubduction magmatism in Baja California, Mexico: Geological Society of America Bulletin, v. 120, no. 3-4, p. 451–462.

Dorsey, R.J., 2010, Sedimentation and crustal recycling along an active oblique-rift margin: Salton Trough and northern Gulf of California: Geology, v. 38, no. 5, p. 443–446.

Dorsey, R.J., Fluette, A., McDougall, K., Housen, B.A., Janecke, S.U., Axen, G.J., and Shirvell, C.R., 2007, Chronology of Miocene – Pliocene deposits at Split Mountain Gorge , Southern California: A record of regional tectonics and Colorado River evolution: Geology, v. 35, p. 57–60.

Ferrari, L., Lopez-Martinez, M., and Rosas-Elguera, J., 2002, Ignimbrite flare-up and deformation in the southern Sierra Madre Occidental, western Mexico: Implications for the late subduction history of the Farallon plate: Tectonics, v. 21, no. 4, DOI: 10.1029/2001TC001302.

Fletcher, J.M., Grove, M., Kimbrough, D., Lovera, O., and Gehrels, G.E., 2007, Ridge-trench interactions and the Neogene tectonic evolution of the Magdalena shelf and southern Gulf of California: Insights from detrital zircon U-Pb ages from the Magdalena fan and adjacent areas: GSA Bulletin, v. 119, no. 11-12, p. 1313–1336.

Gvirtzman, Z., and Nur, A., 1999, Plate detachment, asthenosphere upwelling, and topography across subduction zones: Geology, v. 27, p. 563–566.

Helenes, J., and Carreño, A.L., 1999, Neogene sedimentary evolution of Baja California in relation to regional tectonics: Journal of South American Earth Sciences, v. 12, p. 598–605.

Helenes, J., Carreño, A.L., and Carrillo, R.M., 2009, Middle to late Miocene chronostratigraphy and development of the northern Gulf of California: Marine Micropaleontology, v. 72, p. 10–25.

Henry, C.D., and Aranda-Gomez, J.J., 2000, Plate interactions control middle – late Miocene, proto-Gulf and Basin and Range extension in the southern Basin and Range: Tectonophysics, v. 318, p. 1–26.

Lizarralde, D., Axen, G.J., Brown, H.E., Fletcher, J.M., González-Fernández, A., Harding, A.J., Holbrook, W.S., Kent, G.M., Paramo, P., Sutherland, F., and Umhoefer, P.J., 2007, Variation in styles of rifting in the Gulf of California: Nature, v. 448, p. 466–469.

Lonsdale, P.F., 1991, Structural patterns of the Pacific floor offshore of Peninsular California, *in* Dauphin, J.P. and Simoneit, R.T. eds., The Gulf and Peninsular Province of the Californias, AAPG Memoir 47, p. 87–125.

Montgomery, D.R., and Lopez-Blanco, J., 2003, Post-Oligocene river incision, southern Sierra Madre Occidental, Mexico: Geomorphology, v. 55, p. 235 – 247.

Moore, D.G., 1973, Plate-edge deformation and crustal growth, Gulf of California structural province: GSA Bulletin, v. 84, p. 1883–1906.

Moore, D.G., and Buffington, E.C., 1968, Transform Faulting and Growth of the Gulf of California Since the Late Pliocene: Science, v. 161, p. 1238–1241.

Nieto-Samaniego, Á.F., Ferrari, L., Alaniz-Alvarez, S.A., Labarthe-Hernández, G., and Rosas-Elguera, J., 1999, Variation of Cenozoic extension and volcanism across the southern Sierra Madre Occidental volcanic province, Mexico: Geological Society Of America Bulletin, v. 111, no. 3, p. 347–363.

Oskin, M., and Stock, J., 2003, Marine incursion synchronous with plate-boundary localization in the Gulf of California: Geology, v. 31, p. 23–26.

Ryan, W.B.F., Carbotte, S.M., Coplan, J.O., O'Hara, S., Melkonian, A., Arko, R., Weissel, R.A., Ferrini, V., Goodwillie, A., Nitsche, F., Bonczkowski, J., and Zemsky, R., 2009, Global Multi-Resolution Topography synthesis: Geochemistry Geophysics Geosystems, v. 10, no. 3, DOI: 10.1029/2008 GC002332.

Sawlan, M.G., 1991, Magmatic evolution of the Gulf of California rift, *in* Dauphin, J. and Simoneit, B. eds., The Gulf and Peninsular Province of the Californias, American Association of Petroleum Geologists, p. 301–369.

Sawlan, M.G., and Smith, J.G., 1984, Petrological characteristics, age, and tectonic setting of Neogene volcanic rocks in northern Baja California Sur, Mexico, *in* Frizzel, V.A. ed., Geology of the Baja California Peninsula, Pacific Section, Society of Economic Paleontologists and Mineralogists, p. 237–251.

Seiler, C., Fletcher, J.M., Kohn, B.P., and Gleadow, A.J.W., 2011, Low-temperature thermochronology of northern Baja California, Mexico: Decoupled slip-exhumation gradients and delayed onset of oblique rifting across the Gulf of California: Tectonics, v. 30, DOI: 10.1029/2009TC002649.

Tian, L., Castillo, P.R., Lonsdale, P.F., Hahm, D., and Hilton, D.R., 2011, Petrology and Sr-Nd-Pb-He isotope geochemistry of postspreading lavas on fossil spreading axes off Baja California Sur, Mexico: Geochemistry Geophysics Geosystems, v. 12, no. 2, DOI: 10.1029/2010GC003319.

Umhoefer, P.J., 2011, Why did the Southern Gulf of California rupture so rapidly?—Oblique divergence across hot, weak lithosphere along a tectonically active margin: GSA Today, v. 21, no. 11, p. 4–10.

Zhang, X., and Paulssen, H., 2012, Geodynamics of the Gulf of California from surface wave tomography: Physics of the Earth and Planetary Interiors, v. 192-193, p. 59–67.

Zhang, X., Paulssen, H., Lebedev, S., and Meier, T., 2009, 3D shear velocity structure beneath the Gulf of California from Rayleigh wave dispersion: Earth and Planetary Science Letters, v. 279, p. 255–262.

Appendix 1. Analytical procedures

A1.1 Mineral separation

Apatite and zircon grains were extracted from ~3-5 kg samples of basement granodiorite. Samples were pulverised using a jaw crusher and disc mill, sieved to remove fractions finer than 60 μm and coarser than 500 mm, washed, and dried for up to three days at ~40 °C. A Frantz magnetic separator was used to separate the nonmagnetic fraction, mainly quartz, from the paramagnetic and ferromagnetic fractions, mainly biotite, hornblende, and much of the feldspar. Heavy minerals were concentrated from the nonmagnetic fraction by agitation in tri-bromomethane (density 2.9 g cm^{-3}). Apatite and zircon grains were then separated using di-iodomethane (density 3.3 g cm^{-3}). Yields of apatite and zircon were good from all samples.

Groundmass grains were extracted from lava samples using the same mechanical and magnetic separation methods.

A1.2 U-Pb zircon dating methods

For zircon U-Pb analysis, zircons from one sample from each transect were mounted in resin and polished. Data were produced on a New Wave Nd:YAG 213 nm laser ablation system, coupled to an Agilent 7500a quadrupole mass spectrometer. Real time data were processed using GLITTER v4.4 data reduction software (www.glitter-gemoc.com); isotope ratios and age estimates are shown in Tables A2.1 and A2.2, and U-Pb concordia in Figure A2.1. Repeated measurements of the zircon Plesovice standard with a TIMS reference age of 337.13 ± 0.37 Ma (Slama et al., 2008) and NIST 612 silicate glass (Pearce et al., 1997) were used to correct for instrumental mass bias and depth-dependent inter-element fractionation of Pb, Th and U. Age estimates were calculated using Isoplot v3.6 (Ludwig, 2008). Zircon U-Pb analysis was carried out at Birkbeck College, University of London.

A1.3 Apatite fission track dating methods

For apatite fission track (AFT) analysis, spontaneous tracks in apatite were revealed using 5M HNO_3 at 20 °C for 20 seconds. Etched grain mounts were packed with mica external detectors and Corning glass dosimeters (CN5) and irradiated in the FRM 11 thermal neutron facility at the University of Munich. Ages were determined using the zeta calibration method and IUGS recommended age standards (Hurford, 1990; Galbraith and Laslett, 1993). AFT analysis was carried out at Birkbeck College, University of London; track counting was carried out by Andy Carter.

A1.4 Apatite (U-Th)/He dating methods

For apatite (U-Th)/He analysis, grains free of inclusions and fractures were selected by hand picking using a binocular transmitted light microscope at 60x magnification. Dimensions and characteristics of selected grains were obtained using a Zeiss Axioplan microscope; grains were then loaded into Pt tubules and degassed by laser heating. He and U-Th concentrations were measured by quadrupole mass spectrometer. Total uncertainty on sample age is based on reproducibility of the Limberg apatite standard with a reference age of 16.7 ± 1.0 Ma (Kraml et al., 2006) combined with the U-Th and He analytical uncertainties. Age estimates were corrected for α-ejection assuming hexagonal crystal geometry (Ketcham et al., 2011). The standard deviation of the age replicates is used as the error of the calculated age. He degassing and U-Th measurements were carried out at UMR-IDES, Universite Paris-Sud 11 by Cécile Gautheron.

A1.5 $^{40}Ar/^{39}Ar$ dating methods

For $^{40}Ar/^{39}Ar$ dating, unaltered groundmass grains free of phenocrysts or unaltered hornblende grains were selected by hand-picking using a binocular incident light microscope at 20x magnification. Samples were loaded in Cu foil and irradiated in the Cd-lined facility of the Oregon State University TRIGA reactor. The samples were irradiated in two separate batches. Samples 27, 31, 40, 41, 44, 47, 48, 52, and F09 were irradiated for 0.383 hours; samples 29 and 34 were irradiated for 0.275 hours. The neutron fluence monitor was Alder Creek Tuff sanidine, with a

reference age of 1.193 ± 0.001 Ma (Nomade et al., 2005). Grains were analysed by single crystal total fusion with a focused CO_2 laser. Groundmass samples were step-heated using a resistively heated double-vacuum furnace over a temperature range from 500 to 1750 °C. Isotope data were collected using a GVI ARGUS multi-collector mass spectrometer which has a measured sensitivity of 7 x 10^{-14} moles $volt^{-1}$ (Mark et al., 2009). Samples were heated for 5 minutes prior to 10 minutes cleanup. Extracted gases were cleaned using 3 GP50 SAES getters (two operated at 450 °C and one at room temperature) and a cold finger maintained at -95 ˚C using an acetone-$CO_{2(s)}$ slush trap. The extraction, clean up and data collection processes were entirely automated. Experiments were conducted over 7 hour periods with hot furnace blanks (500 to 1750 ˚C) collected prior to every sample run. Average backgrounds ± standard deviations were used to correct isotope abundances. Air calibrations were collected in batches (n = 10) immediately before and after the individual experiments to monitor mass discrimination. Average $^{40}Ar/^{36}Ar$ ratios ± standard deviation (300.08 ± 0.19, n = 203) was used to calculate discrimination factor using the power law. The atmospheric argon ratios of Nier (1950) were used for discrimination factor determinations, and the decay constants of Steiger and Jager (1977) were utilized. The Berkeley Geochronology Centre software 'MassSpec' was used to regress and reduce age data; isotope data are corrected for blank runs, radioactive decay, mass discrimination and interfering reactions. Plateau calculations are based on the acceptance criteria outlined in (Mark et al., 2011): n = 3 for minimum number of contiguous steps with no resolvable slope, F = 0.6 (that is > 60% of ^{39}Ar released) and P = 0.05 for the probability of fit. Age determinations and isotope measurements and ratios are shown in Table A2.5, and step-heating and inverse isochron plots in Figures A2.2 and A2.3. $^{40}Ar/^{39}Ar$ analysis was carried out at the Argon Isotope Facility, SUERC.

A1.6 References

Galbraith, R.F., and Laslett, G.M., 1993, Statistical models for mixed fission track ages: Nuclear Tracks and Radiation Measurements, v. 21, no. 4, p. 459–470.

Hurford, A., 1990, Standardization of fission track dating calibration: Recommendation by the Fission Track Working Group of the I.U.G.S. Subcommission on Geochronology: Chemical Geology: Isotope Geoscience section, v. 80, no. 2, p. 171–178.

Ketcham, R.A., Gautheron, C., and Tassan-Got, L., 2011, Accounting for long alpha-particle stopping distances in (U–Th–Sm)/He geochronology: Refinement of the baseline case: Geochimica et Cosmochimica Acta, v. 75, no. 24, p. 7779–7791.

Kraml, M., Pik, R., Rahn, M., Selbekk, R., Carignan, J., and Keller, J., 2006, A New Multi-Mineral Age Reference Material for 40Ar/39Ar, (U-Th)/ He and Fission Track Dating Methods: The Limberg t3 Tuff: Geostandards and Geoanalytical Research, v. 30, p. 73–86.

Ludwig, K.R., 2008, Isoplot 3.6: A geochronological toolkit for Microsoft Excel: Berkeley Geochronological Centre Special Publication No.4.

Mark, D.F., Barfod, D., Stuart, F.M., and Imlach, J., 2009, The ARGUS multicollector noble gas mass spectrometer: Performance for 40 Ar/ 39 Ar geochronology: Geochemistry Geophysics Geosystems, v. 10, DOI: 10.1029/2009GC002643.

Mark, D.F., Rice, C.M., Fallick, A.E., Trewin, N.H., Lee, M.R., Boyce, A., and Lee, J.K.W., 2011, 40Ar/39Ar dating of hydrothermal activity , biota and gold mineralization in the Rhynie hot-spring system , Aberdeenshire , Scotland: Geochimica et Cosmochimica Acta, v. 75, no. 2, p. 555–569.

Nier, A.O., 1950, A redetermination of the relative abundances of the isotopes of carbon, nitrogen, oxygen, argon, and potassium: Physical Review, v. 77, no. 6, p. 789–793.

Nomade, S., Renne, P., Vogel, N., Deino, A., Sharp, W., Becker, T., Jaouni, A., and Mundil, R., 2005, Alder Creek sanidine (ACs-2): A Quaternary Ar/Ar dating standard tied to the Cobb Mountain geomagnetic event: Chemical Geology, v. 218, no. 3-4, p. 315–338.

Pearce, N.J.G., Perkins, W.T., Westgate, J. A., Gorton, M.P., Jackson, S.E., Neal, C.R., and Chenery, S.P., 1997, A Compilation of New and Published Major and Trace Element Data for NIST SRM 610 and NIST SRM 612 Glass Reference Materials: Geostandards and Geoanalytical Research, v. 21, no. 1, p. 115–144.

Slama, J., Kosler, J., Condon, D., Crowley, J., Gerdes, A, Hanchar, J., Horstwood, M., Morris, G., Nasdala, L., and Norberg, N., 2008, Plešovice zircon — A new natural reference material for U–Pb and Hf isotopic microanalysis: Chemical Geology, v. 249, no. 1-2, p. 1–35.

Steiger, R., and Jager, E., 1977, Subcommission on geochronology: convention on the use of decay constants in geo- and cosmochronology: Earth and Planetary Science Letters, v. 36, p. 359–362.

Appendix 2. Data tables and results

A2.1 Data tables and results

Zircon U-Pb and $^{40}Ar/^{39}Ar$ data tables are presented below, together with zircon U-Pb concordia, and $^{40}Ar/^{39}Ar$ inverse isochron plots and step-heating plateaux. All sample locations are given using the WGS84 coordinate system.

Table A2.1: Zircon U-Pb data for basement granodiorite sample AP2, Arroyo Perini, northern transect. Location 26.19102, -111.55077; elevation 136 m asl. Ages were calculated using Glitter v4.4 (www.glitter-gemoc.com) and then further refined using the Microsoft Excel Isoplot plug-in (Ludwig, 2008).

Grain or Standard No.	Isotope Ratios						Ages (Ma)					
	$^{207}Pb/^{206}Pb$	±1σ	$^{206}Pb/^{238}U$	±1σ	$^{207}Pb/^{235}U$	±1σ	$^{207}Pb/^{206}Pb$	±1σ	$^{206}Pb/^{238}U$	±1σ	$^{207}Pb/^{235}U$	±1σ
GLASS	0.90514	0.01336	0.46717	0.0089	20.96774	9.02763	-	-	-	-	-	-
GLASS2	0.90725	0.00918	0.45149	0.00675	-22.56971	5.67349	-	-	-	-	-	-
STDCZ1	0.05318	0.00052	0.05363	0.00068	0.39124	0.00698	336.6	21.89	336.7	4.15	335.3	5.09
STDCZ2	0.0537	0.00057	0.05473	0.0007	0.40471	0.00767	358.4	23.64	343.5	4.25	345.1	5.55
STDCZ3	0.05293	0.0005	0.05331	0.00067	0.39221	0.00682	325.5	21.4	334.8	4.12	336	4.97
G1	0.11954	0.00699	0.01527	0.00042	0.26367	0.03664	1949.4	100.93	97.7	2.65	237.6	29.44
G2	0.04743	0.00074	0.01393	0.00018	0.08805	0.00167	70.2	37.46	89.2	1.16	85.7	1.56
G3	0.04635	0.00087	0.01423	0.00019	0.09243	0.00222	15.7	43.86	91.1	1.21	89.8	2.07
G4	0.05	0.00179	0.01447	0.00023	0.12385	0.00924	195.2	81.02	92.6	1.48	118.6	8.35
G5	0.04603	0.00218	0.01553	0.00028	0.07963	0.00577	0.1	109.42	99.3	1.76	77.8	5.43
G6	0.0477	0.00149	0.01482	0.00022	0.08117	0.00386	83.8	73.47	94.8	1.43	79.2	3.63
G7	0.05031	0.0014	0.01404	0.00021	0.09004	0.00379	209.4	63.22	89.9	1.32	87.5	3.53
G8	0.05283	0.00113	0.0145	0.0002	0.10402	0.00302	321.3	47.86	92.8	1.27	100.5	2.78
G9	0.05863	0.00306	0.01639	0.00032	0.19325	0.04327	553.4	109.99	104.8	2.05	179.4	36.82
G10	0.04852	0.0024	0.01508	0.00028	0.14337	0.01908	124.8	112.42	96.5	1.76	136	16.95
G11	0.04659	0.00161	0.01391	0.00022	0.07993	0.00361	28.3	81.07	89.1	1.37	78.1	3.39
G12	0.04947	0.00113	0.01347	0.00019	0.09698	0.00296	170.4	52.62	86.2	1.19	94	2.74
G13	0.07115	0.00561	0.01586	0.00046	0.15079	0.02094	961.7	153.25	101.4	2.91	142.6	18.48

G14	0.04819	0.00146	0.01448	0.00022	0.10053	0.00506	108.6	69.97	92.7	1.38	97.3	4.67
G15	-0.00804	0.00241	0.01225	0.00021	-0.01441	0.00437	0.1	0	78.5	1.34	-14.7	4.5
G16	0.05246	0.00169	0.01419	0.00022	0.08956	0.00485	305.4	71.5	90.8	1.39	87.1	4.52
G17	0.04876	0.00086	0.01436	0.00019	0.09117	0.00213	136.3	40.72	91.9	1.21	88.6	1.98
G18	0.05135	0.00147	0.01468	0.00022	0.10642	0.00519	256.4	64.49	94	1.38	102.7	4.76
G19	0.04739	0.00209	0.01531	0.00026	0.11709	0.01252	68.4	102.31	97.9	1.67	112.4	11.38
G20	0.04991	0.00351	0.01632	0.00035	0.06221	0.0079	190.6	155.8	104.3	2.23	61.3	7.55
G21	0.06148	0.00174	0.01533	0.00023	0.13877	0.00748	656	59.67	98	1.47	131.9	6.67
G23	0.04447	0.00228	0.01542	0.00028	0.07867	0.00695	0.1	36.29	98.7	1.8	76.9	6.54
G24	0.05112	0.00206	0.01492	0.00025	0.08938	0.00648	246.4	90.4	95.5	1.6	86.9	6.04
G25	0.04973	0.00259	0.01575	0.0003	0.14485	0.02391	182.6	117.03	100.7	1.89	137.4	21.21
G26	0.05146	0.00299	0.01556	0.00031	0.08904	0.01187	261.3	128.4	99.5	1.97	86.6	11.07
G27	0.05303	0.00275	0.0157	0.00029	0.08349	0.00867	330.2	113.13	100.4	1.87	81.4	8.12
G28	0.05099	0.00263	0.01568	0.0003	0.06176	0.005	240.5	114.8	100.3	1.89	60.9	4.78
G29	0.05038	0.00281	0.0157	0.00031	0.06694	0.00623	212.4	124.27	100.4	1.96	65.8	5.93
G30	0.05047	0.00331	0.01642	0.00035	-0.59921	0.54956	216.7	144.99	105	2.21	-928.4	1392.3
G31	0.07093	0.00387	0.01621	0.00035	0.07701	0.0081	955.3	107.79	103.7	2.2	75.3	7.64
G32	0.05078	0.00336	0.01654	0.00036	0.07098	0.00882	231	145.68	105.7	2.28	69.6	8.36
STDCZ4	0.05296	0.00063	0.05379	0.00068	0.39652	0.00883	327.1	26.71	337.8	4.15	339.1	6.42
STDCZ5	0.05345	0.00063	0.05371	0.00068	0.39211	0.00864	347.7	26.47	337.3	4.14	335.9	6.3
GLASS3	0.90449	0.01135	0.43477	0.00654	123.12579	182.66916	-	-	-	-	-	-

Table A2.2: Zircon U-Pb data for basement granodiorite sample SA5, Arroyo San Antonio, southern transect. Location 26.10891, -111.47151; elevation 135 m asl. Ages shown here were calculated using Glitter v4.4 (www.glitter-gemoc.com) and then further refined using the Microsoft Excel Isoplot plug-in (Ludwig, 2008).

Grain or Standard No.	Isotope Ratios						Ages (Ma)					
	$^{207}Pb/^{206}Pb$	±1σ	$^{206}Pb/^{238}U$	±1σ	$^{207}Pb/^{235}U$	±1σ	$^{207}Pb/^{206}Pb$	±1σ	$^{206}Pb/^{238}U$	±1σ	$^{207}Pb/^{235}U$	±1σ
STDCZ1	0.05398	0.00056	0.05165	0.00065	0.38113	0.00583	369.9	23.51	324.6	3.96	327.9	4.28
STDCZ2	0.05319	0.00049	0.05371	0.00067	0.38246	0.00538	336.9	20.77	337.3	4.07	328.8	3.95
STDCZ3	0.0529	0.00047	0.05411	0.00067	0.38875	0.0053	324.6	20.03	339.7	4.09	333.5	3.88
G1	0.04838	0.00171	0.01475	0.00023	0.13604	0.00963	118.1	81.3	94.4	1.46	129.5	8.6
G2	0.05104	0.00119	0.01538	0.00021	0.12104	0.00451	242.5	52.99	98.4	1.36	116	4.09
G3	0.02896	0.00229	0.01437	0.00026	0.05515	0.00507	0.1	0	92	1.62	54.5	4.88
G4	0.06704	0.00307	0.016	0.00031	0.43336	0.13071	839.1	92.63	102.3	1.95	365.6	92.59
G5	0.04548	0.00186	0.01543	0.00025	0.15786	0.0178	0.1	65.62	98.7	1.58	148.8	15.61
G6	0.0467	0.00192	0.01572	0.00026	0.09983	0.00785	33.8	95.9	100.6	1.62	96.6	7.25
G7	0.0613	0.00453	0.0172	0.00043	0.11022	0.01833	649.8	151.28	109.9	2.73	106.2	16.76
G8	0.11833	0.00466	0.0167	0.00035	0.33967	0.04849	1931.1	68.91	106.8	2.2	296.9	36.75
G9	0.03643	0.00637	0.01657	0.00056	0.12917	0.04289	0.1	0	106	3.57	123.4	38.56
G10	0.05205	0.00372	0.0161	0.00037	0.83965	0.83476	287.5	155.46	102.9	2.37	619	460.74
G11	0.05006	0.00385	0.01729	0.00042	0.09657	0.01385	197.9	169.33	110.5	2.65	93.6	12.83
G12	0.05838	0.00213	0.01527	0.00025	0.12642	0.00884	544.2	77.97	97.7	1.6	120.9	7.97
G13	0.05686	0.00168	0.01482	0.00023	0.13671	0.0064	485.3	64.54	94.8	1.43	130.1	5.72
G14	0.05013	0.00367	0.01557	0.00037	0.0943	0.01216	201.2	161.66	99.6	2.38	91.5	11.28

G15	0.04828	0.00319	0.01561	0.00034	0.12428	0.01719	112.9	148.75	99.9	2.18	118.9	15.52
G16	0.06003	0.00216	0.0154	0.00026	0.11935	0.00809	604.6	76.12	98.5	1.62	114.5	7.34
G17	0.049	0.00142	0.01499	0.00022	0.12519	0.00668	148	66.42	95.9	1.4	119.8	6.03
G18	0.04785	0.002	0.01561	0.00026	0.12213	0.01129	90.9	96.96	99.9	1.65	117	10.21
G19	0.05706	0.00209	0.01529	0.00025	0.10196	0.00675	493.3	79.29	97.8	1.59	98.6	6.22
G20	0.05529	0.00362	0.01736	0.00037	0.05894	0.0063	424	139.8	111	2.34	58.1	6.04
G21	0.05749	0.00223	0.01587	0.00027	0.1456	0.01445	509.9	83.65	101.5	1.7	138	12.81
G22	0.05846	0.00382	0.01725	0.00039	0.29346	0.09973	547.2	136.56	110.2	2.48	261.3	78.29
G23	0.06359	0.00315	0.01614	0.00031	0.12175	0.01348	728	101.73	103.2	2	116.7	12.2
G24	0.05667	0.0024	0.01556	0.00027	0.10182	0.00785	477.8	91.62	99.6	1.74	98.5	7.24
G25	0.16557	0.00697	0.01815	0.00043	0.31342	0.05299	2513.4	69.13	116	2.72	276.8	40.97
G26	0.05455	0.00311	0.01656	0.00034	0.20704	0.04913	393.6	122.63	105.9	2.13	191.1	41.32
G27	0.06805	0.00296	0.01575	0.00029	0.17287	0.02143	870.2	87.68	100.7	1.85	161.9	18.56
G28	0.07422	0.00309	0.01656	0.00031	0.14389	0.01472	1047.4	81.72	105.9	1.94	136.5	13.06
G29	0.19301	0.00733	0.01526	0.00033	0.46805	0.03667	2768	61	97.7	2.09	389.8	25.36
G30	0.06032	0.00358	0.01679	0.00037	0.34592	0.11976	614.9	123.18	107.4	2.32	301.6	90.35
STDCZ4	0.05122	0.00078	0.05436	0.0007	0.4319	0.01098	250.8	34.85	341.2	4.31	364.5	7.78
G31	0.06473	0.0027	0.0155	0.00028	0.13399	0.01266	765.6	85.52	99.1	1.76	127.7	11.34
G32	0.06219	0.0026	0.01587	0.00029	0.25863	0.03704	680.8	86.85	101.5	1.82	233.6	29.88
STDCZ5	0.05362	0.00049	0.05475	0.00068	0.4454	0.00742	355.1	20.65	343.6	4.15	374	5.21
GLASS2	0.89433	0.00856	0.43682	0.00631	19.03004	3.44187	-	-	-	-	-	-

Table A2.3: $^{40}Ar/^{39}Ar$ data. Neutron fluence monitor was Alder Creek Tuff sanidine, with a reference age of 1.193 ± 0.001 Ma (Nomade et al., 2005). Data were also collected using an ARGUS multi-collector noble gas mass spectrometer (Mark et al., 2009). Nucleogenic production ratios: $(^{36}Ar/^{37}Ar)_{Ca}$ = 2.65 ± 0.2 x10^{-4}; $(^{39}Ar/^{37}Ar)_{Ca}$ = 6.95 ± 0.9 x10^{-4}; $(^{38}Ar/^{37}Ar)_{Ca}$ = 0.196 ± 0.08 x10^{-4}; $(^{40}Ar/^{39}Ar)_{K}$ = 7.30 ± 9.2 x10^{-4}; $(^{36}Ar/^{38}Ar)_{K}$ = 1.22 x10^{-2}; $(^{36}Ar/^{38}Ar)_{Cl}$ = 2.63 ± 0.02 x10^{2}; $^{37}Ar/^{39}Ar$ to Ca/K = 1.96. Isotopic constants and decay rates: $\lambda(^{40}K_{\varepsilon})$/yr = 5.81 ± 0.04 x$10^{-11}$; $\lambda(^{40}K_{\beta-})$/yr = 4.962 ± 0.00043 x10^{-10}; $\lambda(^{37}Ar)$/d = 1.975 x10^{-2}; $\lambda(^{39}Ar)$/d = 7.068 x10^{-6}; $\lambda(^{36}Cl)$/d = 6.308 x10^{-9}; $(^{40}Ar/^{36}Ar)_{Atm}$ = 295.5 ± 0.5; $(^{40}Ar/^{38}Ar)_{Atm}$ = 1575 ± 2.

Step ID	Relative Isotopic Abundances										Derived Results									Inverse Isochron Data				
	^{40}Ar ± 1σ		^{39}Ar ± 1σ		^{38}Ar ± 1σ		^{37}Ar ± 1σ		^{36}Ar ± 1σ		^{39}Ar Mol	^{39}Ar % of total	% $(^{36}Ar)_{Ca}$	Ca/K ± 1σ		%^{40}Ar*	Age (Ma) ± 1σ		w/±J	$^{36}Ar/^{40}Ar$ ± %1σ		$^{39}Ar/^{40}Ar$ ± %1σ		$^{36}Ar/^{39}Ar$ Er. Corr.
Sample 27, 6.194 ± 0.014 Ma, 25.83250 N 111.46167 W, EK62, [24], Packet 13, 400 mg groundmass, J = 0.0163 x10^{-3} ± 3.0 x10^{-8} (1σ)																								
50630-1	4221.9	2.5	4.691	0.008	2.092	0.006	2.037	0.015	10.928	0.010	3.28E-15	9.1	0.005	0.851	0.006	23.5	6.219	0.045	0.05	0.199	0.00259	0.00111	0.183	0.57
50630-2	2929.4	1.7	4.759	0.005	1.254	0.004	2.156	0.012	6.490	0.005	3.33E-15	9.2	0.009	0.888	0.005	34.5	6.247	0.027	0.03	0.194	0.00222	0.00162	0.129	0.66
50630-3	3745	2.4	9.336	0.005	1.205	0.003	3.560	0.011	6.012	0.006	6.54E-15	18.1	0.016	0.747	0.002	52.6	6.195	0.015	0.02	0.205	0.00161	0.00249	0.089	0.69
50630-4	589.88	0.6	1.099	0.004	0.233	0.003	0.381	0.010	1.209	0.003	7.69E-16	2.1	0.008	0.679	0.018	39.5	6.222	0.041	0.04	0.328	0.00205	0.00186	0.369	0.27
50630-5	3897.2	2.5	12.719	0.006	0.900	0.003	4.130	0.012	4.129	0.004	8.90E-15	24.7	0.026	0.637	0.002	68.7	6.184	0.010	0.02	0.209	0.00106	0.00326	0.087	0.68
50630-6	1936.8	1.2	5.492	0.005	0.547	0.004	1.812	0.012	2.636	0.004	3.84E-15	10.7	0.018	0.647	0.004	59.8	6.196	0.014	0.02	0.225	0.00136	0.00283	0.116	0.60
50630-7	1280.7	0.9	3.125	0.004	0.426	0.003	1.189	0.011	2.107	0.003	2.19E-15	6.1	0.015	0.746	0.007	51.4	6.188	0.019	0.02	0.00164	0.00164	0.00244	0.162	0.52
50630-8	1381.1	1.0	2.736	0.005	0.544	0.004	1.583	0.012	2.806	0.003	1.92E-15	5.3	0.015	1.134	0.009	40.0	5.929	0.025	0.03	0.00203	0.00203	0.00198	0.182	0.54
50630-9	2052.5	1.2	6.394	0.005	0.541	0.003	19.417	0.021	2.587	0.004	4.48E-15	12.4	0.199	5.952	0.008	62.8	5.936	0.012	0.02	0.00126	0.00126	0.00311	0.110	0.58
50630-10	517.33	0.6	1.198	0.004	0.186	0.003	3.897	0.011	0.898	0.003	8.39E-16	2.3	0.115	6.374	0.027	48.8	6.198	0.036	0.04	0.00173	0.00173	0.00231	0.332	0.26

Step ID	Relative Isotopic Abundances										Derived Results									Inverse Isochron Data				
	^{40}Ar ± 1σ		^{39}Ar ± 1σ		^{38}Ar ± 1σ		^{37}Ar ± 1σ		^{36}Ar ± 1σ		^{39}Ar Mol	^{39}Ar % of total	% $(^{36}Ar)_{Ca}$	Ca/K ± 1σ		$\%^{40}Ar^*$	Age (Ma) ± 1σ		w/±J	$^{36}Ar/^{40}Ar$ ± %1σ		$^{39}Ar/^{40}Ar$ ± %1σ		$^{36}Ar/^{39}Ar$ Er. Corr.
Sample 31, 2.845 ± 0.009 Ma, 25.88395 N 111.77107 W, EK62, [25], Packet 16, 400 mg groundmass, J = 0.0122 x10^{-3} ± 2.0 x10^{-8} (1σ)																								
50633-1	4195.5	2.4	0.969	0.013	2.632	0.009	0.653	0.017	14.037	0.011	6.79E-16	3.4	0.001	1.32	0.04	1.1	1.079	0.184	0.18	0.19	0.00335	1.37	0.000	0.1143
50633-2	3106.6	1.8	1.861	0.007	1.834	0.005	2.058	0.011	9.821	0.008	1.30E-15	6.6	0.006	2.17	0.01	6.6	2.420	0.069	0.07	0.20	0.00316	0.37	0.001	0.3710
50633-3	2047	1.2	2.114	0.005	1.132	0.003	2.256	0.008	6.015	0.005	1.48E-15	7.5	0.010	2.09	0.01	13.2	2.810	0.039	0.04	0.20	0.00294	0.23	0.001	0.5095
50633-4	1715.1	1.0	2.639	0.004	0.891	0.003	2.447	0.008	4.654	0.005	1.85E-15	9.3	0.014	1.82	0.01	19.8	2.835	0.025	0.03	0.21	0.00271	0.18	0.002	0.5591
50633-5	2167.9	1.2	4.741	0.005	1.018	0.004	3.605	0.009	5.262	0.005	3.32E-15	16.7	0.018	1.49	0.00	28.3	2.846	0.016	0.02	0.20	0.00243	0.12	0.002	0.6653
50633-6	1215.5	0.8	2.698	0.004	0.570	0.003	1.777	0.007	2.943	0.003	1.89E-15	9.5	0.016	1.29	0.01	28.5	2.823	0.017	0.02	0.21	0.00242	0.17	0.002	0.5587
50633-7	2134.3	1.3	5.627	0.004	0.936	0.003	4.056	0.009	4.758	0.005	3.94E-15	19.8	0.023	1.41	0.00	34.1	2.849	0.013	0.01	0.20	0.00223	0.10	0.003	0.6765
50633-8	1373.2	0.8	2.676	0.004	0.669	0.003	2.121	0.008	3.464	0.003	1.87E-15	9.4	0.016	1.55	0.01	25.5	2.874	0.019	0.02	0.20	0.00252	0.18	0.002	0.5742
50633-9	2180.3	1.3	3.010	0.005	1.154	0.003	2.490	0.008	6.100	0.006	2.11E-15	10.6	0.011	1.62	0.01	17.3	2.763	0.029	0.03	0.20	0.00280	0.17	0.001	0.5764
50633-10	1672.7	1.0	1.359	0.005	0.956	0.003	1.460	0.008	5.102	0.005	9.51E-16	4.8	0.008	2.11	0.01	9.9	2.675	0.051	0.05	0.20	0.00305	0.35	0.001	0.3835
50633-11	1173.7	0.7	0.475	0.004	0.709	0.002	13.285	0.014	3.799	0.003	3.32E-16	1.7	0.093	54.84	0.50	4.4	2.460	0.110	0.11	0.20	0.00323	0.96	0.000	0.1603
50633-12	707.26	0.5	0.201	0.004	0.434	0.003	9.678	0.011	2.316	0.004	1.41E-16	0.7	0.111	94.25	1.88	3.3	2.658	0.194	0.19	0.24	0.00327	2.11	0.000	0.0642

Step ID	Relative Isotopic Abundances										Derived Results									Inverse Isochron Data				
	^{40}Ar ± 1σ		^{39}Ar ± 1σ		^{38}Ar ± 1σ		^{37}Ar ± 1σ		^{36}Ar ± 1σ		^{39}Ar Mol	^{39}Ar % of total	% $(^{36}Ar)_{Ca}$	Ca/K ± 1σ		$\%^{40}Ar^*$	Age (Ma) ± 1σ		w/±J	$^{36}Ar/^{40}Ar$ ± %1σ		$^{39}Ar/^{40}Ar$ ± %1σ		$^{36}Ar/^{39}Ar$ Er. Corr.
Sample 40, 0.426 ± 0.007 Ma, 25.85136 N 111.89128 W, EK62, Packet 14, 400 mg groundmass, J = 0.013 x10^{-3} ± 3.0 x10^{-8} (1σ)																								
50627-1	1765.2	1.6	2.977	0.140	1.265	0.052	0.690	0.121	5.907	0.007	2.08E-15	4.7	0.003	0.454	0.082	1.1	0.158	0.033	0.03	0.23	0.00335	4.65	0.00169	0.03
50627-2	2462.5	1.0	4.678	0.009	1.615	0.006	0.724	0.017	8.096	0.006	3.27E-15	7.3	0.002	0.303	0.007	2.8	0.357	0.023	0.02	0.19	0.00329	0.19	0.00190	0.55
50627-3	2553.1	1.5	5.458	0.005	1.624	0.004	0.826	0.011	8.334	0.006	3.82E-15	8.6	0.003	0.297	0.004	3.5	0.395	0.021	0.02	0.19	0.00326	0.11	0.00214	0.69
50627-4	2648.1	1.5	6.931	0.005	1.675	0.004	1.052	0.012	8.550	0.008	4.85E-15	10.9	0.003	0.298	0.003	4.6	0.418	0.017	0.02	0.20	0.00323	0.10	0.00262	0.69
50627-5	2569.9	1.5	7.339	0.005	1.625	0.003	1.157	0.010	8.253	0.008	5.14E-15	11.5	0.004	0.309	0.003	5.1	0.426	0.016	0.02	0.20	0.00321	0.10	0.00286	0.68
50627-6	2621.5	1.6	7.980	0.005	1.651	0.003	1.312	0.010	8.380	0.008	5.59E-15	12.5	0.004	0.322	0.002	5.5	0.434	0.015	0.02	0.20	0.00320	0.10	0.00304	0.69
50627-7	2611.3	1.6	7.716	0.004	1.642	0.004	1.314	0.010	8.366	0.007	5.40E-15	12.1	0.004	0.334	0.003	5.3	0.430	0.015	0.02	0.20	0.00320	0.09	0.00295	0.71
50627-8	2639.5	1.5	6.843	0.005	1.655	0.004	1.192	0.011	8.508	0.007	4.79E-15	10.7	0.004	0.341	0.003	4.8	0.437	0.018	0.02	0.20	0.00322	0.10	0.00259	0.69
50627-9	4561.9	2.8	6.029	0.006	2.860	0.003	1.077	0.010	15.057	0.012	4.22E-15	9.5	0.002	0.350	0.003	2.5	0.445	0.035	0.03	0.20	0.00330	0.13	0.00132	0.66
50627-10	8902.3	5.6	7.777	0.012	5.565	0.006	1.674	0.011	29.472	0.022	5.44E-15	12.2	0.002	0.422	0.003	2.2	0.592	0.052	0.05	0.19	0.00331	0.17	0.00087	0.61

Step ID	Relative Isotopic Abundances										Derived Results									Inverse Isochron Data				
	^{40}Ar ± 1σ		^{39}Ar ± 1σ		^{38}Ar ± 1σ		^{37}Ar ± 1σ		^{36}Ar ± 1σ		^{39}Ar Mol	^{39}Ar % of total	% $(^{36}Ar)_{Ca}$	Ca/K ± 1σ		% $^{40}Ar^*$	Age (Ma) ± 1σ		w/±J	$^{36}Ar/^{40}Ar$ ± %1σ		$^{39}Ar/^{40}Ar$ ± %1σ		$^{36}Ar/^{39}Ar$ Er. Corr.
Sample 44, 0.045 ± 0.009 Ma, 26.06966 N 111.79287 W, EK62, [23], Packet 11, 400 mg groundmass, J = 0.0165 x10^{-3} ± 3.0 x10^{-8} (1σ)																								
50614-1	528.7	0.5	1.531	0.008	0.368	0.005	0.300	0.010	1.722	0.005	1.07E-15	4.2	0.00	0.384	0.012	3.8	0.389	0.034	0.03	0.003	0.34	0.003	0.52	0.18
50614-2	1307.2	0.7	4.375	0.006	0.886	0.003	1.051	0.007	4.373	0.006	3.06E-15	12.1	0.01	0.471	0.003	1.2	0.102	0.020	0.02	0.003	0.22	0.003	0.14	0.55
50614-3	914.0	0.5	3.046	0.005	0.618	0.004	0.810	0.007	3.066	0.005	2.13E-15	8.4	0.01	0.521	0.004	0.9	0.078	0.021	0.02	0.003	0.24	0.003	0.19	0.46
50614-4	1766.0	1.1	6.719	0.004	1.198	0.003	2.574	0.007	5.957	0.007	4.70E-15	18.5	0.01	0.751	0.002	0.3	0.026	0.016	0.02	0.003	0.21	0.004	0.10	0.66
50614-5	780.2	0.5	2.619	0.004	0.529	0.003	1.143	0.007	2.617	0.006	1.83E-15	7.2	0.01	0.855	0.005	0.9	0.077	0.025	0.03	0.003	0.29	0.003	0.18	0.40
50614-6	473.6	0.3	1.436	0.004	0.321	0.003	0.638	0.006	1.601	0.005	1.01E-15	4.0	0.01	0.871	0.009	0.1	0.012	0.035	0.03	0.003	0.35	0.003	0.29	0.25
50614-7	1747.4	1.1	6.165	0.005	1.175	0.003	3.609	0.008	5.895	0.007	4.32E-15	17.0	0.02	1.147	0.003	0.3	0.027	0.018	0.02	0.003	0.21	0.004	0.11	0.64
50614-8	1253.1	0.8	3.490	0.005	0.833	0.003	2.182	0.007	4.220	0.006	2.44E-15	9.6	0.01	1.225	0.004	0.5	0.054	0.024	0.02	0.003	0.23	0.003	0.16	0.54
50614-9	1712.6	1.0	3.927	0.005	1.127	0.003	2.348	0.006	5.772	0.006	2.75E-15	10.8	0.01	1.172	0.003	0.4	0.054	0.027	0.03	0.003	0.21	0.002	0.13	0.62
50614-10	4173.9	2.6	2.926	0.008	2.652	0.003	1.498	0.008	14.107	0.013	2.05E-15	8.1	0.00	1.004	0.006	0.1	0.055	0.085	0.09	0.003	0.20	0.001	0.27	0.47

Step ID	Relative Isotopic Abundances										Derived Results									Inverse Isochron Data				
	^{40}Ar ± 1σ		^{39}Ar ± 1σ		^{38}Ar ± 1σ		^{37}Ar ± 1σ		^{36}Ar ± 1σ		^{39}Ar Mol	^{39}Ar % of total	% $(^{36}Ar)_{Ca}$	Ca/K ± 1σ		% $^{40}Ar^*$	Age (Ma) ± 1σ		w/±J	$^{36}Ar/^{40}Ar$ ± %1σ		$^{39}Ar/^{40}Ar$ ± %1σ		$^{36}Ar/^{39}Ar$ Er. Corr.
Sample 47, 2.585 ± 0.040 Ma, 26.05968 N 111.81866 W, EK62, [26], Packet 18, 400 mg groundmass, J = 0.0163 x10^{-3} ± 3.0 x10^{-8} (1σ)																								
50645-1	4579.2	2.5	1.293	0.043	2.938	0.018	0.513	0.034	15.075	0.014	9.05E-16	13.4	0.00	0.778	0.057	2.7	2.831	0.224	0.22	0.003	0.20	0.0003	3.30	0.05
50645-2	6260.6	3.3	1.897	0.012	3.909	0.005	1.522	0.009	20.622	0.015	1.33E-15	19.6	0.00	1.573	0.013	2.7	2.589	0.182	0.18	0.003	0.19	0.0003	0.60	0.25
50645-3	4802.0	2.8	1.766	0.010	2.968	0.004	2.529	0.009	15.728	0.012	1.24E-15	18.3	0.00	2.807	0.019	3.2	2.576	0.152	0.15	0.003	0.19	0.0004	0.58	0.26
50645-4	3025.6	1.6	1.401	0.009	1.850	0.004	3.263	0.007	9.832	0.008	9.80E-16	14.5	0.01	4.566	0.032	4.0	2.529	0.120	0.12	0.003	0.19	0.0005	0.67	0.22
50645-5	1542.2	0.8	0.939	0.005	0.933	0.003	3.101	0.008	4.938	0.003	6.57E-16	9.7	0.02	6.472	0.040	5.4	2.612	0.089	0.09	0.003	0.19	0.0006	0.57	0.26
50645-6	583.3	0.4	0.414	0.005	0.355	0.002	1.582	0.008	1.854	0.003	2.90E-16	4.3	0.02	7.485	0.092	6.1	2.519	0.095	0.09	0.003	0.23	0.0007	1.12	0.13
50645-7	888.5	0.5	0.955	0.004	0.527	0.003	4.281	0.008	2.723	0.002	6.69E-16	9.9	0.04	8.783	0.042	9.5	2.593	0.052	0.05	0.003	0.20	0.0011	0.45	0.31
50645-8	557.0	0.4	0.478	0.005	0.334	0.002	2.239	0.008	1.759	0.003	3.35E-16	5.0	0.03	9.173	0.092	6.7	2.301	0.085	0.09	0.003	0.25	0.0009	0.96	0.13
50645-9	254.9	0.4	0.189	0.004	0.160	0.002	0.848	0.007	0.819	0.002	1.32E-16	2.0	0.03	8.789	0.198	5.0	2.001	0.132	0.13	0.003	0.33	0.0007	2.10	0.07
50645-10	573.1	0.4	0.323	0.004	0.358	0.002	1.470	0.008	1.883	0.002	2.26E-16	3.3	0.02	8.913	0.108	2.9	1.540	0.114	0.11	0.003	0.22	0.0006	1.10	0.13

Step ID	Relative Isotopic Abundances										Derived Results									Inverse Isochron Data				
	^{40}Ar ± 1σ		^{39}Ar ± 1σ		^{38}Ar ± 1σ		^{37}Ar ± 1σ		^{36}Ar ± 1σ		^{39}Ar Mol	^{39}Ar % of total	% $(^{36}Ar)_{Ca}$	Ca/K ± 1σ		% ^{40}Ar*	Age (Ma) ± 1σ		w/± J	$^{36}Ar/^{40}Ar$ ± %1σ		$^{39}Ar/^{40}Ar$ ± %1σ		$^{36}Ar/^{39}Ar$ Er. Corr.
Sample 48, 14.630 ± 0.040 Ma, 26.09669 N 111.70546 W, EK62, [26], Packet 17, 400 mg groundmass, J = 0.0128 x10^{-3} ± 3.0 x10^{-8} (1σ)																								
50642-1	3104.3	1.5	1.859	0.010	1.248	0.004	1.419	0.010	6.642	0.006	1.30E-15	5.5	0.006	1.495	0.013	36.8	14.132	0.092	0.10	0.002	0.196	0.001	0.530	0.27
50642-2	2673.9	1.4	2.104	0.008	0.859	0.003	1.412	0.008	4.550	0.005	1.47E-15	6.2	0.008	1.315	0.008	49.7	14.536	0.064	0.07	0.002	0.202	0.001	0.367	0.36
50642-3	2715.7	1.4	2.587	0.006	0.689	0.003	1.505	0.009	3.608	0.003	1.81E-15	7.7	0.011	1.140	0.007	60.7	14.674	0.045	0.05	0.001	0.196	0.001	0.256	0.47
50642-4	4568.1	1.3	5.695	0.024	0.804	0.007	2.708	0.017	3.198	0.003	3.99E-15	16.9	0.022	0.932	0.007	79.3	14.637	0.063	0.07	0.001	0.190	0.001	0.424	0.32
50642-5	3613.3	1.7	4.556	0.012	0.529	0.004	2.103	0.012	2.398	0.002	3.19E-15	13.5	0.023	0.905	0.006	80.4	14.670	0.040	0.05	0.001	0.198	0.001	0.257	0.46
50642-6	4565.8	2.5	5.420	0.014	0.732	0.004	2.361	0.010	3.777	0.003	3.79E-15	16.1	0.017	0.854	0.004	75.6	14.643	0.042	0.05	0.001	0.189	0.001	0.271	0.48
50642-7	3961.7	2.1	3.978	0.014	0.937	0.003	1.645	0.008	4.909	0.004	2.78E-15	11.8	0.009	0.811	0.005	63.4	14.523	0.057	0.06	0.001	0.191	0.001	0.364	0.38
50642-8	5448.8	3.1	6.254	0.012	0.923	0.003	12.118	0.014	4.818	0.004	4.38E-15	18.5	0.067	3.798	0.009	73.9	14.826	0.035	0.05	0.001	0.194	0.001	0.210	0.54
50642-9	1985.4	1.2	1.318	0.007	0.734	0.003	4.079	0.008	3.875	0.004	9.22E-16	3.9	0.028	6.068	0.035	42.3	14.704	0.092	0.10	0.002	0.199	0.001	0.543	0.27

Step ID	Relative Isotopic Abundances										Derived Results									Inverse Isochron Data				
	^{40}Ar ± 1σ		^{39}Ar ± 1σ		^{38}Ar ± 1σ		^{37}Ar ± 1σ		^{36}Ar ± 1σ		^{39}Ar Mol	^{39}Ar % of total	% $(^{36}Ar)_{Ca}$	Ca/K ± 1σ		$\%^{40}Ar^*$	Age (Ma) ± 1σ		w/±J	$^{36}Ar/^{40}Ar$ ± %1σ		$^{39}Ar/^{40}Ar$ ± %1σ		$^{36}Ar/^{39}Ar$ Er. Corr.
Sample 52, 5.655 ± 0.152 Ma, 26.17252 N 111.56977 W, EK62, [23], Packet 12, 40 mg hornblende, J = 0.0101 x10^{-3} ± 2.0 x10^{-8} (1σ)																								
50616-1	172.1	0.3	0.028	0.004	0.105	0.003	0.045	0.007	0.554	0.003	1.97E-17	5.8	0.002	3.1	0.7	4.9	5.462	1.007	1.01	0.591	0.003	14.451	0.000	0.01
50616-2	83.1	0.3	0.028	0.004	0.043	0.003	0.076	0.005	0.255	0.002	1.95E-17	5.7	0.008	5.3	0.9	9.2	5.010	0.846	0.85	0.843	0.003	14.641	0.000	0.01
50616-3	62.1	0.3	0.045	0.004	0.028	0.002	0.054	0.008	0.164	0.002	3.12E-17	9.2	0.009	2.4	0.4	21.8	5.492	0.551	0.55	1.214	0.003	8.950	0.001	0.02
50616-4	50.3	0.3	0.050	0.003	0.024	0.002	0.060	0.007	0.121	0.001	3.48E-17	10.2	0.013	2.4	0.3	28.9	5.302	0.410	0.41	1.382	0.002	6.823	0.001	0.04
50616-5	146.7	0.3	0.145	0.004	0.066	0.003	0.499	0.020	0.340	0.005	1.01E-16	29.8	0.039	6.7	0.3	31.4	5.781	0.248	0.25	1.530	0.002	2.669	0.001	0.02
50616-6	44.7	0.3	0.063	0.004	0.012	0.002	0.087	0.007	0.081	0.002	4.43E-17	13.0	0.028	2.7	0.3	46.4	5.929	0.410	0.41	2.236	0.002	6.338	0.001	0.04
50616-7	39.7	0.3	0.052	0.004	0.015	0.002	0.040	0.007	0.080	0.002	3.64E-17	10.7	0.013	1.5	0.3	40.2	5.582	0.484	0.48	2.891	0.002	7.440	0.001	0.03
50616-8	59.4	0.3	0.039	0.003	0.027	0.003	0.046	0.006	0.159	0.001	2.71E-17	8.0	0.008	2.3	0.4	21.0	5.845	0.569	0.57	1.080	0.003	8.750	0.001	0.03
50616-9	60.8	0.3	0.037	0.004	0.026	0.003	0.071	0.006	0.167	0.002	2.60E-17	7.7	0.011	3.8	0.5	18.7	5.549	0.703	0.70	1.155	0.003	11.552	0.001	0.02
50616-1	172.1	0.3	0.028	0.004	0.105	0.003	0.045	0.007	0.554	0.003	1.97E-17	5.8	0.002	3.1	0.7	4.9	5.462	1.007	1.01	0.591	0.003	14.451	0.000	0.01

Step ID	Relative Isotopic Abundances										Derived Results									Inverse Isochron Data				
	^{40}Ar ± 1σ		^{39}Ar ± 1σ		^{38}Ar ± 1σ		^{37}Ar ± 1σ		^{36}Ar ± 1σ		^{39}Ar Mol	^{39}Ar % of total	% $(^{36}Ar)_{Ca}$	Ca/K ± 1σ		$\%^{40}Ar^*$	Age (Ma) ± 1σ		w/±J	$^{36}Ar/^{40}Ar$ ± %1σ		$^{39}Ar/^{40}Ar$ ± %1σ		$^{36}Ar/^{39}Ar$ Er. Corr.
Sample F09, 3.180 ± 0.011 Ma, 26.07995 N 111.76418 W, EK62, [23], Packet 10, 400 mg groundmass, J = 0.0151 x10^{-3} ± 3.0 x10^{-8} (1σ)																								
50612-1	2881.9	1.7	2.020	0.007	1.684	0.004	0.917	0.010	8.940	0.008	1.41E-15	4.1	0.003	0.889	0.010	8.3	3.239	0.073	0.07	0.199	0.003	0.328	0.001	0.40
50612-2	3147.5	1.8	3.378	0.005	1.763	0.004	1.716	0.009	9.308	0.007	2.36E-15	6.9	0.005	0.996	0.005	12.6	3.203	0.044	0.04	0.191	0.003	0.168	0.001	0.61
50612-3	3004.6	1.7	4.596	0.005	1.596	0.004	2.150	0.012	8.364	0.006	3.22E-15	9.4	0.007	0.917	0.005	17.7	3.160	0.030	0.03	0.191	0.003	0.121	0.002	0.68
50612-4	2754.2	1.6	5.447	0.004	1.376	0.004	2.101	0.010	7.162	0.006	3.81E-15	11.2	0.008	0.756	0.004	23.2	3.191	0.023	0.02	0.198	0.003	0.098	0.002	0.69
50612-5	2905.7	1.7	6.754	0.005	1.396	0.004	2.223	0.009	7.176	0.005	4.73E-15	13.8	0.008	0.645	0.003	27.0	3.168	0.018	0.02	0.189	0.002	0.100	0.002	0.72
50612-6	2722.7	1.6	6.396	0.004	1.307	0.004	1.959	0.010	6.701	0.005	4.48E-15	13.1	0.008	0.600	0.003	27.3	3.163	0.018	0.02	0.193	0.002	0.095	0.002	0.72
50612-7	2491.0	1.4	5.558	0.004	1.217	0.004	1.772	0.010	6.236	0.005	3.89E-15	11.4	0.008	0.625	0.003	26.0	3.178	0.020	0.02	0.197	0.003	0.096	0.002	0.70
50612-8	3786.1	2.3	6.073	0.004	1.986	0.004	2.351	0.011	10.370	0.008	4.25E-15	12.4	0.006	0.759	0.004	19.1	3.239	0.029	0.03	0.196	0.003	0.097	0.002	0.71
50612-9	2788.8	1.6	2.837	0.005	1.562	0.004	1.558	0.010	8.224	0.007	1.99E-15	5.8	0.005	1.077	0.007	12.9	3.447	0.048	0.05	0.197	0.003	0.181	0.001	0.58
50612-10	1716.6	1.0	2.192	0.004	0.940	0.004	10.674	0.013	4.893	0.005	1.53E-15	4.5	0.058	9.543	0.021	15.8	3.384	0.039	0.04	0.205	0.003	0.204	0.001	0.52

Step ID	Relative Isotopic Abundances										Derived Results									Inverse Isochron Data				
	^{40}Ar ± 1σ		^{39}Ar ± 1σ		^{38}Ar ± 1σ		^{37}Ar ± 1σ		^{36}Ar ± 1σ		^{39}Ar Mol	^{39}Ar % of total	% $(^{36}Ar)_{Ca}$	Ca/K ± 1σ		$\%^{40}Ar^*$	Age (Ma) ± 1σ		w/±J	$^{36}Ar/^{40}Ar$ ± %1σ		$^{39}Ar/^{40}Ar$ ± %1σ		$^{36}Ar/^{39}Ar$ Er. Corr.
Sample 29, 5.592 ± 0.003 Ma, 25.97035 N 111.67056 W, EK63, Packet 35, 400 mg groundmass, J = 0.078 x10^{-3} ± 1.0 x10^{-8} (1σ)																								
61083-1	1515.7	2.3	6.444	0.110	1.133	0.050	0.775	0.043	4.281	0.005	4.51E-15	1.9	0.03	1.231	0.071	16.6	5.480	0.160	0.16	0.443	0.003	1.708	0.004	0.23
61083-2	925.4	0.5	16.626	0.021	0.367	0.004	1.487	0.006	0.845	0.003	1.16E-14	4.8	0.24	0.915	0.004	73.1	5.723	0.018	0.02	0.558	0.001	0.172	0.018	0.56
61083-3	748.9	0.4	15.804	0.017	0.252	0.003	1.245	0.005	0.361	0.003	1.11E-14	4.6	0.48	0.806	0.003	85.8	5.723	0.015	0.02	0.979	0.000	0.158	0.021	0.32
61083-4	2434.7	1.5	57.57	0.050	0.717	0.003	2.527	0.005	0.383	0.003	4.03E-14	16.6	0.92	0.450	0.001	95.4	5.675	0.009	0.01	0.963	0.000	0.146	0.024	0.33
61083-5	2991.7	1.7	71.537	0.059	0.87	0.004	2.813	0.005	0.377	0.003	5.01E-14	20.6	1.04	0.403	0.008	96.3	5.666	0.009	0.01	0.999	0.000	0.141	0.024	0.32
61083-6	3114.5	1.8	75.005	0.062	0.908	0.003	3.067	0.005	0.314	0.003	5.25E-14	21.6	1.35	0.420	0.001	97.1	5.669	0.009	0.01	1.142	0.000	0.142	0.024	0.28
61083-7	2075.7	1.2	49.79	0.041	0.613	0.004	2.174	0.004	0.241	0.003	3.49E-14	14.4	1.25	0.448	0.001	96.6	5.665	0.009	0.01	1.431	0.000	0.142	0.024	0.22
61083-8	1470.8	0.8	34.702	0.032	0.451	0.004	1.683	0.004	0.251	0.003	2.43E-14	10.0	0.93	0.498	0.001	95.0	5.664	0.010	0.01	1.375	0.000	0.147	0.024	0.23
61083-9	841.2	0.5	19.221	0.016	0.279	0.003	1.126	0.004	0.244	0.004	1.35E-14	5.5	0.64	0.601	0.002	91.5	5.632	0.012	0.01	1.520	0.000	0.143	0.023	0.21

Step ID	Relative Isotopic Abundances										Derived Results									Inverse Isochron Data				
	^{40}Ar ± 1σ		^{39}Ar ± 1σ		^{38}Ar ± 1σ		^{37}Ar ± 1σ		^{36}Ar ± 1σ		^{39}Ar Mol	^{39}Ar % of total	% $(^{36}Ar)_{Ca}$	Ca/K ± 1σ		% $^{40}Ar^*$	Age (Ma) ± 1σ		w/±J	$^{36}Ar/^{40}Ar$ ± %1σ		$^{39}Ar/^{40}Ar$ ± %1σ		$^{36}Ar/^{39}Ar$ Er. Corr.
Sample 34, 2.738 ± 0.002 Ma, 25.55603 -111.72045, EK63, Packet 34, 400 mg groundmass, J = 0.079 x10^{-3} ± 8.0 x10^{-8} (1σ)																								
61085-1	3459.6	28.000	13.57	0.76	3.053	0.260	1.096	0.210	10.985	0.053	9.50E-15	3.6	0.01	0.811	0.162	6.2	2.248	0.384	0.38	1.019	0.003	5.628	0.004	0.1
61085-2	2335.0	1.402	78.93	0.08	1.429	0.004	1.232	0.004	2.647	0.004	5.53E-14	21.1	0.06	0.157	0.000	66.5	2.806	0.009	0.01	0.428	0.001	0.153	0.034	0.7
61085-3	2145.9	1.202	83.01	0.08	1.290	0.004	0.888	0.004	1.714	0.003	5.81E-14	22.2	0.07	0.108	0.000	76.4	2.816	0.007	0.01	0.443	0.001	0.147	0.039	0.7
61085-4	1590.4	1.003	62.25	0.06	0.956	0.004	0.628	0.003	1.218	0.003	4.36E-14	16.6	0.07	0.101	0.001	77.4	2.819	0.007	0.01	0.486	0.001	0.154	0.039	0.7
61085-5	1007.4	0.495	38.08	0.04	0.610	0.003	0.417	0.003	0.860	0.003	2.67E-14	10.2	0.07	0.110	0.001	74.8	2.821	0.008	0.01	0.567	0.001	0.149	0.038	0.6
61085-6	811.8	0.396	31.18	0.03	0.486	0.003	0.379	0.003	0.654	0.003	2.18E-14	8.3	0.08	0.122	0.001	76.2	2.828	0.008	0.01	0.633	0.001	0.147	0.038	0.5
61085-7	685.2	0.357	26.39	0.03	0.408	0.004	0.389	0.003	0.553	0.003	1.85E-14	7.0	0.10	0.149	0.001	76.2	2.820	0.009	0.01	0.676	0.001	0.152	0.039	0.5
61085-8	580.5	0.357	22.88	0.02	0.354	0.003	0.405	0.004	0.435	0.003	1.60E-14	6.1	0.13	0.178	0.002	77.9	2.817	0.009	0.01	0.800	0.001	0.157	0.039	0.4
61085-9	635.5	0.338	15.76	0.02	0.410	0.003	11.233	0.011	1.124	0.003	1.10E-14	4.2	1.37	7.195	0.011	48.5	2.793	0.018	0.02	0.506	0.002	0.157	0.025	0.6
61085-10	135.5	0.080	2.40	0.01	0.089	0.003	3.210	0.004	0.308	0.003	1.68E-15	0.6	1.42	13.504	0.041	33.7	2.726	0.057	0.06	1.042	0.002	0.297	0.018	0.3

Figure A2.1: Zircon U-Pb concordia. Age estimates were calculated using Isoplot v3.6 (Ludwig, 2008).

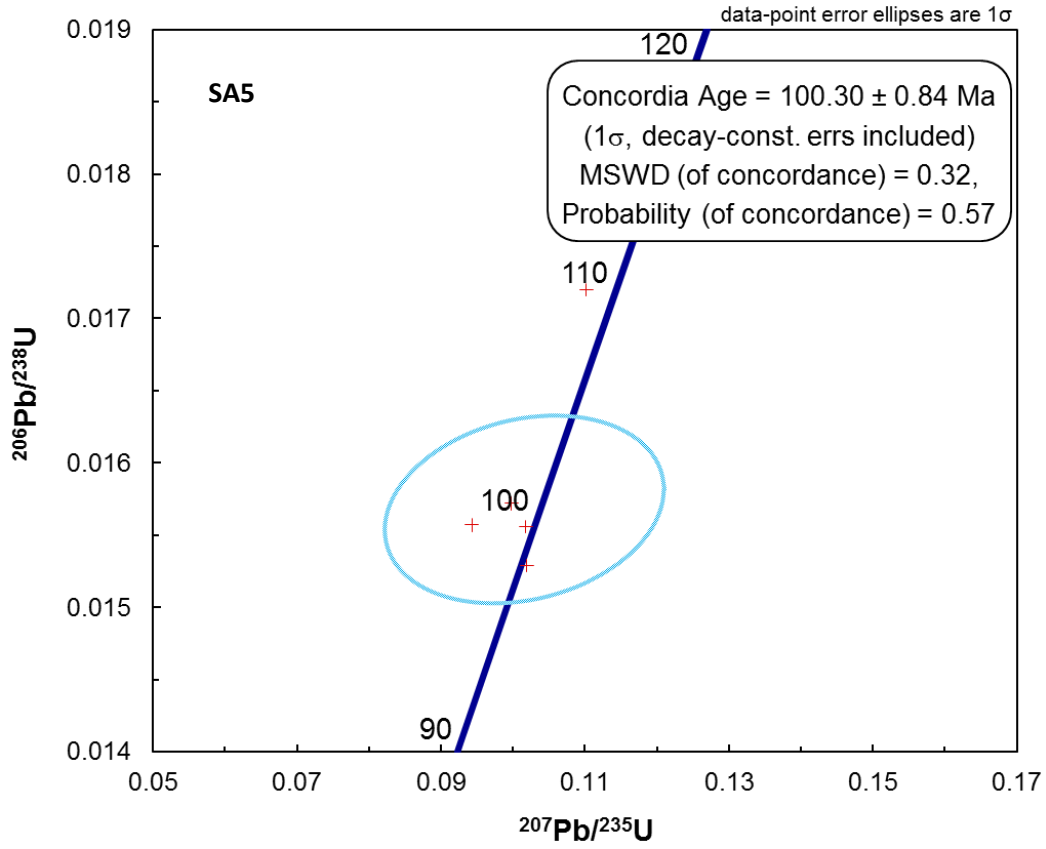

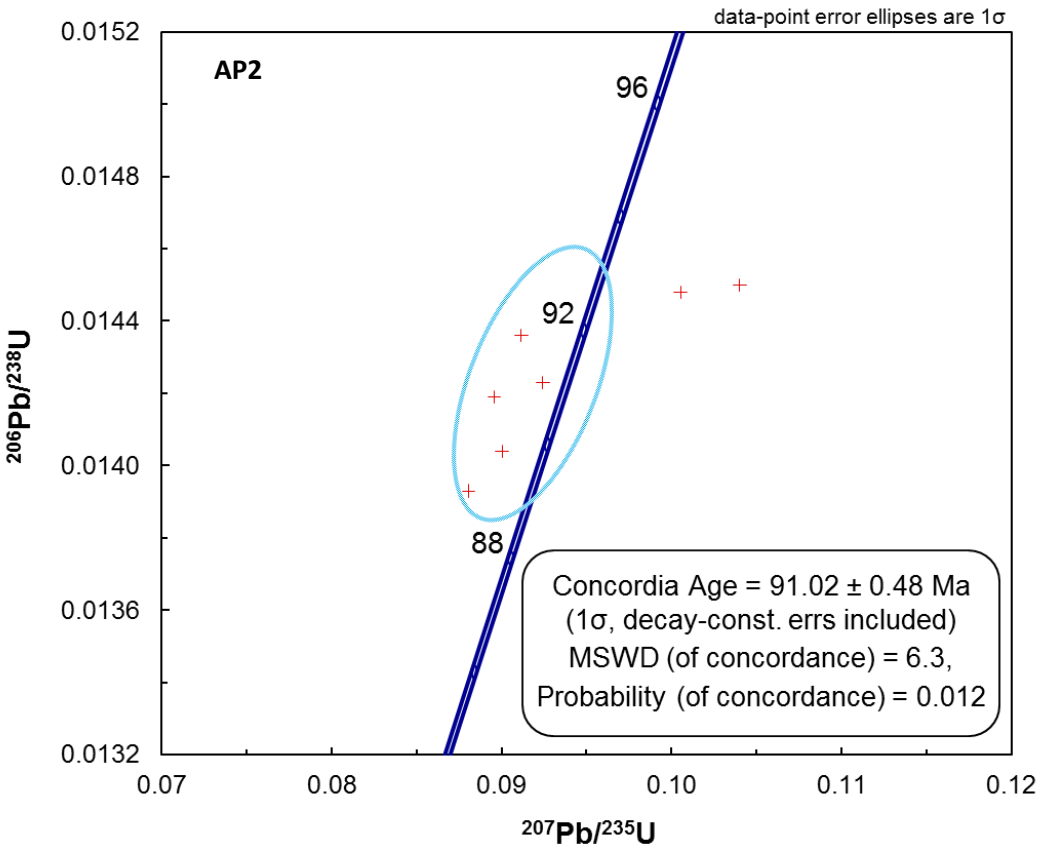

Figure A2.2: $^{40}Ar/^{39}Ar$ step heating plots, showing plateau and integrated ages. Numbers indicate sample.

27

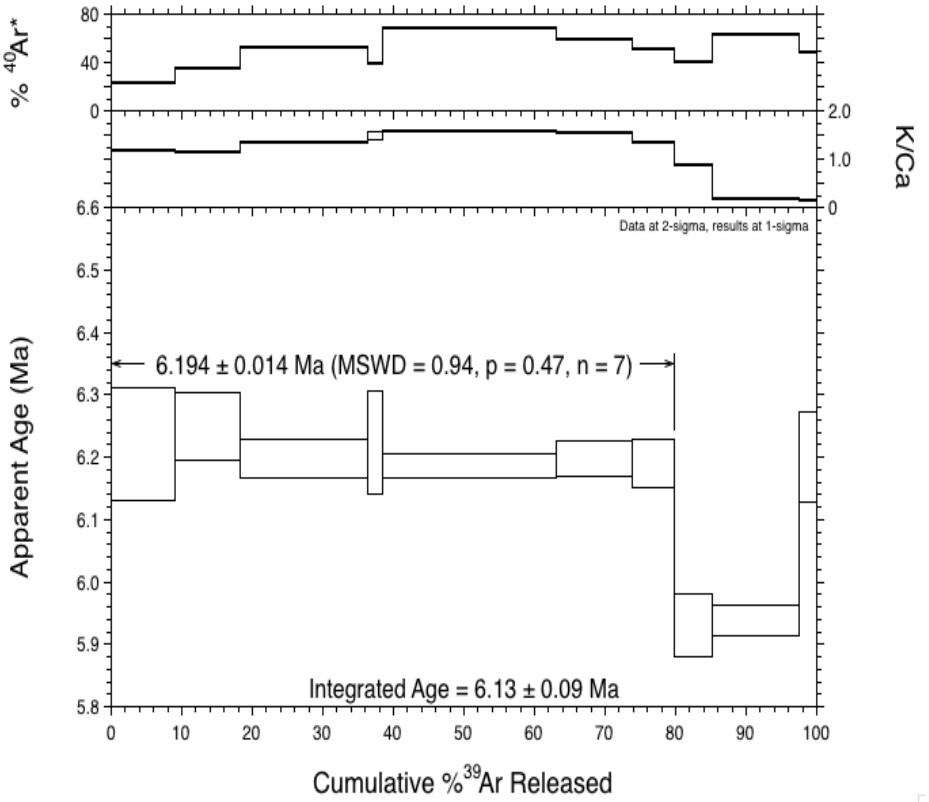

31

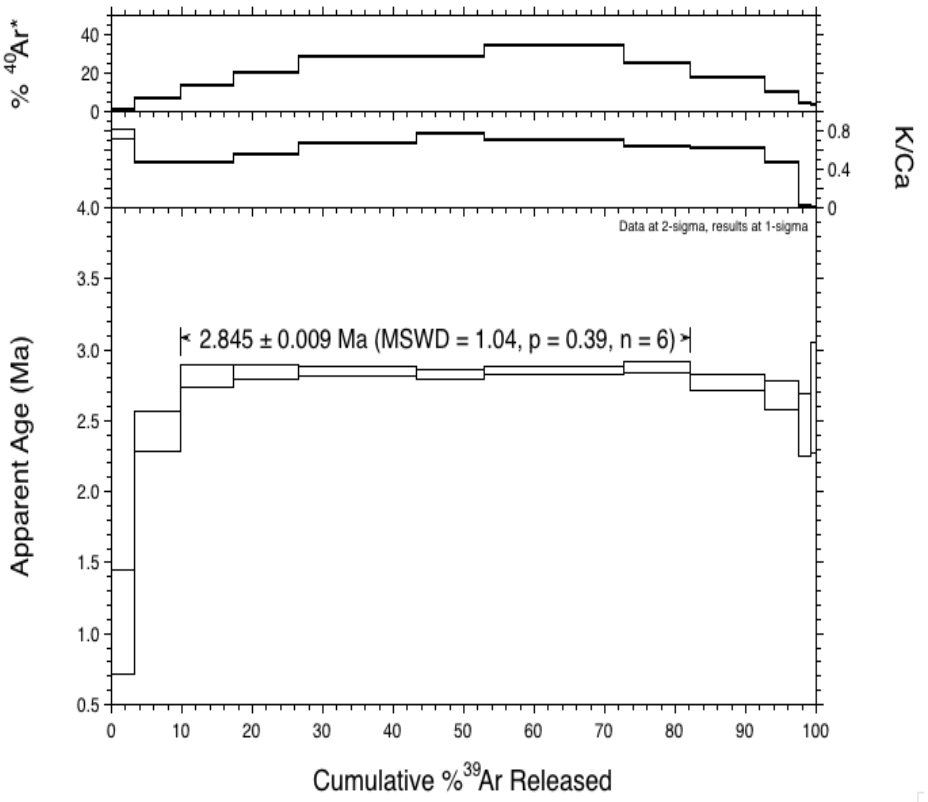

40

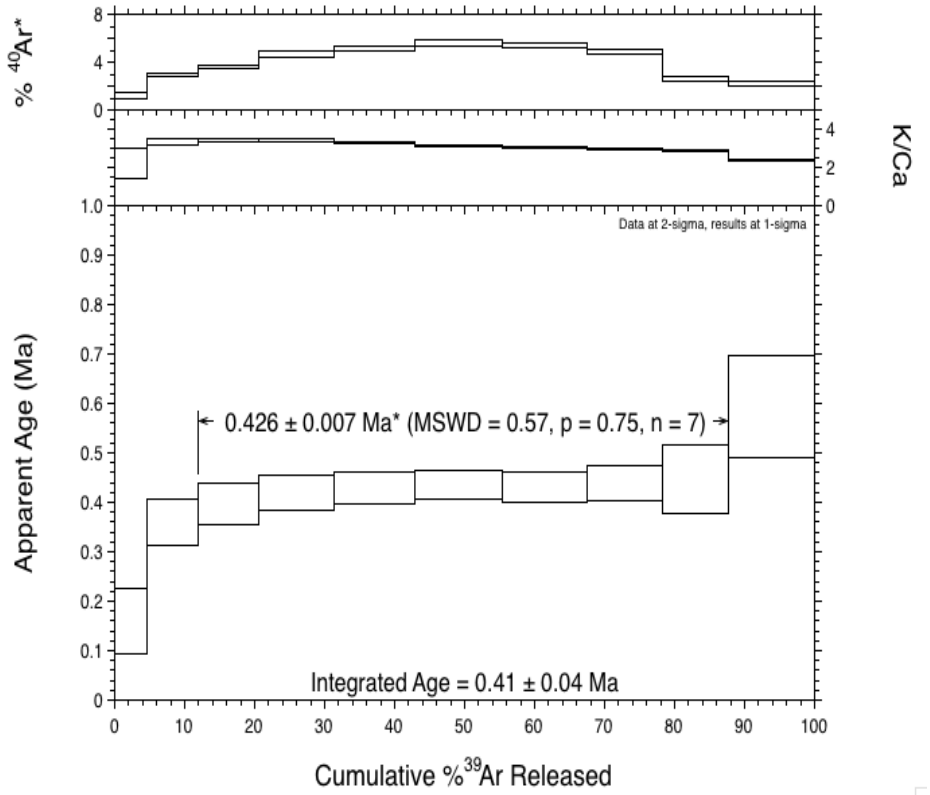
% 40Ar*
K/Ca
Data at 2-sigma, results at 1-sigma
Apparent Age (Ma)
0.426 ± 0.007 Ma* (MSWD = 0.57, p = 0.75, n = 7)
Integrated Age = 0.41 ± 0.04 Ma
Cumulative %39Ar Released

44

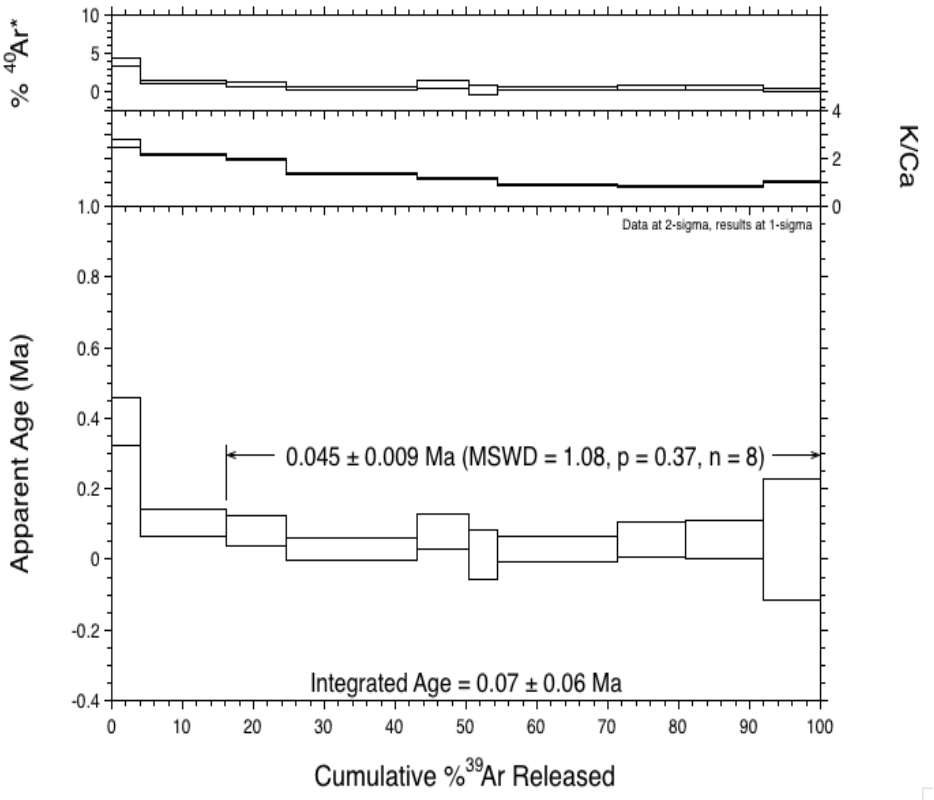
% 40Ar*
K/Ca
Data at 2-sigma, results at 1-sigma
Apparent Age (Ma)
0.045 ± 0.009 Ma (MSWD = 1.08, p = 0.37, n = 8)
Integrated Age = 0.07 ± 0.06 Ma
Cumulative %39Ar Released

47

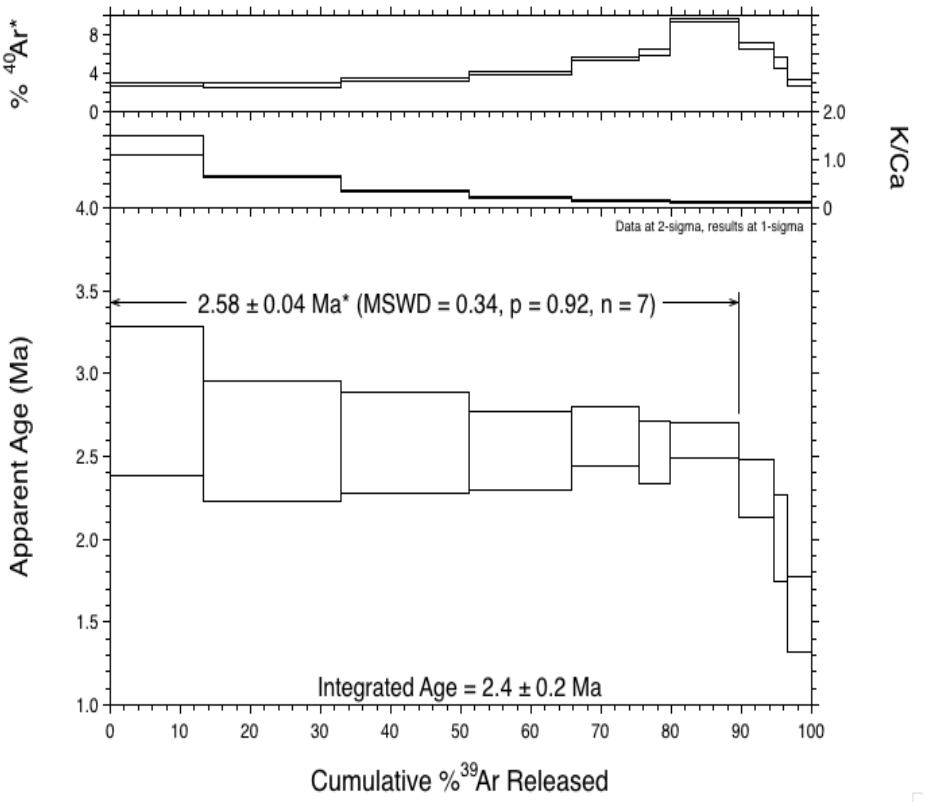
% 40Ar*
K/Ca
Data at 2-sigma, results at 1-sigma
2.58 ± 0.04 Ma* (MSWD = 0.34, p = 0.92, n = 7)
Apparent Age (Ma)
Integrated Age = 2.4 ± 0.2 Ma
Cumulative % 39Ar Released

48

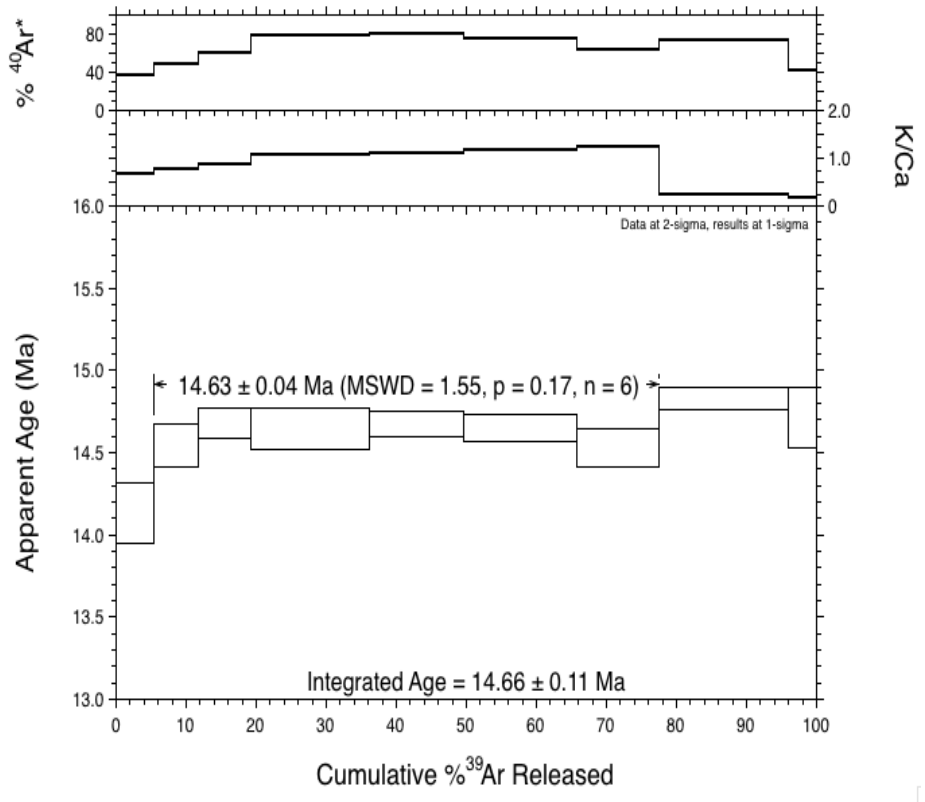
% 40Ar*
K/Ca
Data at 2-sigma, results at 1-sigma
14.63 ± 0.04 Ma (MSWD = 1.55, p = 0.17, n = 6)
Apparent Age (Ma)
Integrated Age = 14.66 ± 0.11 Ma
Cumulative % 39Ar Released

52

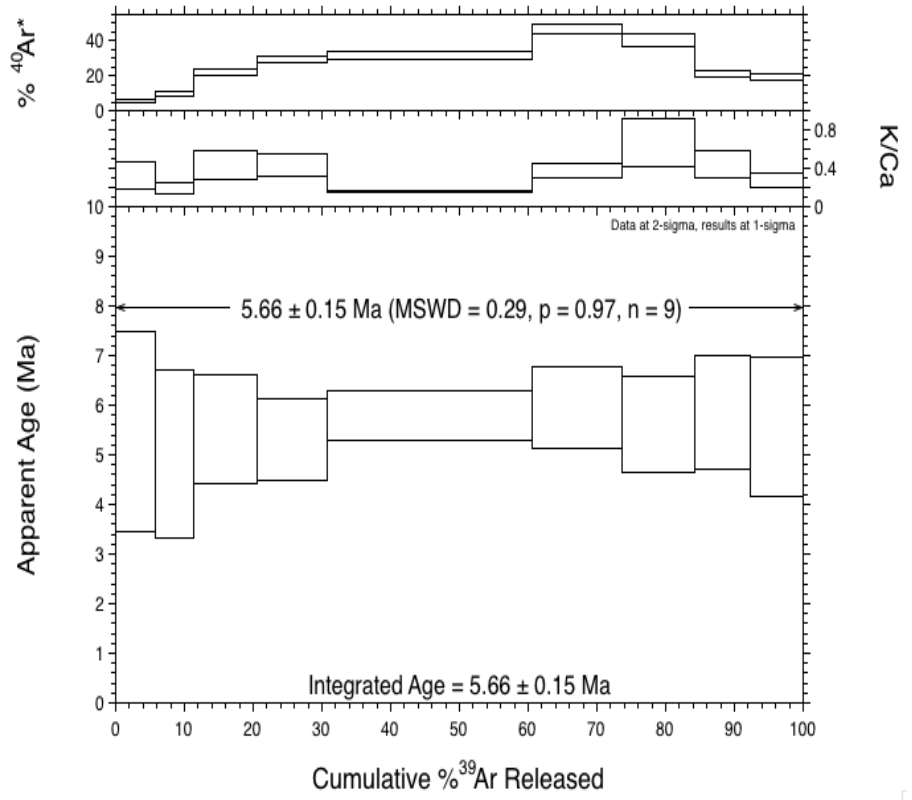
% 40Ar*
K/Ca
Data at 2-sigma, results at 1-sigma
5.66 ± 0.15 Ma (MSWD = 0.29, p = 0.97, n = 9)
Apparent Age (Ma)
Integrated Age = 5.66 ± 0.15 Ma
Cumulative %39Ar Released

F09

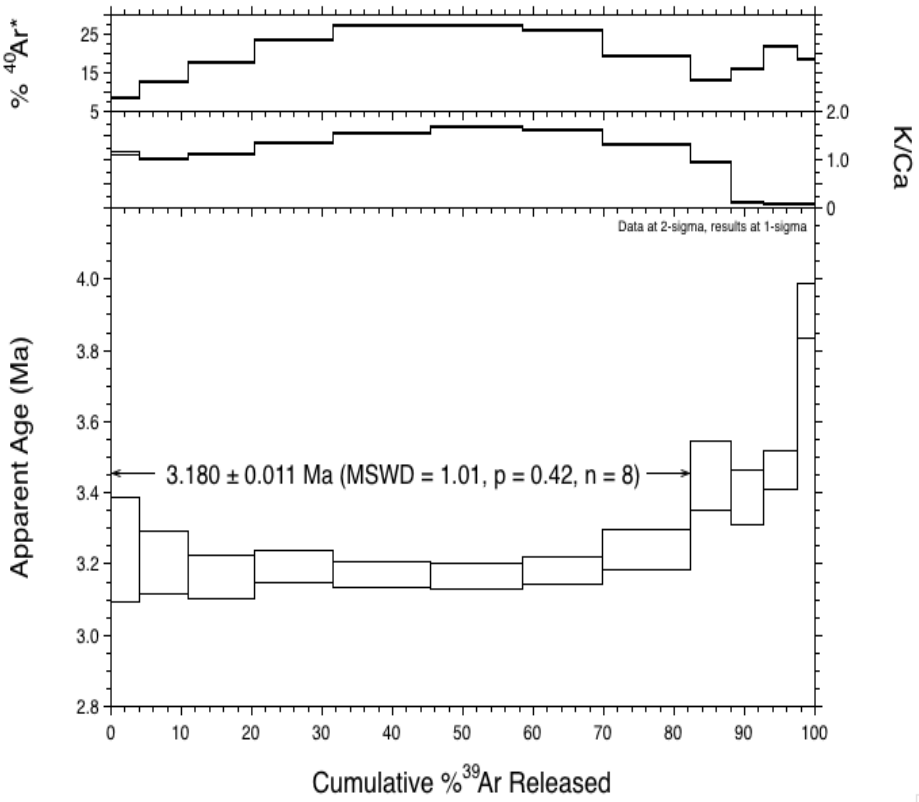
% 40Ar*
K/Ca
Data at 2-sigma, results at 1-sigma
3.180 ± 0.011 Ma (MSWD = 1.01, p = 0.42, n = 8)
Apparent Age (Ma)
Cumulative %39Ar Released

29

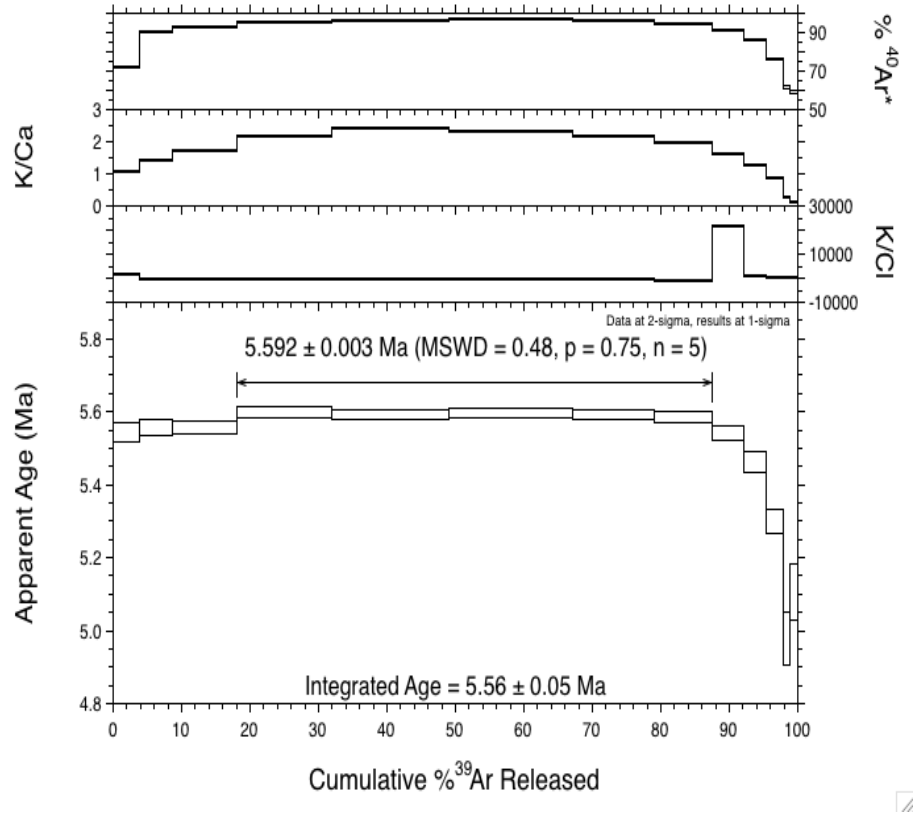
% 40Ar*
K/Ca
K/Cl
Data at 2-sigma, results at 1-sigma
5.592 ± 0.003 Ma (MSWD = 0.48, p = 0.75, n = 5)
Apparent Age (Ma)
Integrated Age = 5.56 ± 0.05 Ma
Cumulative %39Ar Released

34

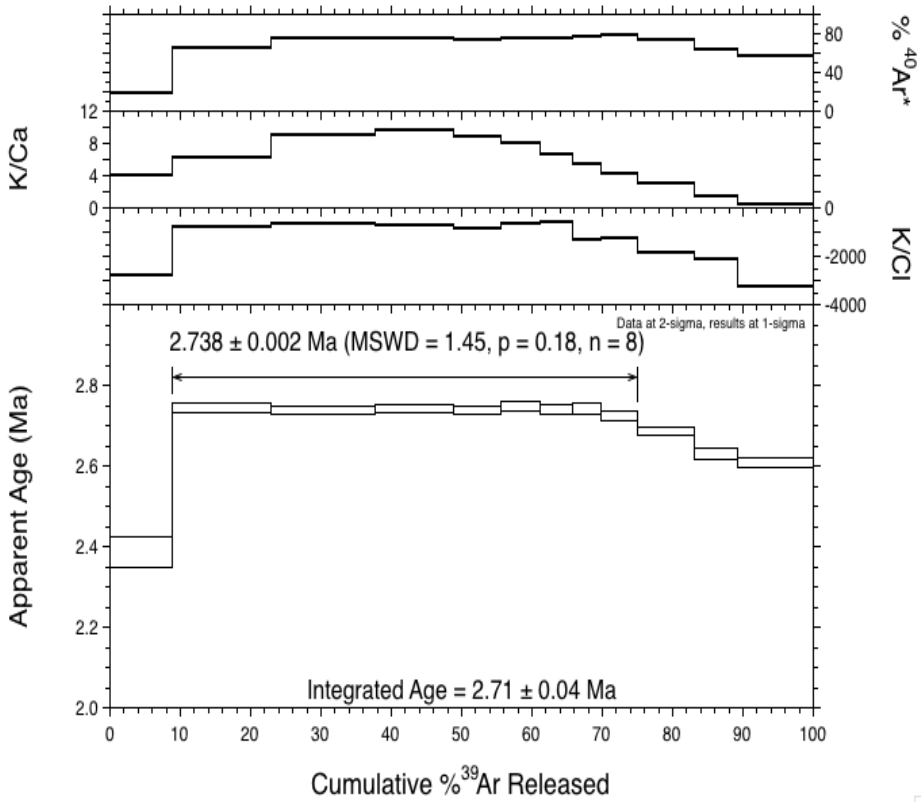
% 40Ar*
K/Ca
K/Cl
Data at 2-sigma, results at 1-sigma
2.738 ± 0.002 Ma (MSWD = 1.45, p = 0.18, n = 8)
Apparent Age (Ma)
Integrated Age = 2.71 ± 0.04 Ma
Cumulative %39Ar Released

Figure A2.3: $^{40}Ar/^{39}Ar$ inverse isochron plots. Numbers indicate sample.

27

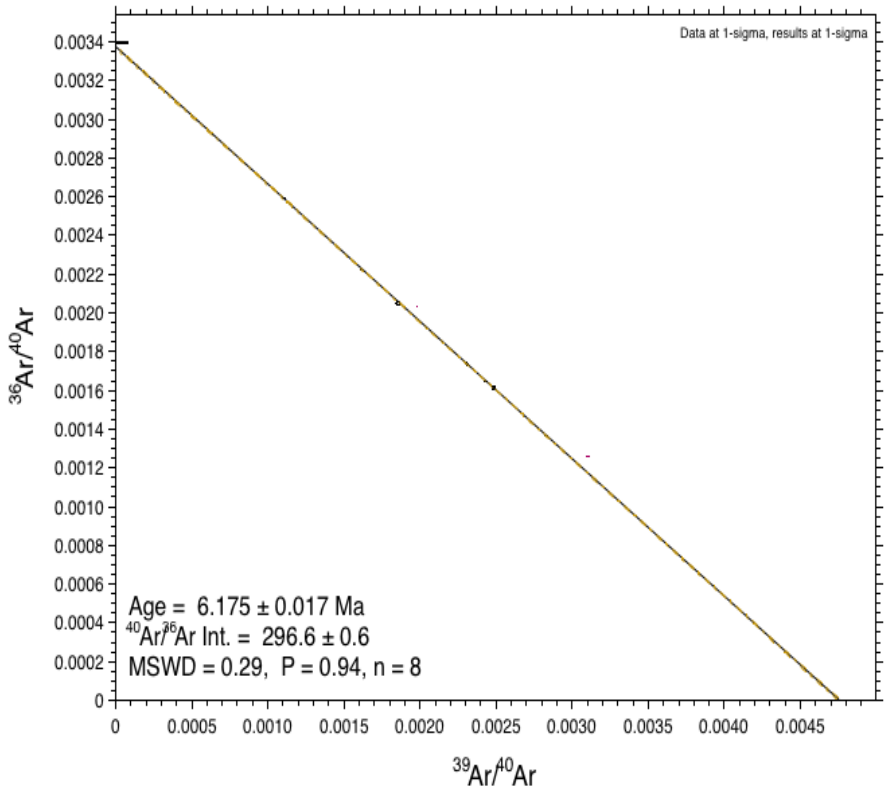

31

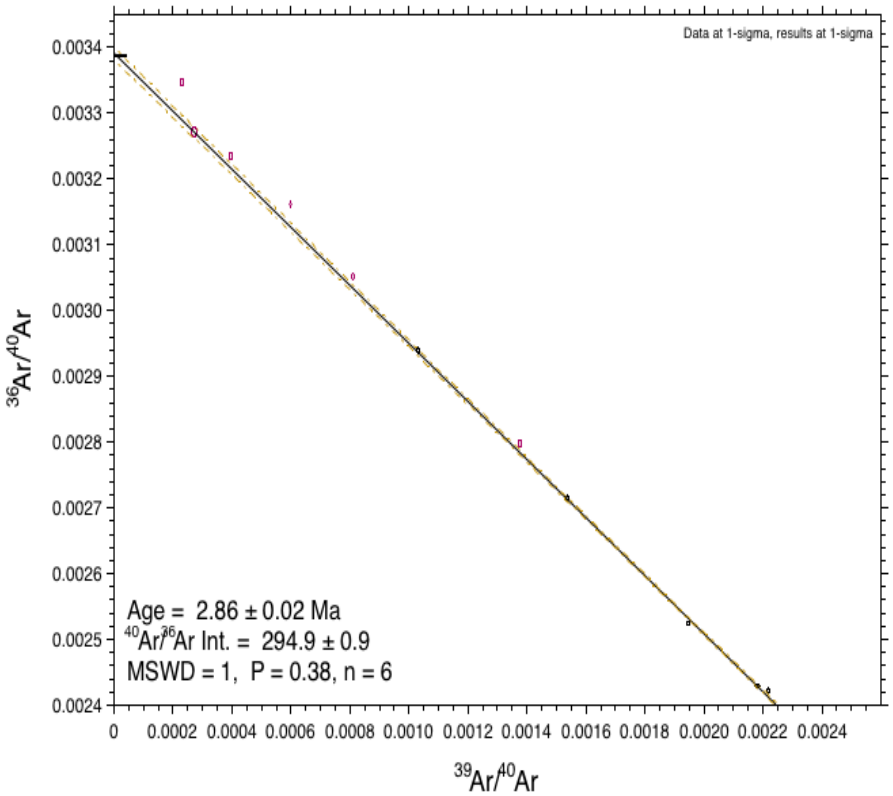

40

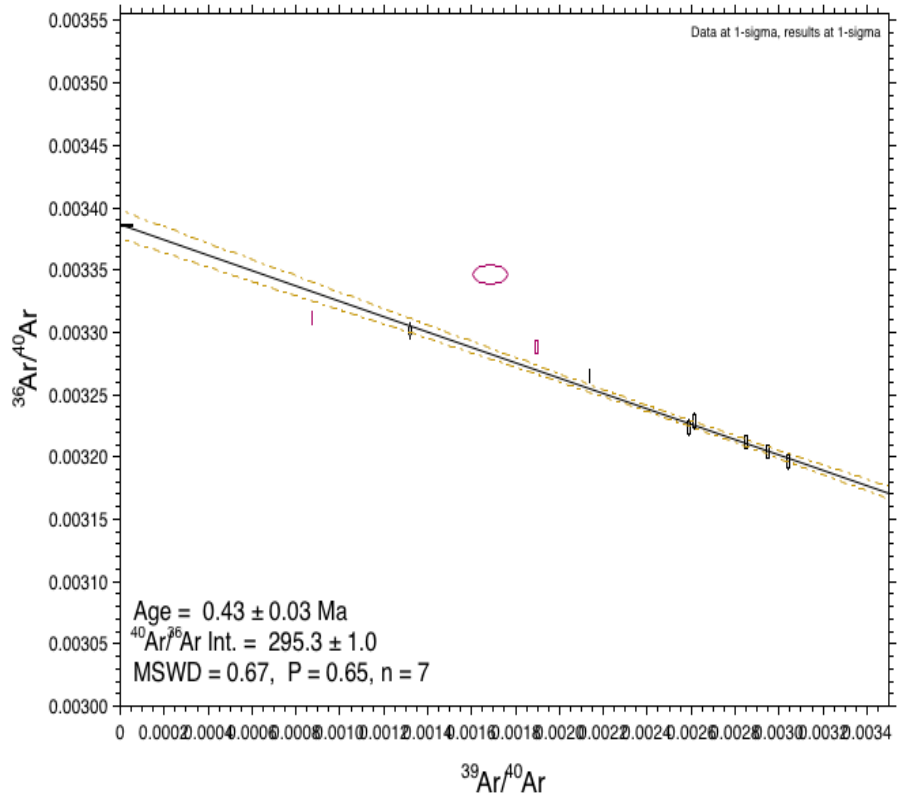
Data at 1-sigma, results at 1-sigma
Age = 0.43 ± 0.03 Ma
40Ar/36Ar Int. = 295.3 ± 1.0
MSWD = 0.67, P = 0.65, n = 7
36Ar/40Ar
39Ar/40Ar

44

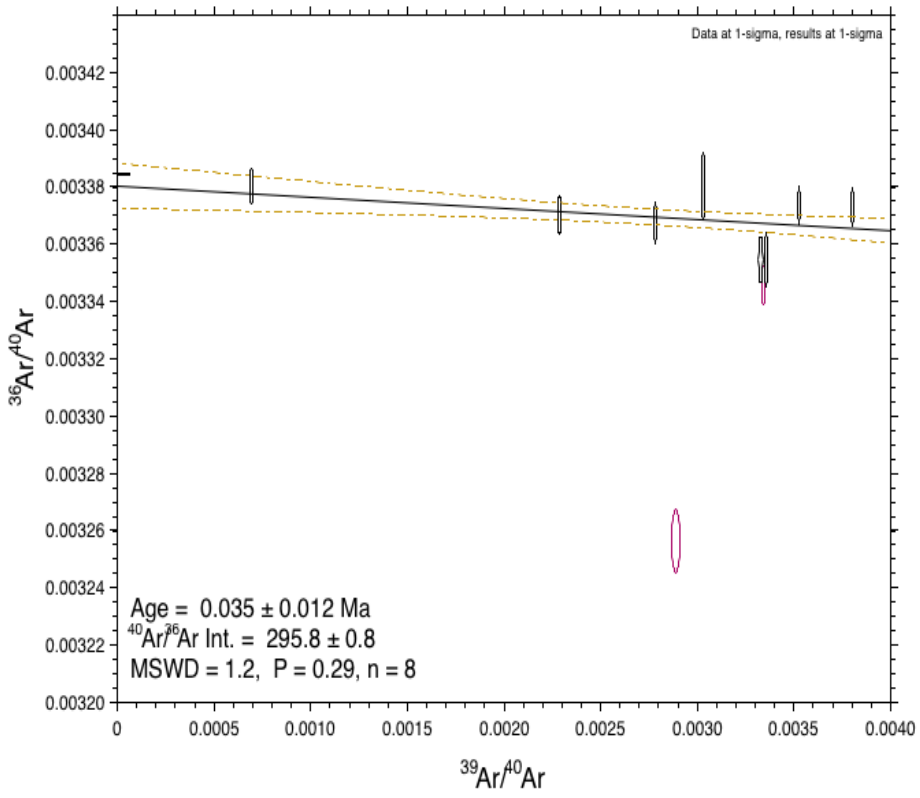
Data at 1-sigma, results at 1-sigma
Age = 0.035 ± 0.012 Ma
40Ar/36Ar Int. = 295.8 ± 0.8
MSWD = 1.2, P = 0.29, n = 8
36Ar/40Ar
39Ar/40Ar

47

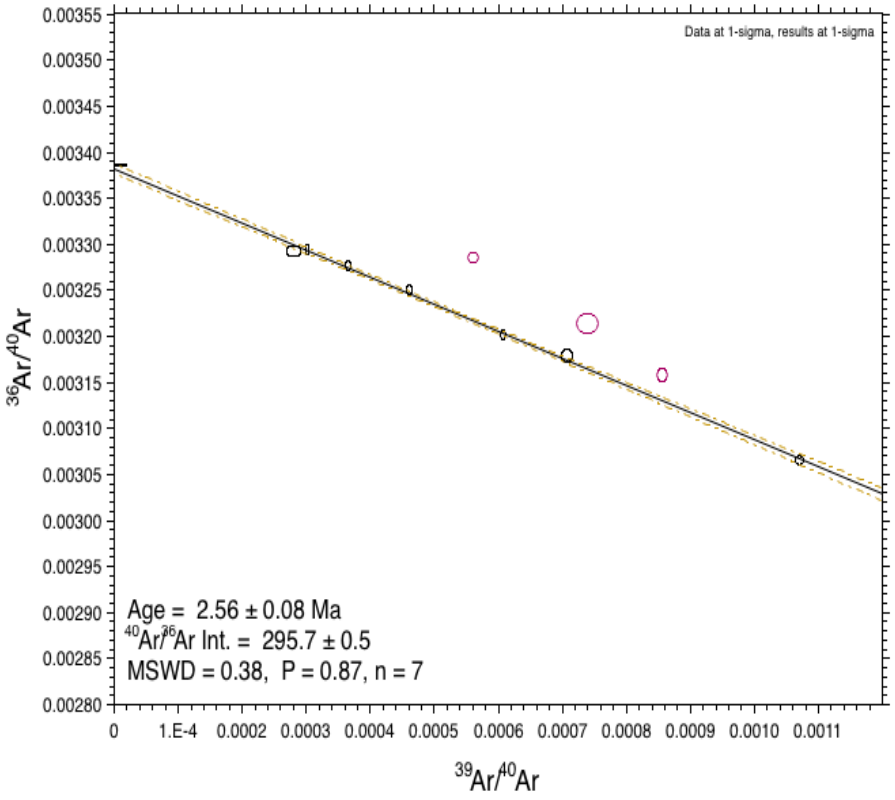
Data at 1-sigma, results at 1-sigma
Age = 2.56 ± 0.08 Ma
40Ar/36Ar Int. = 295.7 ± 0.5
MSWD = 0.38, P = 0.87, n = 7
36Ar/40Ar
39Ar/40Ar

48

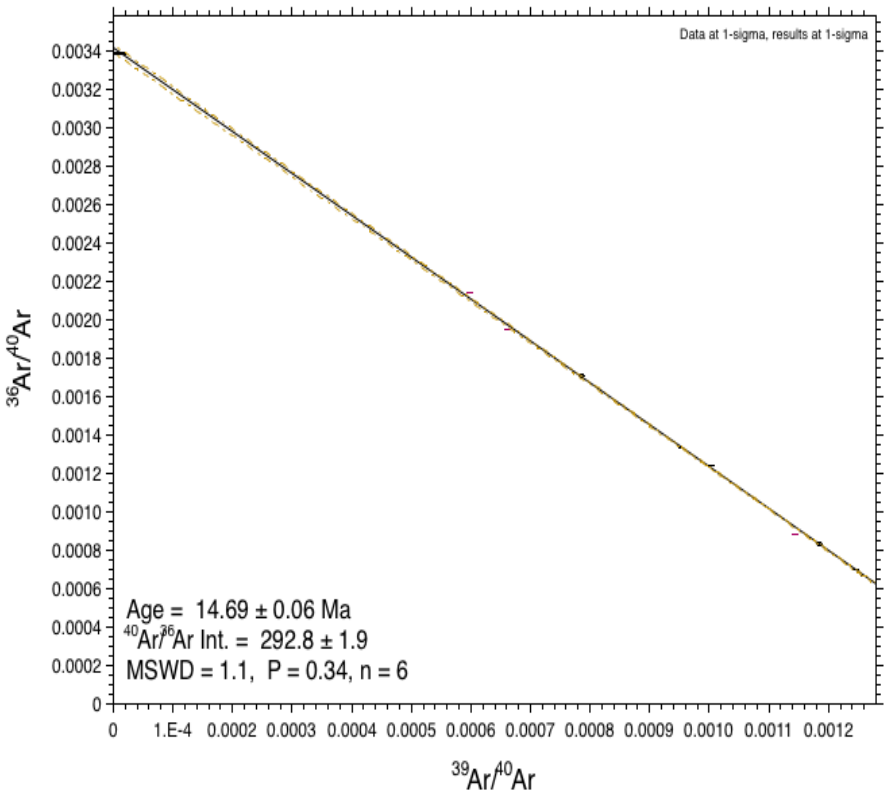
Data at 1-sigma, results at 1-sigma
Age = 14.69 ± 0.06 Ma
40Ar/36Ar Int. = 292.8 ± 1.9
MSWD = 1.1, P = 0.34, n = 6
36Ar/40Ar
39Ar/40Ar

52

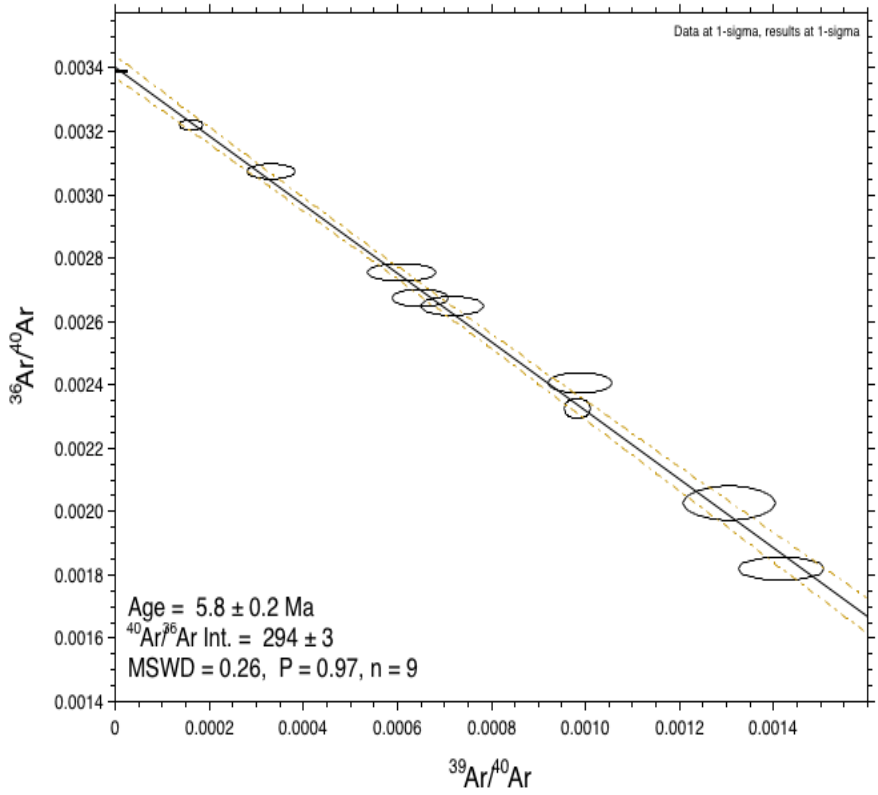
Data at 1-sigma, results at 1-sigma
$^{36}Ar/^{40}Ar$
$^{39}Ar/^{40}Ar$
Age = 5.8 ± 0.2 Ma
$^{40}Ar/^{36}Ar$ Int. = 294 ± 3
MSWD = 0.26, P = 0.97, n = 9

F09

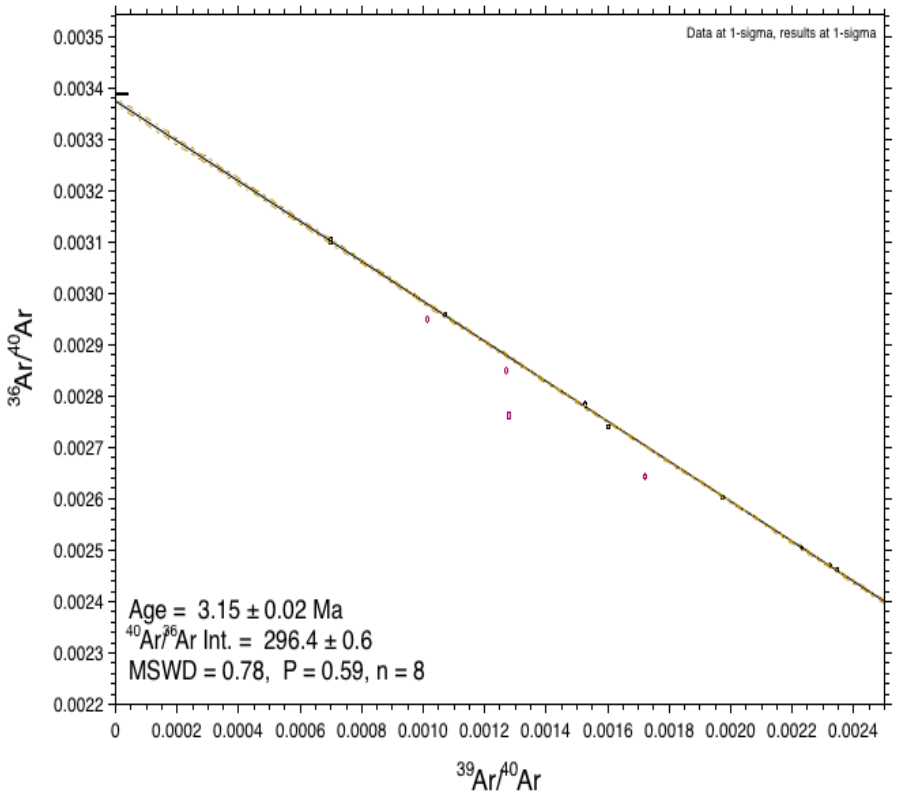
Data at 1-sigma, results at 1-sigma
$^{36}Ar/^{40}Ar$
$^{39}Ar/^{40}Ar$
Age = 3.15 ± 0.02 Ma
$^{40}Ar/^{36}Ar$ Int. = 296.4 ± 0.6
MSWD = 0.78, P = 0.59, n = 8

29

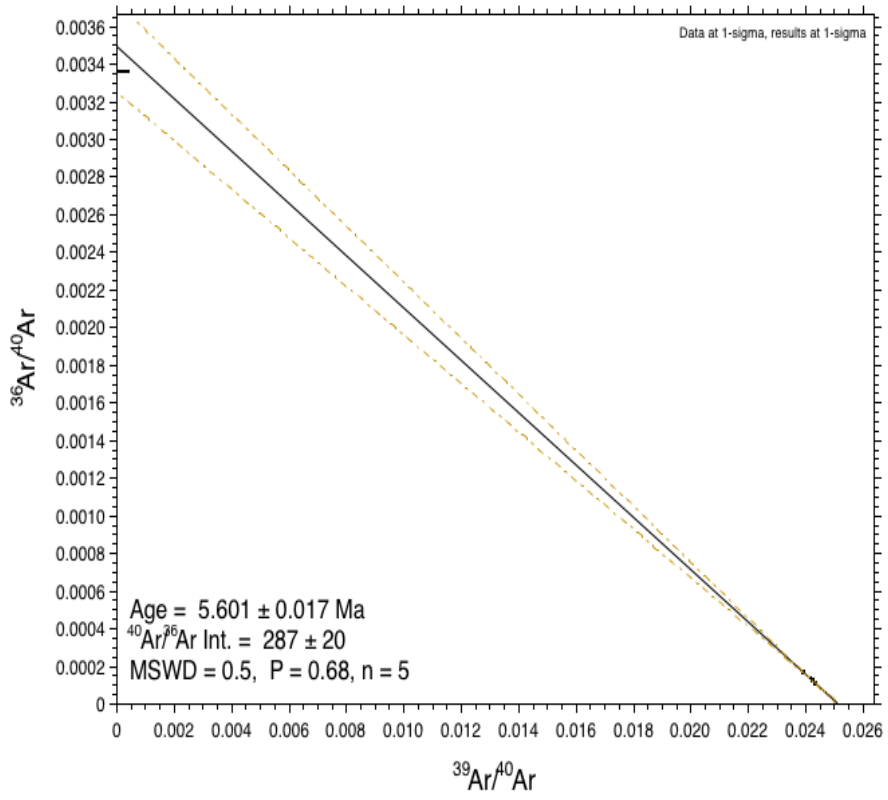
Data at 1-sigma, results at 1-sigma
Age = 5.601 ± 0.017 Ma
40Ar/36Ar Int. = 287 ± 20
MSWD = 0.5, P = 0.68, n = 5
36Ar/40Ar
39Ar/40Ar

34

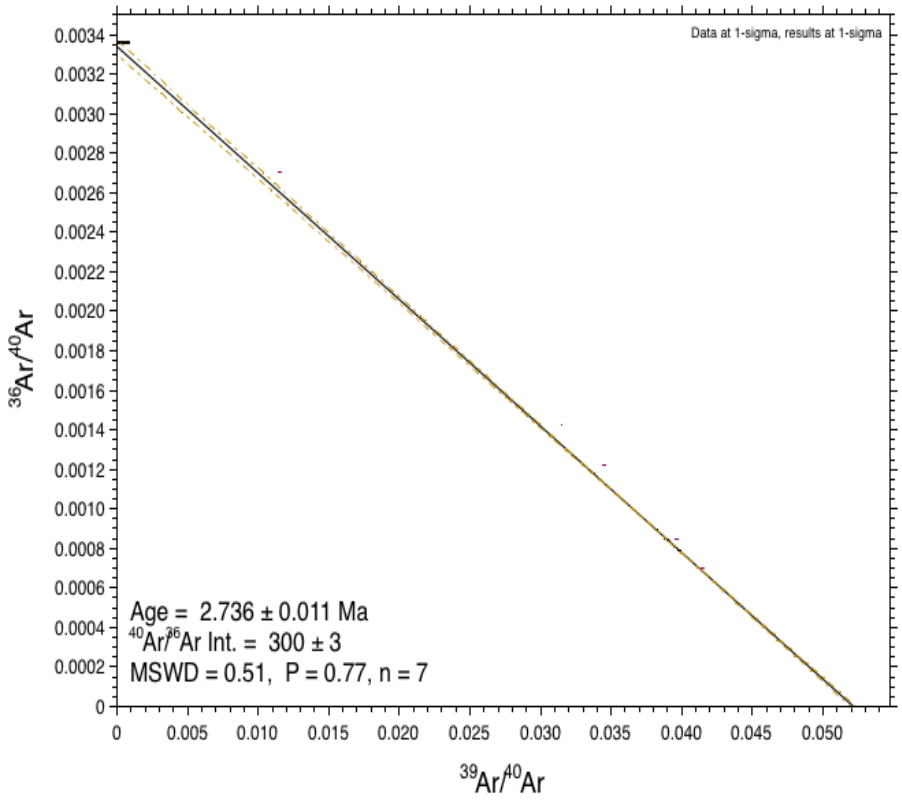
Data at 1-sigma, results at 1-sigma
Age = 2.736 ± 0.011 Ma
40Ar/36Ar Int. = 300 ± 3
MSWD = 0.51, P = 0.77, n = 7
36Ar/40Ar
39Ar/40Ar

A2.2 References

Ludwig, K.R., 2008, Isoplot 3.6: A geochronological toolkit for Microsoft Excel: Berkeley Geochronological Centre Special Publication No.4.

Mark, D.F., Barfod, D., Stuart, F.M., and Imlach, J., 2009, The ARGUS multicollector noble gas mass spectrometer: Performance for $^{40}Ar/^{39}Ar$ geochronology: Geochemistry Geophysics Geosystems, v. 10, DOI: 10.1029/2009GC002643.

Nomade, S., Renne, P., Vogel, N., Deino, A., Sharp, W., Becker, T., Jaouni, A., and Mundil, R., 2005, Alder Creek sanidine (ACs-2): A Quaternary Ar/Ar dating standard tied to the Cobb Mountain geomagnetic event: Chemical Geology, v. 218, no. 3-4, p. 315–338.